Università degli Studi di Pavia

Dipartimento di Fisica Nucleare e Teorica
Dottorato di Ricerca in Fisica - XIV ciclo

# The RPC detectors and the muon system for the CMS experiment at the LHC

Tesi di Dottorato di Giacomo Luca BRUNO



Anno Accademico 2000-2001

# Contents

# Introduction

One of the most important open issues in today's particle physics is the verification of the electroweak symmetry breaking mechanism, which is presently believed to explain the origin of the mass of the elementary particles.
The Standard Model of the electroweak interaction is the simplest theory consistent with present experimental observations which, at the same time, is capable of accommodating the symmetry breaking mechanism. This theoretical model predicts the existence of an undiscovered particle: the Higgs boson.
Moreover, extensions of the Standard Model, which would permit to eliminate some theoretical drawbacks of this basic model, predict the existence of several new elementary particles. These extended models, called supersymmetric theories, also have the attractive feature of providing a theoretical framework in which to include all known fundamental interactions.
The Higgs boson, like the other new particles, is an elusive particle due to its expected high mass and its extremely low production cross section. To permit its discovery, if ever, and in general to extend up to the TeV scale the energy range where to search for new physics phenomena, a very powerful accelerator, the Large Hadron Collider (LHC), is being constructed at the European Laboratory for Nuclear Research (CERN) in Geneva (Switzerland).

The work described in this thesis has concerned the muon detection system of the Compact Muon Solenoid (CMS) experiment, which is one of the four approved experiments that will study the collisions produced by the LHC.
Muons, which are well known elementary particles, play a central role in the LHC experiments and it is not by chance that they appear in the name itself of the experiment. Their detection system must also accomplish one of the most challenging tasks of any LHC experiment: the event on-line selection. In this respect the muon system is a basic element of what is called the experiment trigger system.
The CMS muon system comprises two subsystems of detectors: one of them is based on

precise wire chambers, the other on fast planar detectors, the Resistive Plate Chambers (RPCs). In particular the work has focused on the RPC detectors and on the trigger system based on them.
The thesis includes the analysis of beam test data on two RPC prototypes for CMS as well as a simulation study of the RPC trigger system. The latter results are presented in the general context of the global CMS First Level Trigger.
A work concerning the development of the CMS High Level Trigger is also discussed in this manuscript. These results show the performance in muon track reconstruction of the muon system stand-alone and of the muon system/inner tracker combined measurement with emphasis on the use of RPC information. A final study has been carried out in order to test, by means of simulation, the performance of the First and High Level Trigger on some representative physics channels.

The thesis is organised as follows.
An overview of the motivations and of the physics studies that will be done at the LHC is given in chapter 1. The CMS detector is also described there.
The general CMS First Level Muon Trigger and its performance is presented in chapter 2.
Chapter 3 is dedicated to the data analysis of a beam test carried out on two RPC prototypes for CMS. In the same chapter the description of the RPC operating principle is given.
The obtained experimental results on the performance of the RPCs are used in chapter 4, which is dedicated to a detailed simulation study of the RPC trigger system. Among various results, it is demonstrated that the baseline design of the RPC system is inadequate to handle false triggers caused by RPC noise and spurious hits due to neutral particle background.
Proposed modifications of the RPC trigger system and the resulting performance are presented in chapter 5.
The performance of the High Level Trigger in muon track reconstruction is discussed in chapter 6. In the same chapter the event selection efficiency of the First and High Level Trigger is analysed for some representative physics channels.

# Chapter 1

# The LHC and the CMS detector

## 1.1 Theoretical introduction

### 1.1.1 Fundamental interactions and elementary particles

All matter making up our universe is presently believed to consist of a few elementary constituents. These constituents are called elementary particles and can be divided into two main categories: fermions and bosons. The difference between the two families resides in the spin, which in simple words is the particle intrinsic angular momentum. Fermions have spin that is a half integer multiple of $\hbar$ whereas bosons have spin that is integer multiple of $\hbar$.

Elementary particles are then characterised by the way they interact among each other. Four different fundamental interactions are known to date: electromagnetic, weak, strong and gravitational. There are strong indications that the fundamental interactions can be well described in terms of quantum field theories related to particular gauge symmetries [1]. Among various features, such theories have the fundamental property of assuring renormalisability, which is a property of the theory that assures that its predictions in terms of a finite number of parameters (like particle masses and coupling constants) remain finite at any order in the perturbative computation. In the context of gauge field theories, bosons come into play as they are associated to the symmetry transformations that leave invariant the Lagrangian of the theory.

The theory itself is built to describe a particular interaction among the fermions. For this reason bosons are often referred to as the mediators of the interactions among the fermions. The known fundamental interactions with their associated bosons are listed in Tab.1.1. Not all fermions undergo all the four interactions. Indeed there are two families of fermions:

| **Interaction** | **Mediating bosons** | **Gauge group** |
|---|---|---|
| Electromagnetic and Weak | $\gamma$, $Z^0$, $W^+$, $W^-$ | $SU(2)_L \times U(1)_Y$ |
| Strong | 8 different gluons | $SU(3)$ |
| Gravitational | graviton (?) | ? |

Table 1.1: Known fundamental interactions and their description in terms of quantum gauge field theories.

| **Generation** / **Fermion** | 1 | 2 | 3 |
|---|---|---|---|
| Quarks | u d | c s | t b |
| Leptons | e $\nu_e$ | $\mu$ $\nu_\mu$ | $\tau$ $\nu_\tau$ |

Table 1.2: Known elementary fermions divided by generation.

leptons and quarks. The latter interact via all four interactions while the former do not interact via the strong force. Leptons and quarks come into 3 generations as indicated in Tab.1.2.

### 1.1.2 The Standard Model of the fundamental interactions

The electromagnetic and weak interactions have been unified in one single gauge theory based on the $SU(2)_L \times U(1)_Y$ symmetry group [2]. In this purely symmetric gauge theory all particles are massless. Fermions and bosons can obtain mass through the so called Higgs mechanism [1]. In the minimal formulation this mechanism is such that a new spinless boson, the Higgs boson, comes in and all fermions and bosons pick up a mass. The renormalisability of the theory is preserved. The photon and the neutrinos are left massless. The theory can be extended to give mass to neutrinos too, as recent experimental observations have indicated to be the case.
This theoretical framework is nowadays referred to as the Standard Model of the electroweak interactions (SM). Experimental observations have so far confirmed the SM predictions to the level of precision of the order of 0.1% [3]. Though the theory relies on at least 19 free parameters, it makes the striking prediction of the existence of the Higgs boson that is still to be verified.

**Higgs mass**

The SM does not tell the mass of the Higgs boson ($m_H$), nevertheless limits on its value can be inferred on the basis of theoretical considerations and consistency arguments.
The Higgs potential in the SM Lagrangian includes a quartic term that involves a coupling constant ($\lambda$) on which $m_H$ depends. A first bound can be derived by requiring that spontaneous symmetry breaking actually occurs. This is essentially equivalent to the requirement that $\lambda$ stays positive at all energy scales, since a negative value for it would imply that the potential is unbounded from below and so it has no state of minimum energy [4]. The actual limit depends on the energy scale ($\Lambda$) up to which the SM is supposed to be valid [5, 6]. This bound corresponds to the lower shaded region in Fig. 1.1. On the

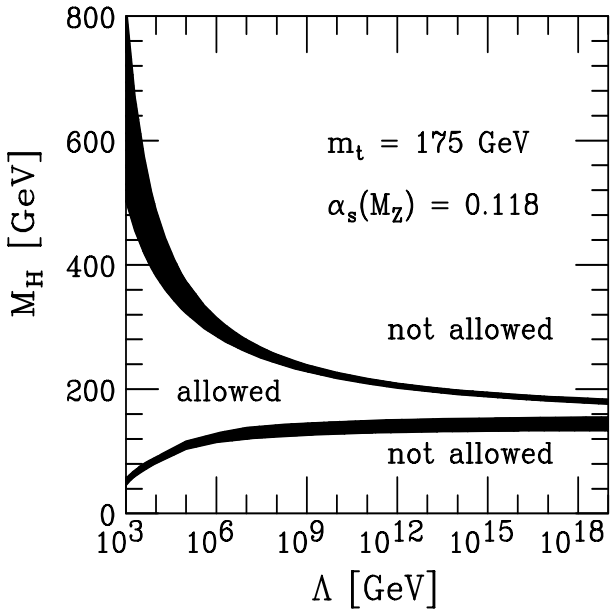


Figure 1.1: The lower and upper Higgs mass theoretical bounds as a function of the energy scale $\Lambda$ at which the Standard Model breaks down. The shaded areas reflect the theoretical uncertainties in the calculation of the Higgs mass bound [6]

other hand the requirement that $\lambda$ remains finite up to some large energy scale $\Lambda$ yields an upper bound on the Higgs mass [5] which is shown as the upper shaded region in fig 1.1; this bound is often referred to as the 'triviality bound'. From inspection of Fig. 1.1 one concludes that if the SM has to be valid up to the Planck scale ($\Lambda = 10^{19}$ GeV) then the Higgs must be lighter than 200 GeV/$c^2$. A lower value, $\Lambda = 1$ TeV, leads to an upper limit

of 700 GeV/$c^2$.

A phenomenological bound on $m_H$ comes from precision electroweak measurements. Indeed the Higgs boson enters one loop radiative corrections in the SM and a global fit to the electroweak data, taking $m_H$ as a variable to be fitted, gives mass limits. The dependence of the $\chi^2$ on $m_H$ is shown in Fig. 1.2. It results an upper limit of 170 GeV/$c^2$

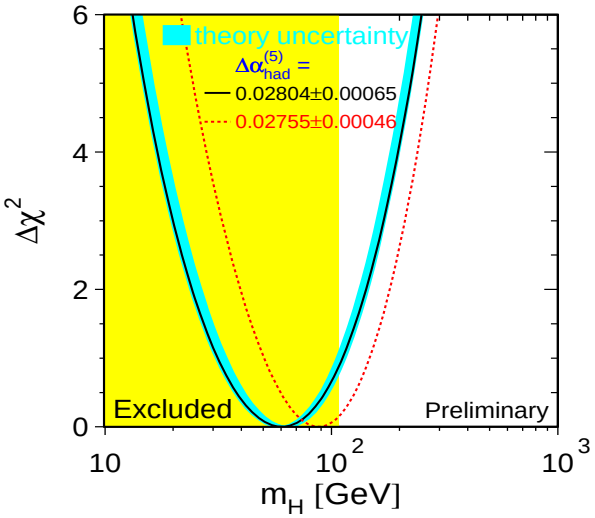


Figure 1.2: $\Delta\chi^2$ of the fit to all measurements of the electroweak observables done at LEP, SLC and Tevatron. The Higgs mass was assumed to be the only free parameter [3].

with 95% confidence level. The latest searches at LEP have excluded at the same confidence level the region below 112.3 GeV/$c^2$[1]. Due to the enormous synchrotron radiation energy loss suffered by electrons, the center of mass energy of $\approx$ 200 GeV obtained at LEP will probably represent the highest ever reached in circular electron-positron colliders. Higher energies would require rings of unreasonable dimensions. Therefore to explore higher energy ranges one has to move either to linear electron-positron colliders or to use muon or hadrons in circular colliders. The lepton colliders are under study and could become available not earlier than ten years from now. On the other hand a new hadron collider has been approved for construction in the former LEP tunnel. Its characteristics will be discussed further on.

[1] A number of events compatible with a Higgs boson production with mass around 114-115 GeV/$c^2$ has been reported in the combined results of the four LEP experiments [7]. The significance of the signal is anyway lower than 5 sigmas.

A fundamental aspect that is worth underlining is the very low Higgs production cross section. In $e^+ - e^-$ collisions the main mechanism for Higgs production is $e^+e^- \rightarrow ZH$ whose cross section for $m_H = 110$ GeV/$c^2$ at the center of mass energy of 210 GeV is less than 1 pb. In $p - p$ collisions (see also Fig. 1.6) at the center of mass energy of 14 TeV the Higgs production cross section is smaller than 100 pb for the same value of $m_H$.

### 1.1.3 Beyond the Standard Model

At present there is no confirmed experimental evidence from accelerators against the SM, and several possible extensions have been ruled out. Nevertheless there are some relevant arguments indicating that the SM is not theoretically satisfactory and cannot be the ultimate theory of the fundamental particles and their interactions.
Among the theoretical drawbacks present in the SM, the hierarchy problem [8] is considered to be one of the most serious. It arises from the difficulty in the theory to keep fundamental scalar particles much lighter than the maximum energy scale up to which the theory remains valid. In fact from Fig. 1.1, it turns out that the consistency of the SM is broken unless $m_H < O(1 \text{ TeV}/c^2)$. However, already at one loop level there are quadratically divergent contributions to the Higgs mass. These terms could be cancelled by mass counterterms, but they should be fine tuned at each order of perturbation theory with a precision of roughly 1 part in $10^{15}$. Although formally there is nothing wrong with this fine tuning, it is considered unnatural.
Another important drawback of the SM is the fact that gravity is left out, which is one aspect of the general problem of unification of the fundamental interactions. It would be very elegant to unify all four interactions in one single gauge group. This solution could also lead to relations among the many free parameters of the SM.
Finally, the SM does not explain the origin of the six flavours in both the quark and lepton sector, nor that of their weak charged-current mixing and of CP violation.
For all these reasons the SM is widely accepted to be an effective field theory, valid up to some energy scale $\Lambda$, as it had already been anticipated.

#### SuperSymmetry

In this context supersymmetry [9, 10, 11, 12, 13, 14] appears to be a suitable working framework. Supersymmetry implies that all particles possess supersymmetric partners having opposite statistics. This is because supersymmetry multiplets consist of equal-mass particles whose spins differ by $1/2\hbar$. So far no supersymmetric partners of any known particles have been discovered, so supersymmetry, if it exists, is not only broken, but broken

at an energy scale beyond the reach of accelerators to date. Nevertheless, supersymmetry remains attractive for several reasons. First it provides the only known solution of the hierarchy problem. Indeed the loop contributions from fermions and bosons have opposite signs and therefore cancel in the correction to the Higgs mass.
The second attractive feature of supersymmetry is that supersymmetric theories have better high energy behaviour than non-supersymmetric ones. In fact some (extended) supersymmetric theories are completely finite, in the sense they do not force to deal with and manipulate infinite quantities.
The third, and most recent, reason for supersymmetry being so well regarded is that it appears to be an indispensable ingredient of the superstring theories [15]. These theories have some quite remarkable properties and at the moment they are the best candidates for 'theories of everything', i.e. quantum theories of the strong, electroweak and gravitational interactions.

The production cross sections for the new particles foreseen in the supersymmetric theories are of the same order (some tens of pb) as the SM Higgs production cross section. However they can be subject to large fluctuations resulting from the actual values of the parameters of the theory and from the type of particle under consideration (Higgses, squarks, gluinos).

**B-physics**

Besides looking for new particles, another way to test the validity of the SM is to quantitatively test the unitarity of the flavour weak rotation matrix, the Cabibbo-Kobayashi-Maskawa (CKM) matrix [16]. This subject is strictly linked to the phenomenon of CP violation, which, although already discovered in 1964 by Christenson, Cronin, Fitch and Turlay in the neutral kaon system [17], is still one of the least constrained phenomena. In this respect, the exploration of physics with $b$ flavoured hadrons offers a very fertile testing ground for the SM description of the electroweak interactions. The Physics of the $b$ quark turns out to be very interesting from this point of view as another main topic is the study of rare $b$ decays induced by flavour changing neutral currents (FCNC) transitions $b \to s, d$ which are loop-suppressed in the SM and thus very sensitive to new-physics effects. During the last few years B-physics has received a lot of attention, both from theorists and experimentalists and we are presently at the beginning of the B-factory era in particle physics. The BaBar (SLAC), BELLE (KEK), HERA-B (DESY), CLEO III (Cornell), CDF-II and D0-II (Fermilab) have already seen their first events. Although the physics potential of these experiments is very promising, it may well be that a definite answer in the search

for new physics in the B-sector could be given by a new generation of experiments at future, more powerful hadron machines. As it will be made clear in the following, the main advantage of a high energy hadron machine is the large statistics achievable. Indeed the $b\bar{b}$ production cross section in $p-p$ collisions at a center of mass energy in the TeV scale is of the order of the mb, while B-factories at $e^+e^-$ colliders deal with nb cross sections. Moreover it must be taken into account that in $p-p$ collisions the $b\bar{b}$ production cross section grows rapidly with the center of mass energy.

## 1.2 The Large Hadron Collider

### 1.2.1 Design considerations for a new particle accelerator

In the previous section some important issues existing in present particle physics have been presented. It has been explained that new physics is expected to appear at the TeV scale, the processes of interest being characterised by extremely low cross sections.
The present lepton machines are inadequate for exploring this energy range, then the natural choice falls on hadron colliders which historically have served the purpose of discovery machines due to the larger cross sections available in strong interactions and the wide energy spectrum that they allow to explore simultaneously[2].

Events characterised by a cross section $\sigma$ are produced at a rate $R$ given by:

$$R = L\sigma \tag{1.1}$$

the proportionality factor $L$ is called luminosity and is a characteristic of the collider and not of the nature of the colliding particles nor of the interactions they undergo. $L$ represents the number of particles that are brought to collision per unit time and unit surface. For circular accelerators that collide bunches of $n_1$ and $n_2$ particles at a frequency $f$ the luminosity reads:

$$L = f\frac{n_1 n_2}{4\pi\sigma_x\sigma_y} \tag{1.2}$$

where $\sigma_x$ and $\sigma_y$ characterise the Gaussian transverse beam profiles in the horizontal (bend) and vertical directions. It is clear that to achieve the highest possible statistics one can act either on the luminosity or on the collision energy at which the cross section is maximised. In Fig. 1.3 some relevant cross sections are reported as a function of the center of mass energy for $p-p$ ($p-\bar{p}$) collisions. It is evident the advantage of having the highest possible

[2]Since hadrons are not elementary particles, the energy available in high energy collisions is the one of the constituents (quarks and gluons) that actually interact, therefore the actual center of mass energy of the collision has a broad spectrum.

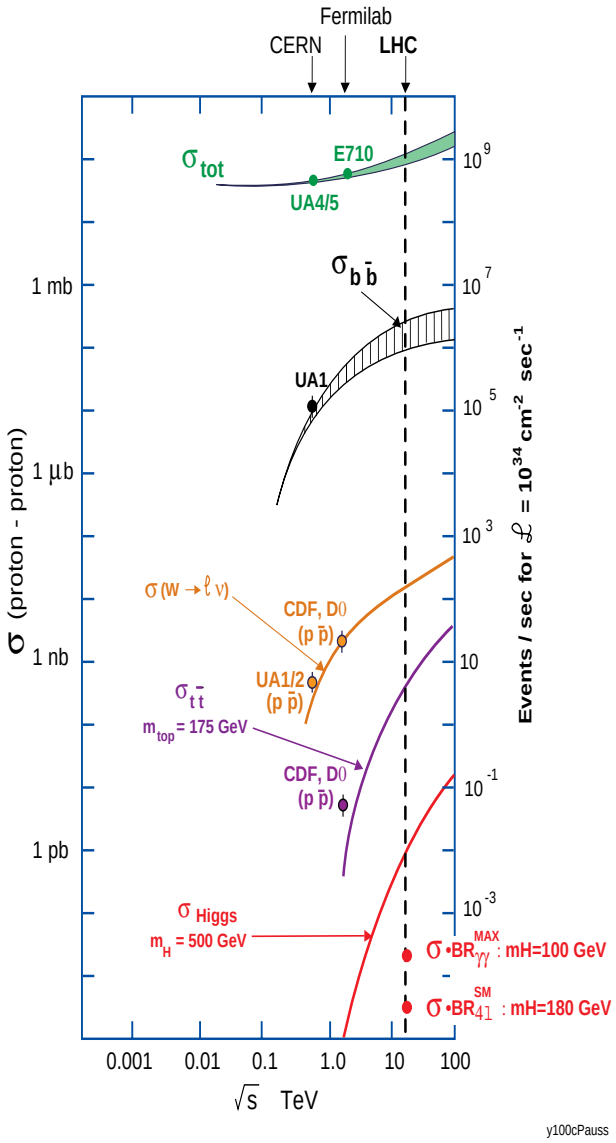


Figure 1.3: Cross sections in proton-proton collisions as a function of the center of mass energy [18].

center of mass energy. Indeed while the total $p-p$ cross section, which mainly determines the background, stays more or less the same, the Higgs production cross section grows rapidly.

On the other hand $L$ is a rate proportionality factor for any type of events. In this respect, if on one side a large luminosity value determines high event rates, on the other it can lead to increasingly more difficult experimental conditions. Indeed the average number of inelastic $p-p$ collision (from now on they will be referred to as Minimum Bias events) per bunch crossing depends linearly on $L$. This means that the rare interesting events that may occur in a bunch crossing are superimposed to a certain number of events (pile-up) whose number grows linearly with $L$. A way to reduce the pile-up while keeping constant the luminosity is to increase the collision frequency and reduce the number of particles per bunch. This, however, poses more and more demanding timing requirements on the detectors, which have to separate in time the signals originating at different bunch crossings.

The main characteristics of the most important hadron colliders are listed in Tab. 1.3. The

| | SPS (CERN) | Tevatron (Fermilab) | LHC (CERN) | SSC (USA) |
|---|---|---|---|---|
| Status | dismantled | in operation | in construction | terminated |
| Collisions | $p-\bar{p}$ | $p-\bar{p}$ | $p-p$ | $p-p$ |
| CM energy (TeV) | 0.63 | 2.0 | 14 | 40 |
| Luminosity ($10^{33}$ cm$^{-2}$s$^{-1}$) | $6\times10^{-3}$ | 0.21 | 10 | 1 |
| Time between collisions (ns) | 3800 | 396 | 25 | 16.68 |
| Particles per bunch (units $10^{10}$) | $p:15$ $\bar{p}:8$ | $p:27$ $\bar{p}:7.5$ | 10.5 | 0.8 |
| Bunch length (cm) | 20 | 38 | 7.5 | 6.0 |
| Beam radius ($\mu$m) | $p:73(H),36(V)$ $\bar{p}:55(H),27(V)$ | $p:34$ $\bar{p}:29$ | 16 | 4.8 |
| Circumference (km) | 6.911 | 6.28 | 26.659 | 87.12 |
| Peak dipole magnetic field (T) | 1.4 | 4.4 | 8.3 | 6.790 |

Table 1.3: High energy hadron collider parameters.

SPS is no longer in operation as a collider, the Tevatron is an existing collider, the SSC is a terminated project while the LHC (Large Hadron Collider) is an approved collider that will be in operation from 2006 and will be built in the former LEP (Large Electron Positron

Collider) tunnel at CERN.

From what has been said above, the SSC project would have provided the best experimental conditions due to its very high center of mass energy, however it has been terminated for cost reasons. The LHC has lower cost since its tunnel already exists, but the energy of its beams is limited to 7 TeV due to the maximum achievable dipole magnetic field. Higher energies could have been reached on a larger curvature radius tunnel like the SSC one.

The LHC will then be the most powerful hadron collider running in the next two decades. As it can be seen in Fig. 1.3, the Higgs production cross section at the LHC is at least two orders of magnitudes higher than the one at the Tevatron. Beside being a machine for new particles searches, the LHC will allow a better understanding of the physics of known particles. Indeed the $b\bar{b}$ and $t\bar{t}$ production cross section will be at least one order of magnitude higher than at the Tevatron. Taking also into account the higher luminosity, the LHC will be by far the only machine capable to answer the fundamental questions exposed in the previous section.

However, the experimental challenges that have to be faced at the LHC are extremely hard. From what has been reported above, the average number of inelastic $p-p$ collisions expected at each crossing for $L = 10^{34}$ cm$^{-2}$s$^{-1}$ is 17.3. This number results from eq. 1.1, the expected value of 55 mb for the total inelastic $p-p$ cross section at $\sqrt{s} = 14$ TeV, the bunch crossing time spacing of 25 ns and from the fact that 20% of bunch crossings will be empty.

Each one of the 17.3 collisions will give rise to about 50 charged tracks. The LHC detectors must then have the capability of isolating and reconstructing the interesting events in an extremely hostile environment. At the same time this capability has to be displayed on-line as only few (about 100) events can be recorded out of the 40 millions each second.

From this point of view it is fundamental to understand what are the most suitable signatures of the interesting physics processes in order to achieve high signal efficiency and high background rejection power. In addition, the characteristics of the signatures must be easily identifiable and cannot involve heavy reconstruction algorithms as the time available on-line to make the decision of selecting the event will be forcedly limited. This subject will be discussed in the next section.

### 1.2.2 Physics searches at the LHC

Before reviewing the useful physics channels to be searched at the LHC, some points need to be discussed. In high energy $p-p$ collisions ($\sqrt{s} \gg m_p$), the inelastic events arise from

the hard scattering among the partons inside the protons (see Fig. 1.4). The interacting

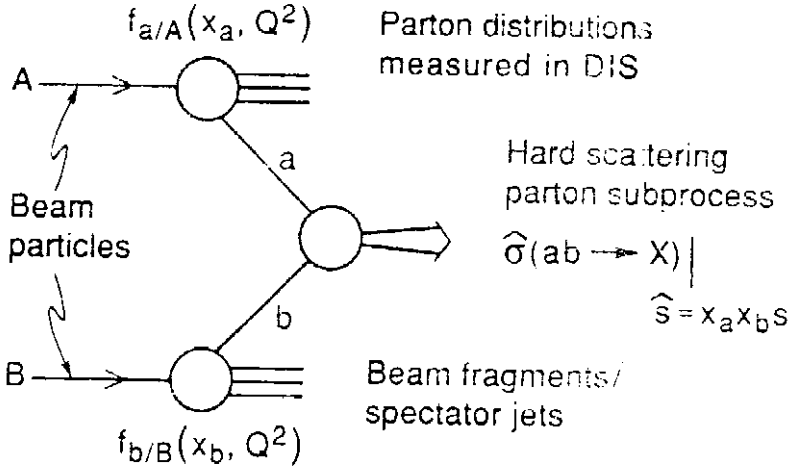


Figure 1.4: Schematic representation of a hadron-hadron collision.

partons ($a$ and $b$) have in general different fractions ($x_a$ and $x_b$) of the total momentum carried by the proton. One consequence of this is that the energy available in the collision is $\sqrt{\hat{s}} = \sqrt{x_a x_b s}$, therefore it varies from event to event. This circumstance allows to explore a wide energy range, as it has been stated above. The second consequence is that the center of mass of the collision is boosted along the beam direction, then to describe consistently phenomena occurring in such collisions one must use variables that are invariant for boosts along the beam direction. The transverse momentum ($p_t$) is clearly invariant for such boosts. Another very useful variable is the rapidity defined as

$$y = \frac{1}{2} \ln \frac{E + p_z}{E - p_z} \tag{1.3}$$

It easy to prove that under a boost in the $z$-direction to a frame with velocity $\beta$ $y \longrightarrow y - \tanh \beta^{-1}$. Hence the shape of the rapidity distribution $dN/dy$ is invariant. For $p \gg m$, the rapidity can be expanded to obtain

$$y = \frac{1}{2} \ln \frac{\cos^2 \theta/2 + m^2/4p^2 + \ldots}{\sin^2 \theta/2 + m^2/4p^2 + \ldots} \approx -\ln \tan \theta/2 \equiv \eta \tag{1.4}$$

where $\cos \theta = p_z/p$. The pseudo-rapidity $\eta$ defined above is approximately equal to the rapidity $y$ for $p \gg m$ and $\theta \gg 1/\gamma$, and in any case can be measured when the mass and momentum of the particle are unknown since only the angle with respect to the beam direction is needed.

**SM Higgs**

In proton-proton collisions the main mechanisms of Higgs production at the SM tree level are represented in Fig. 1.5. The corresponding contributions in terms of cross section are

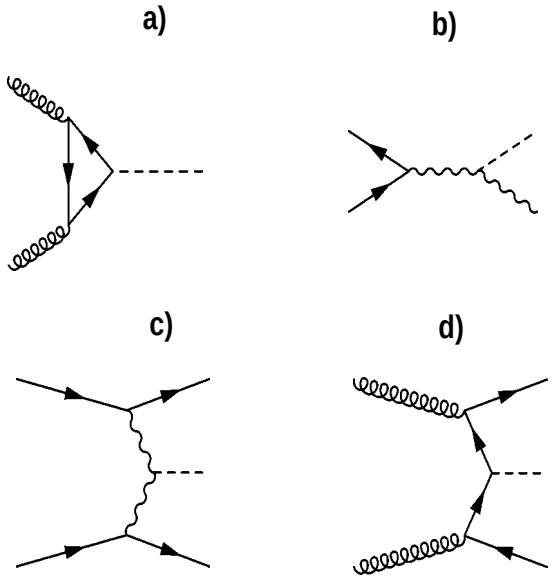


Figure 1.5: Tree level Feynman diagrams contributing to the Higgs production in hadron collisions.

plotted as a function of $m_H$ in Fig. 1.6 [19]. Over the entire mass range shown, the gluon fusion is the dominant production mode, and the vector boson fusion becomes competitive for $m_H > 800$ GeV/$c^2$. However, also the other processes are relevant as the additional heavy objects that are produced in association with the Higgs can facilitate the search in certain mass ranges. The associated production with a $t\bar{t}$ pair is a good example of that. In the mass region of about 130 GeV/$c^2$ to 180 GeV/$c^2$, the total cross section for the Higgs production is of the order of 20 pb, implying that one could expect about $2 \times 10^5$ Higgs events in one year of LHC running at the maximum luminosity.

The branching ratios (BR) and the total natural decay width of the Higgs boson are shown in Figs. 1.7 and 1.8 as a function of $m_H$ [20]. For masses below and around 120 GeV/$c^2$, the decay into a $b\bar{b}$ pair is largely dominant, but it is not so easy to exploit at hadron machines due to an overwhelming QCD background. Since the coupling of the Higgs to fermions is proportional to their mass, the other phenomenologically important

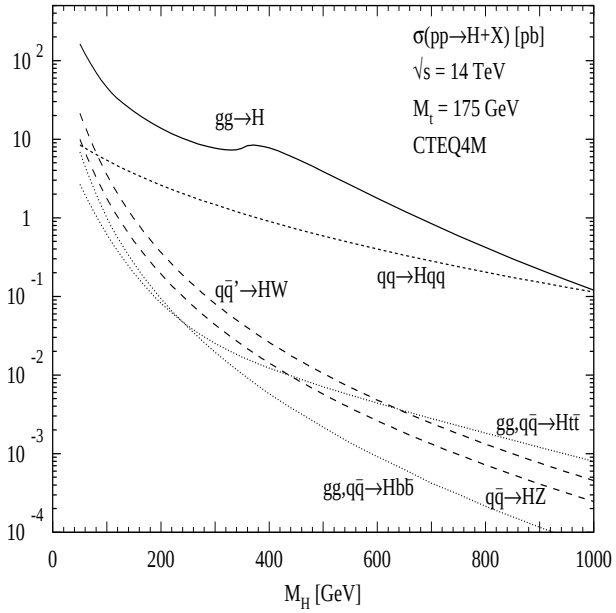


Figure 1.6: Higgs production cross sections (in pb) at the LHC as a function of the Higgs mass [19].

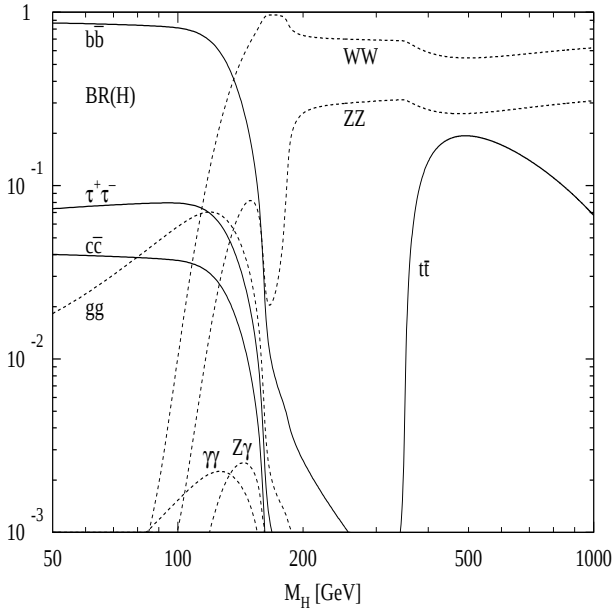


Figure 1.7: The Higgs branching ratio in its main decay modes as a function of the Higgs mass. The QCD and electroweak corrections are included [20].

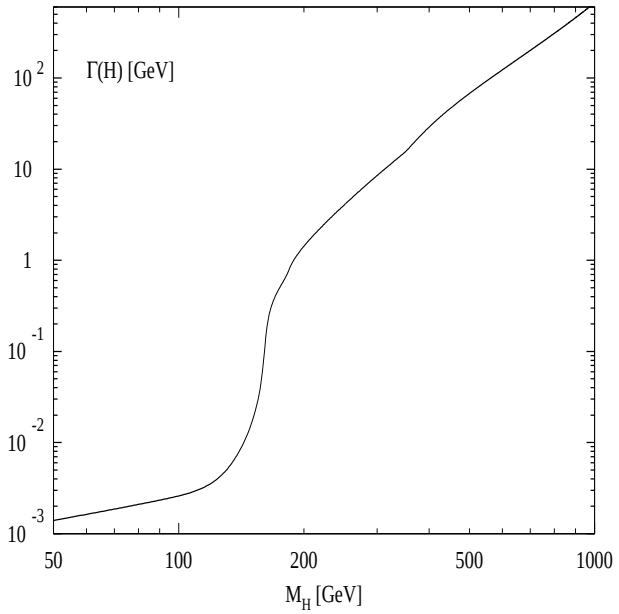


Figure 1.8: The Higgs natural width (in GeV) as a function of its mass. The QCD and electroweak corrections are included [20].

decay modes are the $\tau^+\tau^-$, whose BR is about 10% in the intermediate mass range, and the muonic decay, which has anyway an extremely low BR of the order of $10^{-4}$. The decay mode into a $\gamma\gamma$ pair is also very useful, despite the very low BR (about $10^{-3}$).
Above the $WW$ and $ZZ$ decay thresholds, the decay of the Higgs into pairs of massive gauge bosons becomes dominant. Even below the decay thresholds, the decay BR into a pair of off-shell gauge bosons or into one real and one off-shell gauge boson is important [21, 22]. Given the fact that the $W$ and the $Z$ are not directly detectable particles, the BR must be multiplied by the BR corresponding to the decay of these gauge bosons to detectable particles. For instance BR($ZZ \to \mu^+\mu^-\mu^+\mu^-$)$= 1.13 \times 10^{-3}$.

The most suitable Higgs decay channels in the various possible mass ranges are listed below (see also Fig. 1.9).

- $m_H \lesssim 130$ GeV/$c^2$: the channels $H \longrightarrow \gamma\gamma$ and $H \longrightarrow b\bar{b}$ are the most accessible experimentally. The hadronic decay looks by far more difficult as the total $b\bar{b}$ production cross section is more than 6 orders of magnitudes higher than the signal. The channel $t\bar{t}H$ with $H \longrightarrow b\bar{b}$ however is suitable and has a signal to background ratio of order 1. On the other hand the main background to the two isolated and energetic $\gamma$ from the Higgs decay comes from $\pi^0$ decay $\gamma$ which can be very close to

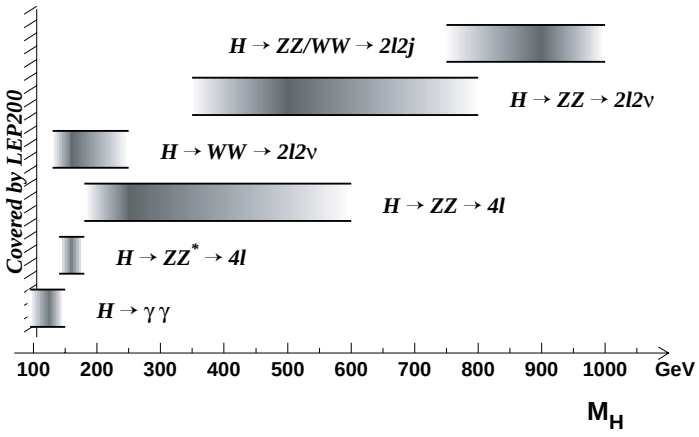


Figure 1.9: Most useful experimental signatures for Higgs search at the LHC and the corresponding mass ranges.

each other faking a single energetic $\gamma$.

- 130 GeV/$c^2$ $\lesssim m_H \lesssim$ $2m_Z$: in this mass range the useful channels appear to be $H \longrightarrow Z^{(*)}Z^* \longrightarrow 4l$ and $H \longrightarrow W^{(*)}W^{(*)} \longrightarrow ll\nu\nu$ ($l = e, \mu$). The latter becomes more important around the $WW$ production threshold where the $ZZ^*$ mode is suppressed. The $WW$ decay mode has to be extracted from a background consisting mainly of $qq \longrightarrow WW$ continuum, $t\bar{t} \longrightarrow bW^+\bar{b}W^- + X$ and $W^{\pm}t(b) + X \longrightarrow WbW(b) + X$. A discriminating feature could be the requirement that no high energy "jet" is present in the event.
  The leptonic decay of $ZZ$ pairs represents an easy and clean experimental signature (in particular the 4 muon final state). The signal selection involves the presence of two pairs of energetic and isolated leptons coming from a common vertex, one pair eventually having an invariant mass compatible with $m_Z$. The background is the continuum $pp \longrightarrow Z^{(*)}Z^* \longrightarrow 4l$ (irreducible), $t\bar{t} \longrightarrow 4l + X$ and $Zb\bar{b} \longrightarrow 4l + X$.

- $m_H > 2m_Z$**:** the most useful decay mode is $H \longrightarrow ZZ$. All has been said above about the leptonic final state applies here with the additional feature that now both lepton pairs must have an invariant mass compatible with $m_Z$.
  For $m_H \gtrsim$ 600 GeV/$c^2$ the Higgs production cross section decreases significantly, therefore it becomes more and more important to look also at other decay modes like

$H \longrightarrow ZZ \longrightarrow ll\nu\nu$, $H \longrightarrow ZZ \longrightarrow lljj$ and $H \longrightarrow WW \longrightarrow l\nu jj$ that have higher BR than the purely charged leptonic decays. When neutrinos are involved a high missing transverse energy ($E_t^{miss}$) must be observed in the event. The background comes mainly from $ZZ$, $ZW$, $WW$, $t\bar{t}$ and $W(Z)j$.

The total Higgs decay width (see Fig. 1.8) plays an important role in the design of the detectors. Up to around 200 GeV/$c^2$ the total Higgs width is below 1 GeV/$c^2$, and therefore the width of the reconstructed Higgs mass distribution will be dominated by the detector resolution. For masses above 200 GeV/$c^2$ the relation $\Gamma(H) = 0.5 \times m_H^3$ TeV/$c^2$ ($m_H$ in TeV/$c^2$) is approximately satisfied [20].

**Supersymmetry**

In the Minimal Supersymmetric Standard Model (MSSM) [23] the neutral bosons decay channels are similar to those of the SM Higgs, however the production cross sections and BR can be significantly different due to supersymmetric couplings. This opens the way to further decay channels like $h^0, A^0, H^0 \longrightarrow \tau\tau$ and $h^0, A^0, H^0 \longrightarrow \mu\mu$. The $\tau$ can be identified either through leptonic decays, in which case one looks for an energetic muon or electron plus some $E_t^{miss}$, or through an hadronic decay ($\tau$-jet), which is a very collimated jet characterised by low multiplicity. The background to the $\tau$ pair final state is represented mainly by $t\bar{t}$ and $b\bar{b}$ production and by QCD two-jet events in case of $\tau$ hadronic decay. For the di-muon final state, the dominant background is the Drell-Yan muon production, $t\bar{t}$ and $WW$ continuum.
The expectations for MSSM searches at the LHC are shown in Fig. 1.10.

**Top physics**

The LHC is a top quark factory. The interesting decay channels involve one or two $W$, decaying leptonically, and a $b$ quark, then the objects to be looked at are energetic muons, electrons and $b$-jets. The physics issues are the determination of the top mass at the level of precision of $\sim 1$ GeV/$c^2$, study of rare top decay modes and of the top spin.

**QCD and electroweak physics**

At the LHC, substantial improvement in the precise determination of electroweak parameters, such as the $W$ boson mass and the electroweak mixing angle, will be feasible. The tests include measurements of inclusive production of $W$, $Z$ and vector boson pair production: $WW$, $WZ$, $ZZ$, $W\gamma$ and $Z\gamma$.

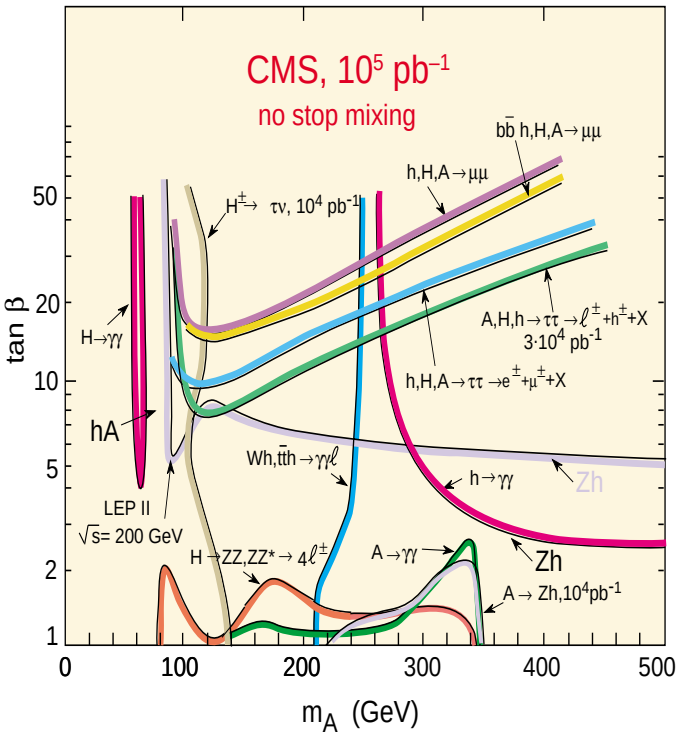


Figure 1.10: $5\sigma$ contours in the MSSM parameter space for the Higgs decay modes to be searched at the LHC.

The processes that have been discussed so far involve in most cases the presence of heavy objects like $W$ and $Z$, therefore the identification of such particles can be considered as a benchmark goal for any detector at the LHC. The $p_t$ spectrum (differential cross section) of muons coming from direct $W$ production obtained with PYTHIA 6.152 [24] is shown in Fig. 1.11. The dominant sources are shown in the plot. The muon spectrum from W decay is peaked at about 35 GeV/$c$ and decreases quite rapidly toward low $p_t$ values. An important characteristic of muons coming from direct $W$ decay is that they are isolated.

### B-physics

The huge $b\bar{b}$ production at the LHC ($\sigma \sim 500$ $\mu$b) offers the possibility to explore a wide range of B-physics channels. The main difficulty is represented by the fact that the leptons from $b$ decays are quite soft and so suffer from the huge background due to pion, kaon and charm (semi)leptonic decays. Muons appear to be much more useful than electrons since

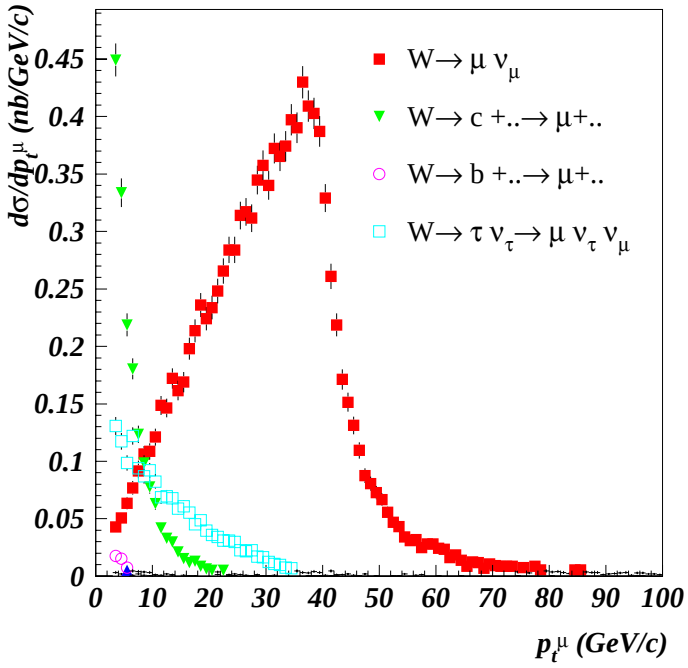


Figure 1.11: Differential cross section (PYTHIA 6.152) as a function of the muon $p_t$ for muons coming from direct $W$ production at the LHC. The dominant sources are shown in the plot.

for the same energy thresholds they are more easily identifiable. In Fig. 1.12 it is shown the differential cross section as a function of the muon $p_t$ for muons coming from decays of B-hadrons produced in direct $b\bar{b}$ production at the LHC.
The cases involving a $J/\psi$ in the final state are accessible through the di-muon decay of such particle. On the other hand, channels like $B_d \longrightarrow \pi\pi$ must rely on the possible semi-leptonic decay of the associated B-hadron ($\mu_{tag}$ or $e_{tag}$).

The large number of pile-up events expected at the highest luminosity will render B event reconstruction a very hard task. For this reason it is foreseen that the most suitable LHC phase for B-physics will be the early one when the luminosity will be about $10^{32}$-$10^{33}$ $\mathrm{cm}^{-2}\mathrm{s}^{-1}$. This phase is commonly referred to as the low luminosity phase of the LHC and B-physics is expected to play a central role in that period.

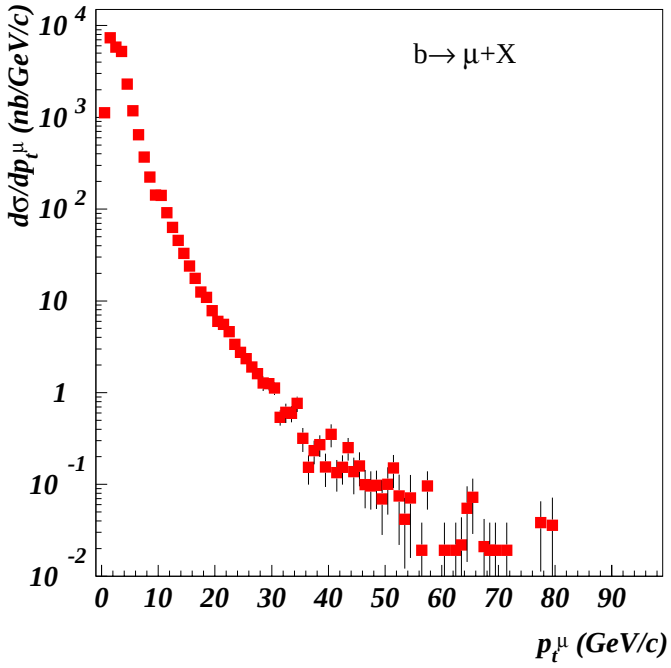


Figure 1.12: Differential cross section (PYTHIA 6.152) as a function of the muon $p_t$ for muons coming from decays of B-hadrons produced in direct $b\bar{b}$ production in 14 TeV $p-p$ collisions.

### Heavy ion physics

In addition to $p-p$ collisions, at the LHC it will be possible to collide heavy ions beams in order to study possible signatures of the formation of the Quark Gluon Plasma [25]. For lead-lead collisions the center of mass energy will be 1150 TeV, which is 30 times higher than what is obtained at the present most powerful working heavy ion collider, the RHIC at the BNL in the USA.

Among a vast variety of searches that can be done with dedicated detectors, some can be carried out even in general purpose experiments designed for the physics program described above. This is the case of $J/\psi$ and $\Upsilon$ production rates that are expected to be significantly modified [26] in a quark gluon plasma scenario. Once more the only imaginable detectable decay mode appears to be the one into two muons.

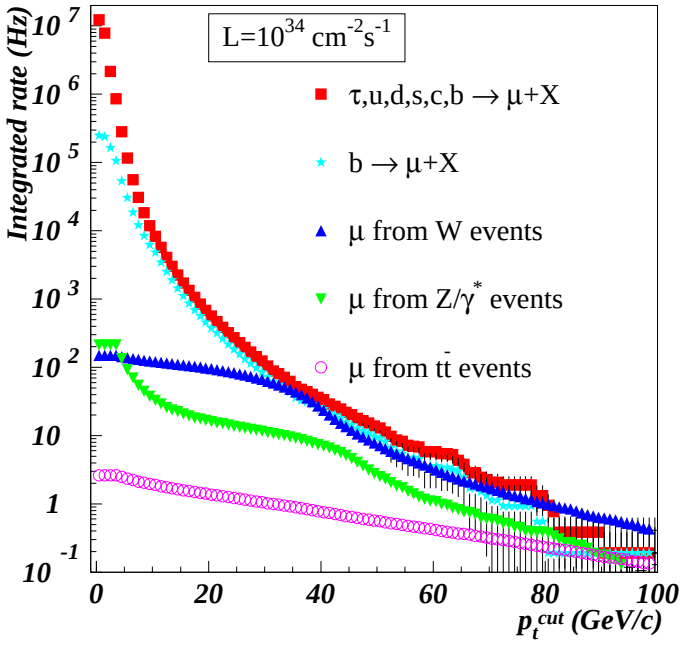


Figure 1.13: Single muon integrated rate at generation level (PYTHIA 6.152) as a function of $p_t^{cut}$ . The different dominant sources are shown in the plot.

**Final considerations**

In this section it has been discussed from an experimental point of view the accessibility of physics processes with a generic detector working on the LHC. It has become evident that the identification of any interesting event relies on the precise measurement of *physics objects* like $\mu$, $e$, $\gamma$, $j$, $\tau_{jet}$ and $E_t^{miss}$. Muons in particular, being the most easily identifiable particles, are considered most useful especially in the crucial phase of the event selection. Another fundamental point is to understand the variables on which the selection has to be based on. The muon $p_t$ distributions that have been shown in this section indicate that accepting events with muons above a given $p_t$ threshold ($p_t^{cut}$) can be an effective means to distinguish events with heavy particles such as $W$ and $Z$ from MB events. This feature can be better appreciated in Fig. 1.13 that shows the integrated rate at generation level of events with muons in the final state as a function of $p_t^{cut}$.

For what concerns muons originating from $b$ decays we see that there is not much to do as

far as single muons are looked at because $b$ decay muons are actually the dominant source in the range $5 < p_t < 30$ GeV/$c$. In fact they represent the main source of background in high luminosity searches: Higgs and supersymmetry.
A fundamental feature of the distributions presented in Fig. 1.13 is that at $L = 10^{34}$ cm$^{-2}$s$^{-1}$ the rate of events with a $W$ going into a muon with $p_t > 20$ GeV/$c$ is about 100 Hz. This already saturates the allowed final bandwidth for permanent event storage. It is therefore evident that at an advanced event selection stage it is not enough to look at simple event topologies like the presence of muons, instead one must perform a much more complex event reconstruction in order to identify the actual process that has occurred and decide whether to keep it or not according to the priorities of the various physics studies. B-physics is particularly critical from this point of view as the rate of production of $b\bar{b}$ events with presence of a muon with $p_t > 10$ GeV/$c$ is almost two orders of magnitude greater than what can be stored (see Fig. 1.13).

## 1.3 The CMS detector at the LHC

### 1.3.1 introduction

Some thirty years ago a single detection device, the bubble chamber, was sufficient to reconstruct the full event information. At the current high centre of mass energies no single detector can accomplish this even though the number of particles whose identity and momenta can be usefully determined is limited. This leads to a familiar onion-like structure of present day high energy physics experiments. Each layer is specialised to measure and identify different classes of particles. Starting from the interaction vertex the momenta of charged particles are determined in the inner tracker which is usually immersed in a solenoidal magnetic field. Identification of $b$-jets and B-hadron decay vertices can be accomplished by placing high spatial resolution detectors such as silicon pixels or microstrip detectors close to the interaction point. Following the tracking detectors are calorimeters which measure the energies and identify electrons, photons, single hadrons or jets of hadrons. Only muons and neutrinos penetrate through the calorimeters. The muons are identified, triggered upon and measured in the outermost subdetector, the muon system, which is usually immersed in a magnetic field. However for muons that are not extremely energetic, the precision on the muon momentum comes largely from the inner tracker measurement.

Four experiments will study the collisions produced by the LHC. Two of them, CMS (Compact Muon Solenoid, Fig. 1.14) and ATLAS (A Toroidal LHC Apparatus, Fig. 1.15), are general purpose detectors, while LHCb and ALICE (A LArge Ion Collider Experiment)

are dedicated detectors. The former is a B-physics experiment while the latter has been designed for heavy ion physics.

The work described in this thesis refers to the CMS detector, however before describing in detail the apparatus some design considerations will be discussed. First the requirements imposed by the detection of the physics observables are reviewed and then some possible general experimental configurations are examined.

### 1.3.2 Detection of the physics observables

#### Muons and electrons

Muon identification is, in principle, easy at any luminosity and can be accomplished down to low momenta (typically 5 GeV/$c$) even in the presence of large hadronic activity. All that is required is a sufficiently thick hadron absorber surrounding the interaction region. For absorber thickness beyond 10 interaction length, measurements [27] show that real muons from meson decays in the early part of hadronic showers start to dominate over hadronic punch-through. Based on experience at previous hadron collider experiments, the main source of contamination of high $p_t$ muons is misreconstruction of low $p_t$ muons due to a lack of redundancy in the definition of the muon tracks. Therefore a robust muon system with several independent momentum measurements and many points per muon track is vital for an LHC apparatus. The design criteria for the muon system can be obtained by requiring that an unambiguous determination is made of the sign for muons of 1 TeV. This implies that $\Delta p/p \approx 10\%$ at $p = 1$ TeV/$c$. Finally it must be noted that an important source of background muons at LHC comes from heavy flavour decays (see Fig. 1.13). Most of these (except those from primary top decays) are produced within jets. Since new physics often manifests itself through isolated high $p_t$ multi-lepton final states, muon isolation tools, based on calorimetry and inner tracking, play a crucial role.

The main disadvantage of electrons with respect to muons lies in the fact that the capability to trigger on, identify and measure them strongly depends on the amount of accompanying hadronic activity. Electron identification relies on calorimetric measurements and tracking information. The background to electrons comes from two main sources: electrons faked by QCD jets and real electrons from photon conversions as well as Dalitz and $b$ decays. The most demanding rejection factor comes from the inclusive one-electron channel. For $p_t > 50$ GeV/$c$ and $|\eta| < 2$, the electron to jet ratio is about $10^{-5}$ for isolated electrons from inclusive $W$ production. This means that a rejection of $10^6$ per jet must be achieved to detect inclusive isolated electrons with a contamination of less than 10%. Experience at previous hadron collider experiments like CDF and UA1 suggests that such

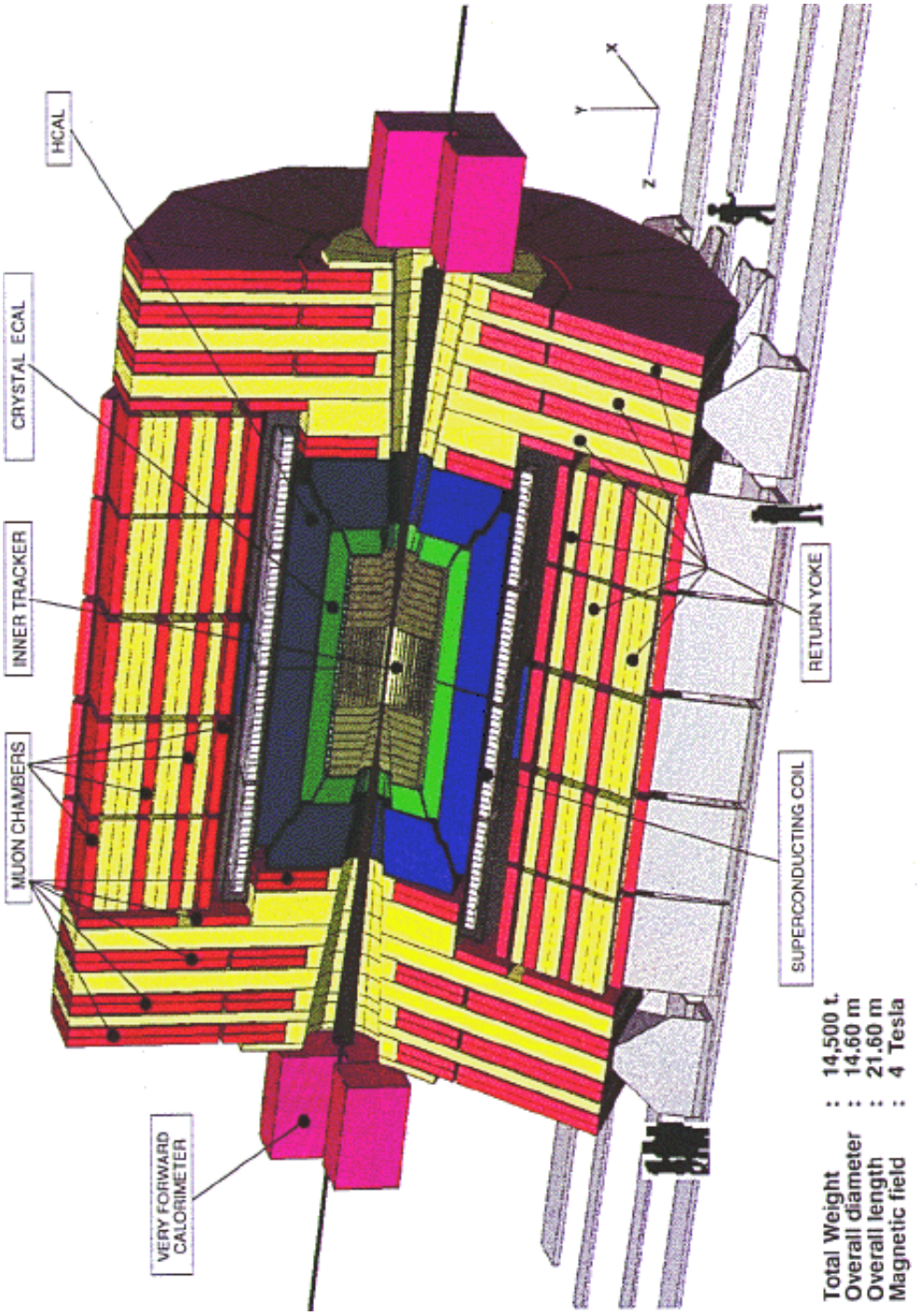


Figure 1.14: 3 dimensional view of the CMS detector at the LHC.

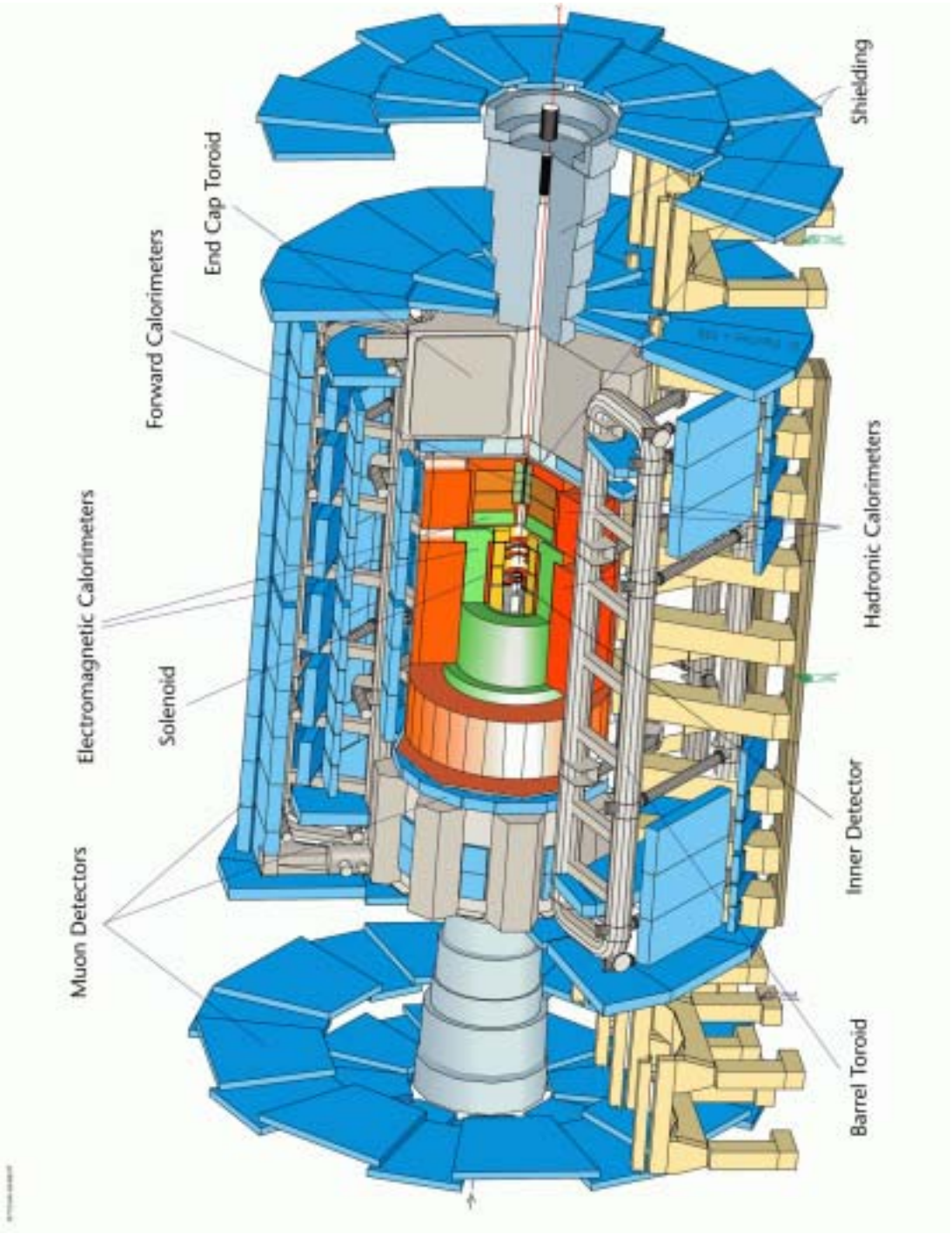


Figure 1.15: 3 dimensional view of the ATLAS detector at the LHC.

a rejection factor can be achieved, in the absence of pile-up, with magnetic tracking and calorimetry. The main tools used are: small hadronic/electromagnetic calorimeter signal ratio, isolation cuts in the calorimeters, isolation cuts with the inner tracker, matching between the calorimeter cluster and a high $p_t$ charged track both in energy ($E/p$) and position. The same tools have also proved to be very efficient against the real background of non isolated electrons conversions, Dalitz and $b$ decays.

**Photons**

Since narrow signals are expected in the $\gamma\gamma$ spectrum from a low mass Higgs, the main benchmark that should determine the performance of an electromagnetic calorimeter is the di-photon mass resolution. The mass resolution has terms that depends on the energy resolution and also on the two photon angular separation. Powerful isolation cuts and two showers separation capability are required to eliminate backgrounds from jets ($\pi^0 \longrightarrow \gamma\gamma$) faking single photons.

**Jets and missing energy**

The physics programme most demanding of good hadronic energy resolution and segmentation is the detection of narrow states decaying into pairs of jets. The di-jet mass resolution includes contributions from physics effects, such as fragmentation, as well as detector effects such as angular and energy resolution. When the jet $p_t$ is small, mass resolution is dominated by physics effects. For high $p_t$ jets angular resolution plays a more important role than energy resolution. The latter is expected to be important only in the decay of extremely heavy objects into two jets [28].
The hadronic resolution is not very critical for $E_t^{miss}$ either, rather it is crucial to reduce the background to such kind of measurement. At high luminosity $E_t^{miss}$ measurements are based on high $p_t$ leptons and jets. It is very important to catch all jets present in the event as the shape and magnitude of the instrumental background is in most cases entirely dominated by the $\eta$ coverage. Hermeticity is therefore a fundamental requirement.

Concerning the identification of $b$-jets ($b$ tagging), there are in general two methods. Charged leptons with relatively high momentum and a large momentum transverse to the jet axis arise mainly from semi-leptonic decays of $b$-hadrons.
A second additional feature that can be exploited is the relatively long ($\approx 1.5$ ps) lifetime of $b$-hadrons, which leads to secondary vertices that are separated from the primary ones. Charged tracks within a jet and with a significant impact parameter (defined to be the distance of closest approach of the track from the primary vertex) are likely to be present

in such events.
In both cases efficient $b$ tagging requires measuring layers close to the interaction vertex. The precision with which the impact parameter can be measured is determined by:

- the closeness of the first measuring layer from the interaction vertex
- the number of measurements close to the interaction vertex
- the spatial resolution of the measured points
- the amount of material in these layers and in the beam pipe leading to a degradation in the significance of the impact parameter due to multiple scattering

### 1.3.3 General detector design considerations

The single most important aspect of the overall detector design is the magnetic field configuration for the measurement of muon momenta. The choice strongly influences the rest of the detector design. The two basic configurations are solenoidal and toroidal. The closed configuration of a toroid does not provide magnetic field for inner tracking. Since a detector without magnetic inner tracking cannot adequately study a number of important physics topics an additional inner solenoid is required to supplement a toroid.
CMS has chosen to use a single large solenoid (see Fig. 1.14), whereas ATLAS will adopt the toroidal configuration with the addition of a small solenoid for inner tracking (see Fig. 1.15). Since a large bending power is needed to measure precisely high momentum charged tracks one is naturally forced to choose superconducting technology for the magnets.

The relative $p_t$ resolution achievable using three equally spaced measuring points with space resolution $\sigma$ in a uniform magnetic field is given by [29]:

$$\frac{dp_t}{p_t} = \frac{\sqrt{3}}{2}\sigma\frac{8p_t}{0.3BL^2} \tag{1.5}$$

where $p_t$ is measured in GeV/$c$, B in T, $\sigma$ and L in m. This equation does not include contributions from energy loss and multiple scattering[3] and has correction factors if the number and relative placement of the measuring points is different.

The number of field lines crossed by a muon track in toroids is constant. In the forward parts of the detector, called endcaps, the magnetic field increases as $1/R$, where R is the distance from the beam axis. Hence toroids, unlike solenoids, have the attractive property that the $p_t$ resolution is constant over a wide range of pseudo-rapidity. The integral of $B.dl$

[3]The relative momentum resolution due to multiple scattering is given by [29] $\frac{dp_t}{p_t} \approx 0.05\frac{1}{B\sqrt{LX_0}}$ ($p_t$ in GeV/c, $B$ in T, $X_0$ and $L$ in m), hence it is independent of $p_t$ .

($\propto 1/\sin\theta$) compensates for the Lorentz boost in the forward direction. In an air-cored toroid a good stand alone momentum resolution can be reached as long as the quantity $BL^2$ is large enough. In Atlas: $\sigma \approx 70$ $\mu$m, $B \approx 0.6$ T, $L \approx 4.5$ m implying $\Delta p/p \approx 0.8\%$ at 100 GeV/$c$. This is even better than what can be achieved with the inner tracker ($B = 2$ T, $L \approx 1$ m), however up to about 200 GeV/$c$ the $p_t$ resolution is actually limited by energy loss fluctuations in the calorimeters and by multiple scattering. At very high $p_t$ muon detector resolution and misalignment effects dominates the resolution (see Fig. 1.16). Thus the space resolution of the muon chambers and alignment precision play a crucial role. Taking into account the large dimensions of the ATLAS muon system, the required precision of the order of 50 $\mu$m represents a real challenge also from the point of view of chamber alignment.
A serious drawback of the toroidal configuration is that the bending does not take place in the transverse plane and hence benefit cannot be drawn from the precise knowledge of the interaction point in this plane, which is known with an error of $\approx 20\mu$m at the LHC to be compared with the much larger uncertainty ($\approx 5$ cm) on the position along the beam direction.

A compact detector with a single magnet results from the use of a large high field solenoid. A large solenoid permits to accommodate the calorimeters inside the coil (in CMS: radius=3 m, length= 13 m, $B = 4$ T). In this way the task of the electromagnetic calorimeter is not disturbed by the coil and above all a good muon system results from magnetic tracking in an instrumented iron yoke, which serves the purpose of returning the magnetic flux produced by the solenoid. The muon stand-alone $p_t$ resolution is worse than that obtainable with toroids as it is limited by the multiple scattering in the iron yoke. However the large product $BL^2$ in the inner tracking ($L = 1.1$ m) allows to achieve extremely good full system resolutions at relatively low $p_t$ .
At very high $p_t$ one can make use of a combined measurement between the inner tracker and the muon system to improve resolution. Indeed a property of solenoids is that, if multiple scattering and energy loss are neglected, which is a good assumptions at very high $p_t$ , then the muon trajectory after the return yoke extrapolates back to the beam-line due to the compensation of the bending before and after the coil. This fact can be used to improve the momentum resolution at high momenta by measuring the perpendicular distance between the outermost inner tracking points and the line joining the beam to the muon after the return yoke (the measurement obtained with this method is indicated with full triangles in Fig. 1.17). The muon momentum resolution foreseen in CMS in the central pseudo-rapidity region is shown in Fig. 1.17; it is about 5 % at $p_t$ =1 TeV/$c$ and $\eta = 0$.
For tracks passing through the end of the solenoid the $p_t$ resolution worsens as $\tan\theta$. The

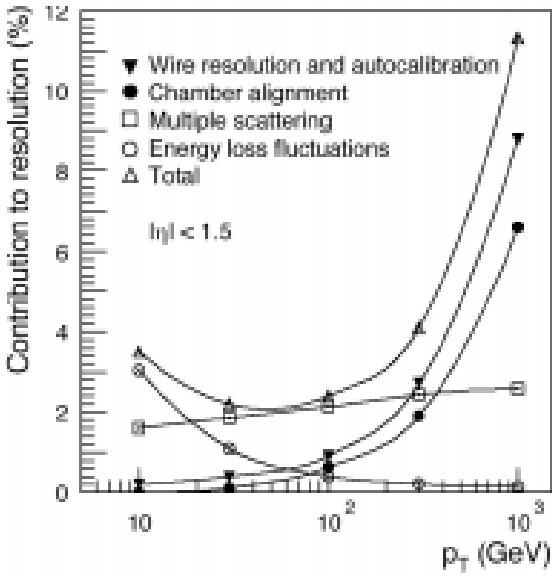


Figure 1.16: The various momentum contribution to the momentum resolution for muons in the ATLAS detector.

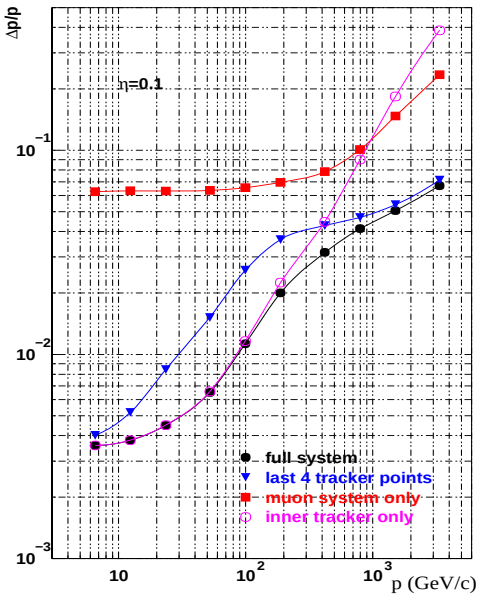


Figure 1.17: The muon momentum resolution achievable in CMS at $\eta = 0.1$ using the inner tracker and the muon system.

CMS momentum resolution is anyway better than 20% up to $\eta = 2.4$.
An advantage of the solenoidal configuration with a 4 T field is that good momentum resolution can be achieved without requiring very good chamber space resolution and more modest requirements on the alignment (of order $\sim 100$ $\mu$m. On the other hand, the main drawback of a scheme with muon chambers packed close to the iron is the presence of an important electromagnetic background due to showering in the iron induced by muon bremsstrahlung, which complicates the track reconstruction. Together with the unavoidable cracks introduced for the supports and the cabling of large detectors, this background is the most important reason for choosing a highly redundant system.

The transverse and longitudinal views of the CMS detector are shown in Figs. 1.18 and 1.19. In the following the characteristics of each subsystem of the CMS detector are reviewed. A very important aspect that has been taken into account in the choice of the detector technology is the radiation hardness and the rate capability. Indeed the LHC will create an extremely hostile radiation environment due to the $\approx 10^9$ inelastic interaction per second and to the unavoidable collisions of the beams with the machine collimators.

### 1.3.4 The CMS inner tracker

The central tracking system has been designed in order to achieve the goal of reconstructing isolated high $p_t$ tracks with an efficiency of better than 95%, and tracks within jets with an efficiency of better than 90% over the region $|\eta| < 2.4$.
To perform efficient $b$ tagging even at the highest luminosities a few layers of silicon pixel detector close to the interaction vertex are used. The design goal in this case is to achieve an impact parameter resolution at high $p_t$ of the order of 20 $\mu$m in the transverse plane and 65 $\mu$m in the longitudinal one. In Fig. 1.20 it is shown a longitudinal section of the tracker system. Starting from the interaction point there are three layers of pixel detectors in the barrel and two discs in each endcap, each pixel has dimensions of $150 \times 150$ $\mu$m$^2$ resulting in an overall number of $50 \cdot 10^6$ channels.
External to the barrel inner tracker there are 5 cylindrical layers of one-sided silicon strip detectors (layer n. 6,7,10,12,13 drawn in red in Fig. 1.20 ) and 5 stereo layers (layer n. 4,5,8,9,11 drawn in blue in Fig. 1.20) obtained by coupling one-sided sensors. In the endcap there are 3 mini-discs plus 9 discs, each having both one-sided and double-sided detectors. The total area covered by the CMS full silicon tracker is 223 m$^2$. This is the largest ever designed silicon detector surface.

The tracker is exposed to a primary particle flux from the interaction region and to neutron albedo emerging from the calorimeters. The main concern in this case is radiation

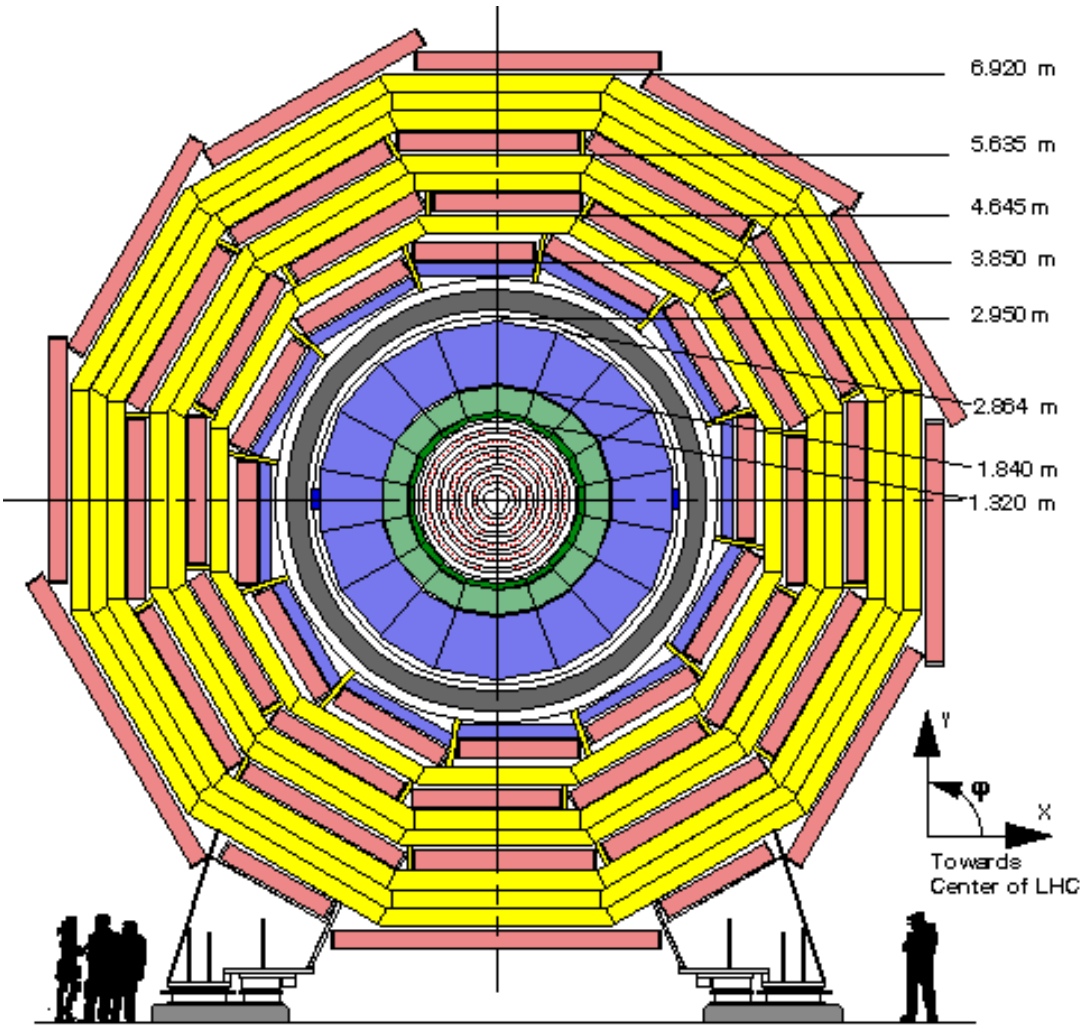


Figure 1.18: Transverse view of the CMS detector.

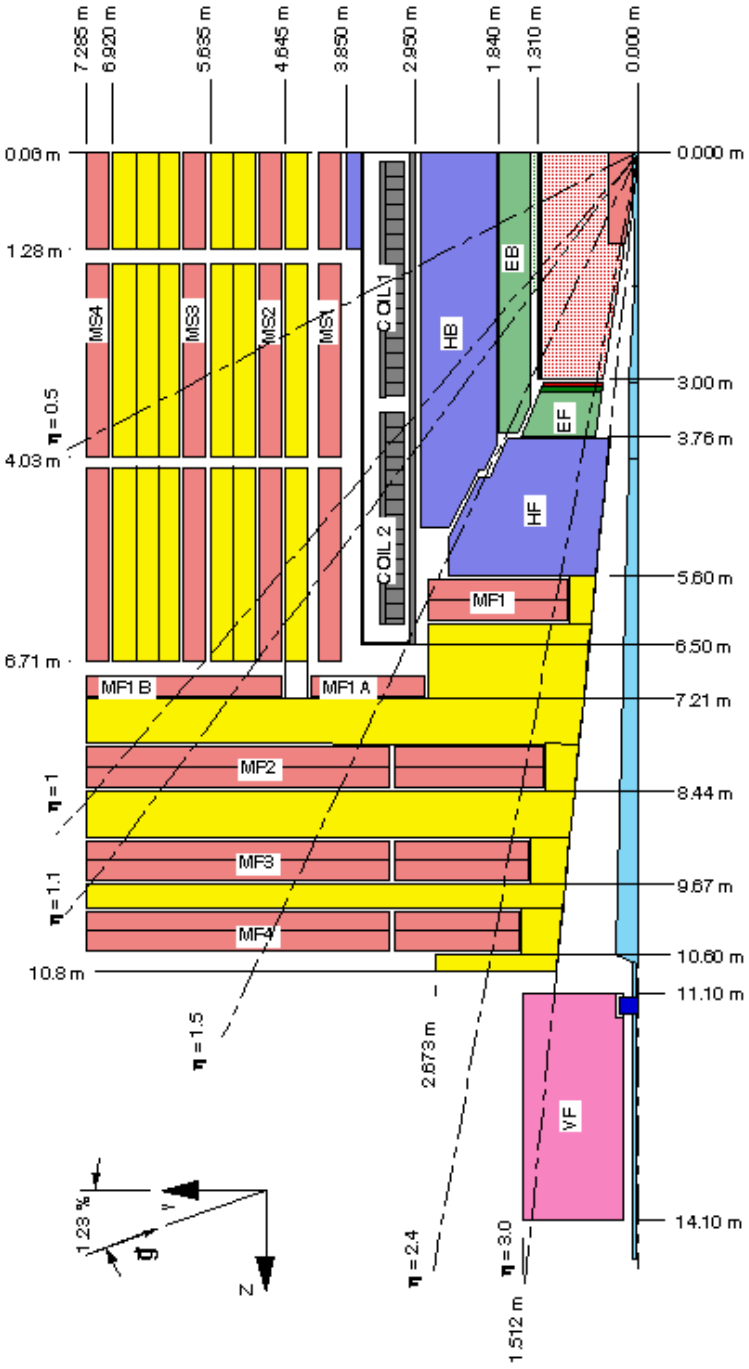


Figure 1.19: Longitudinal view of the CMS detector.

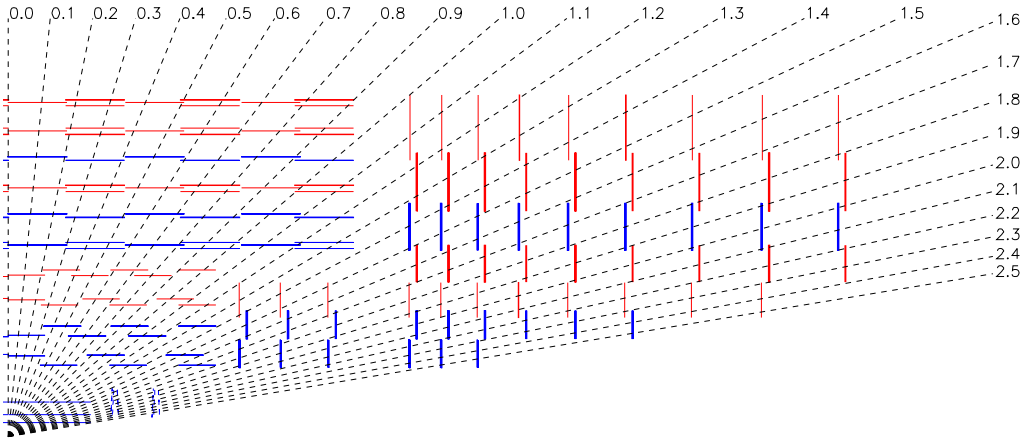


Figure 1.20: Longitudinal view of one quarter of the inner tracker of CMS.

damage of silicon devices. This will perhaps force to replace the innermost pixel layers after some year of operation at the maximum luminosity.

### 1.3.5 The CMS calorimeters

It has been stressed in the previous sections that one fundamental requirement for any general purpose experiment at the LHC is to have a high performance electromagnetic calorimeter (ECAL). CMS has chosen an homogeneous calorimeter made of lead tungstate ($PbWO_4$) crystals. The reasons that have led to the choice of the $PbWO_4$ are the short scintillation decay time constant, the short radiation length ($X_0 = 0.9$ cm) and small Moliere radius (2 cm) leading to a compact ECAL with good radiation hardness. In the barrel ($|\eta| < 1.48$) the crystals will be instrumented with silicon avalanche photodiodes (APDs) which permit to overcome the previous drawback of low light yield by the $PbWO_4$. In the endcap ($1.48 < |\eta| < 3.0$), where the irradiation levels are much higher and would lead to a too high induced leakage current in the APDs, vacuum phototriodes (VPTs) have been chosen.
The crystals have a cross section of $22 \times 22$ mm$^2$ and length of 23 cm. To provide $\pi^0 - \gamma$ separation, a preshower detector consisting of two lead/silicon detector layers will be placed in front of the endcap calorimeter ($1.65 < |\eta| < 2.61$).

The hadron calorimeter (HCAL) consists of two separate systems: the central calorimeter and the very forward calorimeter. Both the barrel and the endcap central hadron calorimeters, HB and HE respectively, experience the 4 T magnetic field of the

CMS solenoid and hence are necessarily fashioned out of non-ferromagnetic material. They are sampling calorimeters that consist of active material inserted between 5 cm thick brass absorber plates. The active elements are 3.7 mm thick plastic scintillators tiles read out using wavelength-shifting plastic fibres and hybrid photodiodes. Because the HB inside the coil is not sufficiently thick to contain all the energy of high energy showers, additional scintillator tiles are placed just outside the coil to form an outer hadronic calorimeter (HOB). The $\eta$ coverage of the central calorimeter is $|\eta| < 3.0$.
To extend the hermeticity of the system up to $|\eta| = 5.0$, CMS employs a separate forward calorimeter (HF) located 6 m downstream of the HE. The HF uses quartz fibres as the active medium, embedded in a steel absorber matrix. Because of its quartz fibre active element, it is predominantly sensitive to Cerenkov light. The photodetectors will be conventional photo-multiplier tubes.

The depth of the HCAL is greater than 11 nuclear interaction length over the full $\eta$ coverage.

### 1.3.6 The CMS muon system

The CMS detector is specifically optimised for muon measurement which is performed in the muon system by Drift Tubes (DTs), located outside of the magnet coil in the barrel region, and Cathode Strip Chambers (CSCs) in the endcap region. The CMS muon system is also equipped with Resistive Plate Chambers (RPCs), whose main task is triggering but will also help reconstruction as it will be proved in this thesis.
Location of the muon detectors is schematically shown in Fig. 1.21. Both in the barrel and in the endcap, the detectors are placed in four muon stations interleaved with the iron of the yoke to make full use of the magnetic return flux ($\approx 1.8$ T). The redundancy is ensured by both number of stations and number of detector layers in each station. In the barrel the stations are labelled MB1-4. The two innermost stations, MB1 and MB2, contain two RPC modules and one DT each, whereas stations MB3 and MB4 house one RPC and one DT. The barrel stations are grouped into 5 wheels, which are in turn divided into 12 $\varphi$ sectors covering roughly $30^0$ (see Figs. 1.18 and 1.19).
One RPC module and one CSC are placed in every endcap station (ME1-4). The stations are grouped in rings. The first layer of stations is composed of three sub-rings labelled ME1/1, ME1/2 and ME1/3, starting from the closest to the beam line. The 3 remaining layers are made up of two sub-rings: MEX/1 and MEX/2 (X=2,3,4). The CMS muon system covers the region $|\eta| < 2.4$, however the RPC system covers only $|\eta| < 2.1$.

An important role in the choice of the detector technology has been played by the

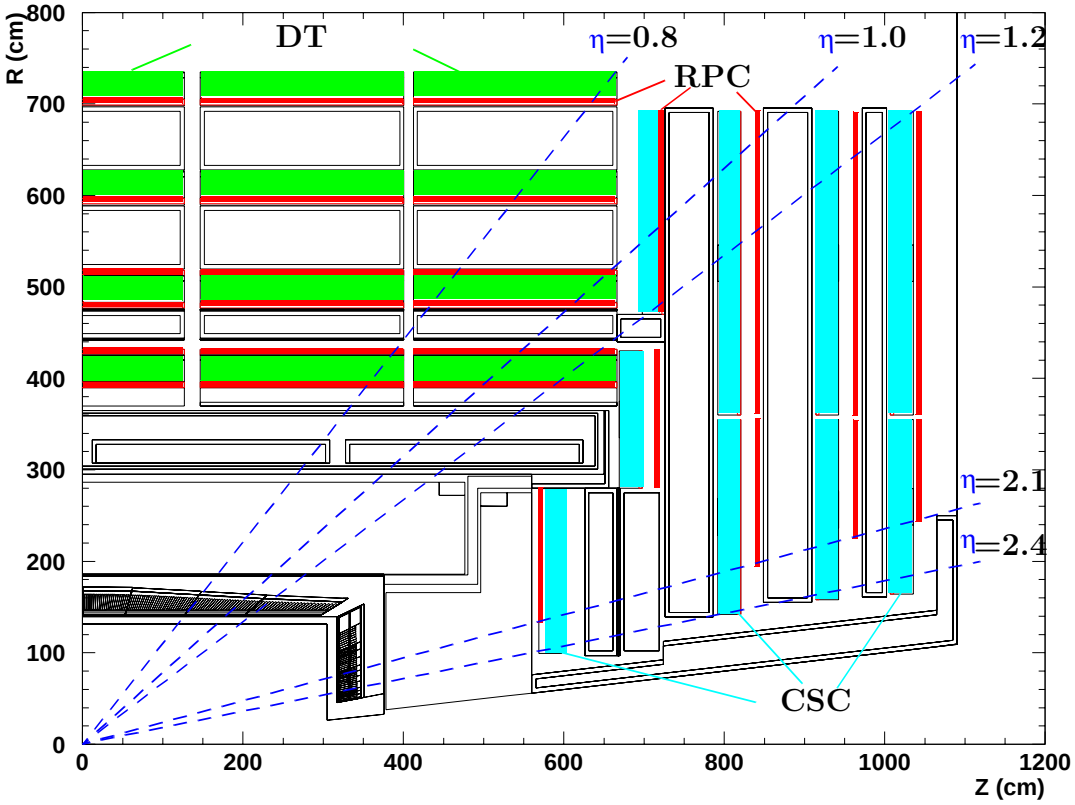


Figure 1.21: The CMS muon detectors.

radiation environment that is expected in the muon system. The main background fluences on the chambers can be classified as follows:

- Low energy radiative electrons following slow neutron capture near or inside the muon chamber. These neutrons originate from hadronic cascades starting somewhere in the detector or in accelerator components.
- Charged hadrons from hadronic cascades: backsplash from HF and albedo, and leakage from HE and the collimator shielding.
- Decay muons coming mostly from $\pi$/K decay inside the inner tracker cavity.

In Fig. 1.22 the background hit rates are shown as a function of $\eta$ for each muon station. It is evident from Fig. 1.22 that the most irradiated chambers are those in the endcap and that everywhere the dominant contribution to the hit rate is due to neutral particles. The

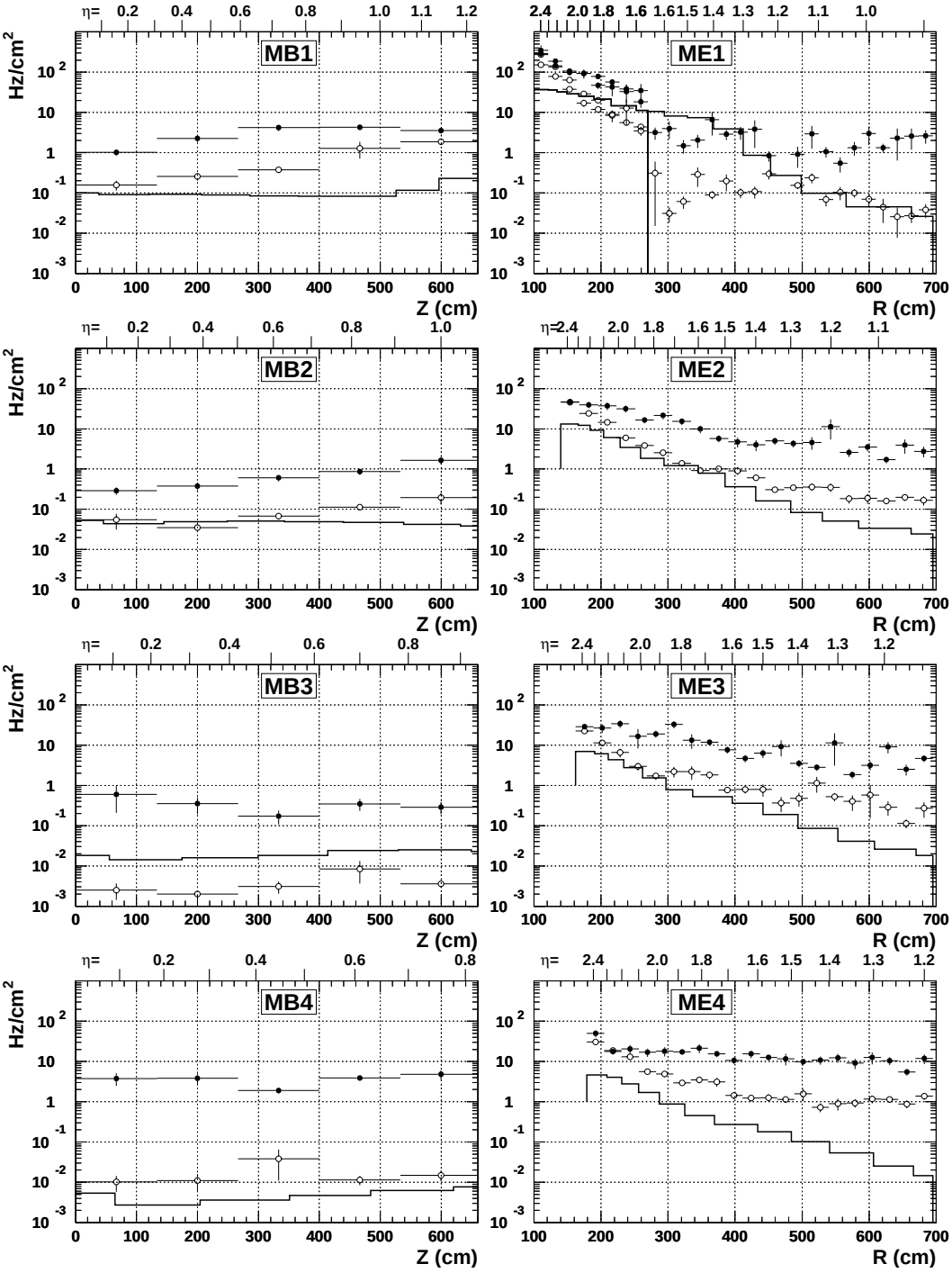


Figure 1.22: Hit rates expected in the CMS muon chambers at $10^{34}$ cm$^{-2}$s$^{-1}$ . Full lines indicate the hit rate due to real muons. Empty circles refer to punch-through hadrons, whereas full circles correspond to hits caused by neutral particles background.

total hit rate at the highest pseudo-rapidity reaches some hundreds Hz/cm$^2$ in ME1/1. The rates in other endcap chamber and in all barrel chambers are much lower, of the order of 10 Hz/cm$^2$ or less.
The analysis of the background sources has shown that the most critical regions in the background generating process are the CMS beam pipe and the forward region, i.e. the HF and the collimator with their shielding.
It is important to note that high energy background like punch-through hadrons and decay muons, are time related to the bunch crossing. On the contrary low energy background, which represents the main contribution, is uncorrelated.
DTs and CSCs on one side and RPCs on the other have different ways to protect themselves against background.
The multi-layer structure of DT and CSC permits them to require coherent track stubs, therefore they have a high rejection power against single hits produced by low range particles. However, their relatively long response time obliges them to carry out a local reconstruction by means of a simultaneous analysis of signals produced over several bunch crossings in the various layers composing them. This also allows them to achieve bunch crossing assignment capability, which would not be possible in a single layer structure. The main concern is then the confusion that may arise in the local reconstruction due to possible additional hits produced in the gas by secondaries accompanying the muons or by uncorrelated background hits that are collected over a certain number of bunch crossings. Energetic muons are particularly involved as the probability of radiating increases with the energy.
On the other hand RPCs, which are extremely fast detectors, can provide immediate and unambiguous assignment of the bunch crossing to each single signal, independently of any other. In addition RPCs do not demand costly readout devices, therefore they can be sufficiently highly segmented in order to reduce further the rate per channel. The drawback in their case is the total absence of protection against isolated uncorrelated hits due to either detector noise or low range background particles.

**The DT detectors**

Each DT module is composed of three superlayers (SL) each one split in four layers of staggered drift tubes as shown in Fig. 1.23: two SL measure the coordinate in the bending plane ($\varphi$ view) and one looks at the longitudinal plane ($\theta$ view). The inner $\varphi$ view SL is separated from the other ones by a 20 cm thick aluminium honeycomb plate that supplies the module with the required stiffness, permits the opening of electromagnetic showers that

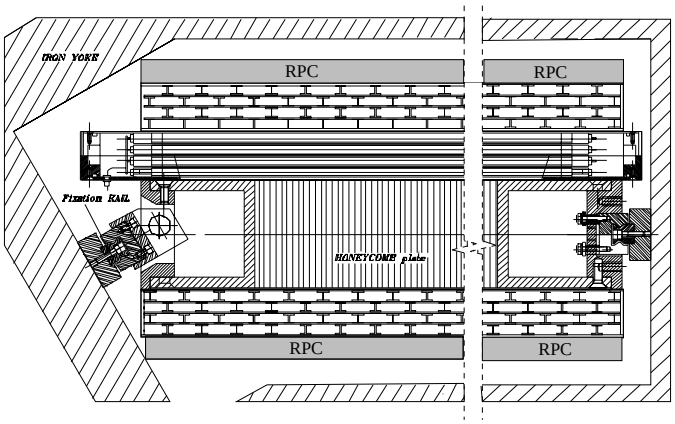


Figure 1.23: Cross section of a barrel muon chamber.

can be generated inside the iron allowing a better measurement in the SL away from the iron and provides a lever arm in the bending plane.
The outermost station differs from the inner ones since it does not have the SL in the $\theta$ view. Its eventual contribution to the muon $\eta$ assignment was found to be marginal.

The baseline cell design, which is shown in Fig. 1.24 , has a pitch of 40 mm by 13 mm. The anode wire is made of stainless steel and is 50 $\mu$m in diameter. The cathodes defining the cell width are aluminium I-beams. A plastic profile, made of 0.5 mm thick extruded polycarbonate plastic, is glued to the upper and lower parts of the I-beams in order to electrically insulate the cathodes from two aluminium plates. These plates, which are kept at ground potential, form the two remaining sides of the cell. With this geometry the drift field is obtained by applying a positive voltage to the wires and a negative voltage to the cathodes. A pair of positively biased field shaping strips is placed at the centre of the cell in order to improve the space-time linearity and consequently the space resolution of the cell. A typical configuration of the potential, leading to the field profile shown in Fig. 1.24, is the following:

$$V_{wire} = +3600 \text{ V} \quad V_{cathode} = -1800 \text{ V} \quad V_{strip} = +1800 \text{ V}$$

Due to the large volume of the muon detector and to its underground operation, gas mixtures are demanded to be non-flammable. Taking into account budget limitations, excluding organic components that may suffer from aging effects, and requiring that the gas should have a saturated drift velocity, since as it will be made clear further on the trigger algorithm

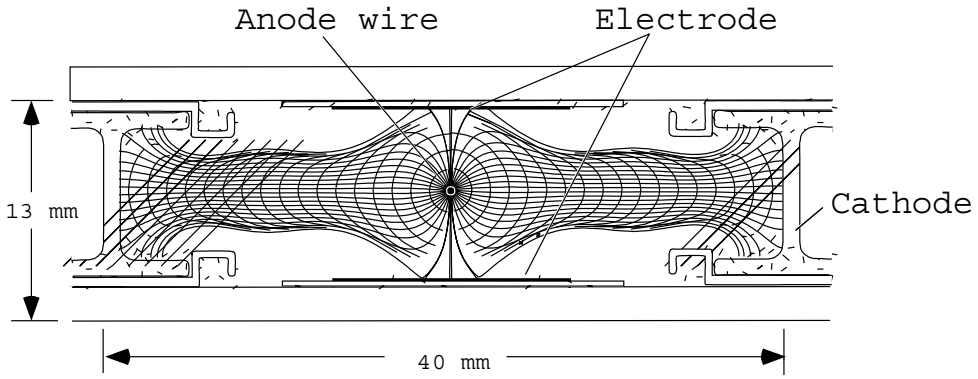


Figure 1.24: Transverse view of the baseline cell; also shown are drift lines and isochrones for a typical voltage configuration of the electrodes.

relies on space-time linearity, one is led to choose $Ar/CO_2$ mixtures. Concentrations of $CO_2$ between 10% and 20% lead to acceptable chamber performance [30].

Despite the long maximum drift time ($\approx$ 400 ns) it has been proved that a group of four consecutive layers of tube has good bunch crossing assignment capability. The principle on which it is based this time tagging capability will be explained in the next chapter.

**The CSC detectors**

In the endcap geometry, an $r$-$\varphi$ view of the bending of a fixed $p_t$ muon track is $\eta$ dependent (see Fig. 1.25). Results of direct simulation (Fig. 1.26) show that the sagitta, if expressed in linear (cm) coordinates, changes by a factor of 5 from $\eta = 1.6$ to 2.4 for fixed $p_t$ muons.

If the same sagitta is measured in $\varphi$-coordinates it is substantially less $\eta$ dependent: it changes by a factor 2 in the same range of $\eta$. Thus $\varphi$-coordinates are more natural for measuring $p_t$. Therefore the chambers have trapezoidal shape and the readout is arranged so as to provide $r$ and $\varphi$ coordinates.

The relatively long drift time of the DT is unacceptable in the endcap, where the hit rate is expected to be much higher than in the barrel. In addition, the endcap chambers have to operate in a more intense magnetic field such that any drift chamber performance would significantly deteriorate. Thus it has been chosen to use CSCs that are multi-wire proportional chambers in which one cathode plane is segmented into strips running across wires.

The passage of an ionizing particle gives rise to an avalanche in the proximity of an anode wire. It has been demonstrated [31] that by interpolating the fractions of charge picked up

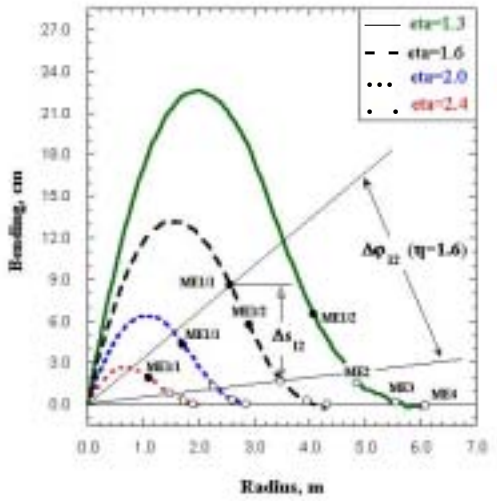


Figure 1.25: Muon tracks of fixed $p_t = 10$ GeV/$c$ as seen in the $r - \varphi$ view. The points at which muons cross the chambers are marked (filled circles for ME1 stations, open circles for ME2, ME3, ME4). The sagitta, for example, as measured between the collision point, ME1 and ME2 $\Delta s12$ (expressed in cm) for fixed $p_t$ muons, is clearly $\eta$ dependent.

by the strips, one can reconstruct the track position along a wire with a precision of 100 $\mu$m or better. The principle of operation is shown schematically in Fig. 1.27. The CSC is a fast detector provided the wires are sufficiently close to each other. Moreover the simultaneous measurement of signals from strips and wires permits to obtain two coordinates from a single detector layer. CSCs can also be operated in large and non uniform magnetic fields without significant deterioration in their performance.

The CMS CSC consists of six detecting layers. The maximum length is 3.4 m and the maximum width is 1.5 m. The chambers cover either $20^0$ or $10^0$. The layers are separated by 16 mm thick polycarbonate plastic honeycomb panels which make the chamber stiff and provide a lever arm necessary to measure angle of tracks. Gas gaps are either 6 mm thick (in ME1/1) or 9.5 mm thick (in all other stations). In each layer, the strips, which give the precise measurement, run radially and their width ranges from 3 to 16 mm. Wires are stretched across strips and for readout purposes are grouped in bunches from 5 to 16. They provide the radial coordinate with a precision of a few cm. For the ME1/1 chamber, which is in a 3 T $B_z$-field, the wires are strung at $25^0$ to a perpendicular to the chamber centerline to compensate for the skewed drift of electrons.

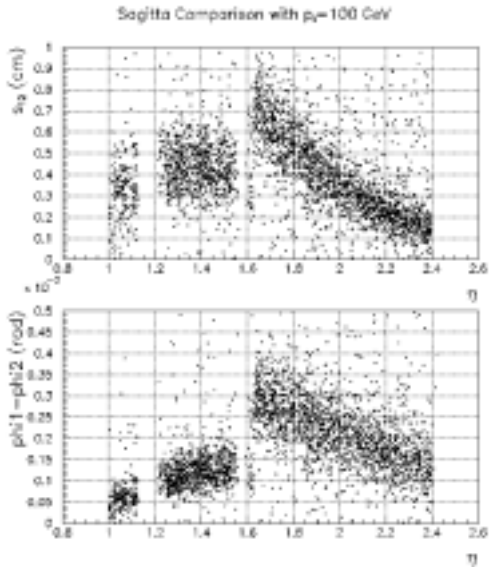


Figure 1.26: Sagitta as measured between the collision point, ME1 and ME2 stations versus $\eta$ : (a) expressed in cm for fixed $p_t$ muons; (b) expressed in $\varphi$ coordinates for fixed $p_t$ muons.

### The RPC detectors

RPCs are gaseous parallel plate detectors with an excellent time resolution (of the order of 1 ns). An RPC consists of two parallel plates, made out of phenoilc resin (bakelite) with a bulk resistivity of $10^{10} - 10^{11}$ $\Omega$cm, separated by a gas gap of a few millimeters. The whole structure is made gas tight. The outer surfaces of the resistive materials are coated with conductive graphite paint to form the HV and ground electrodes. The readout is performed by means of aluminum strips separated from the graphite coating by an insulating PET film. The RPC proposed for CMS is made of two gaps with a common set of strips in the middle. A simplified layout of the double-gap design is shown in Fig. 1.28. The strips run only in the direction orthogonal to the track bending in the magnetic field.

The RPC operating principle and its design for CMS will be discussed in great detail in chapter 3.

In the barrel the RPC chambers in stations MB1, MB3 and MB4 and those in the lower plane of MB2 are divided in two separately read out detectors whereas the chambers in the upper plane of MB2 are divided in three [4]. The RPC strips are about 120 cm (80 cm) long

[4]Recently it has been decided that in the MB2 stations of the three central wheels the chambers in the

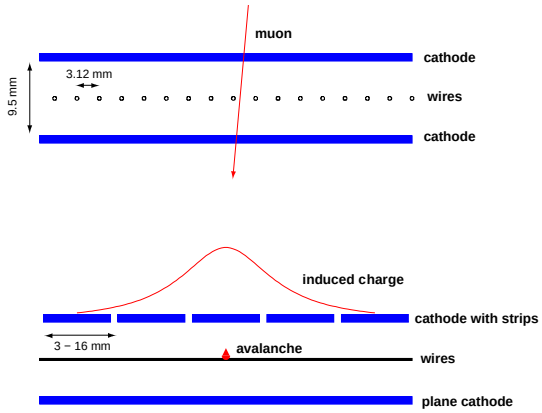


Figure 1.27: Principle of coordinate measurement with a cathode strip chamber: cross-section across wires (top) and across cathode strips (bottom). Close wire spacing allows for fast chamber response, while a track coordinate along the wires can be measured by interpolating strip charges.

in the detectors of the planes divided in two (three) and their pitch varies from 2.1 cm in the inner MB1 plane to 4.1 cm in the MB4 planes.
In the endcaps the RPC chambers have a trapezoidal geometry and the strips run radially. The number of separately read out detectors in which each chamber is divided varies from station to station. The dimensions of the strips vary strongly from detector to detector: they are about 25 cm long and have a pitch of 0.7 cm in the lowest detector of the ME1 chambers (at $\eta = 2.1$) whereas in the chambers at highest $r$ in ME2,3,4 they are about 80 cm in length and have a pitch of roughly 3 cm. This segmentation is dictated by the radial geometry and by the expected neutral background hit rates.

lower plane will be divided in three detectors whereas the upper ones will be divided in two. In the other two wheels the chamber geometry stays unchanged.

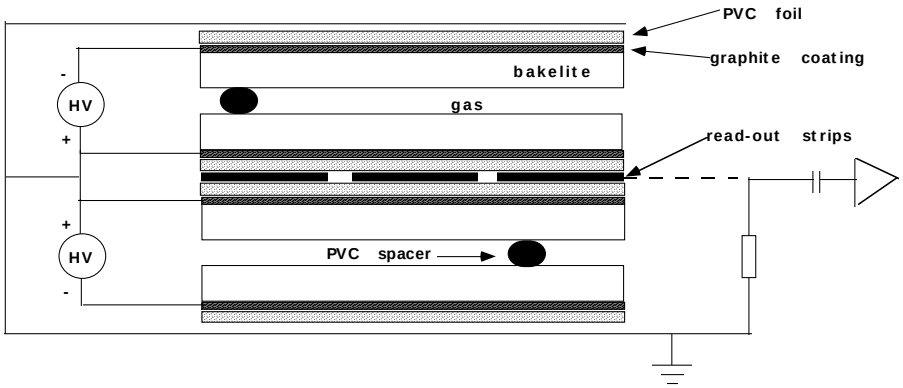


Figure 1.28: Schematic view of a double-gap RPC detector.

# Chapter 2

# The CMS muon trigger

## 2.1 General structure of the CMS Trigger and DAQ

Event selection is one of the most difficult tasks for any experiment at the LHC. The bunch crossing frequency is 40 MHz and at the nominal luminosity of $10^{34}$ $\mathrm{cm}^{-2}\mathrm{s}^{-1}$ the average number of inelastic interactions in a crossing is 17.3. The task of the Trigger and Data Acquisition System (DAQ) is to analyse the full set of interactions occurring in every bunch crossing, identify the presence of an interesting interaction and write on permanent memories the data related to the bunch crossing for all detectors.
The maximum recording rate capability of the CMS on-line computer farm is 100 Hz hence the rate reduction that has to be achieved is 40 MHz / 100 Hz = $4 \cdot 10^5$. CMS has chosen to perform this task in two basic steps. Initially the Level-1 Trigger (L1) reduces without dead time the input rate to no more than 75 kHz. The L1 trigger is based on custom electronics. The selected events are forwarded to the second level selection system: the High Level Trigger (HLT). The HLT relies upon commercial processors, therefore the algorithms it adopts are software implemented. The HLT selection is performed in subsequent filters.
The L1 trigger uses only coarsely segmented data from the calorimeters and the muon detectors, while all the high resolution data of all detectors is held in pipeline memories in the front-end electronics. Following a L1 accept, data is collected by readout units and events are further selected by the filters of the HLT using more and more complete information and more and more sophisticated algorithms as the number of selected events gets smaller. In the first event filter operating on an input rate of 25 kHz (a safety factor of 3 has been applied), also called L2 trigger, it is foreseen that full resolution information from just calorimeters and muon detectors will be used. The L2 is expected to reduce the event rate by roughly an order of magnitude. The inner tracker data, which represents

about 80% of the 1 MByte average event size and requires the most complex algorithms for reconstruction, is expected to be used only after the L2 filter. It is under consideration the option of using in the L2 filter part of the inner tracker data from particular regions of interest indicated by the L1 trigger.
The output of the HLT has to match 100 Hz which corresponds to the maximum rate that can be managed by the DAQ for permanent storage. The design of the CMS Trigger and DAQ system is illustrated in Fig. 2.1

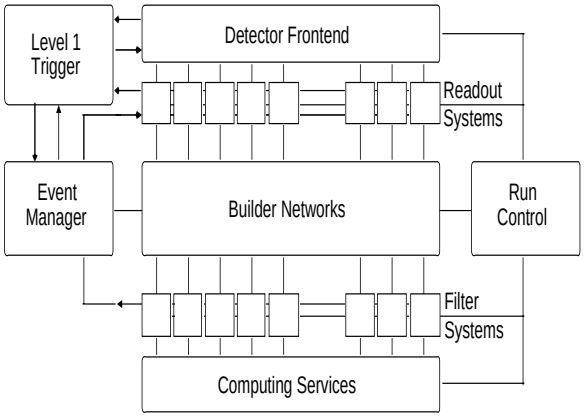


Figure 2.1: CMS Trigger and Data Acquisition System.

## 2.2 The First Level Trigger

The L1 trigger system is organized into three major subsystems: the L1 Calorimeter Trigger, the L1 Muon Trigger, and the L1 Global Trigger. The Muon Trigger is further organized into subsystems representing the 3 different muon detector systems, the DT trigger in the barrel, the CSC trigger in the endcap and the RPC trigger covering both barrel and endcap up to $\eta = 2.1$. The L1 Muon Trigger is also called Global Muon Trigger (GMT) and combines the trigger information from the DT, CSC and RPC trigger systems and sends this to the L1 Global Trigger. A diagram of the L1 trigger system is shown in Fig. 2.2. The data used as input to the DT, CSC and RPC trigger systems as well as the input data to the GMT, Calorimeter Trigger and the Global Trigger are transmitted to the DAQ for storage along with the event readout data. In addition, all trigger objects found, whether they were responsible for the L1 trigger or not, are also sent.

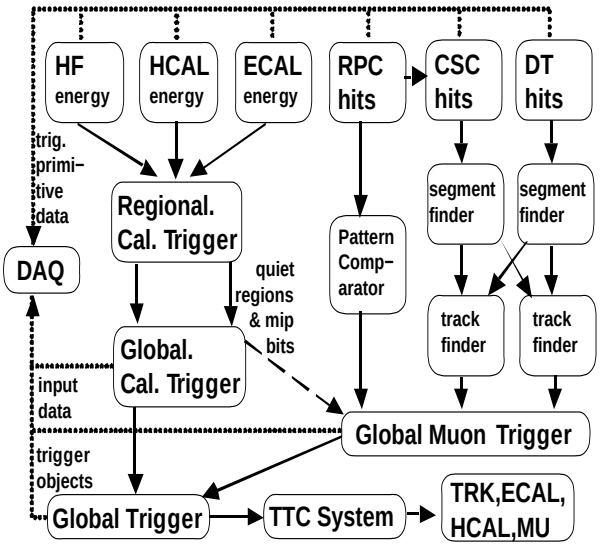


Figure 2.2: Overview of the CMS Level 1 Trigger.

### 2.2.1 Requirements

The L1 trigger has to be deadtimeless therefore data has to be pipelined while waiting for the decision whether to discard it or keep it. A decision has to be made on every bunch crossing, i.e. every 25 ns. The L1 pipeline data storage time is 3.2 $\mu$s. Since signal propagation delays are included in this pipeline time, the L1 trigger calculations must be done in many cases in less than 1 $\mu$s. Such fast algorithms can only be accomplished by means of custom electronics.
The limit of 3.2 $\mu$s is imposed by the amount of data storable in the inner tracker and preshower front-end buffers.
Physics requirements for the L1 Trigger should be derived from the discussions of the previous chapter. One can see that most of the interesting physics processes produce at least two trigger objects. Only very few channels require single-object triggers *per se*. Some of these channels are:

- $B_d^0 \longrightarrow \pi^+\pi^-$ with $b \longrightarrow \mu_{tag}$ or $b \longrightarrow e_{tag}$

- inclusive $W$

In the first channel one can still try to apply multi-object triggers by treating the $\pi^+\pi^-$ pair as a kind of narrow jet.
The fact that multi-object triggers are of primary importance at LHC has very substantial implications for the principle of the trigger operation. Different combination of objects may require different trigger thresholds. Therefore one should avoid any explicit cut on single objects on the level of Muon or Calorimeter Trigger. The purpose of these triggers is to identify objects, estimate their $p_t$ or $E_t$ and send them to the Global Trigger. The Global Trigger is the only place where the objects are combined and the cuts are applied depending on a given combination.
Single-object triggers are used mainly to recover the multi-object events which were not recognised by the multi-object triggers, because of incomplete acceptance or failure of algorithms. Therefore, the criteria on their thresholds are not very strict. The actual working point should be chosen as a result of the trade off between the efficiency and the rate. A useful lower limit for $\mu/e/\gamma$ at $10^{34}$ cm$^{-2}$s$^{-1}$ is about 20-30 GeV/$c$ (see Fig. 1.13). Below this value one cannot further improve the efficiency for objects like $W$, $Z$ or heavier, and the rate is dominated by leptons from quark decays (except the top quark). At this point, the rate of every single object is of the order of a kHz (see Fig. 1.13). Adding all the channels together and allowing a factor 10 for instrumental background, which is mainly due to mismeasured low energy objects, one can expect the total L1 output of the order of some tens of kHz. Thus, in order to have some safety margin, the HLT should be able to receive $\approx 10^5$ Hz of events. The exact requirement chosen for the CMS startup is 75 kHz. Assuming a safety factor of 3, the L1 output rate should be within 25 kHz. This bandwidth is equally divided between triggers involving at least a muon (muon triggers) and triggers not involving muons (calorimeter triggers).

### 2.2.2 Calorimeter Trigger

The Calorimeter Trigger has to fulfil the following requirements:

- Identify in the calorimeters, the following objects:
  - the four most energetic isolated electron/photon candidates in $|\eta| < 2.5$.
  - the four most energetic non-isolated electron/photon candidates in $|\eta| < 2.5$.
  - the four most energetic jets in the central region, $|\eta| < 3$
  - the four most energetic jets in the forward region, $3 < |\eta| < 5$;
  - the four most energetic $\tau$-jets in $|\eta| < 2.5$.

- Provide a measurement of the transverse energy and position information for the objects identified.
- Identify the bunch crossing each object is originating from.
- Count the number of jets fulfilling several programmable energy and position cuts.
- Measure the missing transverse energy and the total transverse energy in the calorimeters using the complete system, i.e. $|\eta| < 5$.
- Flag the quiet regions in the calorimeters and the regions with an energy deposit compatible with a minimum ionising particle for use by the muon trigger.
- Create histograms for luminosity monitoring accumulated over several bunch crossings and accessible by detector control system at about few seconds intervals.
- The Calorimeter Trigger should provide the selectivity and the energy resolution necessary to keep the total output rate of the calorimeter triggers below 12.5 kHz at high luminosity.

The Calorimeter Trigger begins with trigger tower energy sums formed by the ECAL, HCAL and HF upper level readout Trigger Primitive Generator (TPG) circuits from the individual calorimeter cell energies. For the ECAL, these energies are accompanied by a bit indicating the transverse extent of the electromagnetic energy deposit. For the HCAL, the energies are accompanied by a bit indicating the presence of minimum ionising energy. The TPG information is transmitted over high speed copper links to the Regional Calorimeter Trigger (RCT), which finds candidate electrons, photons, taus, and jets. The RCT separately finds both isolated and non isolated electron/photon candidates. The RCT transmits the candidates along with sums of transverse energy to the Global Calorimeter Trigger (GCT). The GCT sorts the candidate electrons, photons, taus, and jets and forwards the top 4 of each type to the global trigger. The GCT also calculates the total transverse energy and total missing energy vector. It transmits this information to the global trigger as well. The RCT also transmits an ($\eta$ , $\varphi$) grid of quiet regions to the GMT for muon isolation cuts.

### 2.2.3 Muon Trigger

The enormous muon rate expected at the LHC (see Fig. 1.13) is the primary reason for having an extremely redundant muon system. In CMS the redundancy is realized with the two sets of muon detectors: wire chambers (DT and CSC) and RPC.

At the L1 trigger the two systems are completely independent and can run in stand-alone mode. However, properly combining the information from both systems results in high efficiency and powerful background rejection. Two extreme cases of such combinations would be the logical OR, which is optimised for efficiency, and the logical AND, optimised for background rejection. However, neither of these operations results in full use of the complementary functions of the muon trigger components and a more sophisticated algorithm is used. Details on that will be given later on. More complex algorithms are possible, because both the DT/CSC and RPC trigger deliver information about the $p_t$ and the quality of detected muon candidates.
Another important advantage of the two component system is the possibility of cross-checks and cross calibration. Trigger data from the two components collected by the DAQ can be compared on-line. This enables the quick discovery of possible problems and gives a possibility of immediate action. In particular the RPC trigger, being a lot simpler than the one based on the wire chambers, will be perhaps the only one running in the initial phase of operation and will permit tuning of the DT and CSC triggers.
Another important point is that when cross sections, asymmetries etc. are studied it is very important to know the trigger efficiency and acceptance. Usually this is done by running with thresholds much lower than the measurement range. A two component system offers a unique ability to measure these quantities in a more unbiased way.
Complementary features of DT/CSC and RPC make them respond in different ways to various backgrounds. As it has been explained in detail in the previous chapter, DTs with long drift time ($\sim$ 400 ns) and CSCs with charge weighting are more vulnerable than RPCs to muon radiation. This point is particularly important for the detection of very energetic muons ($p > 100$ GeV/c). They have non negligible probability of being accompanied by electromagnetic showers due to direct $e^+e^-$ pair production, bremsstrahlung or photo-nuclear interactions. These showers can confuse the local reconstruction and cause inefficiency in the wire chambers. On the other hand RPCs have almost no defence against low range background particles or intrinsic noise. Accidental coincidence of three of four background hits can be recognised by the RPC trigger as a real muon. This is very unlikely for DT/CSC as they look for coincidence of several planes in each station.

The functional relations between the components of the Muon Trigger system are shown in Fig. 2.3. Some data is exchanged between DT and CSC in the region around $\eta = 1.0$. In this way the Barrel Track Finder covers $|\eta| < 1.04$, whereas the Endcap Track Finder covers $1.0 < |\eta| < 2.4$. The RPC trigger covers both barrel and endcap but only up to $\eta = 2.1$. Optionally, coarse RPC data can be sent to the CSC trigger in order to help solving spatial and temporal ambiguities in multi-muon events. This option has not been implemented yet

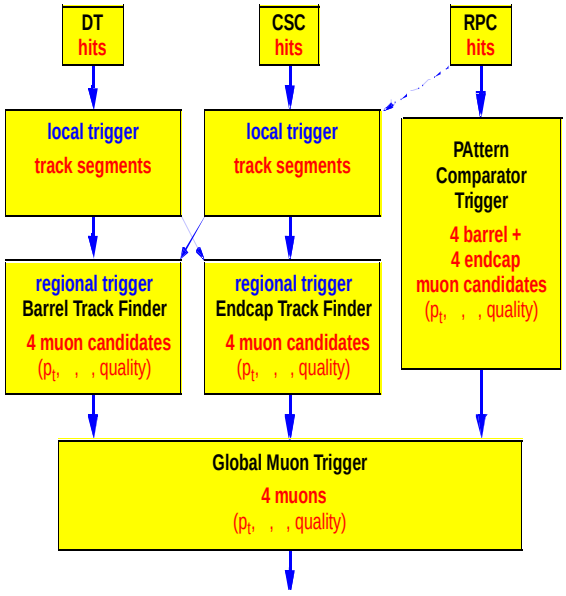


Figure 2.3: Muon Trigger data flow.

in the simulation and the results presented in this thesis do not include it.
The RPC trigger works on a grid of $\Delta\eta \times \Delta\varphi \sim 0.1 \times 2.5^o$, which determines its two muon resolution. The DT and CSC triggers do not work on a fixed grid. The $\eta$ and $\varphi$ coordinates are calculated with precision of 0.05 $\eta$ -unit and $2.5^o$ respectively.

DT and CSC electronics first process the information from each chamber locally. Therefore they are called local triggers. As a result vectors (position and angle) are delivered by each station. Vectors from different stations are collected by the Track Finder which combines them to form a muon track and assigns a transverse momentum value. Up to 4 best (highest $p_t$ and quality) muon candidates from each system are selected and sent to the GMT.
In the case of RPCs there is no local processing apart from synchronisation and cluster reduction. Hits from all stations are collected by the so called Pattern Comparator Trigger (PACT) logic. If they are aligned along a possible muon track, a $p_t$ value is assigned and the information is sent to the Muon Sorter. The RPC Muon Sorter selects the 4 highest $p_t$ muons from the barrel and 4 from the endcaps and sends them to the GMT.
The GMT compares the information from the DT/CSC Track Finder and RPC PACT. So called quiet and MIP bits delivered by the Calorimeter Trigger are used to form a possible isolated muon trigger. The 4 highest $p_t$ muons in the whole event are then transmitted to

the Global Trigger. More details on the principles of the various muon trigger components are given below.

### DT Trigger

The drift chambers deliver data for track reconstruction and triggering on different data paths. The local trigger is based on two SuperLayers (SL) in the $\varphi$ view of the muon station. The trigger logical blocks are shown in Fig. 2.4. The trigger front-end device,

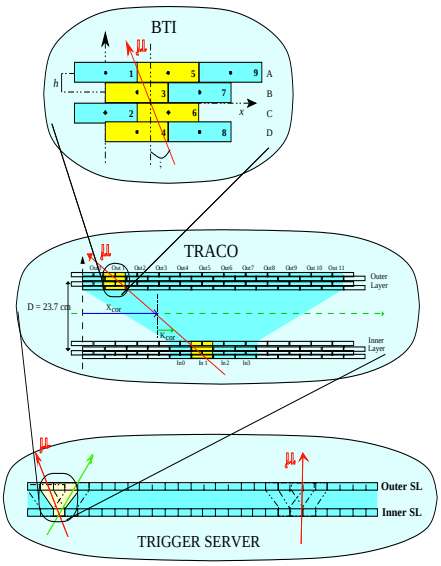


Figure 2.4: Block scheme of the local trigger of a drift chamber.

which is directly interfaced to the wire front-end readout electronics, is called Bunch and Track Identifier (BTI). It is used in both $\varphi$ and $\theta$ view and performs a rough muon track fit in one station measuring position and direction of trigger candidate tracks with at least three hits, in different planes of a SL. The algorithm fits a straight line within programmable angular acceptance. Since it accepts three points tracks, the device is still working even if the drift time of a tube is missing, due to inefficiency, or wrong, due to the emission of a $\delta$-ray, since there are still three useful cells giving the minimum requested information. It is also insensitive to all uncorrelated single hits. In the $\theta$ view only tracks pointing to the vertex are selected. The BTI uses an internal resolution of 0.7 mm for its calculations, but the resolutions on the output parameters are $\sim$ 1.4 mm on the impact position and $\sim$ 60

mrad on the track direction.
This device performs the bunch crossing assignment of every found muon track segment candidate. The algorithm used in the device is a generalisation of the mean-timer method [32]. Since this method must foresee alignment tolerances and needs to accept alignments of only three hits, the algorithm can generate false triggers. Hence in the bending plane a system composed by a Track Correlator (TRACO) and a chamber Trigger Server (TS) is used to filter the information of the two $\varphi$ SLs of a chamber in order to lower the trigger noise. The TRACO/TS block selects, at every cycle among the trigger candidates, at most two tracks with the smallest angular distances (i.e. higher $p_t$) with respect to the radial direction to the vertex.
In particular the TRACO improves the angular resolution of the muon candidate track to $\sim 10$ mrad using the larger lever arm available and is converting the triggering variables to $p_t$ related quantities (the position in the detector is given as the angle $\varphi$ and the bending angle $\varphi_B$), while the TS system is governing the two tracks selection decision and it is therefore deciding dimuon detection efficiency. The TS outputs at most two track segments in cells of size $\Delta\varphi \sim 1.5$ mrad and $\Delta\varphi_B \sim 12$ mrad. This cell defines the minimal de facto separation between two segments necessary for their identification, although two identical objects are allowed on output.
The $\eta$ segmentation is variable along the detector, being at fixed $z$ values: there are 40 pseudo-rapidity cells in the range $|\eta| < 1.2$.

Track segments found in each station are then transmitted to a regional trigger system called Drift Tube Track Finder. The task of the Track Finder is to connect track segments delivered by the stations into a full track and assign a $p_t$ value to the finally resolved muon track. The system is divided in sectors, each of them covering $30^o$ in the $\varphi$ angle. The Sector Processors are organized in twelve wedges along the $\eta$ coordinate. The Sector Processors in the outermost barrel wheels receive track segment data also from the Cathode Strip Chambers system, in order to handle the overlap region track finding. Each Sector Processor is logically divided in three functional units: the Extrapolator Unit, the Track Assembler and the Assignment Unit.

The Extrapolator Unit attempts to match track segments pairs of distinct stations. Using the spatial coordinate $\varphi$ and the bending angle of the source segment, an extrapolated hit coordinate may be calculated. The match is considered successful if a target segment is found at the extrapolated coordinate, within a certain tolerance. Memory based look up tables are used in the calculation of the extrapolated hit coordinate and tolerance values. Since tracks may cross detector sector boundaries, the Extrapolator Unit can use the neighbouring sector track segments as targets in the extrapolations. The two best

extrapolations per each source are forwarded to the Track Assembler.

The Track Assembler attempts to find at most two tracks in a detector sector with the highest rank, i.e. exhibiting the highest number of matching track segments and the highest extrapolation quality. This task is performed in three steps. First the track segment pairs formed by the Extrapolation Unit are joined to full tracks, which are then forwarded to a Track Selector unit. The Track Selector contains a cancellation logic that reduces the number of duplicated tracks. Finally it selects the two highest rank tracks. As a last step, the Address Assignment sub-unit extracts the corresponding track segment data from the data pipeline, and forwards them to the Assignment Unit.

Once the track segment data are available to the Assignment Unit, memory based look up tables are used to determine the transverse momentum, the $\varphi$ and $\eta$ coordinates, and a track quality. At least two segments from different stations are required to find a muon. The transverse momentum is assigned using the difference in the spatial $\varphi$ coordinate of the two innermost track segments. The $\varphi$ coordinate is defined as the spatial coordinate of the track segment in the second muon station. Quality is assigned looking first at the number of segments used in the track and then at the stations where they were found. Better qualities are assigned to tracks including segments found in MB1 and then MB2.

A preliminary coarse $\eta$ assignment is derived from the place the track crossed detector wheel boundaries. A dedicated board has been designed for a finer $\eta$ measurement; this measurement is derived by using the data from central SLs of the three innermost muon stations, which give a measurement of the $z$ coordinate of the track segments. The $\eta$ Track Finder board tries to match tracks along the $\eta$ coordinate. At the Assignment step, the $\eta$ Track Finder board attempts to match the found candidates with the $\varphi$ Track Finder candidates. If the matching is successful, the fine $\eta$ measurement is assigned to the Track Finder candidate, otherwise the coarse measurement is assigned.

Each Sector Processor forwards the two best ranking candidates to the Wedge Sorter, which selects the two track candidates with the highest $p_t$ . Each of the twelve Wedge Sorters sends the muon candidates to the Muon Sorter, which reduces the number of split tracks performing a check over the neighbouring wedges candidates. The four highest momentum tracks are selected and then forwarded to the Global Muon Trigger for the final decision.

**CSC Trigger**

At large rapidities, high backgrounds are expected from punch-through pions, primary muons, secondary muons, and neutron induced gamma rays. The high-rapidity muons also have higher momentum corresponding to a particular $p_t$ and hence radiate more. The

CSC Local Trigger provides high rejection power against these backgrounds by finding muon segments, also referred to as Local Charged Tracks (LCTs), in the 6-layer endcap muon CSC chambers. Muon segments are first found separately by anode and cathode electronics (see Fig. 2.5) and then time correlated, providing precision measurement of the bend coordinate position and angle, approximate measurement of the non-bend angle coordinate, and identification of the correct muon bunch crossing with high probability.

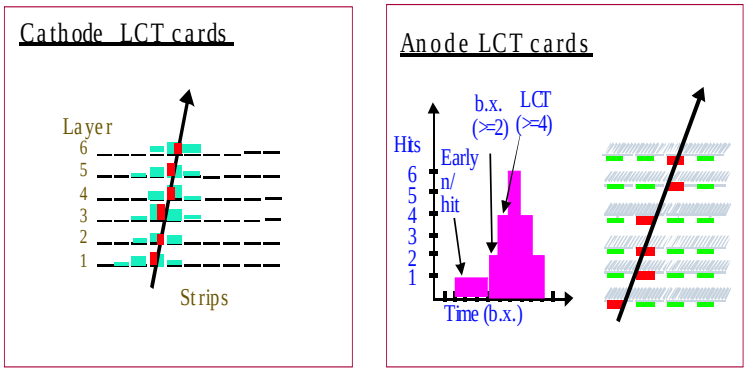


Figure 2.5: Principle of the CSC Local Trigger.

The primary purpose of the CSC anode trigger electronics is to determine the exact muon bunch crossing with high efficiency. Within the CSC chambers, anode wires are hard-wired together or 'ganged' at the readout end in groups of 10-15 wires in order to reduce channel count. Anode signals are fed into amplifier/constant-fraction discriminators. Since the drift time can be longer than 50 ns, a multi-layer coincidence technique in the anode LCT pattern circuitry is used to identify a muon pattern and find the bunch crossing. For each spatial pattern of anode hits, a low coincidence level, typically 2 layers, is used to establish timing, whereas a high coincidence level, typically 4 layers, is used to establish the existence of a muon track.

The primary purpose of the CSC cathode trigger electronics is to measure the $\varphi$ coordinate precisely to allow a good muon momentum measurement up to high momentum. The charge collected on an anode wire produces an opposite sign signal on several strips, and precision track measurement is obtained by charge digitization and precise interpolation of the cathode strip charges, as it has already been pointed out in the previous chapter. However for the L1 trigger purposes, a simpler and more robust method is used. Localisation of the muon track is achieved to one-half of a strip width in each cathode layer. This is done with a 16-channel "comparator" ASIC that inputs amplified and shaped signals and

compares the charges on all adjacent and next-to-adjacent strips. If a strip charge is found to be larger than those on its neighbours, a hit is assigned to the strip. Simultaneous comparison of left versus right neighbour strip charges allows assignment of the hit to the right or left side of the central strip, effectively doubling the resolution. The six layers are then brought into coincidence in LCT pattern circuitry to establish position of the muon to an RMS accuracy of 0.15 strip widths. Strip widths range from 6-16 mm.

Cathode and anode segments are brought into coincidence and sent to CSC Track Finder electronics which links the segments from the endcap muon stations. Each Track Finder unit finds muon tracks in a $60^o$ sector. Because of the limited bending in the endcap region, information is not shared across sector boundaries. Each CSC Track Finder can find up to three muon candidates. Two segments from different chambers is the minimum required to find a muon candidate. A CSC muon sorter module selects the four best CSC muon candidates and sends them to the Global Muon Trigger. Quality is assigned according to the number of segments used in the track: three or more segments correspond to quality 3, two segments, one of them coming from ME1, gives quality 2, any two other segments result into quality 1.

**RPC Trigger**

The RPC trigger will be examined in detail in chapter 4. The detailed description of its algorithm is given in section 4.2. It suffices here to say that the trigger is based on 3 out of 4 (3/4) coincidences of signals coming from the strips of the detectors in the 4 muon stations. The $p_t$ is assigned according to the matched pattern of strips. Highest quality (3) is given to 4/4 coincidences, quality 2 to 3/4 coincidences with absence of the third or fourth plane and quality 1 (0) when the missing plane is the first (second). The RPC trigger finds up to 4 muons in the barrel and 4 in the endcaps in every bunch crossing.

**Global Muon Trigger**

The GMT receives the best four barrel DT and the best four endcap CSC muons and combines them with 4+4 muons sent by the RPC trigger. It performs a matching based on the proximity of the candidates in ($\eta$ ,$\varphi$) space. If two muons are matched their parameters are combined to give optimum precision. If a muon candidate cannot be confirmed by the complementary system quality criteria can be applied to decide whether to consider it. Special attention is given to ghost suppression, i.e. to the correct identification of the same muon seen twice.
The muon candidates are ranked based on their transverse momentum, quality and to some

extent pseudo-rapidity and the best four muon candidates in the entire CMS detector are sent to the Global Trigger.

The Global Muon Trigger also receives information from the calorimeters. The Regional Calorimeter Trigger sends two bits based on energy measurements representing isolation and compatibility with a minimum ionising particle in $\Delta\eta \times \Delta\varphi = 0.35 \times 0.35$ trigger regions. The GMT extrapolates the muon tracks back to the calorimeter trigger towers and appends the corresponding isolation and minimum ionising particle bits to the track data consisting of $p_t$, sign of the charge, $\eta$, $\varphi$ and quality. In this thesis no result concerning isolation will be presented.

### 2.2.4 Global trigger

The final decision of keeping on considering an event after the L1 is ultimately accomplished by the L1 Global Trigger.
As it has been explained above, the GT receives the best four of each of the following objects: muons, isolated electrons or photons, non-isolated electrons or photons, central jets, forward jets and isolated hadrons or $\tau$-jets. The trigger objects are ordered by rank, which is a function of transverse energy or momentum and quality. In addition, the GT receives the magnitude and the direction of the missing transverse energy as well as the total transverse energy and eight numbers of jets passing different $E_t$ thresholds.
A basic principle of the CMS L1 Trigger is that details of the highest rank trigger objects are always sent to the Global Trigger. It is the job of the Global Trigger to apply thresholds and other selection criteria based on this detailed information. These criteria may be adapted as needed. All results presented in this thesis will refer either to the single muon trigger or to the di-muon trigger therefore the cuts can be imagined to be applied directly by the GMT.
Another special and important feature of the L1 Global Trigger is that it not only receives particle energies or momenta but also location information, namely pseudo-rapidity and azimuth. Trigger conditions based on event topology can therefore be applied already at L1. Furthermore, the space coordinates can be used in the High Level Trigger to select regions of interest.

## 2.3 L1 Muon Trigger performance

The results presented in this chapter have been obtained assuming for the RPC detectors uniform efficiency of 95%, Gaussian time resolution of 2.7 ns and average cluster size of

about 2 strips (corresponding to the parameter $cs = 1.5$, see section 3.2 in chapter 4) but **neither intrinsic noise nor spurious hits due to the neutral particle background have been added**. For a detailed explanation of the simulation of the response of RPCs the reader is referred to section 3 in chapter 4.
**The complete simulation of the RPC trigger stand-alone with inclusion of intrinsic noise and neutral particle background is examined in chapter 4**. There, it will be shown that, in fact, intrinsic noise and neutral particle background drastically affect the behaviour of the system that then needs to be modified to restore the original performance that is assumed to be valid for the results presented here. The proposed modifications to the system are discussed in chapter 5.

### 2.3.1 The event samples

Two main event samples have been used to obtain the results presented in this section. Muon Trigger efficiency and ghost occurrence have been studied by means of a sample of single muons (SAMPLE 0) produced by a simple built-in generator in the CMSIM 121 program [33] based on GEANT3 [34]. $10^5$ muons of both signs have been generated. The muons are flat distributed in $p_t$, $\eta$ and $\varphi$ in the region $2.5 < p_t < 100$ GeV/$c$, $-2.4 \leq \eta \leq 2.4$ and $0 \leq \varphi < 2\pi$.
The trigger rate is instead calculated by means of a set of Monte Carlo events (SAMPLE 1) produced with PYTHIA 6.152 [24]. The events are split into several data sets corresponding to the different physics processes. Three data sets are dedicated to MB production. They contain altogether $2.2 \cdot 10^5$ MB weighted events with presence of at least a muon passing either of the following cuts:

- $p_t > 3.0$ GeV/$c$ in $0 < |\eta| < 1.2$ or
- $p_t > 1.8$ GeV/$c$ in $1.2 < |\eta| < 1.7$ or
- $p > 3.5$ GeV/$c$ in $1.7 < |\eta| < 2.6$

The other data sets are signal samples of non weighted events: inclusive $W$ production, inclusive $Z$ production and $t\bar{t}$ events. In all three cases the presence of a muon with $p_t > 3$ GeV/$c$ in $|\eta| < 2.6$ is required. More details on this Monte Carlo production can be found in [36].
The differential cross sections as a function of the muon $p_t$ for the different sources of muons are shown in Fig. 2.6. The corresponding integrated rates as a function of the cut on $p_t$ have been shown in Fig. 1.13.

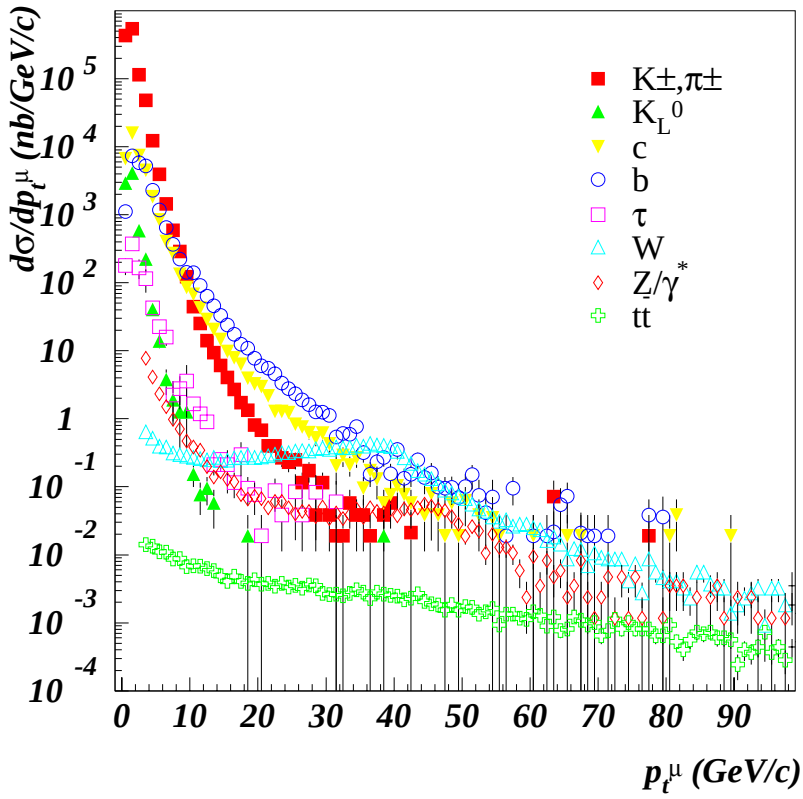


Figure 2.6: Differential cross section as a function of the muon $p_t$ for the different sources of muons in $p-p$ collisions at the center of mass energy of 14 TeV.

Tracking of the particles through the CMS detector has been simulated with CMSIM (GEANT3). Simulation of the response of the detectors and of the trigger algorithms have been accomplished with the ORCA 5 program [35]. More details on these simulation tools are given in section 4.3.

### 2.3.2 Results

From the discussion of section 2.1 it turns out that the primary requirement for optimising the GMT is to keep the single muon output rate within 10 kHz with a $p_t^{cut}$ of 25 GeV/$c$ at $L = 10^{34}$ cm$^{-2}$s$^{-1}$. At the same time efficiency must be kept as high as possible. Ghost

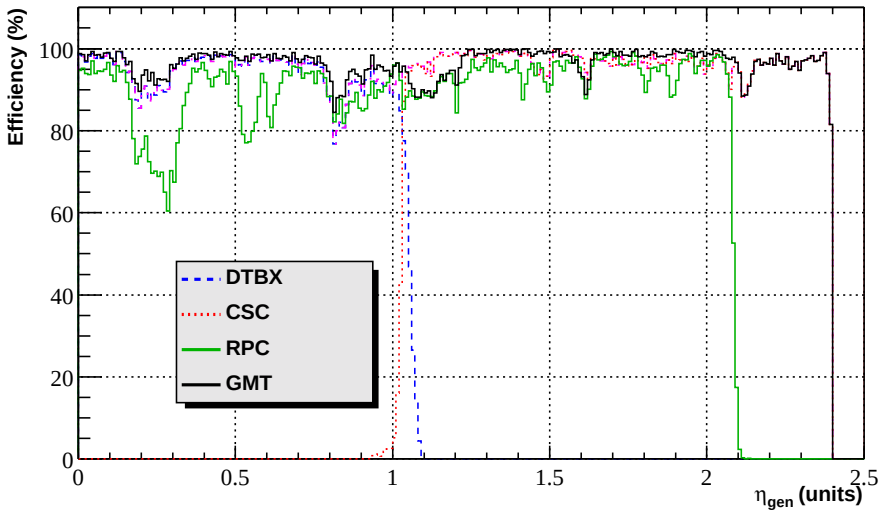


Figure 2.7: Efficiency as a function of $\eta$ for the GMT, DT, CSC and RPC triggers.

occurrence, i.e. the appearance of two reconstructed muons when only one real muon is present, is another fundamental issue. As a limit one can require that the di-muon trigger rate due to one real muon and a ghost should be less than 10% of the total di-muon trigger rate.

In the results presented in this section a muon is accepted by the GMT regardless of its quality if it is found by both systems, the final $p_t$ is the minimum of the two estimations. This choice permits, as it will be shown, to keep the output rate very low and at the same time to keep efficiency high. Overestimation of the $p_t$ by any system is in fact very likely to occur as the individual triggers are tuned in order to give 90% efficiency at any threshold. If a muon is found by only one of the two systems then it will be confirmed according to its quality. Best compromise between rate increase and efficiency gain is the criterium adopted to accept unmatched muons of a given quality. For unmatched muons the GMT $p_t$ estimation is obviously the one assigned by the system that found it. In what follows any result concerning the performance of the individual triggers (DT/CSC or RPC) has been obtained without applying any requirement on the quality of the reconstructed muons.

The reconstruction efficiency as a function of $\eta$ for the GMT, DT, CSC and RPC triggers obtained on SAMPLE 0 is shown in Fig. 2.7. The GMT efficiency is almost everywhere higher than 90%. Non perfect geometrical coverage (see Fig. 1.21) causes the presence of

delicate regions: in the barrel in correspondence of the cracks between the muon stations and in the so called overlap region of barrel and endcap ($0.8 < |\eta| < 1.2$). In the overlap quite strict requirements on the matching of muons found by the DT/CSC and RPC trigger are applied also because of frequent ghost occurrence from the DT/CSC triggers, as it will be shown in the following. The efficiency turn-on curves for all systems divided into barrel and endcap regions are shown in Fig. 2.8. On the x-axis is plotted the muon $p_t$ at generation and on the y-axis the probability of reconstructing muons of that $p_t$ and assigning to them a $p_t$ greater than the $p_t^{cut}$ to which the curve refers. The DT/CSC and RPC triggers have been tuned in order to provide approximately 90% efficiency at the nominal thresholds. From the output rate point of view it is important to make these curves as steep as possible. This feature is essentially determined by the $p_t$ resolution. Since the muon $p_t$ is measured from the track curvature, which is proportional to $1/p_t$ , it is more correct to plot the variable $(1/p_t^{rec} - 1/p_t^{gen})/1/p_t^{gen}$. This distribution is shown in Fig. 2.9 for the various systems. It is evident the bias introduced by the requirement of 90% efficiency at threshold. The strange shape of the RPC distribution derives from this requirement and from the pattern selection procedure.

The single muon trigger rate as a function of $p_t^{cut}$ is shown in Fig. 2.10 together with the generation rate (SAMPLE 1) and the trigger rates of the individual systems. It is evident the superior performance of the GMT over the individual systems. In particular one can see that to meet the requirement of 10 kHz with just the DT/CSC or the RPC trigger one should apply a threshold much higher than 25 GeV/$c$. An alternative solution is to discard muons of certain qualities but in this case the loss in efficiency would be very high as can be seen in Fig. 2.11 where the efficiency of the various systems is split among the contributions from the various qualities. In the case of the GMT the largest contributions to the rate come from unmatched muons therefore, since their contribution to the efficiency is quite limited, big rate reductions can be achieved without significant efficiency losses.

The trigger rate split between the barrel and endcap region is shown in Fig. 2.12. It is evident that the largest contribution to the rate comes from the endcap due to the much higher rate of low $p_t$ muons, which in this region have higher penetration power. In the barrel the superior space resolution of DTs makes the role of RPCs less important above all at high values of $p_t^{cut}$. In this region efficiency maximisation plays a more important role than rate control.

The probability of ghost creation accompanying the detection of a single real muon is shown in Fig. 2.13 for the various trigger systems. Two critical regions for the individual systems stand out. The RPC trigger suffers from large ghost occurrence in its very forward part. This is caused by the necessity to connect the same strip to different trigger processors

and by the low effectiveness of the RPC ghostbusting algorithm [37]. The DT/CSC trigger produces ghosts with high probability in the overlap region. Indeed the DT and the CSC Track Finders are obliged to share segments where they overlap. This and the fact that only 2 segments are enough to reconstruct a muon makes this region very problematic.
Smart use of the information from the two systems at the GMT level allows almost complete elimination of these ghosts. The GMT ghost probability is in fact well below 1% all over the $\eta$ range.

As anticipated above, ghost occurrence is of fundamental importance for the di-muon trigger. The di-muon trigger rate as a function of $p_t^{cut}$ on the higher $p_t$ reconstructed muon and for the various systems is shown in Fig. 2.14. The $p_t^{cut}$ on the other muon is fixed at 4 GeV/$c$. The GMT rate is split among its various contributions, including single real muons accompanied by a ghost. Unlike previous plots the rates are computed for $L = 2 \times 10^{33}$ cm$^{-2}$s$^{-1}$ therefore to compare the results with the single muon rate one has to multiply the rate by a factor 5. In the curves showing the rate for the DT/CSC and RPC trigger the contribution of single muons accompanied by a ghost is not included. The requirement that the contribution to the GMT di-muon rate from single muons accompanied by a ghost should be lower than 10% of the total di-muon rate is fulfilled.
It is important to observe that a common threshold as low as 4 GeV/$c$ on the muons would result in a di-muon trigger output rate of about 3.5 kHz at $L = 10^{34}$ cm$^{-2}$s$^{-1}$. This is still acceptable provided the single muon trigger is capable to adapt its output rate in order to meet the final limit of 12.5 kHz allocated for the comprehensive Muon Trigger.

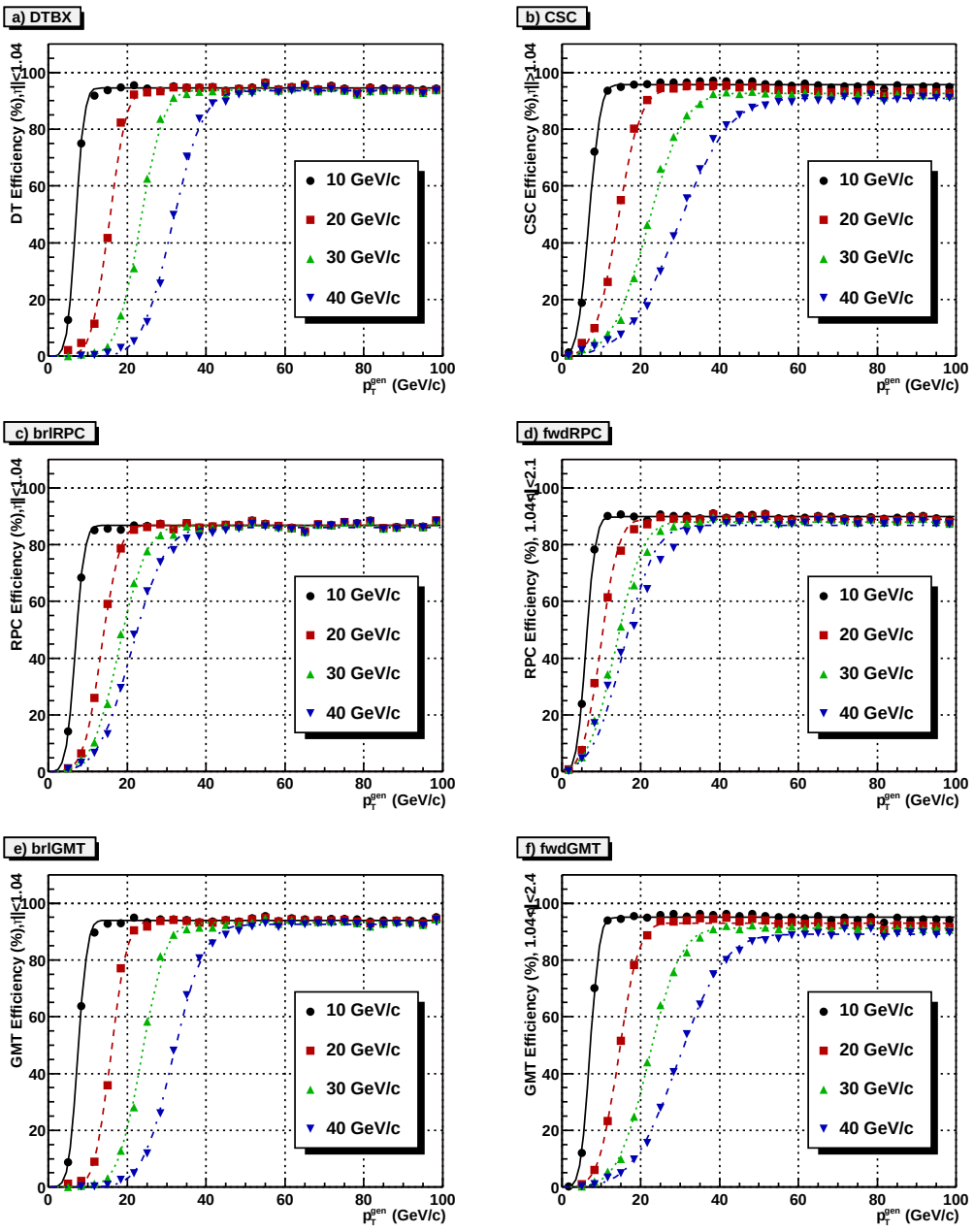


Figure 2.8: Efficiency turn-on curves for all systems divided into barrel (left) and endcap (right). On the x-axis is plotted the muon $p_t$ at generation and on the y-axis the probability of reconstructing it and assigning to it a $p_t$ greater than the $p_t^{cut}$ to which the curve refers.

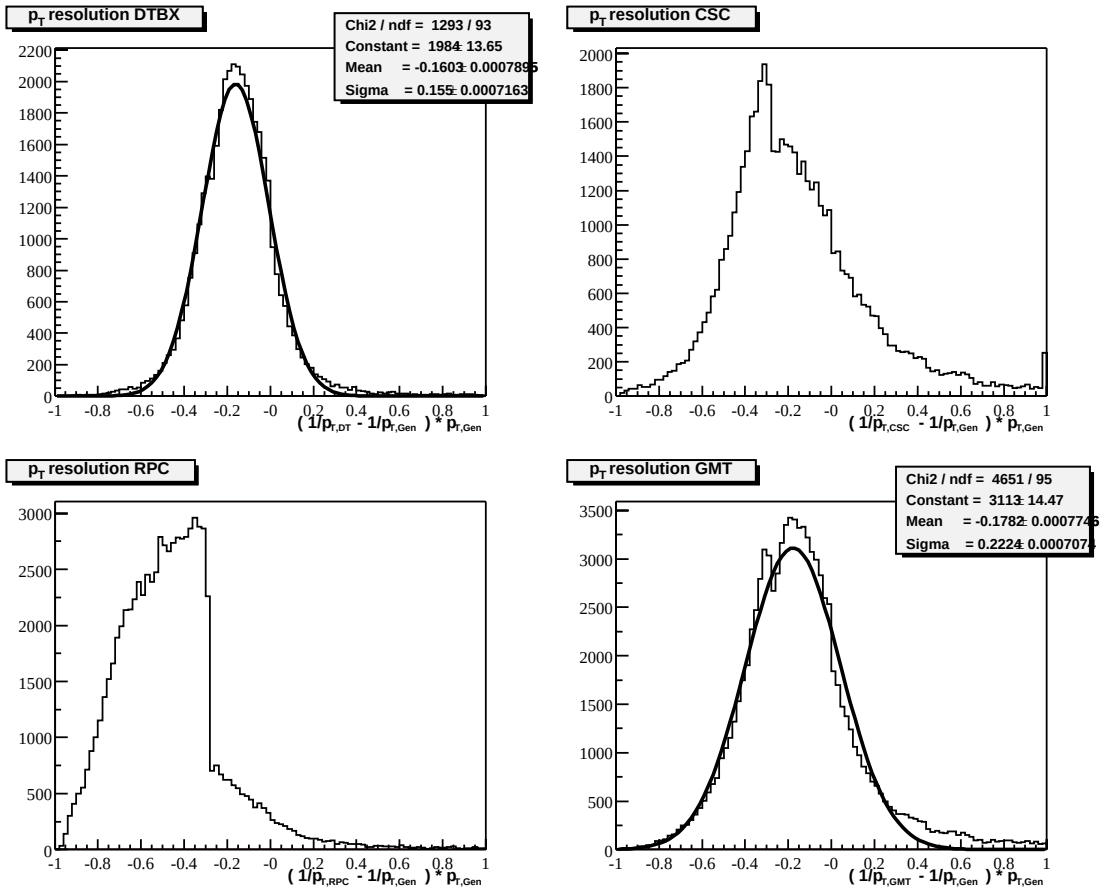


Figure 2.9: $1/p_t$ resolutions for all systems.

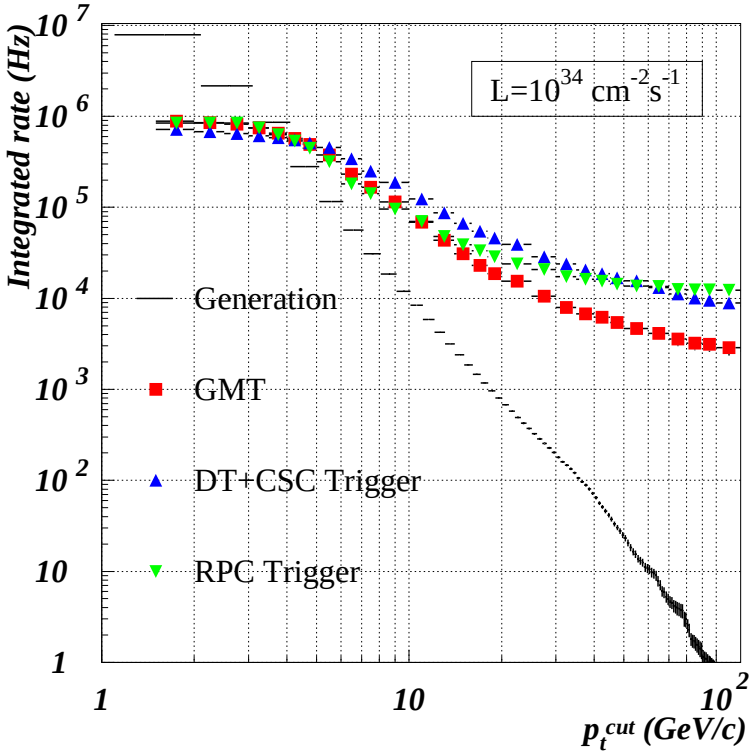


Figure 2.10: L1 single muon trigger rate as a function of $p_t^{cut}$. The rate at generation level and the rate of the individual triggers are also shown.

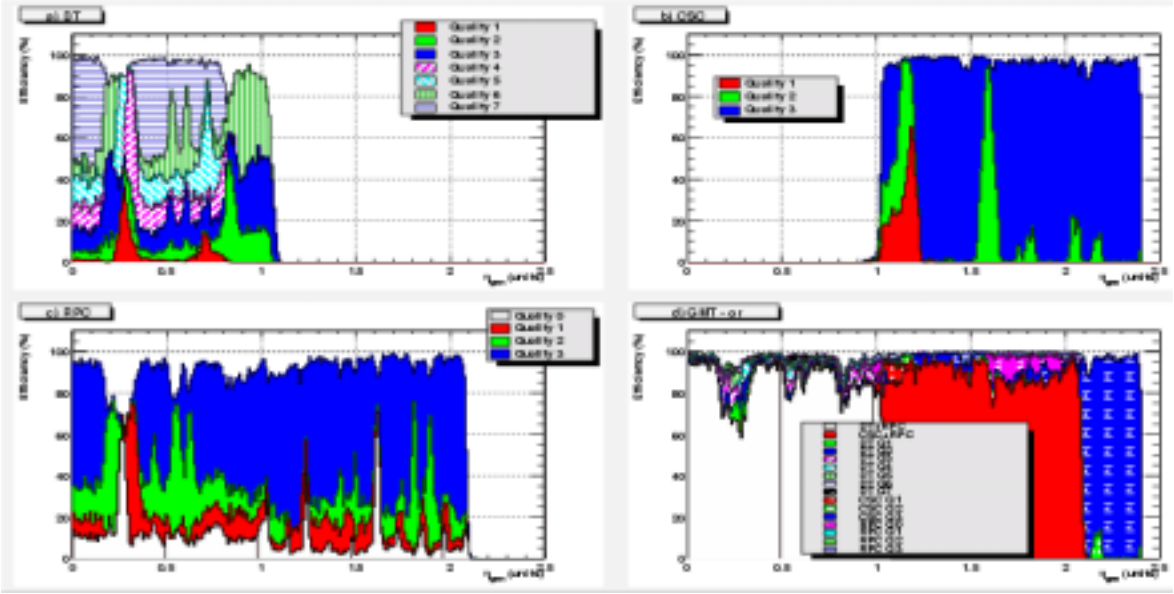

Figure 2.11: Efficiency for the various systems split between the various reconstructed muon qualities.

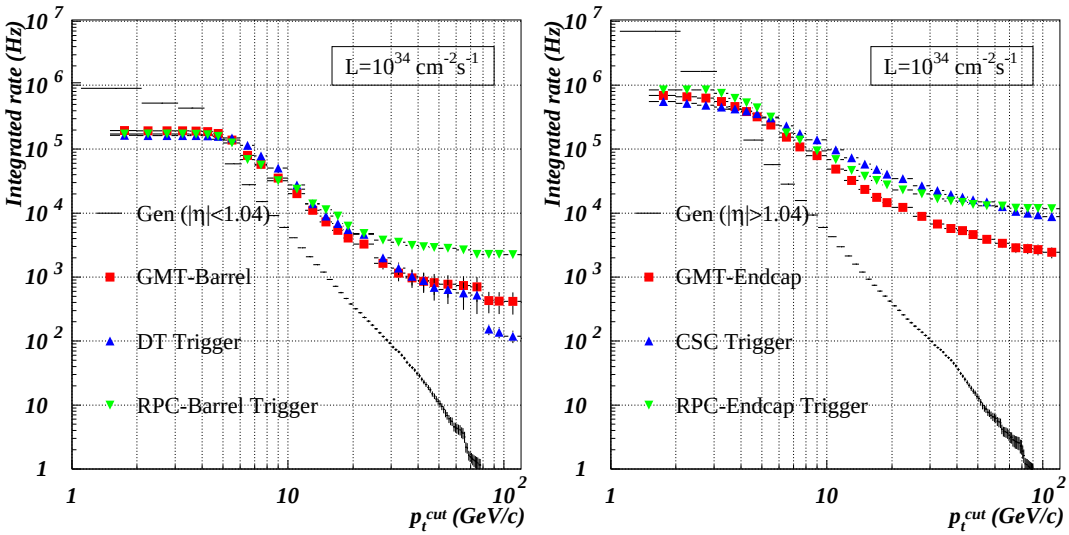


Figure 2.12: L1 single muon trigger rate as a function of $p_t^{cut}$ in the barrel ($|\eta| < 1.04$, plot on the left) and in the endcap ($1.04 < |\eta| < 2.4$, plot on the right). The rate at generation level and the rate of the individual triggers are also shown.

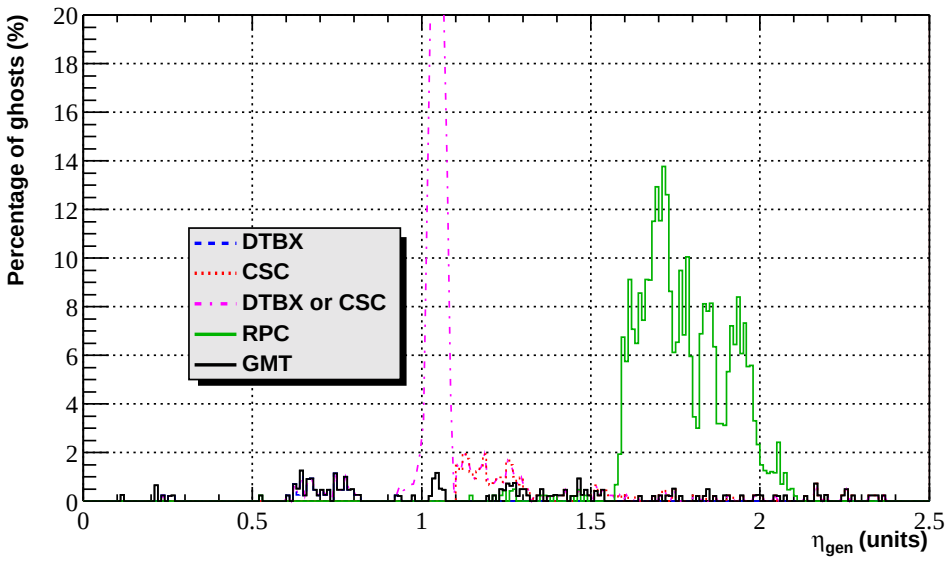


Figure 2.13: Probability for the various trigger systems to reconstruct two muons when only one single real muon is present in the event. The $\eta$ at generation of the real muon is shown on the x-axis.

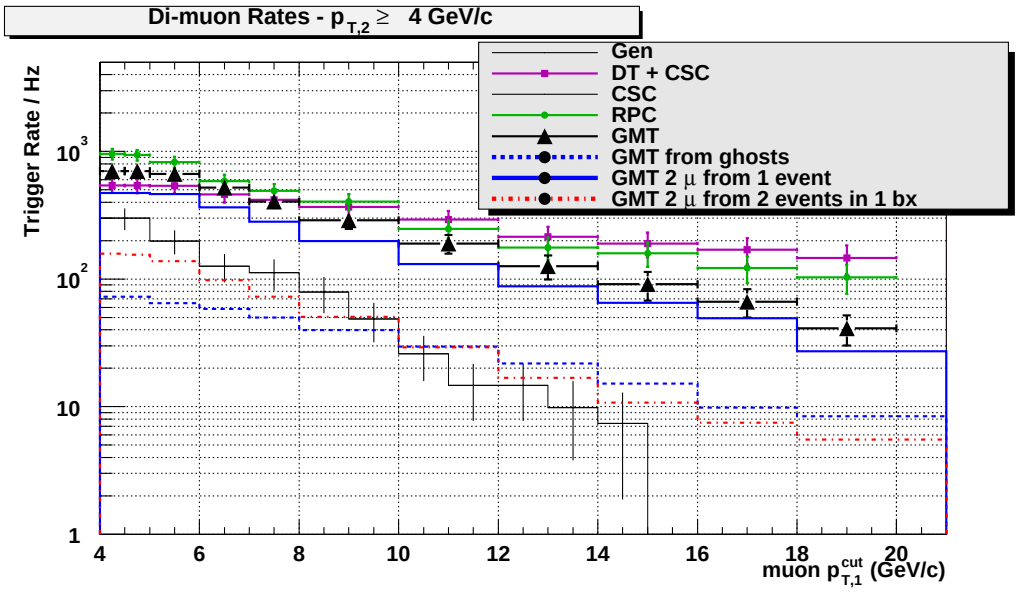


Figure 2.14: Di-muon L1 rates as a function of the $p_t^{cut}$ on the higher $p_t$ reconstructed muon. The $p_t^{cut}$ on the other muon is fixed at 4 GeV/$c$. The output of the various trigger systems are shown. The rate at generation level and the various contributions to the GMT rate are also shown. In the curves showing the rate for the DT/CSC and RPC trigger the contribution of single muons accompanied by a ghost is not included. All rates are computed for $L = 2 \times 10^{33}$ cm$^{-2}$s$^{-1}$.

# Chapter 3

# The RPC detectors for the CMS experiment

## 3.1 The Resistive Plate Chamber

Resistive Plate Chambers are gaseous detectors of ionising particles. They are characterised by a large area coverage (of order of the $m^2$), time resolution better than 2 ns and space resolution of the order of the cm. They have already been used in several experiments: NADIR, FENICE, E771, WA92, E831, MINI [38], L3 [39] and BABAR [40].
RPCs have been approved as dedicated detectors for the muon trigger systems at the LHC experiments: ATLAS [41] and CMS. In these experiments RPCs will be operated in avalanche mode, while in the previous ones they have been operated in streamer mode. The difference between these two operating regimes will be made clear below.

### 3.1.1 Gaseous Detectors

The physical process upon which any gas detector is based is ionization: the passage of a charged particle through a gas volume gives rise to the production of electron-ion pairs. If an intense enough electric field is applied throughout the gas volume then the primary electrons will be capable to produce further ionizations. This is the multiplication mechanism which results in a distribution of free charge in the gas which has the characteristic shape of an avalanche due to the much higher drift velocity of electrons with respect to ions. Recombination processes usually take place during the avalanche development. Photons are produced in such recombinations and they can in turn start the development of secondary avalanches. These are mainly produced along the axis of the primary avalanche. The regime

in which several secondary avalanches are produced causing large amounts of free charge in the gas is called *streamer* regime [42]. Moreover, if the ion-electron plasma is so large as to connect the two electrodes one can have the so called *spark*.

A large fraction of gaseous detectors presently in use has wire-like anode electrodes. This geometry leads to a strong dependence of the electric field magnitude on the distance $r$ from the wire: $E \propto 1/r$. The electron multiplication takes place in the proximity of the wire and the path over which it occurs is usually limited to dimensions of the order of the wire diameter. The electric field near the cathodes is instead quite low. This geometry allows to achieve extremely good space resolution ($\sim 100\mu$m) as in the case of multi-wire proportional chambers or drift chambers. On the other hand the time resolution of wire detectors is generally rather poor due to fluctuations in the drift time of the primary electrons. No signal can indeed be detected until primary electrons have reached the wire. This is because no multiplication occurs before that time.
Much better time resolutions can be obtained with detectors in which the electric field is uniform and intense enough. In such conditions multiplication can start right after primary ionization. Time fluctuations are thus minimised. This possibility was investigated for the first time in the late '40s when the Parallel Plate Counter (PPC) [43] was first constructed. PPCs had metal electrodes and needed a switching-off circuit that prevented the electrodes from being short-circuited by the spark produced in the gas. The PPC had therefore a quite long dead time ($\sim 1$ s), which posed limits on the maximum detection rate it could sustain. In addition it worked with low-pressure gas and had a very short lifetime.

Later in the '70s resistive electrodes made their first appearances. The discharge in the detector causes a voltage drop between the two electrodes. As it will be shown further on, electrodes gets recharged with a time constant that is much longer than the typical time scale of the avalanche development. It then turns out that the multiplication process is self-extinguishing when resistive electrodes are used. Moreover, if organic gases with high UV absorption capability are used then charge diffusion in the gas will be prevented and the actual area of the detector which suffers from the voltage drop is localised around the primary ionization region.
The main advantage of the use of resistive electrodes is that High Voltage (HV) switching-off circuits are no longer necessary and consequently higher detection rate can be achieved. The first detector mounting resistive electrodes was the Planar Spark Chamber (PSC), which was built by Pestov [44]. The gas gap is only 0.5 mm thick and the gas is fluxed at high pressure (10 atm). The signal is extracted by means of copper strips glued on the

anode. High mechanical precision is required and extremely good time resolution ($\sim$ 100 ps) can be obtained.
A few years later the Resistive Plate Chamber was invented [45]. With respect to a PSC, an RPC includes numerous simplifications: no high pressure gas was needed, plastic resistive materials, like bakelite, replaced glass and less stringent constraints on the mechanical precision were required. The low cost of RPCs makes them the natural substitute for scintillators in all those experiments in which large detection areas are needed. The detection rate capability strongly depends on their mode of operation. This issue will be examined in detail in the following.

### 3.1.2 The RPC working principle

The RPC detector in its simplest configuration is shown in Fig. 3.1. Two planar electrodes

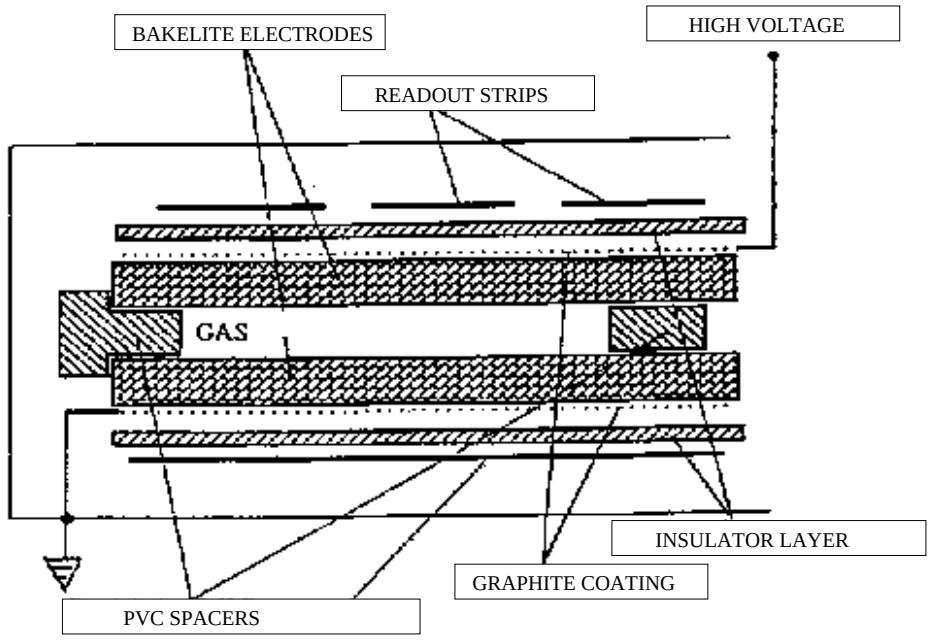


Figure 3.1: Schematic view of a single gap RPC.

made out of a resistive material (typically bakelite) having bulk resistivity of $10^{10}-10^{12}$ $\Omega$cm are spaced by a few mm. The electrodes are connected to a HV generator in order to create a uniform and intense electric field (about 5 kV/mm) in the gap between them. A thin layer

of graphite is coated over the external surface of the electrodes to permit uniform application of the high voltage. The electrodes are kept apart by means of small PVC cylindrical spacers having a diameter of $\sim 10$ mm and a bulk resistivity greater than $10^{13}$ $\Omega$cm. A generic gas mixture could be composed of argon, isobutane and an electronegative gas like freon. Argon acts as target for ionising particles while the isobutane, being an organic gas, helps absorb the photons that result from recombination processes thus limiting formation of secondary avalanches far from the primary ones. An electronegative gas may serve the purpose of limiting the amount of free charge in the gas. This type of gas is particularly important when one wants to avoid the onset of streamers.
The surface resistivity of the graphite coating is high enough to render it "transparent" to the electric pulses generated by the charge displacement in the gas gap. For this reason electric signals can be induced on metallic strips capacitively coupled to the gap. The strips are generally glued on the external surface of the gap from which they are separated by a layer of insulator. Two different sets of strips oriented in orthogonal directions can be glued on both sides of the detector to obtain measurements in both directions. The strips behave like transmission lines of impedance 50 $\Omega$.
Microscopic imperfections are unavoidably present on the bakelite surfaces in contact with the gas. Their main effect is the generation of accidental discharges due to extraction of electrons from the bakelite. Traditionally the internal surfaces are treated with linseed oil diluted in pentane [46]. This compound is laid on the bakelite plates to make them smoother. The oil also helps absorb photons that could extract electrons from the bakelite.

As anticipated in the previous section, the formation of the electric signal is based on the process of electron multiplication. Following the passage of an ionising particle, a certain number of primary electrons are created; they are grouped in clusters each of which is created by a single ionization. The $n_0$ electrons of a given cluster are accelerated by the electric field and start the multiplication in the gas. This process is characterised by the parameter $\alpha$ (first Townsend coefficient), which represents the number of ionizations per unit length, and by $\beta$ which is the attachment coefficient, i.e. the number of electrons that are captured by the gas per unit length. The parameter $\beta$ becomes particularly important in the presence of electronegative gases. If $x$ is the distance between the anode and the point where the cluster is produced then the number of electrons that reach the anode will be given by $n = n_0 e^{\eta x}$ where $\eta = \alpha - \beta$. The gain factor of the detector is defined as $M = n/n_0$.
Two main operating regimes exist: the proportional mode and the streamer mode. They can be distinguished by the value of $M$. If $M$ is greater than $10^8$ then primary ionizations will give rise to streamers with high probability. On the contrary values of $M$ much lower

than $10^8$ are low enough to prevent formation of additional secondary avalanches and the simple charge multiplication phenomenon occurs. In this case smaller amounts of charge are created and the detector is said to operate in proportional mode.
In both operating regimes the high resistivity of the bakelite prevents the HV generator from providing the electric charge that would be necessary to maintain the discharge between the electrodes. Therefore the electric field drops drastically in the region of the discharge causing it to extinguish. This behaviour can be understood by observing that the typical discharge time is 10 ns while the time constant ($\tau$) with which the electrodes are recharged is independent of the detector surface dimensions and is of the order of $\rho\epsilon$ [47], where $\rho$ and $\epsilon$ are the resistivity and dielectric constant of the bakelite. Assuming $\rho = 5 \times 10^{10}\ \Omega cm$ and $\epsilon = 5\epsilon_0$ then $\tau \approx 10$ ms. The large difference between $\tau$ and the typical discharge time in the detector ensures that the electrodes behave like insulators during the discharge hence only a limited area of their surface suffers from a HV drop. This area stays inactive for a time interval of order $\tau$. This represents the detector dead time in the region of the primary ionization.
As suggested by Y. N. Pestov, a planar detector with resistive electrodes can be modelled as a set of discharge cells which at first order can be considered independent of each other. The simple expression of the capacitance of a planar condensator leads to the result that the area of such cells is proportional to the total average charge $Q$ that is produced in the gas gap:

$$S = \frac{Qd}{\epsilon_0 V} \tag{3.1}$$

where $d$ is the gap thickness and $V$ is the voltage applied to the electrodes. Expression 3.1 explains the important role played by the parameter $Q$ in the maximum detection rate that an RPC is capable to sustain efficiently: the smaller the value of $Q$ the smaller the surface of the discharge cells and therefore the higher the rate capability.
So far RPCs have been always operated in streamer mode in which $Q \sim 100$ pC. Their measured rate capability has been limited to a few tens of Hz/cm$^2$ [48]. The expected hit rates in the muon stations of the CMS experiment are shown in Fig. 1.22. In most of the apparatus they are below 10 Hz/cm$^2$ but values of some hundreds Hz/cm$^2$ are expected in the high pseudo-rapidity region of the endcap. Efficient operation of such detectors at the LHC experiments can be achieved in proportional mode where a typical value for $Q$ is 1 pC. Operation in proportional mode requires however sophisticated front-end electronics. Indeed the basic idea is to transfer a large fraction of the gain factor characterising the streamer regime ($10^9$) from the gas gap to the front-end electronics. The latter must provide

large amplification factors and at the same time a large bandwidth in order not to spoil the detector time resolution.

### 3.1.3 Choice of the RPC structural parameters

This section is dedicated to the discussion of the structural parameters of an RPC. Vast use of a fully simulated model [49] for the signal formation in an RPC will be made. The simulation has been developed within the CMS-RPC Italian group and is particularly suitable to understand the role played by parameters of the RPC like the gap width and the gas mixture. For the sake of brevity only the salient features of the model will be described here. The model includes the number ($n_{cl}$) of primary clusters, their initial position ($x_{0j}$) in the gap width and the number of primary electrons within each clusters ($n_{0j}$).
The distribution of the variable $n_{0j}$ has been obtained experimentally for a few gases: $CH_4$, Ar, He and $CO_2$ [50]. In some other cases one can make use of theoretical predictions [51]. The variables $n_{cl}$ and $x_{0j}$ follow the Poisson statistics and their distribution depends on the cluster density $\lambda$, which is defined as the average number of primary ionizations caused by a MIP per unit length in the gas under consideration.
The process of electron multiplication is subject to fluctuations too. The avalanche development and its fluctuations can be described to a good level of accuracy by means of the Polya distribution [52]. The amount of free charge due to electrons at a given distance $x$ from the cathode can then be expressed as

$$q_e(x) = \sum_{j=1}^{n_{cl}} q_{ele} n_{0j} F_j \exp \eta(x - x_{0j}) \tag{3.2}$$

where the coefficient $F_j$ is extracted from the Polya distribution.
An interesting aspect of RPCs is that, unlike wire detectors, the useful signal is due to the fast charge, i.e. the electrons, and not to the ions. The expression for the current induced on the strips by the fast charge is obtained by making use of the generalised Ramo theorem [53] applied to a detailed equivalent circuit of an RPC [49]. The expression reads

$$i_{ind}(t) = -v_d \frac{k}{d} q_{ele} \sum_{j=1}^{n_{cl}} n_{0j} F_j \exp \eta(x(t) - x_{0j}) \tag{3.3}$$

where $v_d$ is the electron drift velocity, $d$ is the gap width, $k = \dfrac{\epsilon_r d/s}{2 + \epsilon_r d/s}$ and $s$ is the width of the bakelite plates. The charge induced on the strip is obtained by integrating eq. 3.3. From eq. 3.2 and 3.3 it is easy to see that for an RPC having $s = d = 2$ mm, $\epsilon_r = 5$ and $\eta d = 18$ the induced fast charge is only 5% of the total charge collected by the anode.

From the equations derived above it is possible to define the following fundamental characteristics of RPCs:

1. **Efficiency**: for charge sensitive amplifiers it is defined as
   $\epsilon(q_{thr}) = 1 - \int_0^{q_{thr}} P_q(q_{ind}) dq_{ind}$
   where $P_q$ is the probability that an event gives rise to an induced charge $q_{ind}$ and $q_{thr}$ is the amplifier threshold.

2. **Time resolution**: it is then defined as the sigma of a Gaussian fit to the signal time distribution. The time of a given electric signal is defined as the one at which its charge becomes greater than the threshold of the discriminator.

3. **Streamer probability**: it is defined as the probability that the ratio of the total final electron charge in the gas and the charge of the primary electrons is greater than $5 \times 10^8$.

### Gap width

The simulated charge distributions for two different values of the gap width, $d = 2$ mm and $d = 9$ mm, are shown in Fig. 3.2. The cluster density has been fixed to the value

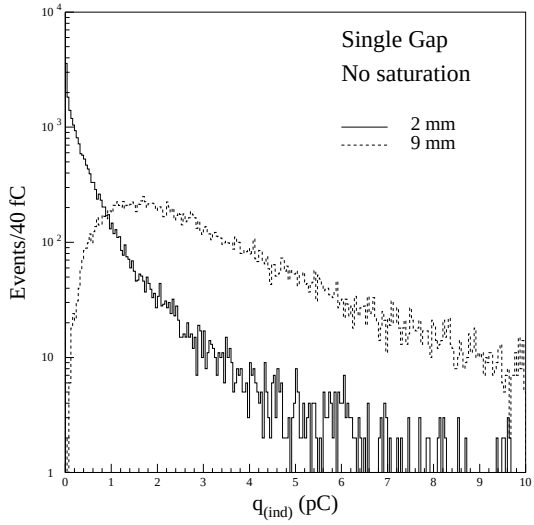


Figure 3.2: Simulated charge distributions for two different values of the gap width, $d = 2$ mm and $d = 9$ mm. In both cases $\lambda = 5.5$ mm$^{-1}$ and $\eta d = 18$.

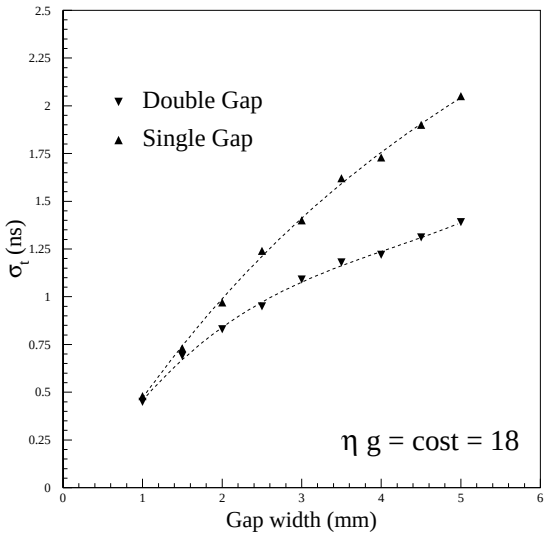


Figure 3.3: Simulated time resolution as a function of the RPC gap width. The gain has been kept constant, as indicated in the plot.

$\lambda = 5.5$ mm$^{-1}$ while $\eta d = 18$. The most relevant difference between the two curves is their behaviour at very low charge values. Narrow gap widths lead to divergent charge distributions whereas larger ones tend to have a maximum for $q_{ind} > 0$ C. Smaller gaps are therefore characterised by a larger fraction of events below a given thresholds. This results in a more critical operation of the detector from the point of view of efficiency. Higher efficiency can be achieved by increasing the gain but the price to pay is higher streamer probability.

Time resolution is another important RPC characteristic affected by the gap width. The simulated time resolution as a function of the gap width is shown in Fig. 3.3. The gain has been kept constant. It is evident that the more narrow the gap the better the time resolution. The values reported in Fig. 3.3 are however unrealistically optimistic as they refer to uniform chambers without mechanical imperfections. Presence of spacers, mechanical tolerances, poor smoothness of the electrode surfaces are all factors that result into a worsening of the RPC time resolution mainly because they make the average signal delay change from point to point. Moreover one should not forget that propagation time along the read-out strips is another factor that degrades the global timing performance of large detectors. Good time resolution is of particular importance in CMS where individual signals have to be assigned

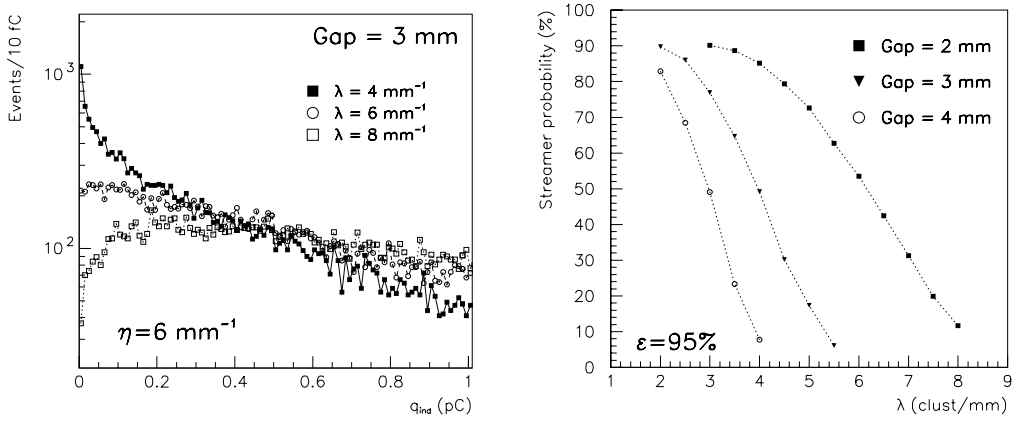


Figure 3.4: Left: simulated charge spectra for three different $\lambda$ values. Right: streamer probability as a function of $\lambda$ for three different gap widths.

to 25 ns spaced bunch crossings. In addition one would also like to have the largest possible freedom on the width of the acceptance gates in order to have more rejection power against uncorrelated background hits and detector intrinsic noise.
Choice of the gap width is therefore not obvious. This point has been studied in detail in a dedicated test beam whose scope was a more general one: understanding of the global performance of a CMS-like RPC. Results of this test are presented in the following section and refer to two prototypes differing only in the gap width: 2 and 3 mm. Larger gaps have been excluded as they are expected to result in too poor time resolution, while gaps more narrow than 2 mm have been excluded for instability reason from the point of view of efficient operation in the presence of low streamer probability.

### Gas mixture

It has been underlined that a fundamental parameter characterising the gas mixture is the cluster density $\lambda$. Typically gas mixtures with $2 < \lambda < 8$ mm$^{-1}$ are used; smaller values would result in very low efficiency due to frequent lack of primary clusters close enough to the cathode.
The simulated charge spectra for three different $\lambda$ values in an RPC having $d = 3$ mm and $\eta = 6$ mm$^{-1}$ are reported in the left plot of Fig. 3.4. The behaviour of the various distributions leads to making the same considerations as before: gases with larger $\lambda$ values are more convenient from the point of view of streamer-free efficient RPC operation. This

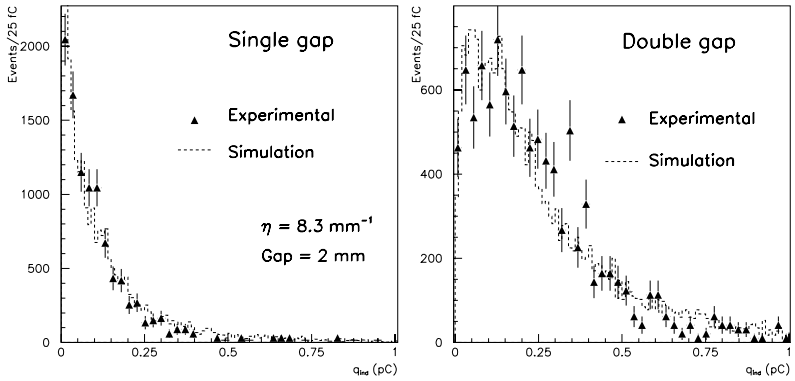


Figure 3.5: Experimental and simulated charge distributions in a single and double gap RPC.

is evident in the right plot of Fig. 3.4 which shows the streamer probability as a function of $\lambda$ for three gap thicknesses ($d$=2, 3 and 4 mm). Efficiency is fixed at 95% in all cases. It is also evident that a gas with high $\lambda$ is particularly necessary in narrow gaps. Therefore gas mixtures with high percentages of freon ($\lambda \approx 5.5$ mm$^{-1}$) are preferable over argon ($\lambda \approx 2.5$ mm$^{-1}$) based mixtures. The gas mixture that is expected to be used in the RPCs for CMS is indeed composed of 90% freon and 10% isobutane. Possibly a small fraction of $SF_6$ will be added as it has been proved to reduce further the occurrence of streamers [54].

**Number of gaps**

The discussion will be limited to two basic options: single and double gap RPC. A schematic view of a double gap RPC has been shown in Fig. 1.28. It is simply composed of two superimposed single gaps. The read-out strips are placed in between the two gaps so that they are sensitive to discharges in any of the two gaps. The charge induced on the strips is the sum of the signals produced by the two gaps hence the charge distribution of a double gap is the convolution of the charge distributions of two identical single gaps. The simulated and experimental charge distributions in a single and a double gap RPC having the same $\eta$ value are shown in Fig. 3.5. As expected the double gap has a less critical behaviour for low charges and therefore allows efficient operation with relatively low gas gain, which implies low streamer probability. A double gap RPC has also the attractive feature of enabling the option of switching off one gap in case of problems since the HV channels can be separated. All these advantages have led to the choice of the double gap design for the RPC of the

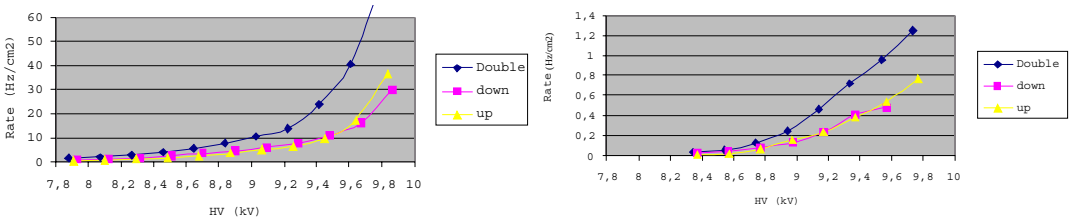


Figure 3.6: Left: intrinsic noise rate in a non oiled RPC. Right: intrinsic noise rate in an oiled RPC (in Hz/cm$^2$). In both cases single gap and double gap noise levels are reported. The working point of the detector was at HV = 9.5 kV.

CMS experiment.

**Characteristics and treatment of the electrode surface**

In the previous section it has been recalled that the RPC recovery time is proportional to the electrode bulk resistivity. Therefore better rate capability can be achieved with low resistivity bakelite. However too low resistivity can render the detector unstable by making discharges more frequent. The RPCs for the CMS detector will use 2 mm thick bakelite plates with resistivity ranging from $1. \times 10^{10}$ to $6. \times 10^{10} \Omega$cm.

A fundamental issue is the use of linseed oil for the treatment of the electrodes. The measured rate of accidentals per cm$^2$ for a non-oiled and an oiled chamber are shown in Fig. 3.6. Single gap and double gap noise levels are reported. The working point of the detector was at HV = 9.5 kV. It can be seen that oiled chambers have noise rates as low as 1 Hz/cm$^2$, at least one order of magnitude lower than what is observed in non-oiled RPCs. However big concern exists about the use of an organic compound like linseed oil in detectors that have to be operated for several years under extremely high radiation fluxes standing detection rates as high as hundreds of Hz/cm$^2$. In other words aging effects are particularly feared in case of use of oil. To date, as in the original baseline CMS design, RPCs are not oiled. This thesis work has not involved any experimental evaluation of aging effects on RPCs. Instead the impact of the noise rate on the CMS RPC trigger system has been thoroughly investigated. Indeed the following chapter is dedicated to the RPC trigger system simulation and to the impact on its performance of RPC parameters like efficiency, time resolution, strip multiplicity and noise.

## 3.2 Experimental results on RPC local and global performance

In avalanche mode, the useful range of operation is defined as the voltage range where efficiency is $> 90\%$ and streamer probability is $< 10\%$. Local disuniformities in the gap width can cause this voltage range to change from one region to another of a single detector, thus resulting in a narrowing of the overall operation range.
Also local time properties could vary from point to point due to mechanical disuniformities. Again the final result could be a deterioration of the global detector performance.
Since the gap width is defined by a $10\times10$ cm$^2$ array of spacers having a diameter of 1.2 cm, it is crucial to verify whether the technology used at present in the mass production meets the requirements of uniform response over areas of several square meters.
A detailed study on efficiency and time properties of two double gap chambers (having gap widths of 2 and 3 mm respectively), as developed in the context of the CMS R&D project, is presented in this section.

### 3.2.1 Experimental set-up

The chambers were $130\times120$ cm$^2$ in surface. The electrode plates were made of bakelite of nominal resistivity $\sim2\times10^{11}$ $\Omega$cm, without linseed oil surface treatment. The sensitive volume was filled with a $C_2H_2F_4$/iso-$C_4H_{10}$ 90%/10% gas mixture. The spacers that define the gap width were selected with a tolerance of $\pm20$ $\mu$m around the nominal value (2 or 3 mm) [55]. They had 12 mm diameter and were distributed on a $10\times10$ cm$^2$ grid so that they overlapped when the RPCs were superimposed to form the double gap.
Signals were read-out by means of $3.5\times130$ cm$^2$ aluminium strips, located between the two gaps forming the chamber. They were terminated at one end on a 40 $\Omega$ resistor. At the other end the strips were connected to a hybrid charge amplifier with 40 $\Omega$ input impedance, 10 MHz bandwidth, 1.5 ns rise-time of delta response and $\sim$1.6 mV/fC sensitivity. Output signals were discriminated by a 30 mV threshold (corresponding to about 20 fC) and input to a multi-hit TDC (LeCroy 3377A), with 512 ns time window and 0.5 ns sensitivity, operated in common stop mode. Each channel could register up to 16 hits before the trigger signal stopped the DAQ cycle.
The test has been carried out during summer 1997, at the CMS-H2 beam line of the CERN SPS. A 220 GeV/$c$ muon beam, characterised by a roughly Gaussian spatial profile with $\sigma \approx$ 2 cm, was used. The beam intensity around the maximum was about 200 Hz/cm$^2$ (constant during all runs) and was measured by two $2\times2$ cm$^2$ scintillators located just downstream

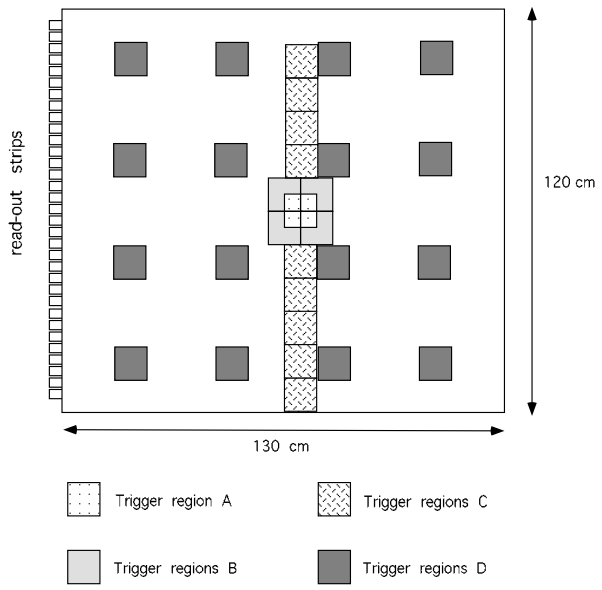


Figure 3.7: Schematic view of the RPC with the trigger regions in evidence.

the RPCs. Another set of two 10×10 cm$^2$ scintillators gave the trigger, characterised by a jitter smaller than 0.5 ns. The beam spill was 2.5 s long.
To scan different regions, the chambers were displaced horizontally and vertically ($X$ and $Y$ axes). In total thirty different 10×10 cm$^2$ regions were scanned, corresponding to about 20 % of the whole sensitive area of the RPCs, as shown in Figure 3.7.

### 3.2.2 Experimental methods

Two drift chambers [56] were used to determine the space (±1 mm) coordinates of the muons crossing the RPCs and to predict the position of the fired strips.
The applied procedure of alignment consisted of minimising, during the data analysis, the difference between the crossing points, extrapolated with the drift chambers, and the position of the RPC fired strips.
The RPCs were considered efficient if the predicted strip, or the adjacent one closest to the reconstructed crossing point, gave a signal detectable in a 60 ns window centred around the observed time distributions. The selected events were used to study also the time properties. If more than one strip was fired, the time properties were studied considering only the fastest signal. In order to compute the fraction of accidental coincidences biasing the evaluation of the chamber performance, the same procedure was applied to events acquired in random

trigger mode. The percentage of accidentals was found to be less than 0.2%.
Each trigger area was then subdivided in 1×1 cm$^2$ squares to study local effects on efficiency and timing.

### 3.2.3 Efficiency

First the results obtained in the trigger region located in the middle of the chambers (region "A" in Fig. 3.7), having the spacers at the four corners, are reported. Global efficiency is evaluated as the average of local efficiencies over all the 1×1 cm$^2$ cells. This procedure simulates a uniform illumination on this 10×10 cm$^2$ region and ensures that the result is independent of the beam profile.
The response uniformity has been studied by computing cell-to-cell efficiency fluctuations around the average. An upper and a lower estimate of these fluctuations was obtained defining the following "up" and "down" variances:

$$\sigma^2_{up} = \frac{1}{N}\sum_{i}^{\epsilon_i>\overline{\epsilon}}(\epsilon_i - \overline{\epsilon})^2 \tag{3.4}$$

$$\sigma^2_{dw} = \frac{1}{N}\sum_{i}^{\epsilon_i<\overline{\epsilon}}(\epsilon_i - \overline{\epsilon})^2 \tag{3.5}$$

where:

- $\overline{\epsilon}$ is the average efficiency over the whole trigger region
- $\epsilon_i$ is the i-th cell efficiency
- $N$ is the total number of cells.

These definitions were chosen since, above the plateau knee, the $\epsilon_i$ distributions are strongly asymmetric around 100% efficiency.
Figs. 3.8a and 3.8b show efficiencies versus operating high voltage for the 2 and 3 mm chamber respectively; dashed lines represent local fluctuations around the average, computed as explained above. The difference $\Delta I$ between the in-spill and off-spill current drawn by each chamber is also shown.
The 3 mm chamber reaches full efficiency at a lower electric field with respect to the 2 mm one; this is also predicted by simulation studies [49] described in the previous section.
The effect of the spacers has been studied considering four adjacent trigger regions (regions

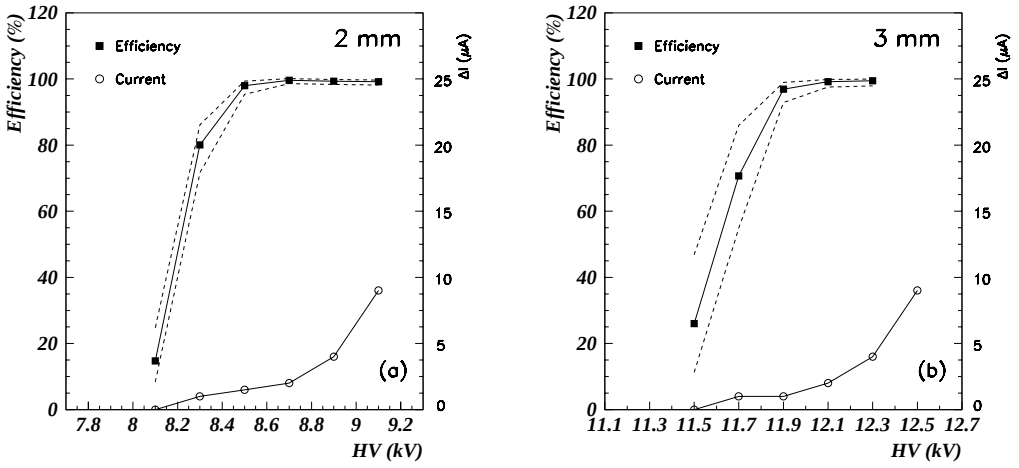


Figure 3.8: Average efficiency and current versus HV for the 2 mm (a) and 3 mm (b) chamber in the central 10×10 cm$^2$ trigger region. Fluctuations around the average are also shown.

"B" in Fig. 3.7, total area 20×20 cm$^2$) each centred on a spacer. The inefficiency map for the 2 mm chamber is shown in Fig. 3.9. In this figure, the area of each square is proportional to the inefficiency measured in the corresponding cell. The geometrical extension of the spacers accounts for the observed inefficiency. Similar results have been obtained for the 3 mm chamber.

In order to study the response uniformity over the whole chamber, several trigger regions have been investigated. First, 9 regions located along a vertical line ($Y$ direction, orthogonal to the strips) in the middle of the chambers (regions "C" in Fig. 3.7) are considered. Fig. 3.10 and Fig. 3.11 show the efficiency versus the position along the $Y$ direction, at different HV, for the 2 mm and 3 mm chamber respectively. The reported efficiency is again the average value over the 100 basic cells into which each trigger region is subdivided. It can be clearly seen that, as HV increases, point-to-point fluctuations tend to decrease becoming negligible at the detector working points.

Finally all regions labelled "D" in Fig. 3.7 have been studied. The average efficiency over a total of 1600 cells is reported in Figs. 3.12a and 3.12b for the 2 and 3 mm chamber respectively. Again, dashed lines indicate the fluctuations around the average computed according to definitions 3.4 and 3.5.

The comparison between the curves reported in Fig. 3.8 and Fig 3.12 shows that the

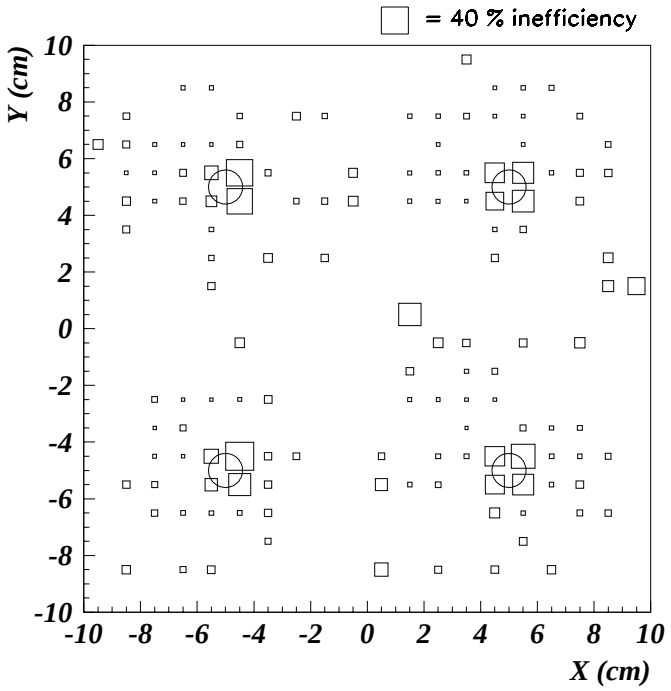


Figure 3.9: Inefficiency map (2 mm, HV=8.9 kV) in the central 20×20 cm$^2$ area of the chamber (circles represent the spacers).

fluctuations differ significantly; this means that long scale disuniformities are also present and are by far more important than the short scale disuniformities.
Although one might have expected the opposite effect, Fig. 3.8 and Fig. 3.12 show that at low HV the 3 mm chamber efficiency has a slightly larger spread around the average. This could be due to the treatment used in the construction of the 3 mm spacers, which is different from the one used for the 2 mm.

### 3.2.4 Time properties

Good detector time properties are important for the performance of the muon trigger at future LHC experiments, where the short bunch crossing time separation (25 ns) imposes strict requirements on time resolution and "time walk". The time walk is defined as the variation of the signal average arrival time per kV of HV.
The time response has been studied extracting from the data an equal number of events

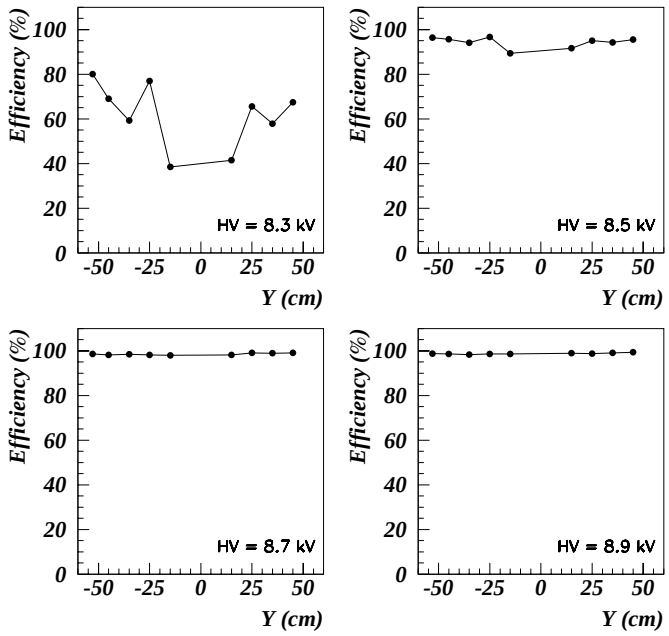


Figure 3.10: Efficiency versus $Y$, at different HV for the 2 mm chamber. Each value is the average over 100 cells.

for each of the 1600 ($1\times1$ cm$^2$) cells belonging to the trigger regions "D". In this way the resulting hits are uniformly distributed over the investigated area.

The overall signal arrival time distributions (arbitrary zero) are shown in Figs 3.13a and 3.13b for the 2 and 3 mm chamber respectively. A Gaussian fit has been superimposed on each distribution. The sigmas of the Gaussian fits are 3.0 ns (2 mm chamber) and 3.4 ns (3 mm chamber). As expected, the 3 mm one shows worse time resolution.

The tails on the left hand side are consistent with the observed noise background and account for the cases in which the fastest signal in the 60 ns gate is not associated with a real track. Since only the fastest strip is considered for these distributions, a spurious hit can be observed on the right hand side only if the chamber has not given a signal associated to the track. This is highly unlikely because at the considered HV the chambers were almost fully efficient.

The overall time resolution is in general spoiled by both possible local disuniformities and

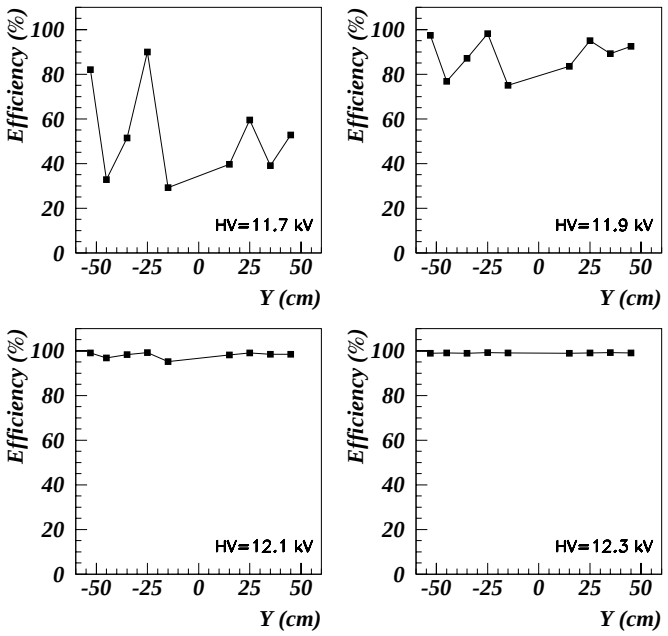


Figure 3.11: Efficiency versus $Y$, at different HV for the 3 mm chamber. Each value is the average over 100 cells.

by the different signal propagation time along the read-out strips. The latter changes according to the avalanche location along the strip. Likewise, disuniformities can cause the time response of the chamber to be different from point to point. Both phenomena lead to a broadening of the overall time distribution.

The broadening effect due to the signal propagation time can be cancelled by subtracting the time needed by each signal to reach the front-end board. The corrected distributions, obtained assuming a signal speed along the read-out strips of 0.66 $c$, are shown in Figs 3.14a and 3.14b for the 2 and 3 mm chamber respectively. The value assumed for the signal propagation speed is consistent with the average shift of the signal arrival time observed in data samples taken at different positions along the read-out strips.

This procedure improves the time resolutions to 2.1 ns and 3.0 ns for the 2 and the 3 mm chamber, respectively.

As remarked previously, the time resolution would improve if local disuniformities were

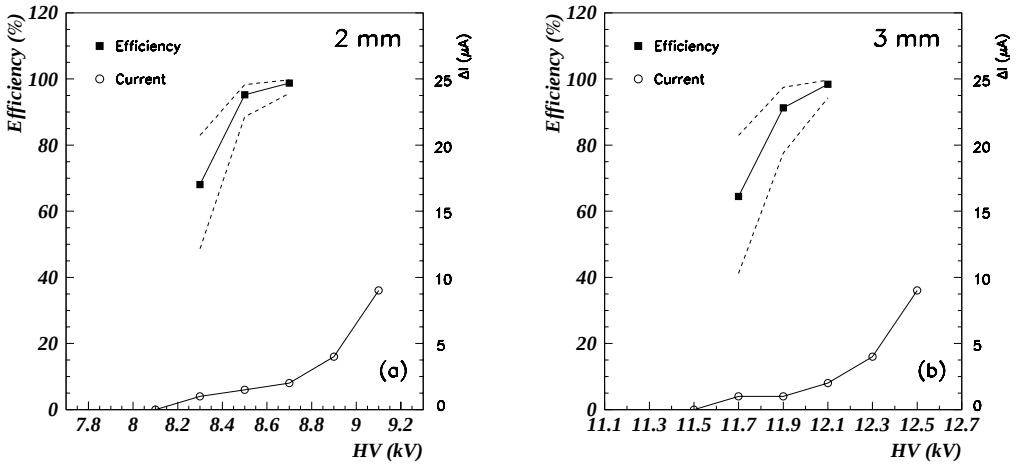


Figure 3.12: Efficiency versus HV for the 2 mm (a) and the 3 mm (b) chamber, computed as the average over 1600 cells.

absent. Time disuniformities for the 2 mm chamber are shown in Figs 3.15a and 3.15b, which show the distribution of the sigmas $\sigma_t^{(i)}$ ($i = 1, ..N$ where $N$ is the total number of cells) and mean values of the gaussian fits to all the local time distributions obtained in the 1 cm$^2$ cells at HV=8.7 kV. The corresponding plots for the 3 mm chamber are shown in Figs 3.16a and 3.16b (HV=12.1 kV). In both chambers the spread of the sigma values is quite relevant and mean values distributions are wider than expected for perfectly uniform chambers.

The average value of the $\sigma_t^{(i)}$ distribution is 1.6 ns for the 2 mm and 2.0 ns for the 3 mm; these values can be referred to as the local time resolution of the detectors and are of course sensibly smaller than the global values reported above. The difference between local and global time resolution after correction for the signal propagation time along the strips, is an indication of the degree of disuniformity of the chambers.

In Figs 3.17a and 3.17b the results concerning time resolution are summarised as a function of HV. The dashed lines above and below the local values select a $\pm 1$ RMS area around the mean value. Time disuniformities become smaller as HV increases.

In Figs 3.18a and 3.18b the average arrival times are plotted as a function of HV for the 2 and 3 mm chamber. Both chambers exhibit a time walk of approximately 13 ns/kV.

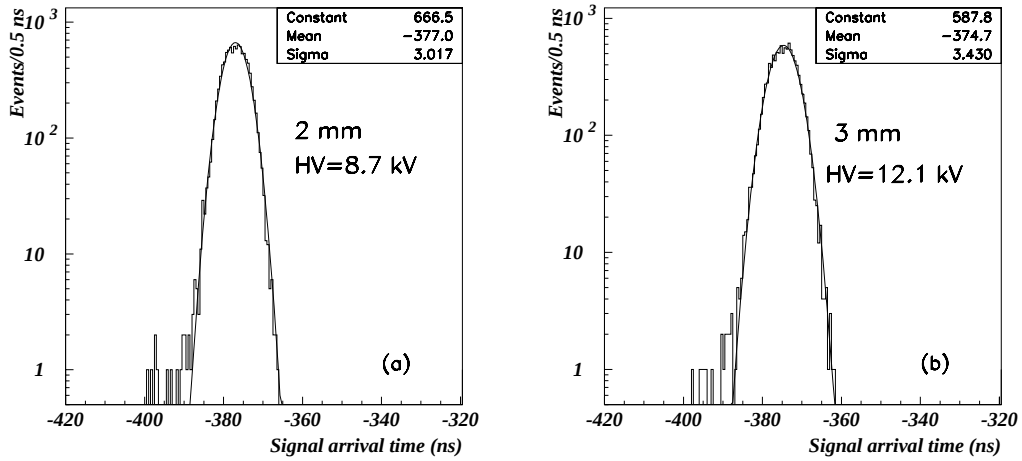


Figure 3.13: Signal arrival time distribution (arbitrary zero) for the 2 mm (a) and the 3 mm (b) chamber.

## 3.3 Conclusions

In this chapter the RPC detector working principle has been explained with emphasis on the role played by its structural characteristics.
New results concerning the global performance of two large double gap RPC operated in avalanche mode, as developed in the context of CMS R&D, have been presented.
Both chambers have exhibited a global efficiency at the plateau of 98%. The efficiency plateau is wide enough in both cases, the one of the 3 mm chamber being slightly narrower due to more important disuniformities. Both chambers have proved to stand the detection rate of 200 Hz/cm$^2$ without problems. The main difference in behaviour resides in the accuracy of their timing, the 2 mm chamber ($\sim$ 2 ns) performing better than the 3 mm one ($\sim$ 3 ns). Local variations have been found (which however decrease at increasing HV values), concerning both time resolution and efficiency. As an example, the time resolution computed in small cells is considerably better than the quoted global values, and approaches the expected theoretical limits for this kind of detector (see Fig. 3.3).
This effect is certainly due to unavoidable variation of the gap thickness that could arise both during the assembly of the electrodes and as a consequence of pressure produced by the mechanical frame which supports the gaps which form the chamber. Nevertheless great progress has been made on the uniformity by releasing the "staggering" requirement of

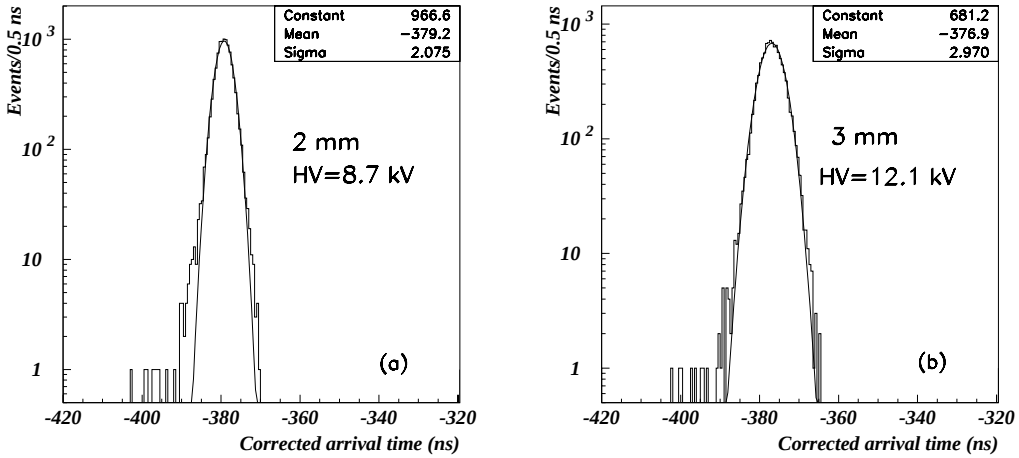


Figure 3.14: Corrected signal arrival time distributions (arbitrary zero) for the 2 mm (a) and the 3 mm (b) chamber.

the spacers in the two gaps. Indeed previous detectors were assembled in such a way that spacers in the two gaps did not overlap. This layout prevents the drop of efficiency to very low values in the regions where the spacers are located, since at least one gap is always sensible to the ionising particle.
However tests made on this double gap layout, whose results are reported in [57], have clearly shown that the uniformity response is very poor (compare figure 6 in paper [57] with figure 3.9). This happens because, with no overlap, the strength on each spacer is transferred to the underneath gap, which is then deformed. The new adopted geometry (no staggering) has determined striking improvements in the uniformity of efficiency and time properties.

The measured values of the RPC efficiency, time resolution, and intrinsic noise will be used in the following chapter to understand their impact on the performance of the CMS RPC trigger.

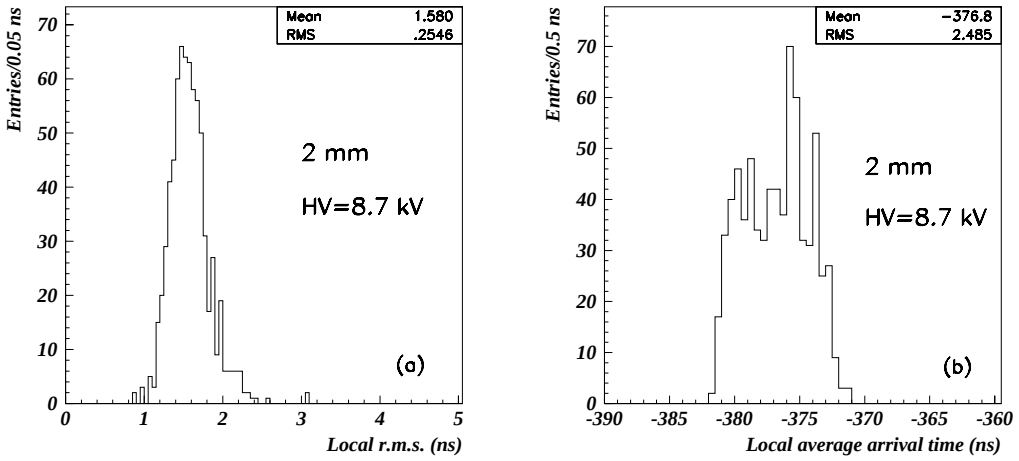


Figure 3.15: Sigmas (a) and mean values (b) of the Gaussian fits to all the local (1×1 cm$^2$ cells) time distributions for the 2 mm chamber at HV=8.7 kV.

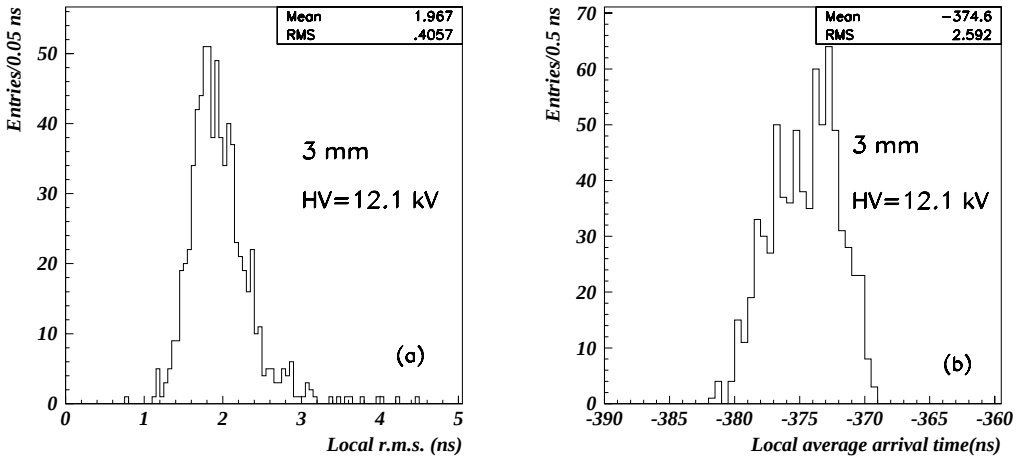


Figure 3.16: Sigmas (a) and mean values (b) of the Gaussian fits to all the local (1×1 cm$^2$ cells) time distributions for the 3 mm chamber at HV=12.1 kV.

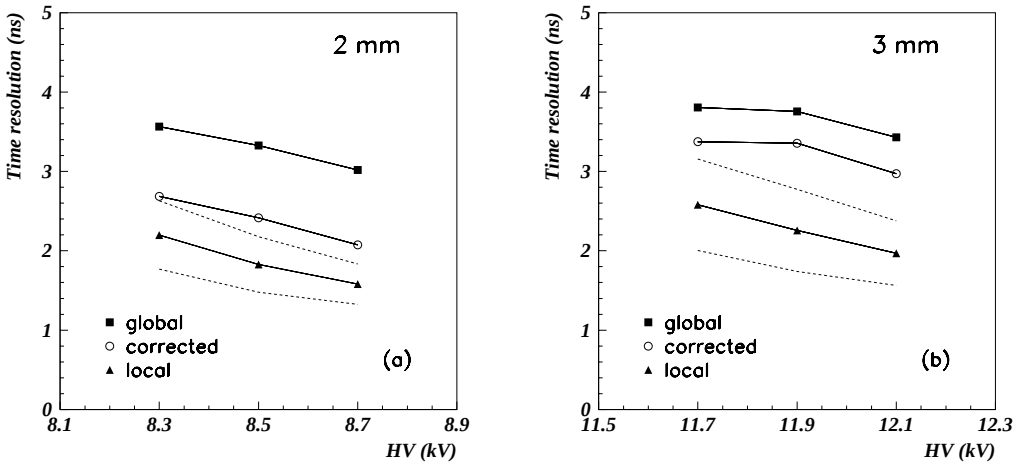


Figure 3.17: Time resolution versus HV for the 2 mm (a) and 3 mm (b) chamber.

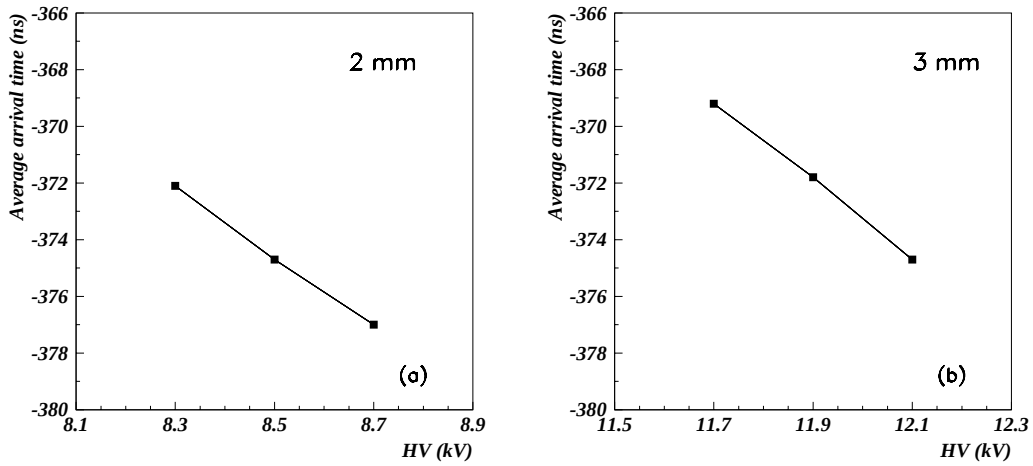


Figure 3.18: Average arrival time (arbitrary zero) versus HV for the 2 mm (a) and 3 mm (b) chamber.

# Chapter 4

# Simulation of the baseline RPC trigger system for CMS

## 4.1 Introduction

Resistive Plate Chambers will be used as dedicated muon trigger detectors in the CMS experiment. The CMS L1 muon Trigger, which also includes a second trigger system based on wire chambers (DT and CSC), has been discussed in great detail in chapter 2. Results on its performance have been presented by assuming for the RPCs efficiency 95%, time resolution 2.5 ns and average cluster size of 2 strips. Neither intrinsic noise nor spurious hits due to neutral particle background (see Figs. 3.6 and 1.22) were included in the simulation. This chapter describes in detail the performance of the RPC trigger stand-alone when all effects are included. All the presented results are concerned with the single muon trigger.

As explained in chapter 1, the RPC trigger should efficiently detect the so called prompt muons, that is, muons that are produced very close to the collision point; particularly important are those that come from the decay of heavy particles like $W^{\pm}$, $Z^0$ and $t$ quark, which will be mainly studied at high luminosity where the single muon trigger $p_t$ threshold is expected to be about 20 GeV/$c$. In the low luminosity LHC phase muons from $J/\psi$ and $B$ hadrons will also be very important and the single muon trigger $p_t$ threshold will be as low as 10 GeV/$c$. At the same time the RPC trigger output rate is required to be reasonably low at the threshold values reported above in order for the GMT to handle it properly and produce an output rate fitting the assigned value of about 10 kHz reserved for the single muon trigger. In this respect, one should keep in mind that prompt muons are not the only source of triggers. Muons coming from the decay of pions and kaons in the tracker or calorimeters are expected to give an important contribution. Last but not least, the RPC

intrinsic noise, which can reach values as high as 50 Hz cm$^{-2}$ (the number refers to the cluster rate, see Fig. 3.6) in non-oiled chambers, combined with uncorrelated background hits due to neutral particles, whose rate is particularly high at high pseudo-rapidity ($\eta$) values (see Fig. 1.22), should not be neglected. Not only these random hits can produce a totally false trigger, but they may also be able to "promote" real low $p_t$ muons to higher $p_t$ reconstructed ones by making up a coincidence with the hits released by these soft muons in the inner stations.

It is extremely important to understand the impact of detector effects, such as the already mentioned intrinsic noise, on the system performance. The trigger efficiency is mainly affected by the efficiency of the chambers, their time resolution and the correct adjustment of the acceptance time gates with respect to the arrival time of the signals. On the other hand the output rate is expected to depend mainly on the intrinsic noise and the cluster size, i.e. the number of adjacent strips with signals following the crossing of an ionizing particle. Indeed, cluster size values larger than 1 strip per event result in making random coincidences more probable and in causing soft muons to be more likely recognised as harder ones. The latter effect is caused by the trigger algorithm logic which is such that among all possible patterns of four single strips in four planes prefers the straightest one, that is the one corresponding to the highest $p_t$.
Generation of single muons as well as *minimum bias* events, detailed tracking through the apparatus, realistic response of the detectors and simulation of the trigger algorithm logic in an environment that includes RPC intrinsic noise and neutral particle background have been accomplished to fully understand all these effects.

This chapter is organised as follows: first the basic ideas underlying the project of the baseline RPC trigger system are reported, then details on the simulation programs used in this study are described, finally the results on efficiency and total output rates are presented.

## 4.2 The RPC trigger system

The RPC based muon trigger for CMS (see Fig. 4.1) covers the pseudo-rapidity region $|\eta| < 2.1$. Four RPC planes are used for triggering both in the barrel and in the endcap region. The planes are located in the muon stations MB1-4 (barrel) and ME1-4 (endcap). Muons with $3 < p_t < 6$ GeV/$c$ in the barrel are not able to reach the outer muon stations MB3 and MB4, therefore an additional plane is inserted in each of the two inner stations MB1 and MB2 in order to trigger on these muons too. The RPC chambers in stations MB1, MB3 and MB4 and those in the lower plane of MB2 are divided in two separately

read out detectors whereas the chambers in the upper plane of MB2 are divided in three [1]. The RPC strips are about 120 cm (80 cm) long in the detectors of the planes divided in two (three) and their pitch ranges from 2.1 cm in the inner MB1 plane to 4.1 cm in the MB4 planes. In the endcap the muon chambers have a trapezoidal geometry and the RPC strips run radially. The number of detectors in which each chamber is divided varies from station to station. The dimensions of the strips vary strongly from detector to detector: they are about 25 cm long and have a pitch of 0.7 cm in the lowest detector of the ME1 chambers at $\eta = 2.1$ whereas in the chambers at highest $r$ in ME2,3,4 they are about 80 cm in length and have a pitch of roughly 3 cm. More details on the geometry of the RPC system can be found in [58].

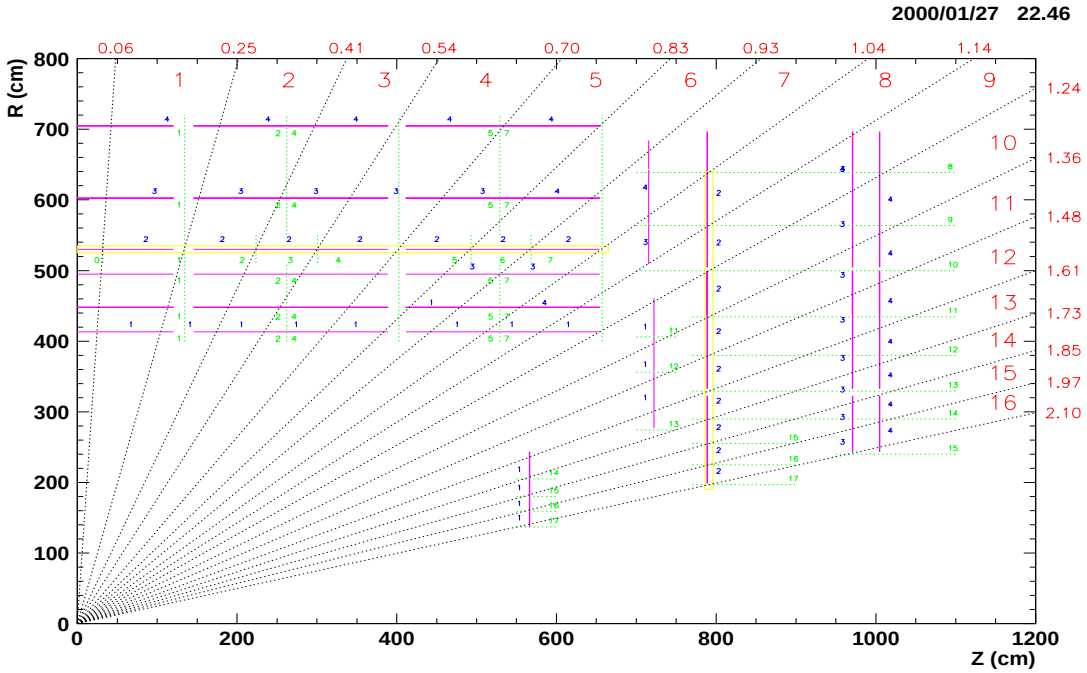


Figure 4.1: CMS geometry implemented in the GEANT based CMSIM 118 program. The tower boundaries and the RPC planes are reported in the picture.

The trigger basic principle is shown in Fig. 4.2; it relies on the magnetic field in the iron return yoke which can be as high as 1.8 T. Muon tracks are bent in the $r\varphi$ plane while the $\eta$ value of their trajectory remains almost unchanged. The muon $p_t$ can then

[1] Recently it has been decided that in the MB2 stations of the three central wheels the chambers in the lower plane will be divided in three detectors whereas the upper ones will be divided in two. In the other two wheels the chamber geometry stays unchanged. The new geometry version is the one adopted in the studies presented in chapter 2 and the following ones

be measured from the bending of the track. A muon travelling through the apparatus

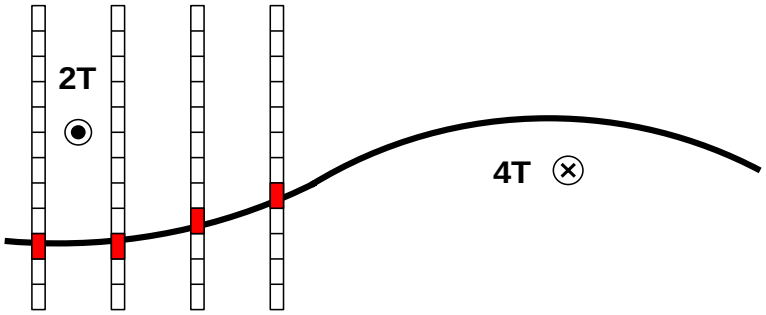


Figure 4.2: The basic principle of the RPC muon trigger.

produces hits on the RPC read-out strips and in this way it generates a pattern of hits that carries the information about the bending. The $p_t$ assignment is accomplished by means of trigger processors that compare the observed patterns with predefined valid ones, each corresponding to a certain $p_t$ value. In the barrel there are additional low $p_t$ processors which deal with signals coming from the four inner planes.

Each trigger processor covers a geometrical region called *segment* which is defined by 8 strips in the reference RPC plane. In the barrel the reference plane is the upper one in stations MB2, which is the one in which each chamber is divided in three detectors [2], whereas in the endcap it is the one in stations ME2. A segment covers roughly $\Delta\eta \approx 0.1$ pseudo-rapidity units and $\Delta\varphi = 2.5^0$. Segments having the same $\varphi$ are grouped into 33 rings called *towers* (-16, .., 0, .., 16) whose $\eta$ limits are reported in Fig. 4.1.

Thanks to the excellent RPC time resolution, every single hit can be immediately assigned to a given bunch crossing by just accepting it in a suitably synchronised time gate whose width cannot be larger than 25 ns. This task is accomplished in the link board device [59] which is placed at the periphery of the CMS detector. The time gates are opened every 25 ns and their opening time depends on the location of the strip in the apparatus. Muon time of flight, detector response delay, signal propagation along the strips, front end electronics delay and propagation of the digital signals along the cables to the link board have to be taken into account for correct synchronisation. A declustering procedure aiming at reducing the size of clusters of strips carrying signals is applied before delivering the hits to the trigger processors that perform the muon search. At present the procedure consists

[2] In the new geometry the reference chambers will also be the ones divided in three detectors

of discarding the two strips at the edges of the clusters with three or more strips. The surviving hits are then sent to the trigger processors which search for coincidences with the predefined patterns of 4 strips in the 4 planes to which they are connected. Also 3 out 4 coincidences are allowed but they are associated to lower quality muons.
For low $p_t$ muon search the full RPC granularity is not necessary since the $p_t$ resolution is dominated by multiple scattering hence patterns made out of ORed strips are used. At present the valid patterns are obtained with a simulation procedure [60], but they will be updated when real muon reconstructed tracks will be available.
Every processor sorts the found muons according to quality and $p_t$ value associated to the matched pattern. Quality has higher priority with respect to a higher $p_t$ value. Only the best muon is forwarded to following devices that accomplish further selection. In fact the 4 best muons in the barrel and the 4 best ones in the endcaps are finally delivered to the GMT as a result of a three step selection performed by dedicated hardware first on the muons found in the segments comprised in $30^0$ tower sectors, then in full towers and finally in the barrel and endcap regions. At every step the best 4 muons in the region under consideration are selected, the sorting being based again first on quality and then on $p_t$.
The algorithm used by the RPC trigger system can create ghosts in segments near the one containing a true muon. Candidates in neighbour $\varphi$ segments are created because strips from planes other than the reference one have to be connected to more than one processor to account for the muons that cross segment boundaries. Ghosts in adjacent towers also result from multiple connections which are necessary as a consequence of the geometry of the chambers and of the definition of the tower boundaries. Both a $\varphi$ and an $\eta$ ghost busting procedure are applied [37]. The former takes place before the sorting in $30^0$ tower sectors, the latter after tower sorting.

## 4.3 Simulation tools

As anticipated in the previous section, the trigger signals produced by the RPC system can be split into three main components according to their source, namely

1. Prompt muons, possibly in coincidence with accidental hits (due to detector noise or neutral particles background).

2. Muons coming from the decay of pions and kaons in the tracker or calorimeters, possibly in coincidence with accidental hits.

3. False triggers created by coincidence of accidental hits.

A dedicated study has been carried out for each of these components. The simulation chain is organised in the following steps (the output of each step represents the input to the following one):

- **Event generation:** production of the particles at the collision point of the apparatus. Initial positions and momenta of the particles are obtained.
- **Event simulation:** tracking of the particles through the CMS detector. The impact points (hits [3]) of the charged particles on the simulated RPC gas volumes are obtained. At this level, hits due to the RPC intrinsic noise and to the neutral particles background (from now on they will be referred to as noise and background hits, respectively) are added.
- **Digitization:** response of the RPC detectors to the hits. For each hit the set of fired strips whose signal is successfully assigned to the current bunch crossing is obtained.
- **Trigger algorithm:** search for the muons in the event and sorting of the found muons.

The only difference in the study of the three trigger sources resides in the event generation and simulation step. All the other steps are common to the three studies.

### 4.3.1 Event generation and simulation

The response of the RPC trigger to prompt muons has been studied by means of a sample of single muons events (SAMPLE A) produced by a simple built-in generator in the CMSIM program [33] version 118. Muons of both signs have been generated in $p_t$ bins ($2 \times 10^4$ events per bin and per muon sign) whose boundaries are reported in Tab.4.1. The muons are flat distributed in $\eta$ and $\varphi$ in the region $-2.4 \leq \eta \leq 2.4$ and $0 \leq \varphi < 2\pi$ whereas the $p_t$ distribution in each bin is parametrised with a decreasing exponential [33, 61] that reflects the expected single muon spectrum at the vertex. In calculating the trigger efficiency and the output rate, a parametrisation of the prompt single muon $p_t$ spectrum at the vertex, which has been obtained in a dedicated study [62] based on the PYTHIA program [24] version 6.136, has been used as described in section 4.4 and 4.5. The spectrum has been obtained considering only the muons originating in the decay of B and D hadrons which is the dominant source up to $p_t = 30$ GeV/$c$ as can be seen in Figs. 1.13 and 2.6. The

[3] previously in this chapter a hit was referred to as a unit of a generic pattern, typically a strip or a set of strips (in the case of patterns of ORed strips). Here a hit takes up a different meaning, as explained in the text. The double significance will be kept and not specified every time, unless it will not be clear from the context.

contribution from muons produced by $\tau$, $W$, $Z/\gamma$ and $t$ does not play an important role for the aim of the results shown in this chapter because, as it has been made clear in chapter 2, the RPC output rate for $p_t^{cut} > 20$ GeV/$c$ is largely dominated by mismeasured lower $p_t$ muons. The black curve in Fig. 4.8 shows the integrated single prompt muon spectrum as a function of $p_t$ for $L = 10^{34}$ cm$^{-2}$s$^{-1}$ and $|\eta| < 2.1$.

| $p_t$ (GeV/$c$) | 0. | 1. | 1.2 | 1.5 | 2.0 | 2.5 | 3.0 | 3.5 | 4. | 5. | 6. | 7. | 8. |
|---|---|---|---|---|---|---|---|---|---|---|---|---|---|
| | 10. | 12. | 14. | 17. | 20. | 25. | 30. | 35. | 40. | 50. | 70. | 100. | 999. |

Table 4.1: Boundaries of the $p_t$ intervals in which muons from SAMPLE A have been generated.

For what concerns the study of muons coming from the decay of pions and kaons, PYTHIA 6.136 has been used to generate about $8.84 \times 10^6$ *minimum bias* events out of which $1.39 \times 10^5$ were selected (SAMPLE B). The event selection was based on the requirement that at least one muon originating from the decay of $\pi^{\pm}$, $K^{\pm}$ or $K_L^0$ satisfying either of the following $\eta$ dependent $p_t$ cuts be present:

- $p_t > 2.0$ GeV/c in $|\eta| < 1.24$
- $p_t > 1.5$ GeV/c in $1.24 \leq |\eta| < 1.85$
- $p_t > 1.0$ GeV/c in $1.85 \leq |\eta| < 2.4$

The choice of these cuts will be justified in section 4.5.3. The PYTHIA program was allowed to evolve the event in a cylindrical volume having a 4 m diameter and a 9 m height. Since magnetic field (and thus track bending) and propagation through matter are not simulated in PYTHIA, this cylinder represents the fiducial volume in which it has been assumed that the decays can take place: it includes the full CMS tracker and part of the calorimeters. A further requirement for an event to be selected was the absence of muons of different origin (typically muons from B or D hadron decay near the vertex) satisfying the same conditions reported above. Discarding such events was necessary in order to avoid double counting in the total output trigger rate since the contribution from prompt muons is studied separately. The occurrence of such events was anyway smaller than 0.5% of the statistics of the finally selected sample. The distribution of the distance from the interaction point of the muon production vertex and the muon $p_t$ distribution for the selected events are shown in Fig. 4.3. All decay muons in the event contribute to both histograms.

The event tracking step for both SAMPLE A and SAMPLE B was performed by means of the CMSIM 118 program [33] based on GEANT3 [34]. The GCALOR package [63] was

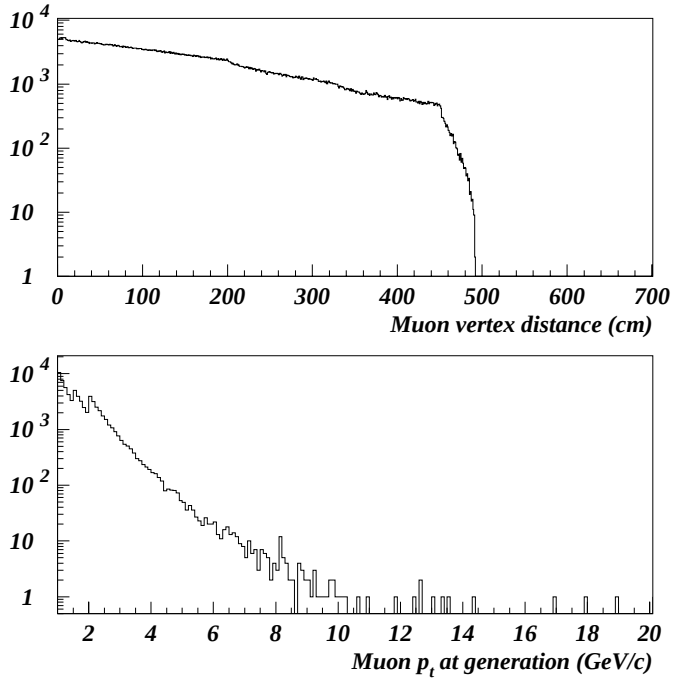


Figure 4.3: Muon vertex distance from the interaction point (upper plot) and $p_t$ spectrum of the decay muons (lower plot) obtained with PYTHIA 6.136. All decay muons in each event of SAMPLE B contribute to both histograms.

used for hadronic interactions. A detailed description of the relevant parameters adopted at the PYTHIA generation step and in the GEANT3 simulator can be found in [36]. The case of SAMPLE B is somewhat more involved. Indeed, to take into account the effect of the magnetic field and of the interactions with matter, which are not simulated by PYTHIA, the events have been re-propagated by CMSIM starting from those particles that covered more than 10 cm before decaying or before reaching the boundary of the cylindrical fiducial volume. This procedure allows to assign the proper position, direction and momentum to the decay muon after the curvature in the magnetic field and to check for possible hadronic interactions along the pion/kaon path before its decay.

Once all hits deriving from the particles generated at the collision point have been produced in the RPC chambers, noise and background hits are added.

Noise simulation has been implemented in a rather simplified way: hits are added randomly with flat probability over the surface of the chambers and their occurrence is parametrised according to a Poisson distribution whose average will be indicated as $noise_{RPC}$ (units: Hz cm$^{-2}$) which is the same for all detectors. It must be kept in mind anyway that there are strong experimental indications that non-oiled chambers are more noisy along their edges than at their centre [64].
For what concerns the simulation of background hits, in this case too they are randomly added over the chamber surface. Their occurrence is again Poisson distributed but the average value changes according to the chamber location in CMS. In the barrel it is used the rate value predicted at the chamber central point by parametrisation functions fitting the distributions of the background hit rate reported in Fig. 1.22. In the endcap, where variations across a chamber are sharper, the average of the Poisson distribution is calculated as the exact average rate using again some parametrisation functions fitting the distributions reported in Fig. 1.22 and this value is used to add hits all over the chamber surface. This procedure still does not take into account the rate variations across the endcap chambers, but the results will show that this effect is not important. In what follows a multiplicative factor for the background hit rate will be indicated as *ratefac*. The value *ratefac* = 1 corresponds to the background hit rates expected at $L = 10^{34}$ cm$^{-2}$s$^{-1}$. In the barrel these values typically fall in the range 0.1 - 10 Hz cm$^{-2}$ whereas in the endcap they range from few Hz cm$^{-2}$ to 300 Hz cm$^{-2}$, depending on the chamber.

In every event both noise and background hits are added over an interval of 75 ns centred around the time of flight that would be assigned to a particle of infinite momentum crossing the chamber at its centre. The correct subset of these hits that should be considered for the current event is recovered at the bunch assignment step performed at the digitization level which is described below.

### 4.3.2 Digitization code

The RPC efficiency is assumed to be uniform over the chamber surface, it will be indicated as $\epsilon_{RPC}$ and will have the same value for all chambers and for both physical and noise/background hits. This description does not take into account the presence of the spacers which play an important role in the localisation of the chamber inefficiency as it has been shown in the previous chapter.
Once the detector is considered efficient for the current hit, the number of fired strips (cluster size) is calculated. First a real number $R$ is extracted from a decreasing exponential distribution of the form $exp(-R/cs)$, where $cs$ is a parameter, then the cluster size is

obtained as $INT(R)+1$, where $INT(R)$ indicates the integer part of $R$. The cluster size distribution obtained with $cs = 1.5$ strips fits quite well the present experimental data [64], but it does not account for streamer events in which a large number of strips ($> 7$) is fired. However, in chapter 3 it has been shown that the occurrence of streamers is below 5%. The average values of the cluster size distributions resulting from using some representative $cs$ values are reported in Tab. 4.2. The same value of cs is used for all chambers regardless of the strip width. Investigations are being carried on to understand how important the role played by the strip width is.

Following what is observed experimentally [57], the cluster is centred around the strip

| cs (strips) | 0.0 | 1.3 | 1.5 | 2.0 | 3.0 |
|---|---|---|---|---|---|
| Average cluster size (strips) | 1. | 1.87 | 2.06 | 2.54 | 3.53 |

Table 4.2: Correspondence between some values of the $cs$ parameter and the average cluster size of the resulting distribution.

covering the region that includes the hit; if the cluster size is even then the last fired strip will be chosen according to the closeness to the hit position.

Every hit is associated to the time of flight of the particle that produced it (see previous subsection for the time of flight assignment to noise and background hits). It is worth noticing that, depending on the muon $p_t$, the time of flight may suffer variations as large as 6 ns, therefore its contribution to the time spread of the signal arrival times in a given detector with respect to the collision time is not negligible.
The time response of the chamber is assumed to be Gaussian and so is the jitter introduced by the electronics and the cables to the link board. The sigma of the former will be referred to as the detector time resolution and will be considered as a parameter ($\sigma_{RPC}$) whereas the sigma of the latter has been fixed to 1 ns.
Experimental tests [57, 64] have shown that, in a given cluster, the signals produced on strips far from the crossing point of the ionising particle arrive later than those produced on strips closer to such point. This effect has been simulated by parametrising the relative delay of signals produced in adjacent strips with a decreasing exponential function $exp(-delay/3)$ where $delay$ is measured in ns. Such a distribution fits quite well the experimental data.
Another effect that affects the spread in time of the signals produced in a given chambers is the signal propagation time along the strips which depends on the length of strip to be covered by the signal before reaching the end at which the electronics sits This effect has been simulated by assuming a constant signal propagation speed of $0.66c$.

A constant off-set of 50 ns is finally added to take into account the time response of the detector, the electronics response delay and the propagation along the cables to the link board. It is worth noticing that at the experiment start-up the value of this off-set, which in principle will vary from chamber to chamber, together with the average time of flight to the given chamber will be fundamental calibration constants for proper adjustment or synchronisation of the signal acceptance gates.
No *time walk* effects, i.e. variation of the average detector response time as a function of the detection rate, have been simulated. These may play an important role in case of strong luminosity variations during the runs.
All the contributions described above make up the final arrival time of each signal, which is checked, for bunch crossing assignment, against chamber dependent time gates whose width will be considered as a further parameter (*gatewidth*) common to all chambers. Large gate width values provide safer margins against loss of interesting signals. On the other hand smaller values will have the advantage of greater rejection of noise and background hits. The optimum compromise should be found by keeping in mind also the precision with which actual synchronization will be achieved. The set of the opening times of all the gates was obtained by calculating the mean value of the signal arrival time distribution of each chamber resulting from running the simulation and digitization steps on the subset of SAMPLE A satisfying $p_t > 8$ GeV/$c$. It must be stressed that, for the way it is obtained, this set corresponds to a very optimistic scenario from the point of view of synchronization. Only the strips that have produced signals which have been successfully assigned to the current bunch crossing are forwarded to the trigger simulation step. This means that the contribution from signals produced by physical particles (not by noise and background hits) originating in previous or following bunch crossings and wrongly assigned to the current one is not included in the simulation. This contribution can be neglected with very good approximation since the hit rate is largely dominated by noise and background hits which are correctly taken into account in the simulation.

### 4.3.3 Trigger code

The working principle of the RPC trigger has been outlined in sect. 4.2. The simulation package MRPC in the CMSIM program mimics accurately the functioning of the trigger using a set of valid patterns obtained by means of a simulation procedure [60]. The input to the MRPC program is the set of strips whose signals have been assigned to the current bunch crossing. Before starting the search for pattern coincidences, a declustering procedure is performed in order to reduce the number of adjacent strips carrying signals. The adopted

algorithm consists of discarding the two strips at the edges of the clusters with three or more strips.

In this study only the best muon found in the event has been considered. No information on the possible remaining 7 muons has been used. In towers 9-12 only 4 out of 4 coincidences are allowed in order to reduce the trigger rate from real muons, which would be too high as a consequence of the poor $p_t$ resolution in this region. In tower 9, it is in fact a 3 out of 3 coincidence algorithm, since only 3 planes are fully present and are the only ones which are used by the trigger logic (see Fig. 4.1). This points will be examined in greater detail in the following sections.

## 4.4 Efficiency of the system

The results presented in this section are intended to show the efficiency of the system for the interesting muons, therefore only the events in SAMPLE A have been used. In order to avoid overestimation of the trigger efficiency due to possible false triggers created as a result of a coincidence of just noise and background hits, in every event only the segment processors receiving at least one signal produced by the real muon are allowed to deliver reconstructed muons. The trigger efficiency will be always referred to a given value of the $p_t$ threshold ($p_t^{cut}$).

The turn-on curves in all the towers of the RPC system relative to some representative values of the $p_t^{cut}$ (1, 3, 5, 10, 20, 40, 100 GeV/$c$) are shown in Figs. 4.4 (towers 0-8) and 4.5 (towers 9-16). The trigger efficiency is defined as the probability of reconstructing muons of a given generated $p_t$ (variable on the x axis) and assigning to them a $p_t$ above the $p_t^{cut}$ under consideration. The values of the parameters are the following: $\epsilon_{RPC} = 0.95$, $\sigma_{RPC} = 2.5$ ns, $cs = 1.5$ strips, $noise_{RPC} = 50$ Hz cm$^{-2}$, $ratefac = 1$, $gatewidth = 20$ ns. These values represent what is presently considered a realistic scenario. The steepness of the curves is greatest in towers 0-8 due to the larger bending power of the magnetic field in the barrel region. The most problematic situation appears in towers 9-12 where the magnetic field bending power is quite low and the first measuring station is very far from the interaction point and does not provide full $\varphi$ geometrical coverage; this leads to a poor $p_t$ resolution which, as already mentioned, obliges to require only 4 out of 4 coincidences (3 out of 3 in tower 9) in order to keep the output rate reasonably low. This also explains the reduced plateau efficiency in these towers. In all towers the plateau efficiency values are solely determined by the effective 3 out of 4 hits (4 out of 4 in towers 9-12) acceptance (geometrical + detection efficiency + correct bunch assignment) of the RPC system because mismatching of the produced pattern with the patterns stored in memory is highly unprobable for high

$p_t$ muons. This implies that the plateau points in all curves do not change if parameters like *cs*, $noise_{RPC}$ and *ratefac* are varied. This does not hold for the other points in the curves where cluster size hits or random hits in coincidence with hits produced by the muon raise the efficiency values that would be obtained with an ideal system. Such effects are particularly important for what concerns the output rate and will be analysed in the following section.

A more general idea of the trigger efficiency is given in Fig. 4.6 which shows the efficiency in all towers for $p_t^{cut} = 20$ GeV/$c$. Here the trigger efficiency is defined as the probability of reconstructing the muons that have $p_t > 20$ GeV/$c$ at generation and assigning to them a reconstructed $p_t$ value above this threshold. The single prompt muon spectrum (black curve in Fig. 4.8) has been taken into account in obtaining the tower efficiency. Several cases are considered in Fig. 4.6: three cases of constant time resolution ($\sigma_{RPC} = 2.5$ ns) but decreasing efficiency ($\epsilon_{RPC} = 0.95, 0.90, 0.80$) and a final case with $\epsilon_{RPC} = 0.95$ but worse time resolution ($\sigma_{RPC} = 4.5$ ns). The other parameters are common to all cases ($noise_{RPC} = 50$ Hz cm$^{-2}$, *ratefac* = 1, *gatewidth* = 20 ns) but, as explained above (comments on the plateau points of the efficiency curves), they do not play a key role in this plot. The ideal trigger curve (full efficiency, perfect timing, no cluster size, no noise and background hits) is also shown for reference. The trigger efficiency is particularly sensitive to drops in RPC efficiency and time resolution in towers 9-12 as expected from the requirement of 4 out of 4 coincidences.

Narrowing the width of the time gates is perhaps the only effective tool to reject accidental hits, which is particularly important for purposes of accidental trigger rate reduction. On the other hand more narrow gates put the system in a more critical position from the point of view of detector time resolution and synchronization. The effect on the trigger efficiency caused by narrowing the gate width and by misalignment of the time gates is shown in Fig. 4.7. The misalignment has been simulated by shifting the optimal values of the opening time of the gates by a random and Gaussian distributed time. The sigma of this distribution is the parameter of interest here and is indicated as $\sigma_{shift}$. Three cases of different *gatewidth* values (20 , 15 and 12 ns) without misalignment and two different misalignment scenarios ($\sigma_{shift} = 3$ , 6 ns) with *gatewidth* = 20 ns are considered. It can be seen that narrowing the time gate down to 12 ns does not have dramatic consequences on the efficiency, but it is clear that particular care must be taken in the alignment procedure.

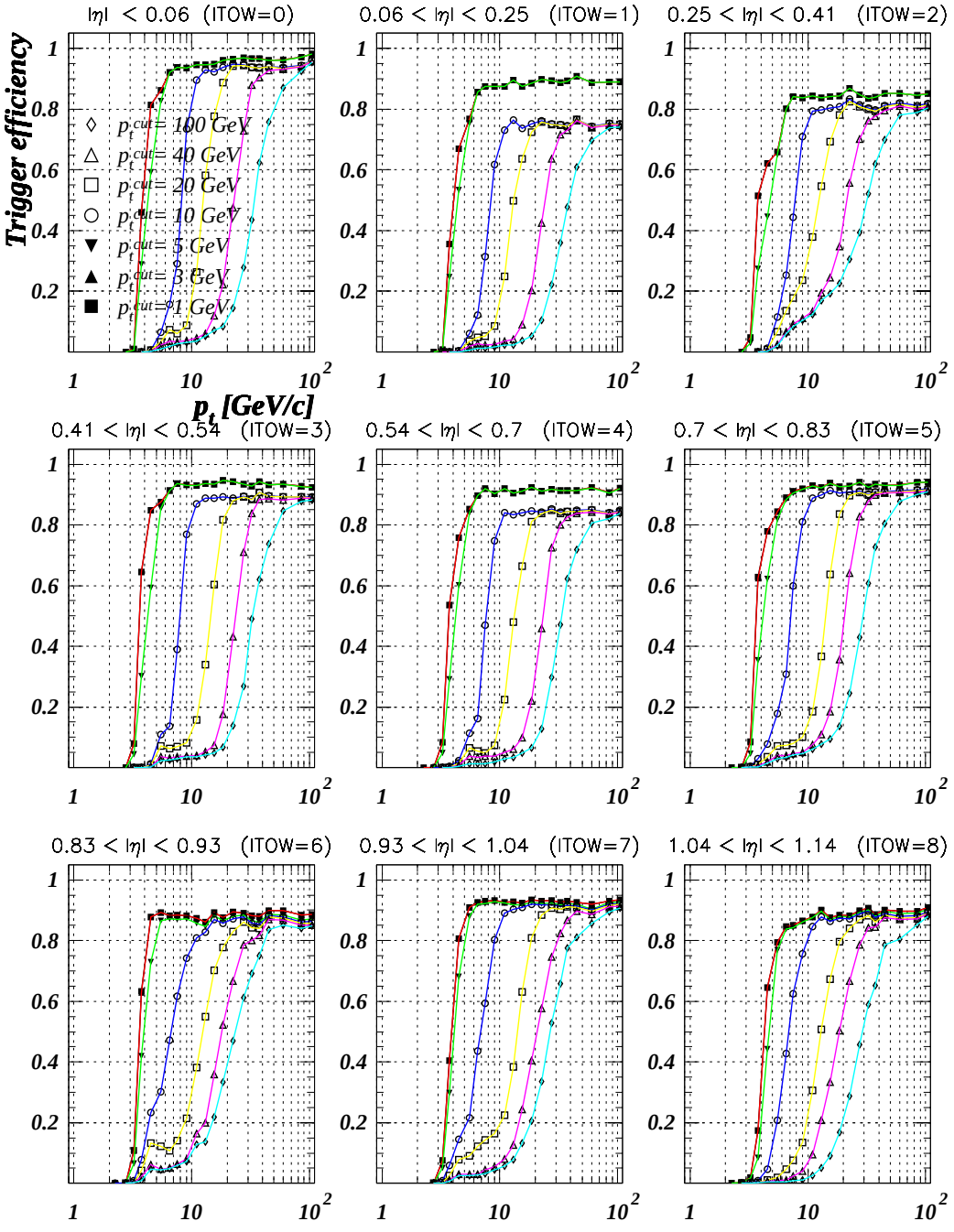


Figure 4.4: Turn-on efficiency curves in towers 0-8 of the RPC system relative to some representative values of the $p_t^{cut}$ as reported on the first plot. The values of the parameters are the following: $\epsilon_{RPC} = 0.95$, $\sigma_{RPC} = 2.5$ ns, $cs = 1.5$ strips $noise_{RPC} = 50$ Hz cm$^{-2}$, $ratefac = 1$, $gatewidth = 20$ ns.

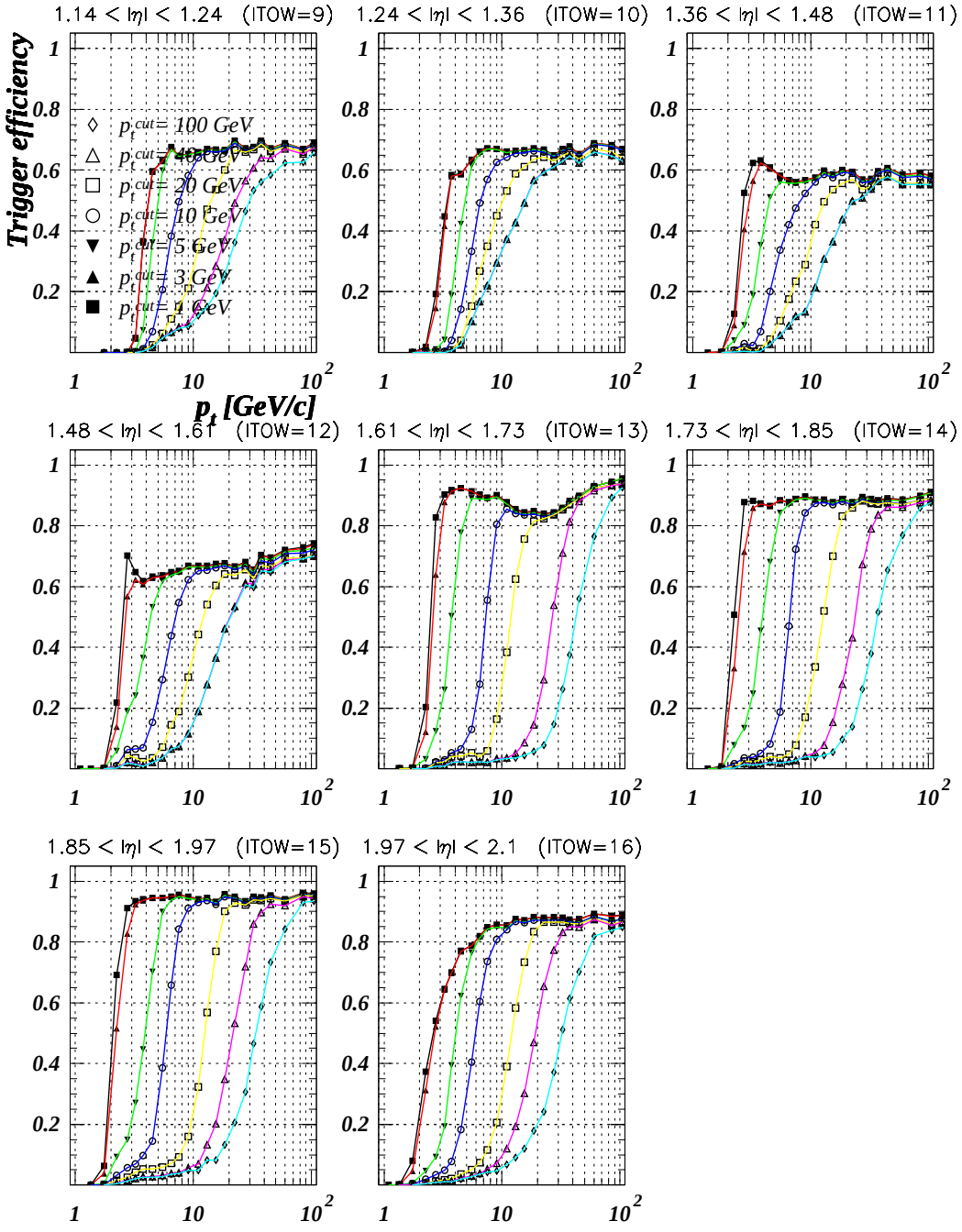


Figure 4.5: Turn-on efficiency curves in towers 9-16 of the RPC system relative to some representative values of the $p_t^{cut}$ as reported on the first plot. The values of the parameters are the following: $\epsilon_{RPC} = 0.95$, $\sigma_{RPC} = 2.5$ ns, $cs = 1.5$ strips $noise_{RPC} = 50$ Hz cm$^{-2}$, $ratefac = 1$, $gatewidth = 20$ ns. Only 4 out of 4 coincidences are allowed in towers 9-12.

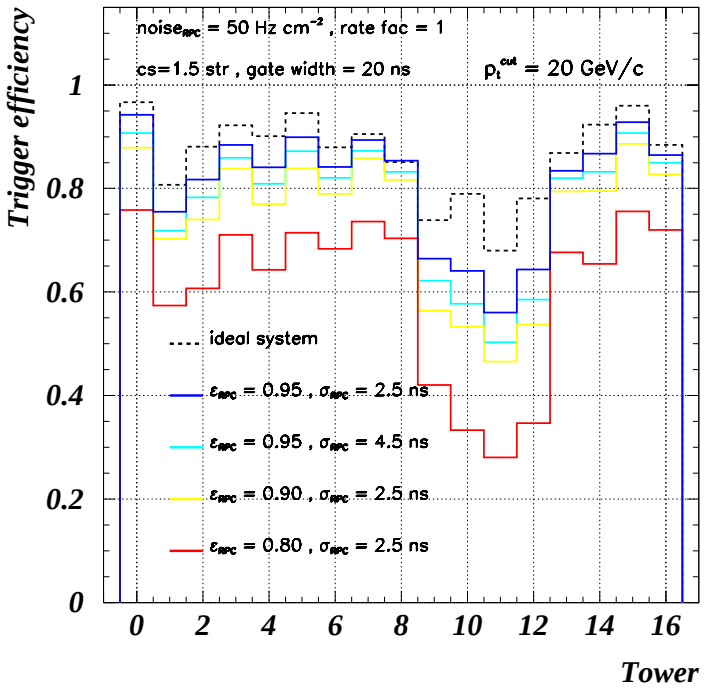


Figure 4.6: RPC trigger efficiency versus tower for $p_t^{cut} = 20$ GeV/$c$. Various scenarios from the point of view of RPC efficiency and time resolution are considered. The ideal trigger curve is also reported for reference.

## 4.5 Output rates

The output rates due to the three sources indicated in section 4.3 can be treated separately and finally added up in order to get the total output rate for the RPC single muon trigger. This procedure is correct to a very good approximation because the trigger probability per bunch crossing due to any of the three different sources is $\ll 1$ (well below $10^{-2}$) for reasonably high values of the applied $p_t^{cut}$. This will be proved below.

### 4.5.1 Prompt muons

The output rate due to prompt muons is calculated in each tower by convoluting the tower efficiency curve (such as those reported in Figs. 4.4 and 4.5) corresponding to the considered

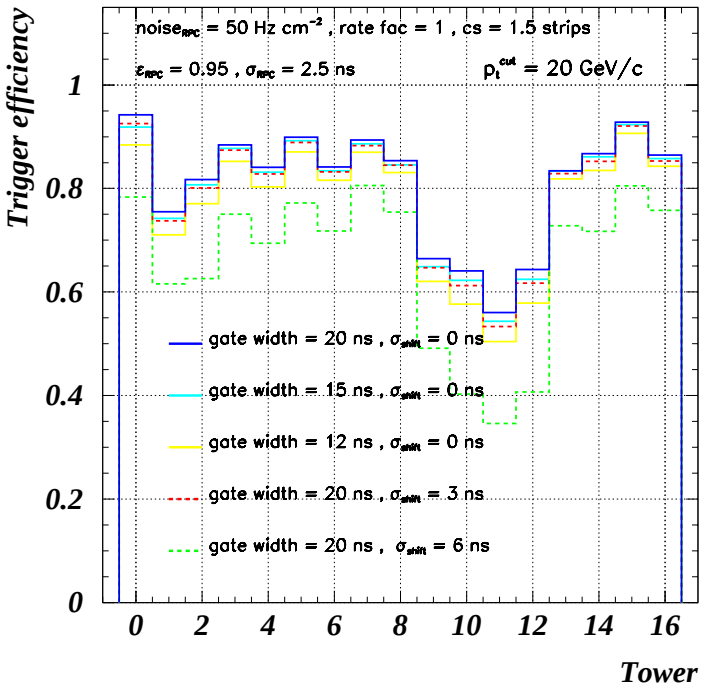


Figure 4.7: RPC trigger efficiency versus tower for $p_t^{cut} = 20$ GeV/$c$. Various scenarios from the point of view of the width and misalignment of the time gates are considered.

$p_t^{cut}$ with the expected prompt muon spectrum rate in the given tower. The muon spectrum is expected to be flat in $\eta$ [61], therefore one can use the global spectrum scaled to the $\eta$ interval covered by each tower. The trigger rate in the full system is then obtained as a sum of the rates in the various towers.

In Fig. 4.8 the result of such calculation at $L = 10^{34}$ cm$^{-2}$s$^{-1}$ is shown for three values of $cs$ (1.3, 2.0 and 3.0 strips). Three curves are calculated for $noise_{RPC} = 10$ Hz cm$^{-2}$ and $ratefac = 1$. A fourth one corresponding again to $cs = 2.0$ strips but with $noise_{RPC} = 50$ Hz cm$^{-2}$ and $ratefac = 5$ is also reported. The ideal trigger curve (full efficiency, perfect timing, no cluster size, no noise and background hits) is also shown for reference. Statistical errors are everywhere smaller than 2% and cannot be appreciated on the plot. It must be stressed that practically no contribution from pure false triggers is present in the output rates shown in Fig. 4.8 (and in the following Figs. 4.9 and 4.10) because, as said above, the

efficiency curves are obtained by allowing only the very few segment processors that have received at least a signal produced by the muon or by any of its secondaries in the event to deliver a trigger. It is clear that the key factor in the output rate due to prompt muons is the cluster size. The output rate for $p_t^{cut} = 20$ GeV/$c$ is increased by a factor 1.5 when passing from the ideal case to $cs = 1.3$ strips, and this factor increases as the $p_t^{cut}$ gets larger.
The other important result that turns out from the plot is the relative unimportance of the phenomenon referred to as *muon promotion*, i.e. the overestimation of the $p_t$ of soft muons due to coincidence with noise or background hits. Indeed, the rate difference between the curves corresponding to the same *cs* value but different $noise_{RPC}$ and *ratefac* values is of the order of 5% at $p_t^{cut} = 100$ GeV/c and decreases as the $p_t^{cut}$ gets smaller.
The trigger rate distribution among the various towers is shown in Fig. 4.9. It is evident that larger contributions comes from the endcap region as a consequence of the poorer $p_t$ resolution.
Narrowing the gate width does not have a large impact on the prompt muon output rate as it was easily predictable from the small trigger efficiency drop of the system which has been shown in the previous section. The results are shown in Fig. 4.10 for three different values of *gatewidth* (20 , 15 and 12 ns).

### 4.5.2 False triggers due to noise and background

To estimate the rate of pure false triggers, only the digitization and the trigger step have been performed on event samples containing just noise and background hits. The main results of this study are summarised in Fig. 4.11, where the trigger probability per bunch crossing (the trigger rate can be read on the right y axis) is reported versus the $p_t^{cut}$. Three sets of curves are reported. Each set refers to a $noise_{RPC}$ value of 10, 20 or 50 Hz cm$^{-2}$ (with $ratefac = 1$) and each curve in a given set corresponds to a different *cs* value (1.3, 2.0 or 3.0 strips). The trigger rate at $p_t^{cut} = 20$ GeV/$c$ is about 40 , 4 and 0.4 kHz for $noise_{RPC}$ =50, 20, 10 Hz cm$^{-2}$ respectively, with differences within a factor 2 due to the cluster size. There is also a curve (dashed line) corresponding to $noise_{RPC} = 50$ Hz cm$^{-2}$, $cs = 3.0$ strips and $ratefac = 5$.
It must be recalled that only 79.5% of the LHC bunches will be full, therefore, assuming that there will be a trigger veto on the empty crossings, the actual false trigger rate should be reduced by 20.5% (this means that the false trigger rate out of the full crossings can be read on the right y axis scale by substituting the number 3.2 for 4).

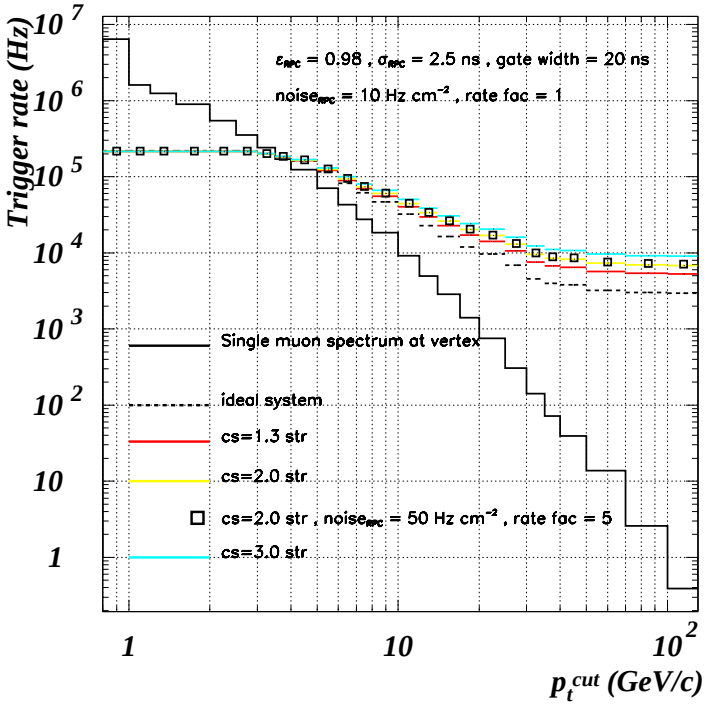


Figure 4.8: RPC single muon trigger rate due to prompt muons versus $p_t^{cut}$ for $L = 10^{34}$ cm$^{-2}$s$^{-1}$. Various scenarios from the point of view of cluster size, noise and background hit rates are considered as reported on the plot.

The distribution of the false triggers among the towers is shown in Fig. 4.12 for three different combinations of the parameters $noise_{RPC}$ and *ratefac*. The distributions corresponds to the pessimistic cluster size parameter value of $cs = 3.0$ strips in order to have higher statistics. On the y axis one can read the number of false triggers per tower obtained in a totality of $10^6$ events. One can see that increasing $noise_{RPC}$ from 10 to 50 Hz cm$^{-2}$ while keeping constant the background hit rate ($ratefac = 1$) results in a much more dramatic effect in the barrel, where the rate is increased by a factor 100, rather than in the endcap, where it is increased by a factor 10. On the other hand increasing *ratefac* to 5 while keeping $noise_{RPC} = 50$ Hz cm$^{-2}$ causes a faster growth in the endcap (a factor 20 against a factor 2 in the barrel). Still, anyway, the rate from the barrel dominates. This behaviour can be easily explained by recalling (see Fig. 1.22) that the background hit rate

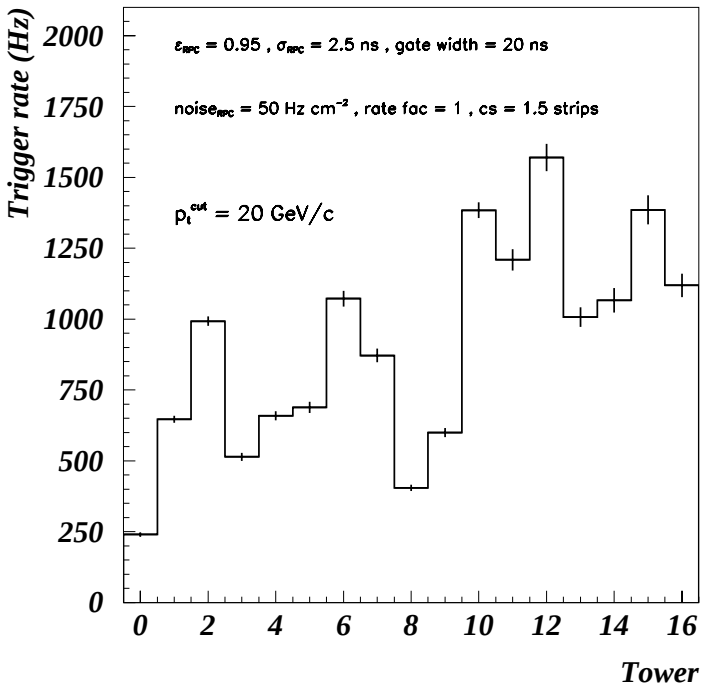


Figure 4.9: RPC single muon trigger rate due to prompt muons versus tower for $p_t^{cut} = 20$ GeV/$c$ and $L = 10^{34}$ cm$^{-2}$s$^{-1}$.

corresponding to *ratefac* = 1 in the endcap is comparable to and some time dominant even over a noise rate of $noise_{RPC} = 50$ Hz cm$^{-2}$, whereas in the barrel a noise rate of the order of 50 Hz cm$^{-2}$ is dominant even when *ratefac* is increased to 5. The large area covered by each single barrel strip is the basic reason for this result.
Concentrating on the case $noise_{RPC} = 50$ Hz cm$^{-2}$ and *ratefac* = 1, it is evident that the false muons are created almost exclusively in the barrel region, which gives 50 kHz of false trigger rate, whereas in the endcap the false trigger rate is about 0.4 kHz. In general the false trigger rate is largely dominated by the barrel as long as the ratio $noise_{RPC}/ratefac$ $> 10$ Hz cm$^{-2}$.

As anticipated in the previous section, the most natural way to reduce the false trigger rate is to narrow the gate width. The false trigger rate as a function of $p_t^{cut}$ for $gatewidth = 20, 15, 12$ ns is shown in Fig. 4.13. A factor 4 reduction is achieved by narrowing

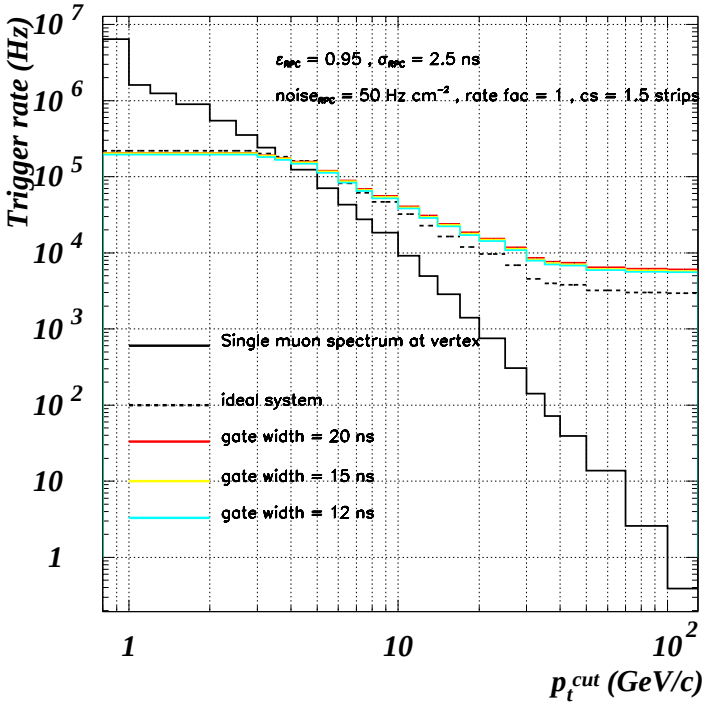


Figure 4.10: RPC single muon trigger rate due to prompt muons versus $p_t^{cut}$ for $L = 10^{34}$ cm$^{-2}$s$^{-1}$. Various scenarios from the point of view of the gate width are considered as reported on the plot.

the gate width from 20 to 12 ns.

### 4.5.3 Muons from $\pi$ and $K$ decays

The contribution to the trigger rate from decay muons has been calculated with SAMPLE B. The cuts on the $p_t$ of the decay muon, which have been adopted in the selection procedure described in section 4.3.1, can now be justified by looking at the trigger efficiency values for prompt muons reported in Fig. 4.4 and 4.5. The efficiency curves corresponding to $p_t^{cut} > 5$ GeV/$c$ gets to 0% efficiency for muon $p_t$ values well above the $p_t$ cuts used in the selection of the decay muons. Looser cuts should have been used to estimate correctly the output rate corresponding to lower $p_t^{cut}$ values. For this reason the trigger rate values reported in the following and corresponding to $p_t^{cut} \leq 5$ GeV/$c$ are likely to underestimate the actual

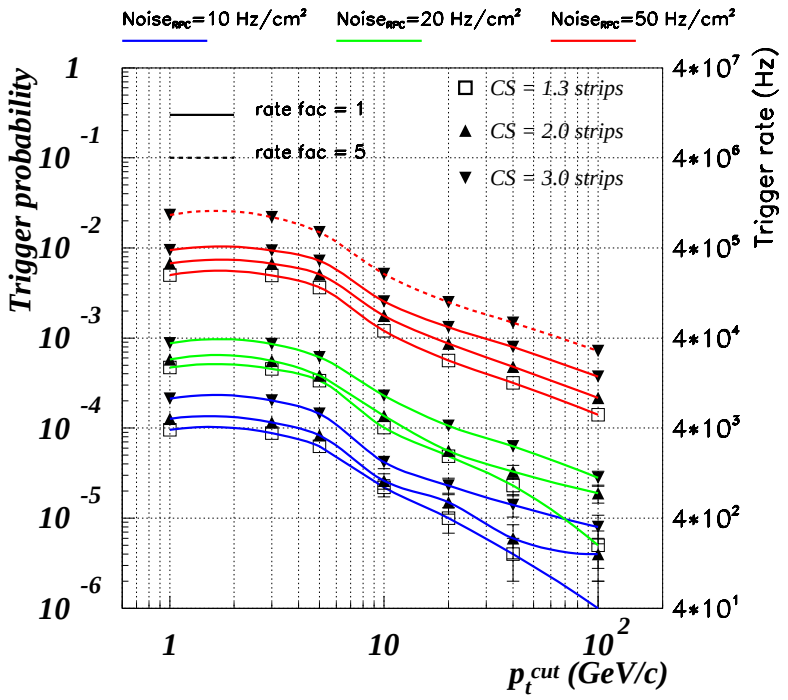


Figure 4.11: RPC false single muon trigger rate due to coincidences of noise and background hits versus $p_t^{cut}$ for various combination of $noise_{RPC}$, *ratefac* and *cs*. The rates are calculated for $\epsilon_{RPC} = 0.98$, $\sigma_{RPC} = 2.5$ ns and $gatewidth = 20$ ns. In towers 9-12 only 4 out 4 coincidences are accepted.

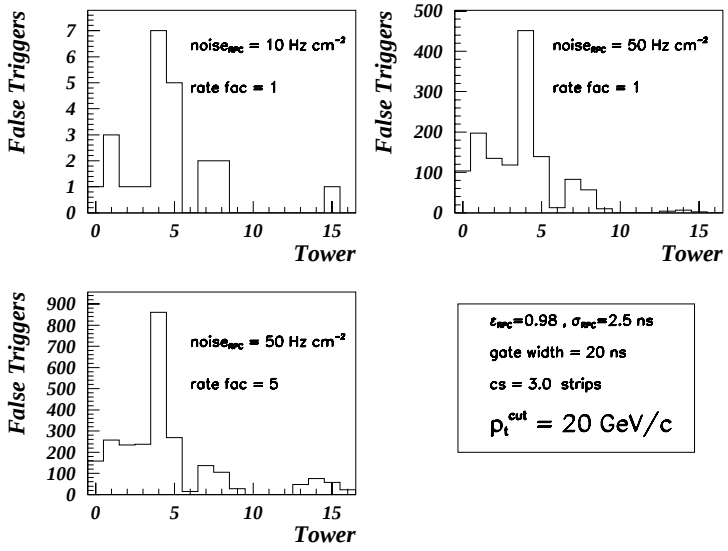


Figure 4.12: Distribution of false trigger events among the towers of the RPC system for $p_t^{cut} = 20$ GeV/c. The plotted events have been selected out of samples of $10^6$ events. In the bin corresponding to tower $n$ the events found in both tower $n$ and $-n$ are reported. Three different combinations of $noise_{RPC}$ and *ratefac* are considered. In towers 9-12 only 4 out 4 coincidences are accepted.

values.

At the LHC design luminosity of $10^{34}$ cm$^{-2}$s$^{-1}$ the total inelastic cross section of 55 mb predicted by PYTHIA for $p-p$ collisions at 14 TeV implies an average number of 13.75 events per bunch crossing. This number and the rejection factor 63.6 obtained at the sample selection step allows to compute to a very good approximation the trigger rate due to decay muons (at $L = 10^{34}$ cm$^{-2}$s$^{-1}$) as $13.75 \cdot (S-B)/(63.6 \cdot N) \cdot 40 \cdot 10^6$, where $N$ is the statistics of SAMPLE B ($1.39 \times 10^5$ events), $S$ is the number of reconstructed muons with $p_t \geq p_t^{cut}$ and $B$ is the number of pure false coincidences giving a false muon with $p_t \geq p_t^{cut}$ expected in $N$ events. The value of $B$ is computed from the false trigger probability calculated in the dedicated study described in the previous subsection. This procedure was necessary

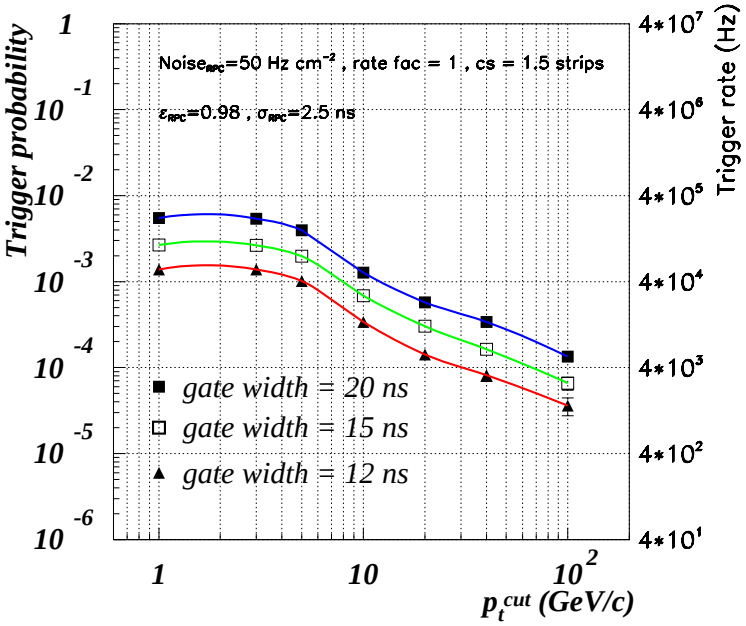


Figure 4.13: RPC false single muon trigger rate due to coincidences of noise and background hits versus $p_t^{cut}$ for various values of *gatewidth*. The rates are calculated for $\epsilon_{RPC} = 0.98$ and $\sigma_{RPC} = 2.5$ ns. In towers 9-12 only 4 out 4 coincidences are accepted.

because, due to the complexity of the tracked events, the information on the particles producing the hits could not be made available and therefore it was not possible, unlike in the prompt muon study, to switch on just the trigger processors receiving signals produced by the muons. The adopted procedure allows anyway to avoid double counting and to take into account the muon promotion from noise and background hits although the statistical errors on the computed rate values, which are much larger than those on the prompt muon trigger rate, do not allow to resolve tiny effects.

The results are shown in Fig. 4.14 in which the trigger rate is reported versus the $p_t^{cut}$ for different scenarios. Three curves correspond to different *cs* values (1.3, 2.0 and 3.0 strips) and common *ratefac* and $noise_{RPC}$ (1.0 and 10 Hz cm$^{-2}$ respectively) while a fourth one has been obtained with $cs = 2.0$ strips, $ratefac = 5$ and $noise_{RPC}$ =50 Hz cm$^{-2}$. The

main result here is that the rate due to decay muons is practically the same as that due to prompt muons. For what concerns the effect of the detector performance, the same conclusions drawn for the prompt muons hold: the cluster size plays a major role especially at large $p_t^{cut}$ values. The two curves corresponding to the same *cs* value but different noise and background rates superimpose within the errors, which are anyway as large as 20% in the high noise/background curve (where $B$ is comparable to $S$) and 10% in the low noise/background one at the highest $p_t^{cut}$ value. Therefore, as in the case of prompt muons, muon promotion appears not to be a crucial issue at least for the $noise_{RPC}$ and *ratefac* values that have been considered.

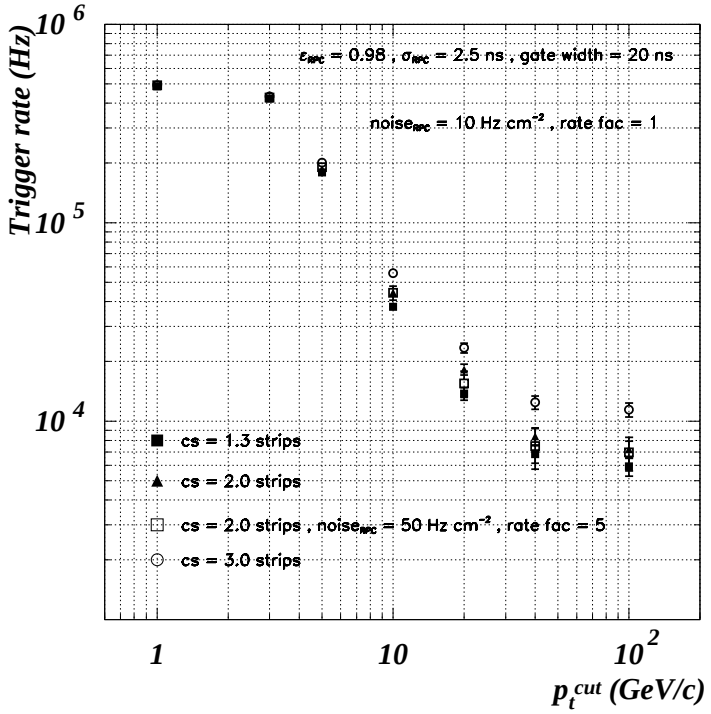


Figure 4.14: Decay muons trigger rate versus $p_t^{cut}$ at $L = 10^{34}$ cm$^{-2}$s$^{-1}$. Various scenarios from the point of view of cluster size and noise and background hit rates are considered as reported on the plot. The contribution from pure coincidences of noise and background hits has been subtracted out as described in the text.

The largest fraction of the output rate comes from the endcap as a consequence of the greater penetration power of low $p_t$ muons and of the poorer $p_t$ resolution of the system

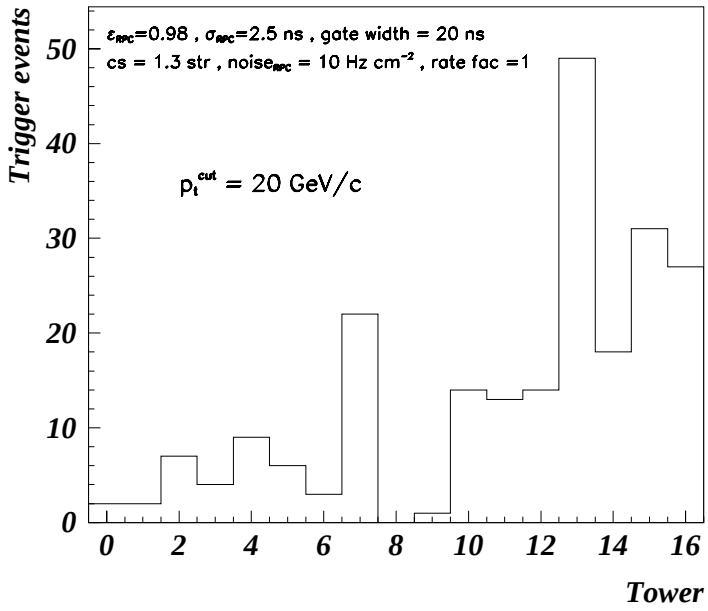


Figure 4.15: Distribution of trigger events due to decay muons among the RPC trigger towers. The plotted events have been selected out of SAMPLE B ($1.39 \times 10^5$ events). In the bin corresponding to tower $n$ the events found in both tower $n$ and $-n$ are reported. The expected number of pure coincidences of noise and background hits in the distribution is 1.4.

in this region. The result is shown in Fig. 4.15 where it is reported the distribution of the trigger events among the towers. The values of the parameters can be read on the picture. The expected number of pure false coincidences in the distribution plotted in Fig. 4.15 is 1.4.

### 4.5.4 Total output rates

As stated at the beginning of this section, the trigger rates due to the three investigated mechanisms can be added up in order to obtain the total single muon trigger rate from the RPC system. The results corresponding to $L = 10^{34}$ cm$^{-2}$s$^{-1}$ are summarised in tables 4.3 and 4.4 for $p_t^{cut} = 20$ and 100 GeV/$c$ respectively. In each cell the three numbers represent

the contribution (in kHz) from prompt muons, accidental coincidences and decay muons. Statistical errors are reported too.

| $L = 10^{34}$ cm$^{-2}$s$^{-1}$ , $p_t^{cut} = 20$ GeV/$c$ | | | | |
|---|---|---|---|---|
| $noise_{RPC}$(Hz cm$^{-2}$) | cs (strips) | 1.3 | 2.0 | 3.0 |
| 10 | prompt | 14.12±0.11 | 16.86±0.13 | 20.46±0.14 |
| | false | 0.40±0.13 | 0.60±0.15 | 0.92±0.19 |
| | decay | 13.8±1.0 | 18.2 ±1.2 | 23.4±1.3 |
| 50 | prompt | 14.50±0.11 | 16.92±0.12 | 20.83±0.14 |
| | false | 22.6±1.0 | 34.8±1.2 | 52.8±1.5 |
| | decay | 13.9±1.6 | 16.6±1.9 | 21.9±2.3 |

Table 4.3: Single muon output rates in kHz at $p_t^{cut} = 20$ GeV/$c$ and $L = 10^{34}$ cm$^{-2}$s$^{-1}$ for several combinations of cluster size and intrinsic noise values. The other parameters have the following values: $\epsilon_{RPC} = 0.98$, $\sigma_{RPC} = 2.5$ ns, *gatewidth* = 20 ns and *ratefac* = 1. In each cell the trigger rate due to prompt muons (first value), accidental coincidences (second value) and decay muons (third value) with the respective statistical errors are reported.

Single muon trigger $p_t$ thresholds as low as 10 GeV/$c$ would be desirable in the initial low luminosity LHC phase. It is reasonable to assume that the prompt and decay muon output rate will scale with the LHC luminosity, therefore the rate values expected at $L = 10^{33}$ cm$^{-2}$s$^{-1}$ from these two sources can be read off Figs. 4.8 and 4.14 after applying a factor 10 reduction. This does not hold for the false trigger contribution. Indeed, while the background hit rate should actually scale with the luminosity, the RPC noise does not in principle depend on it. Table 4.5 shows the single muon RPC trigger rate values (in kHz) for $p_t^{cut} = 10$ GeV/$c$ and $L = 10^{33}$ cm$^{-2}$s$^{-1}$. The value of *ratefac* is again 1 instead of 0.1 but this is not expected to have any importance since the false trigger rate is anyway determined by the noise rate for $noise_{RPC} = 50$ Hz cm$^{-2}$ whereas for $noise_{RPC} = 10$ Hz cm$^{-2}$ it is very low; moreover the muon promotion, as it has been proved, is expected to be negligible for such low values of *ratefac*. The numbers show that in the low luminosity scenario the rates due to physical muons are acceptable, the cluster size being also less important. On the other hand the absolute contribution from false triggers is even higher than for high luminosity as a consequence of the lower $p_t^{cut}$.

| $L = 10^{34}$ cm$^{-2}$s$^{-1}$ , $p_t^{cut} = 100$ GeV/$c$ | | | | |
|---|---|---|---|---|
| $noise_{RPC}$(Hz cm$^{-2}$) | cs (strips) | 1.3 | 2.0 | 3.0 |
| 10 | prompt | 5.30±0.07 | 6.83±0.10 | 9.05±0.10 |
| | false | 0.04±0.04 | 0.16±0.08 | 0.32 ±0.11 |
| | decay | 5.9±0.6 | 7.2 ±0.7 | 11.4±0.9 |
| 50 | prompt | 5.30±0.07 | 6.84±0.08 | 9.34±0.10 |
| | false | 5.6±0.5 | 8.6±0.6 | 14.9±0.8 |
| | decay | 5.4±0.9 | 8.0±1.1 | 10.0±1.4 |

Table 4.4: Single muon output rates in kHz at $p_t^{cut} = 100$ GeV/$c$ and $L = 10^{34}$ cm$^{-2}$s$^{-1}$ for several combinations of cluster size and intrinsic noise values. The other parameters have the following values: $\epsilon_{RPC} = 0.98$, $\sigma_{RPC} = 2.5$ ns, $gatewidth = 20$ ns and $ratefac = 1$. In each cell the trigger rate due to prompt muons (first value), accidental coincidences (second value) and decay muons (third value) with the respective statistical errors are reported.

## 4.6 Conclusions

From the point of view of trigger efficiency the RPC system is particularly sensitive to drops in detector efficiency. Care should then be taken in order to ensure that all chambers have an efficiency well above 90%.
Time resolution appears not be an issue provided precise adjustment of the time gates is achieved (misalignments not larger than 3-4 ns) and *time walk* effects due to detection rate variations are not large.

For what concerns the trigger rate, an important role is played by the cluster size, which turns out to increase the total output rate by about a factor 2 at the maximum $p_t^{cut}$. Improvements of the presently adopted declustering algorithm could be of help though their feasibility should be verified. It has also been shown that the contribution to the total rate from decay muons is very similar to that from prompt muons. In both cases the increase of the trigger rate caused by muon promotion is limited to a few percents as long as $noise_{RPC} \leq 50$ Hz cm$^{-2}$ and $ratefac \leq 5$.
The effect of punch-through hadrons has not been considered and need to be studied in detail.

However, the main concern about the single muon output rate is the contribution from false triggers. The problem is particularly relevant if the noise rate is higher than 20 Hz cm$^{-2}$, which is definitely the case for non-oiled chambers, and is largely more serious in the barrel region as long as the ratio $noise_{RPC}/ratefac > 10$ Hz cm$^{-2}$. At low luminosity the

| $L = 10^{33}$ cm$^{-2}$s$^{-1}$ , $p_t^{cut} = 10$ GeV/$c$ | | | | |
|---|---|---|---|---|
| $noise_{RPC}$(Hz cm$^{-2}$) | cs (strips) | 1.3 | 2.0 | 3.0 |
| 10 | prompt | 4.01±0.02 | 4.43±0.02 | 5.01±0.02 |
| | false | 0.88±0.19 | 1.04±0.20 | 1.68±0.26 |
| | decay | 3.77±0.16 | 4.45±0.18 | 5.58±0.20 |
| 50 | prompt | 4.04±0.02 | 4.45±0.02 | 5.04±0.02 |
| | false | 48.1±1.4 | 70.6±1.7 | 102.0±2.0 |
| | decay | 3.81±0.25 | 4.27±0.29 | 5.97±0.33 |

Table 4.5: Single muon output rates in kHz at $p_t^{cut} = 10$ GeV/$c$ and $L = 10^{33}$ cm$^{-2}$s$^{-1}$ for several combinations of cluster size and intrinsic noise values. The other parameters have the following values: $\epsilon_{RPC} = 0.98$, $\sigma_{RPC} = 2.5$ ns, $gatewidth = 20$ ns and $rate\ fac = 1$. In each cell the trigger rate due to prompt muons (first value), accidental coincidences (second value) and decay muons (third value) with the respective statistical errors are reported.

situation appears even more difficult.

Deeper investigations and possible solutions to the RPC false trigger problem are the subject of the next chapter. The impact of the RPC false triggers on the Global Muon Trigger response and on the di-muon trigger topology will also be examined there.

# Chapter 5

# The RPC L1 trigger: further insight and proposed modifications

## 5.1 Introduction

In the previous chapter it has been examined the performance of the stand-alone L1 RPC trigger. It has been shown that noise values typical of oiled chambers, i.e. 1 Hz/cm$^2$, give negligible false output rates, whereas values around 50 Hz cm$^{-2}$, typical of non-oiled chambers like the ones proposed for the baseline CMS RPC trigger, lead to an unacceptably high false trigger rate. The barrel region dominates as long as $noise_{RPC}/ratefac > 10$ Hz cm$^{-2}$, but, as it will be made clearer in the following, the endcap can quickly become critical and care has to be taken in this region too. Concerning this last point it must be recalled that in the study presented in the previous chapter some towers (9-12) were allowed to deliver only 4 out 4 coincidences (from now on the notation 4/4 will be used), which is a quite strict requirement. Moreover, no results were presented on the di-muon trigger rate though these are computable in a straightforward way from the single muon results.

Two possible ways can be followed to cure the problem:

1. act on the chambers by oiling them or by increasing their segmentation.

2. act on the trigger algorithm.

Increasing the segmentation seems out of discussion as it would lead to unaffordable system costs and to a complete redesign of the mechanical structure of the muon system: chamber design, services, chamber integration, etc.
Oiling the chambers would be the fastest and least painful solution, nevertheless great

concern exists about aging effects that could be introduced by an organic material like linseed oil. This concern, in fact, had dictated the decision of using non-oiled chambers in the early time of the apparatus design. For this reason the whole R&D program on the RPCs for CMS has involved non-oiled chambers. Despite the recent improvements in the oiling procedure, the negative experience with oiled chambers gained by the BABAR collaboration reinforces the doubts on choosing this way. The oiling issue will not be discussed further on in this thesis. It is only worth noticing that oiling the chambers is by far less risky in the barrel and in the low $\eta$ endcap region than it would be in the high $\eta$ endcap region since the detection rate to which RPCs will be subject is much lower.

This chapter is instead dedicated to the second possible solution, which involves modifications of the trigger algorithm.
Significant improvements without loss of efficiency can only be achieved if more information is made available. This information can come either from other unused RPC chambers, as it can be the case in the barrel region where six planes are present but only four are used at a time, or by the other detectors of the muon system, namely DT and CSC. In this respect the redundant structure of the GMT is particularly suitable to this aim.

In the following it is first examined the response of the GMT with the baseline, fully simulated RPC trigger. It will be shown that improvements are possible by optimising the algorithm that combines the information of the RPC and DT/CSC triggers. Then the results of a study of the performance of algorithms involving data from all the available detecting planes are presented. The possibility of inserting new detector planes has been investigated too.

## 5.2 False RPC triggers and GMT

RPC trigger muon candidates are assigned a quality that depends essentially on the planes where the hits that make up the observed pattern are found. The possible quality values are the following:

- **quality 0**: 3/4 coincidence, $2^{nd}$ plane missing.
- **quality 1**: 3/4 coincidence, $1^{st}$ plane missing.
- **quality 2**: 3/4 coincidence, $3^{rd}$ or $4^{th}$ plane missing.
- **quality 3**: 4/4 coincidence.

As explained in chapter 2 the RPC trigger reconstructs all 3/4 and 4/4 muons and forwards them to the GMT. The algorithm adopted in chapter 2 for the GMT is such that

- Accept RPC muons of any quality if they are matched with muons found by the DT or CSC trigger.
- Accept unmatched RPC muons only if:
  1. the quality is 3 or 2
  2. the quality is 0 and the tower is 1-4, 6-7 or 11-13

However these conditions are the result of an optimisation which aimed at keeping the rate from real muons and ghost occurrence as low as possible with the minimum efficiency loss. RPC false triggers had not been considered at all for this optimisation. The probability that the DT/CSC trigger finds a muon that matches a false muon from the RPC trigger is extremely low, therefore one can make the very safe assumption that any RPC false muon is unmatched.
All the results presented in this chapter have been obtained with the simulation tools described in section 4.3 except for the fact that digitization and simulation of the trigger algorithm have been accomplished with the ORCA program [35], which is the C++ substitute for the CMSIM FORTRAN program. As far as the RPC digitization and trigger algorithm are concerned there is no difference between the two programs.
If all muons of any quality are considered then the resulting RPC single false muon trigger rate as a function of $p_t^{cut}$ is shown in Fig. 5.1. In the same plot it is also shown the response of the GMT implementing the conditions reported above. The RPC parameters used to obtain this result are the following: $\epsilon_{RPC} = 0.95$, $\sigma_{RPC} = 2.5$ ns, $noise_{RPC} = 50$ Hz cm$^{-2}$, $cs = 1.5$ strips, $ratefac = 3$ and $gatewidth = 20$ ns. It is remarkable the fact that the GMT false trigger output rate is about 12 kHz at $p_t^{cut} = 20$ GeV/$c$. This value would already saturate the allowed L1 Muon Trigger bandwidth.
Note that the RPC rate significantly differs from what has been reported in the previous chapter. There are two reasons for this. The first reason is that in the previous chapter towers 9-12 were allowed to deliver only 4/4 coincidences. The second and less important one is that the geometry used to obtain the results of Fig. 5.1 is CMSIM 121 in which the most recent version of the RPC system is implemented (see Fig. 5.2 and read footnote at the end of chapter 1).

It is very interesting to have the RPC false trigger rate distribution among the various muon qualities and towers. This result is shown in Fig. 5.3 for a $p_t^{cut} = 20$ GeV/$c$. The sample size was $489{\cdot}10^3$, then one event contributes 81 Hz. The RPC false muons that are rejected at the GMT level because of the request of matching with a DT/CSC muon are marked in green (squared line).

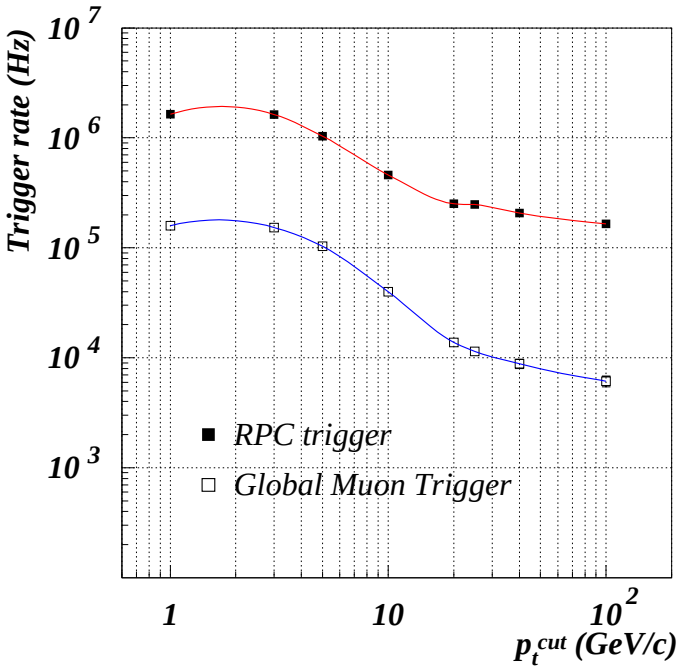


Figure 5.1: RPC false trigger rate as a function of $p_t^{cut}$. The rate accepted by the GMT adopting its standard selection algorithm is also shown.

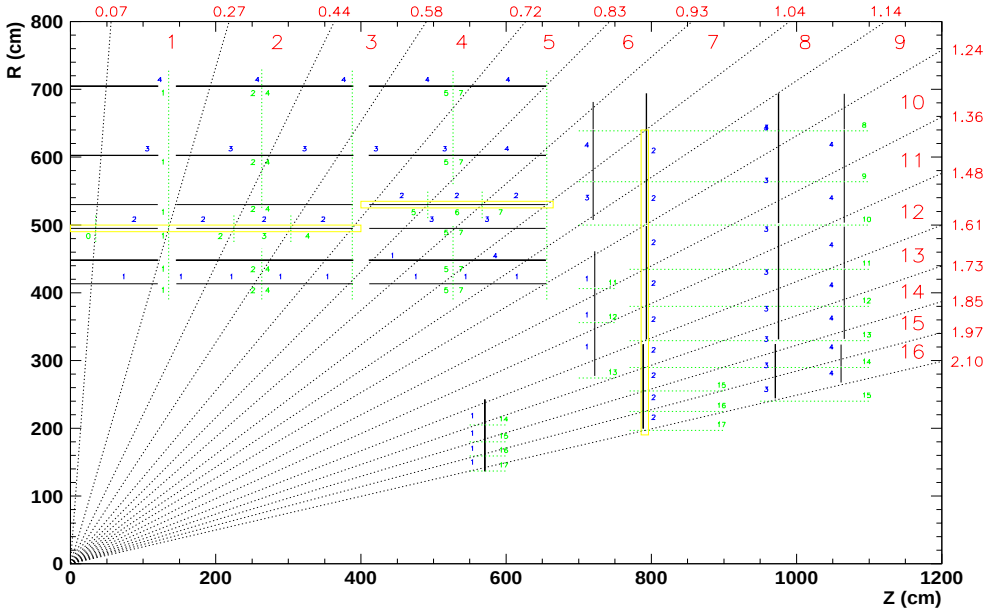


Figure 5.2: CMS geometry implemented in the GEANT based CMSIM 121 program. The tower boundaries and the RPC planes are reported in the picture.

A salient feature of this rate decomposition is the enormous contribution from quality 0 and quality 1 muons in tower 9. This tower is particularly critical because only three detector planes are actually present. This has forced to connect the third plane to both the third and the fourth input of the trigger processor. As a consequence, every time there is a spurious hit in the third plane there will automatically be two aligned logical hits in the last two logical planes. It suffices then to have another properly aligned spurious hit in the first or in the second plane to make up a false trigger. Another consequence is that quality 2 is not allowed in tower 9, since two planes would be missing. Quality 3, in this case, means a 3/3 coincidence.

The great rate reduction achieved at GMT level is mainly due to the exclusion of low quality muons from tower 9. The remaining rate fraction is mainly due, as it is already well known from the previous chapter, to low quality false muons produced in the barrel.

The region in Fig. 5.3 marked in purple (oval line) represents a proposed additional set of muons to be excluded at the GMT level in case of unsuccessful matching with a DT/CSC muon. It can be seen that this option allows to reduce the GMT false output rate at $p_t^{cut} = 20$ GeV/$c$ from 12 kHz to less than 1 kHz.

The loss in efficiency that results from these extra requirements can be seen in the right

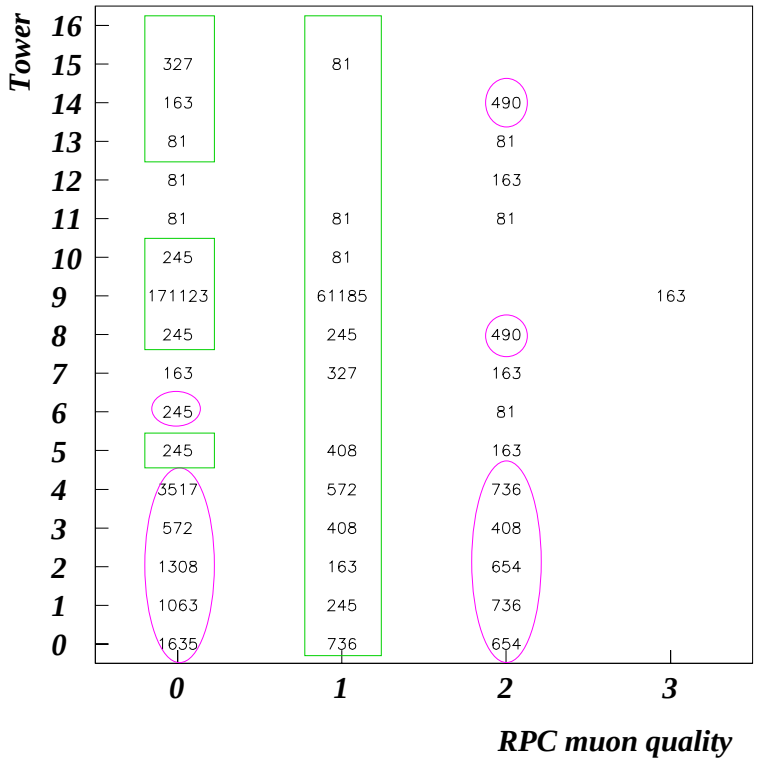


Figure 5.3: RPC false trigger rate (in Hz) decomposition in towers and qualities.

lower plot of Fig. 2.11. One must look at the fraction of unmatched RPC muons of quality 0 and quality 2 in the barrel. They correspond to less than 2% of the GMT efficiency in the barrel.

Another important point is to evaluate the occurrence of two false muons in the same event. This result is shown in Fig. 5.4 as a function of a common $p_t^{cut}$ on both muons. In

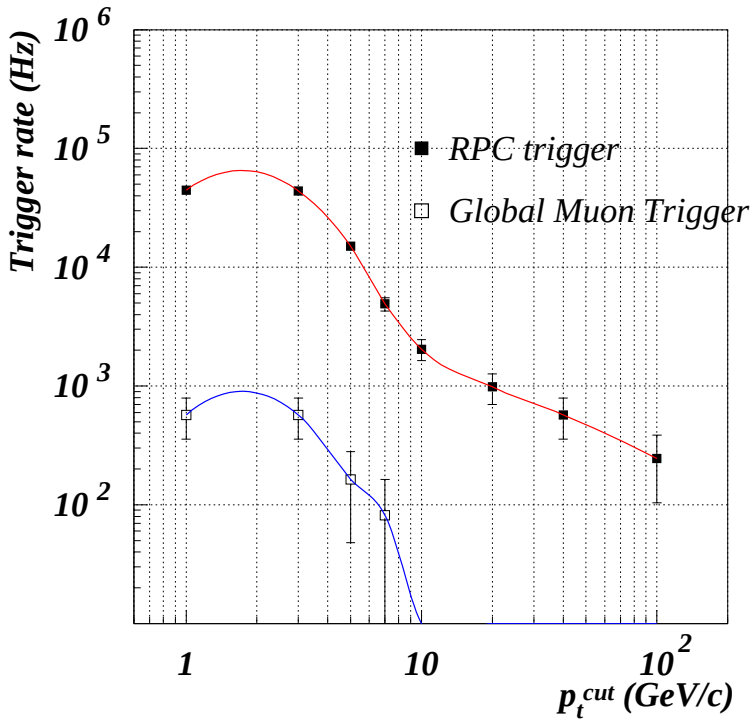


Figure 5.4: RPC false di-muon trigger rate as a function of the common $p_t^{cut}$ on both muons. The rate accepted by the GMT adopting its standard algorithm is also shown.

the same plot it is also shown the false di-muon output rate of the standard GMT. The latter is already at the low level of 200 Hz for reasonable $p_t^{cut}$ values of 5 GeV/c. Adopting the proposed extra conditions would push this rate to negligible levels.

The above discussion proves that the use of the information of the other muon trigger systems is a very effective way to face the RPC false trigger problem. However this solution can only be an extreme one because it would deprive the muon system of part of its redundancy from the start. It is necessary to cure the RPC trigger in order for it to be able to work independently of the other muon detectors. As it has been stressed in the introduction, this implies important modifications to the system. These are discussed in

the next section.

## 5.3 Modifications to the RPC trigger

In the baseline design the RPC trigger uses four RPC planes at a time. In the barrel, however, there are six RPC planes, therefore it has been examined the possibility of using all these planes in the trigger algorithm. In addition, it has been considered the option of inserting new additional planes. In the barrel the option consists of an extra double gap layer placed next to the innermost existing RPC plane, whereas in the endcap the extra layer has been placed next to the existing one in station ME2. Having more than four planes, one could in principle consider replacing 4-fold coincidences with 5, 6 or 7-fold ones, according to the actual number of planes available.
So far it was impossible to fit the logic for 4-fold patterns into any existing FPGA chip. This was achieved in an ASIC prototype implementing 0.35 $\mu$m technology. Anyway the chip covers $\sim 100$ mm$^2$ of silicon, which is near the technological limit. Therefore straightforward implementation of $>$ 4-fold patterns with full resolution looks a very challenging task.
In the following 4-fold coincidences with full resolution are used for momentum measurement. This is exactly what is done in the baseline algorithm. The additional planes, either the existing ones or eventually the new ones, are only used to confirm the decision of the baseline processors. Only 3/4 coincidences are required a confirmation. The 4/4 ones are accepted without any further requirement. Confirmation consists of requiring the presence of hits in one or more of the additional planes within the cone serviced by the given processor. The cone size is 32, 8, 24, 24 strips ($10^o$, $2.5^o$, $7.5^o$, $7.5^o$) in stations 1, 2, 3 and 4 respectively. This idea implies that the tested $>$ 4-fold patterns algorithms do not exploit the full resolution of the detectors. Therefore there could still be room for further improvements if ever full resolution algorithms proved to be feasible from the hardware point of view.
Possible improvements to the low-$p_t$ algorithm have also been investigated. In the baseline design this algorithm uses the four planes in the first two stations. The natural extension is to accept all 4/4 coincidences and confirm the 3/4 ones with the plane in MB3. This would however move the lowest triggerable $p_t$ from 4 to about 5 GeV/$c$. The use of a new extra plane in station MB1 for confirmation does not have this drawback.

All the results presented in this section have been obtained setting the RPC parameters to the following values:

- $\epsilon_{RPC} = 0.95$.

- $\sigma_{RPC} = 2.5$ ns.
- $cs = 1.5$ strips
- $noise_{RPC} = 50$ and 100 Hz cm$^{-2}$
- $ratefac = 3$
- $gatewidth = 20$ ns
- noise statistics = 500 000 events, i.e. 1 event = 80 Hz.
- statistics of muons = 5000 per tower, i.e. 85 000 $\mu$ in total. Only muons having $p_t = 100$ GeV/$c$ have been used to calculate the efficiency.

### 5.3.1 Results

For the purpose of this study the RPC system has been divided into six regions each containing trigger towers characterised by similar geometrical features. The regions are defined by the following sets of towers: 0-5, 6-7, 8, 9, 10-12 and 13-16. Each region has been optimised separately. The following conventions apply to all figures shown in the following. Efficiencies and rates have been calculated only for the options listed in the legend of each figure. If an option is listed in the given legend and the marker is not present then the corresponding rate is beyond the scale of the figure. Options involving extra RPC layers are indicated by the cross shape marker.
The study has concentrated on two main values of the $p_t$ threshold: 10 and 25 GeV/$c$, which correspond to the nominal threshold for the low and high luminosity scenarios.

#### Towers 0-5

Various options considered for towers 0-5 are illustrated in Fig. 5.5. The little squares corresponds to the six RPC layers available in these towers, the innermost one corresponding to the lowest square. Full squares indicate the planes in which a hit is required for the given option. The four planes connected to the trigger processors are the ones indicated by the full squares of the first option on the left which represents the 4/4 algorithm. As stated above, hits in the other planes are only used for confirmation of a 3/4 coincidence and they are requested to be within the cone serviced by the given processor. Going from left to right it is the 3/4 algorithm, the 4/4 and then the various 4/6 and 5/6 combinations considered. In order to optimize the trade off between efficiency and rate, one has to select combinations giving the highest efficiency and lowest rate. It can be seen in Fig. 5.5 that there are no large

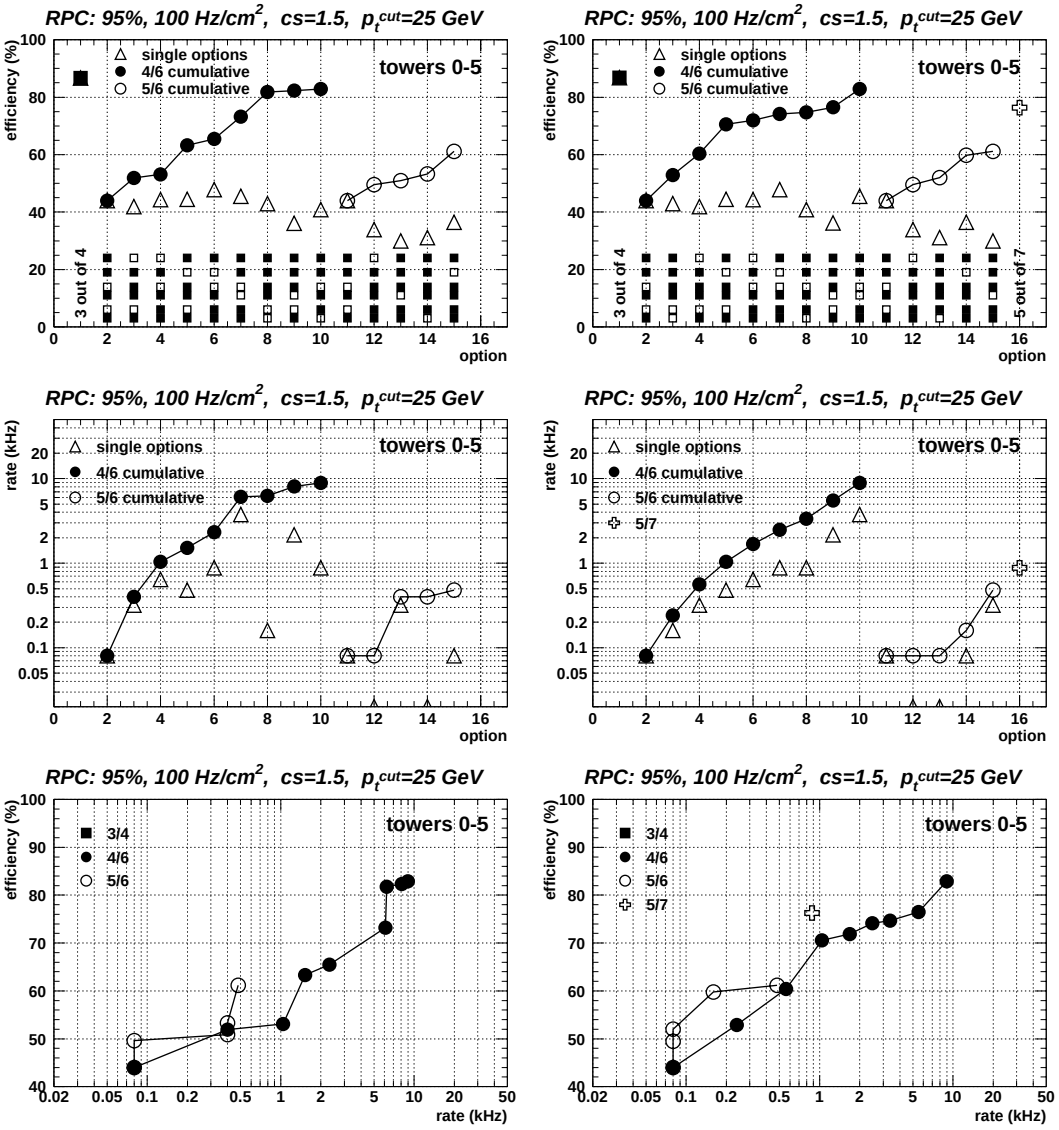


Figure 5.5: Trigger performance for different combinations of hits in RPC planes. Left column: non optimised order of combinations. Right column: combinations are ordered by the trigger rate.

differences in efficiency among the different options. On the contrary the various options have significantly different rates. Therefore the options have been reordered by rate. This is shown in the plots on the right in Fig. 5.5. The option involving a new RPC plane is indicated by the cross shape marker. Out of 7 planes, 4 are connected to the processor for the $p_t$ measurement and the remaining 3 are used for confirmation. The option denoted 5/7 then requires hits in 2 out of these 3 confirmation planes in addition to the usual positive answer from the 3/4 standard algorithm. The trigger performance in towers 0-5 for the two considered couple of $noise_{RPC}$ values and $p_t^{cut}$ are shown in Fig. 5.6.

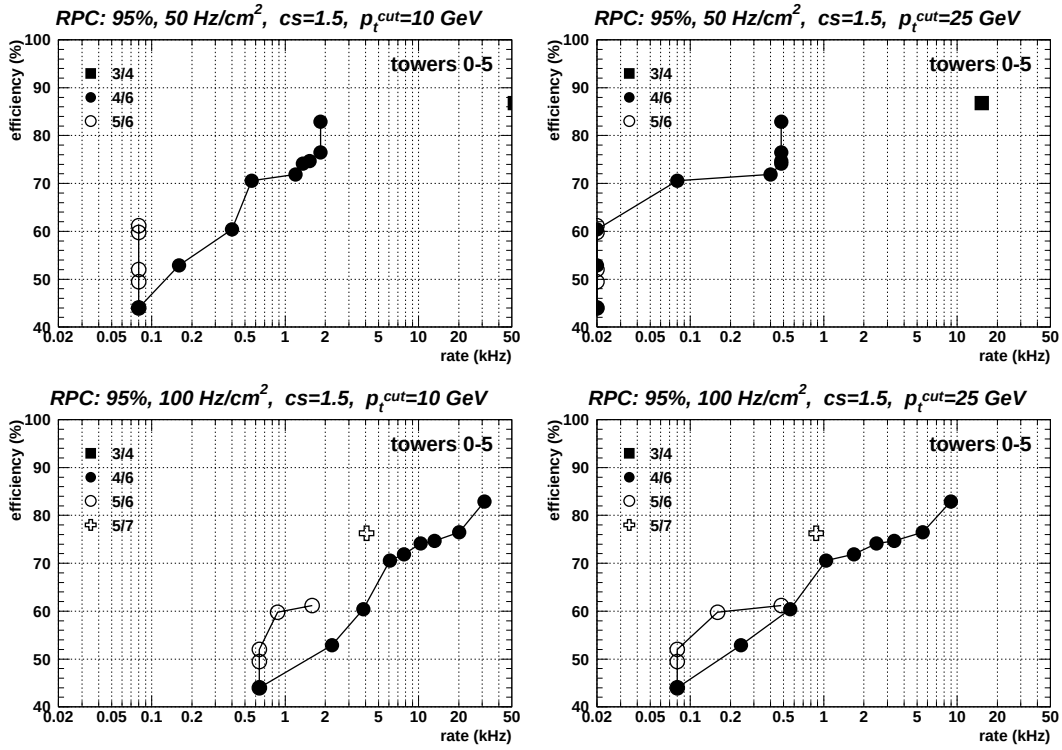


Figure 5.6: Trigger performance in towers 0-5 for various options.

### Towers 6-7

This region is beyond the coverage of MB4, therefore it contains only 5 RPC planes. The only possible extension of the current algorithm without new chambers is a 4/5 coincidence, which is indicated by a star in Fig. 5.7. That means that all patterns 4/4 are accepted, whereas 3/4 coincidences are required a confirmation from the plane that is not connected to

the processor. The option involving a new plane in the barrel, which was previously referred to as 5/7, now becomes actually a sort of 4/6. The 3/4 processor decision is confirmed by a hit in either of the two planes not connected to it. In Fig. 5.7 this option is still indicated with 5/7 to underline the use of an eventual extra plane.
It turns out that more restrictive 3/4 options do not allow significant rate reduction and at the same time the efficiency loss is quite relevant. On the other hand the 4/5 and 5/7 options looks promising from the point of view of rate reduction but the price to pay in efficiency is about 10%. The extra plane, in this case seems not to help a lot.

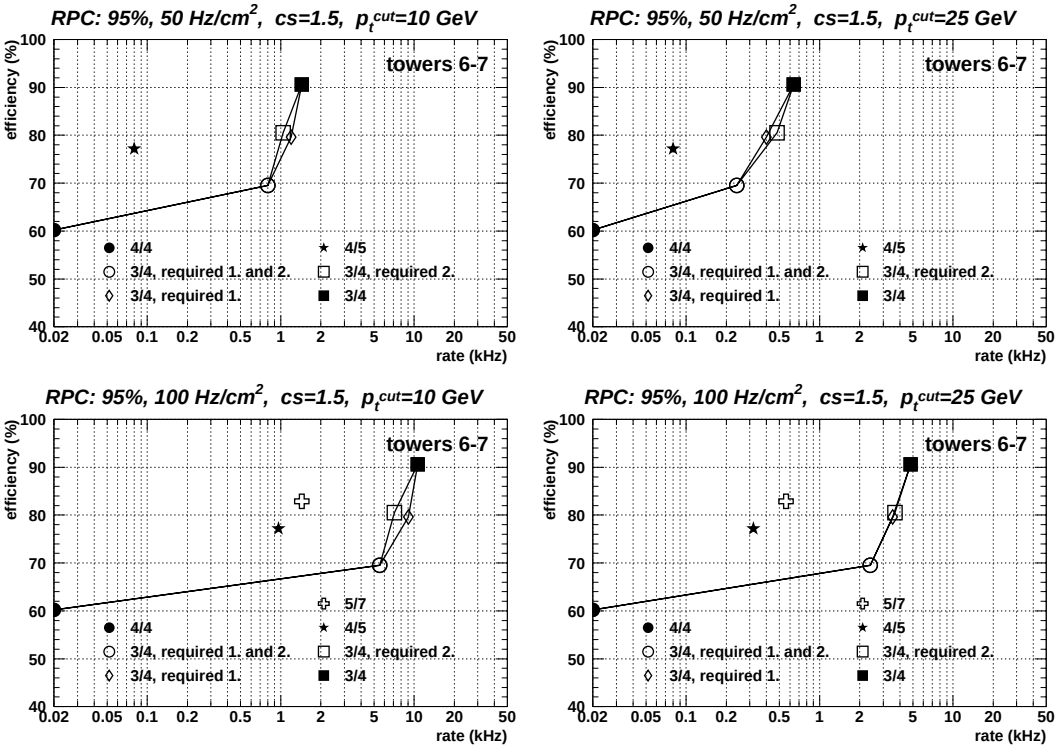


Figure 5.7: Trigger performance in towers 6-7 for various options.

### Tower 8

Tower 8 sees only four RPC planes. Thus, there is no possibility to add a new plane in the current geometry. Installing a new chamber in MB1 would enable to run a 4/5 algorithm. Again, in this simulation it has been assumed that 3/4 patterns have to be confirmed by a hit in the additional plane MB1 within the processor cone. The results are shown in

Fig. 5.8. It turns out that in this tower too, more restrictive 3/4 algorithms do not help a lot. On the contrary an additional plane would reduce the false trigger rate by more than an order of magnitude and leave the efficiency almost unchanged.

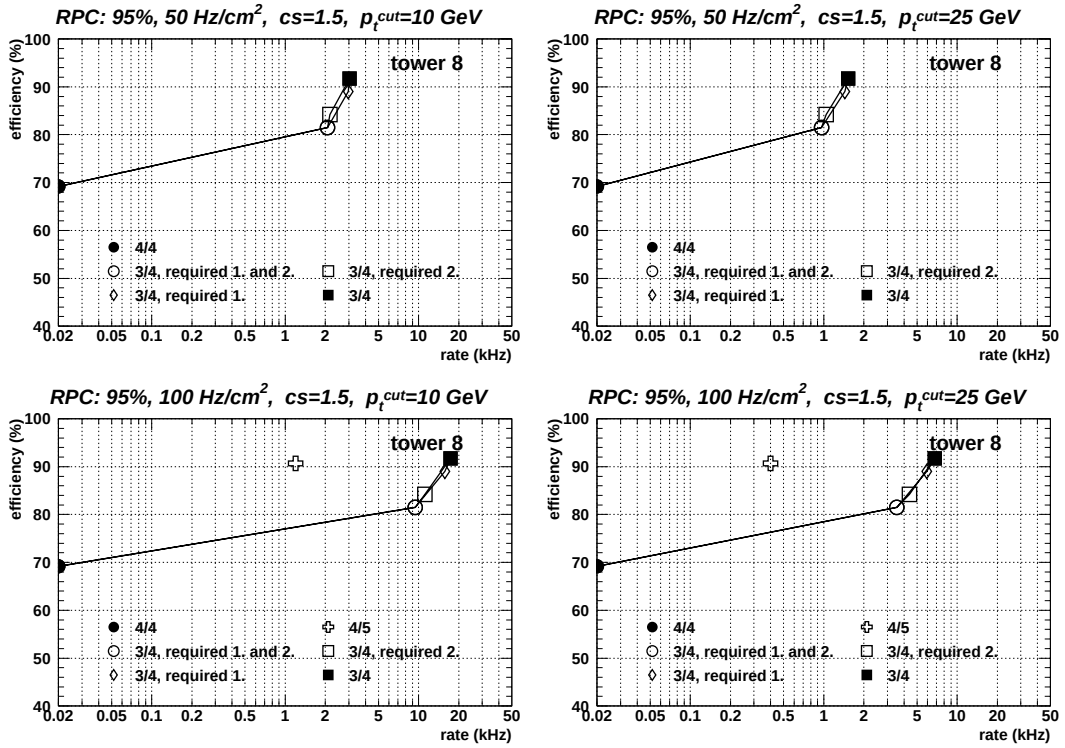


Figure 5.8: Trigger performance in tower 8 for various options.

### Tower 9

This tower is by far the worst. Only three detector planes are available. As it has been explained in detail above, the standard algorithm is actually a 3/3 one. The 3/4 algorithm would result in an extremely high rate as reported in Fig. 5.3. The extra plane in the barrel or in the endcap would enable a 4/4 algorithm, which, as shown in Fig. 5.9, would reduce the rate by an order of magnitude and cause a small efficiency reduction.

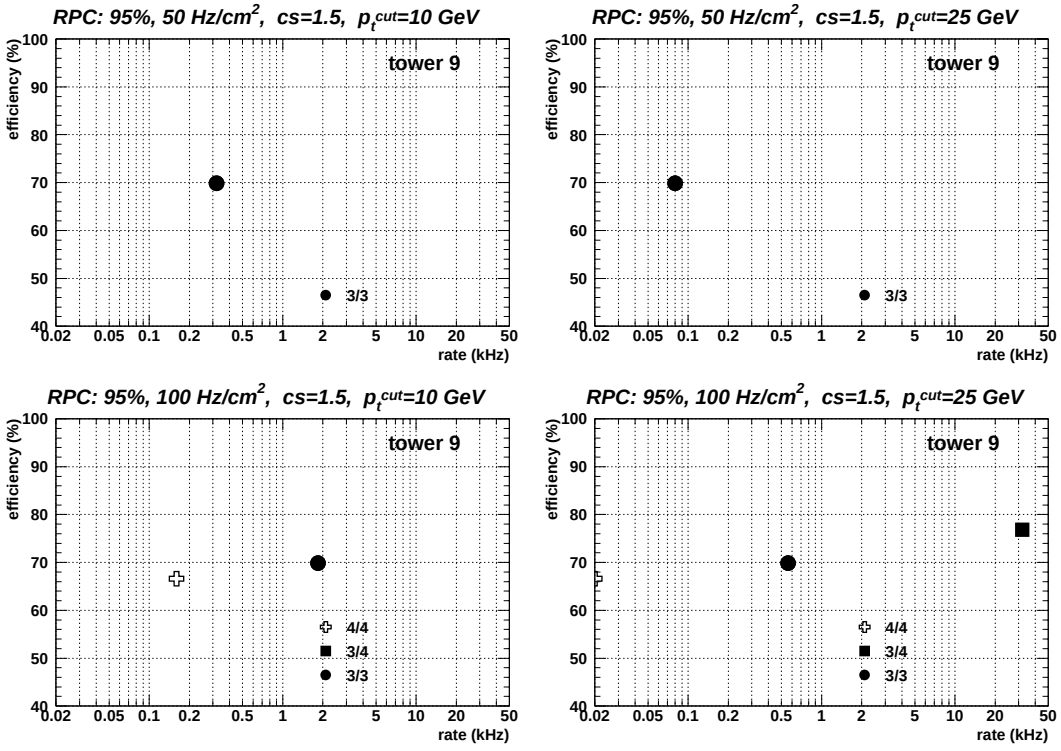


Figure 5.9: Trigger performance in tower 9 for various options.

**Towers 10-12**

These towers are entirely in the endcap and in the current geometry they contain only 4 RPC planes. Therefore the situation is similar to that of tower 8. A new extra endcap plane would enable a 4/5 algorithm, otherwise one can choose between various 3/4 combinations. The results are shown in Fig. 5.10. The 4/5 option leads to a significant efficiency drop.
A major difficulty in this region is related to real muons. About half of the trigger rate due to real muons comes just from this region (see Fig. 4.12). This is caused by low momentum resolution in this region due to the configuration of the magnetic field and to the poor geometrical coverage of ME1/2. The chambers in these stations do not overlap in $\varphi$ . The dead area between two adjacent sensitive areas is $\sim 7$ cm. This is repeated every $10^o$. If a muon misses this station then the $p_t$ measurement will be extremely difficult. This can be seen in Fig. 5.11, in which the track bending between ME1 and ME2 is plotted against the bending between ME2 and ME3. A measurement with ME1 and ME2 gives good $p_t$ estimates, whereas one based on ME2 and ME3 can hardly distinguish different momenta. For this reason it is important to look more carefully into the geometrical design of that region to explore possible ways of improving the coverage.

**Towers 13-16**

This region is very similar to the previous one, except that the $p_t$ measurement is better because of good ME1/1 geometrical coverage. The results shown in Fig. 5.12 indicate the usefulness of an extra endcap plane.

**Overall trigger performance**

In order to summarise the results of the optimisation described above two options for each region have been selected. One option called "loose cuts" was chosen requiring that the efficiency should be at least 80%. The second option called "tight cuts" has been tuned optimising the rate by requesting that the rate per region at $p_t^{cut} = 25$ GeV/$c$ should not exceed much 1 kHz. These two options, available with the baseline RPC geometry, are compared to options available with the additional planes: a fifth plane in the endcap and a seventh plane in the barrel. The results are shown in Fig. 5.13. It can be seen that an additional plane in the endcap would significantly improve the performance of the trigger. The gain introduced by the extra barrel layer is much smaller.
The effect of the RPC efficiency and noise on these results is presented in Fig. 5.14. Each option is represented as a rectangle indicating the range of trigger efficiency and false trigger rate values corresponding to the $\epsilon_{RPC}$ range 95-98% and the $noise_{RPC}$ range 50-100 Hz

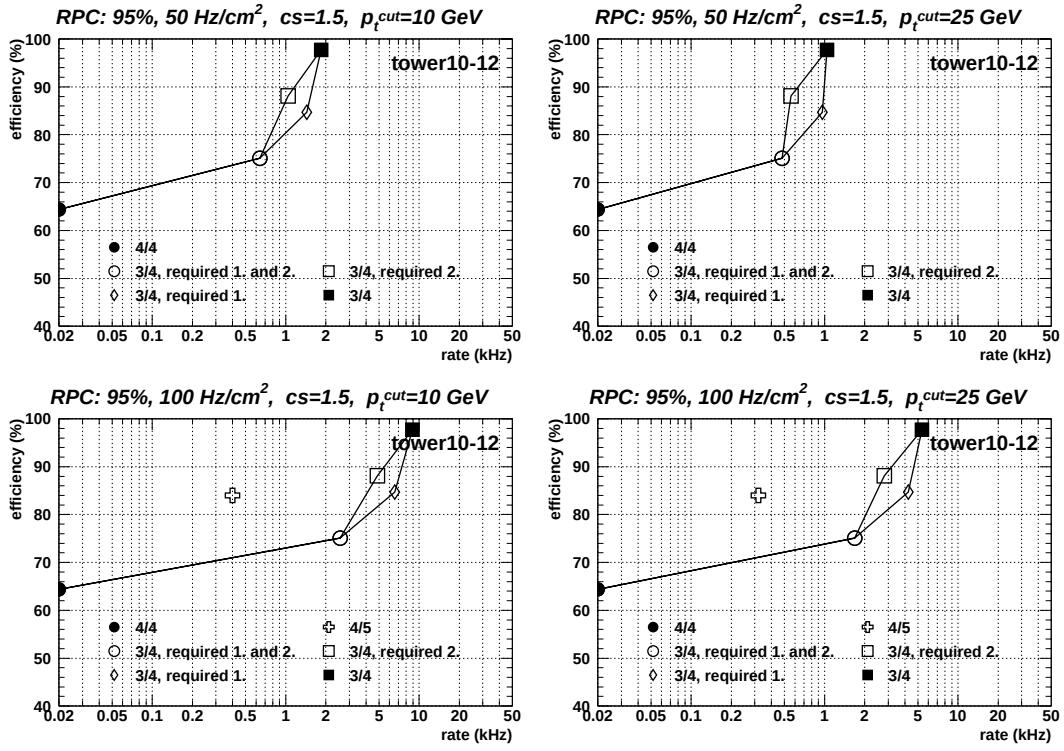


Figure 5.10: Trigger performance in towers 10-12 for various options.

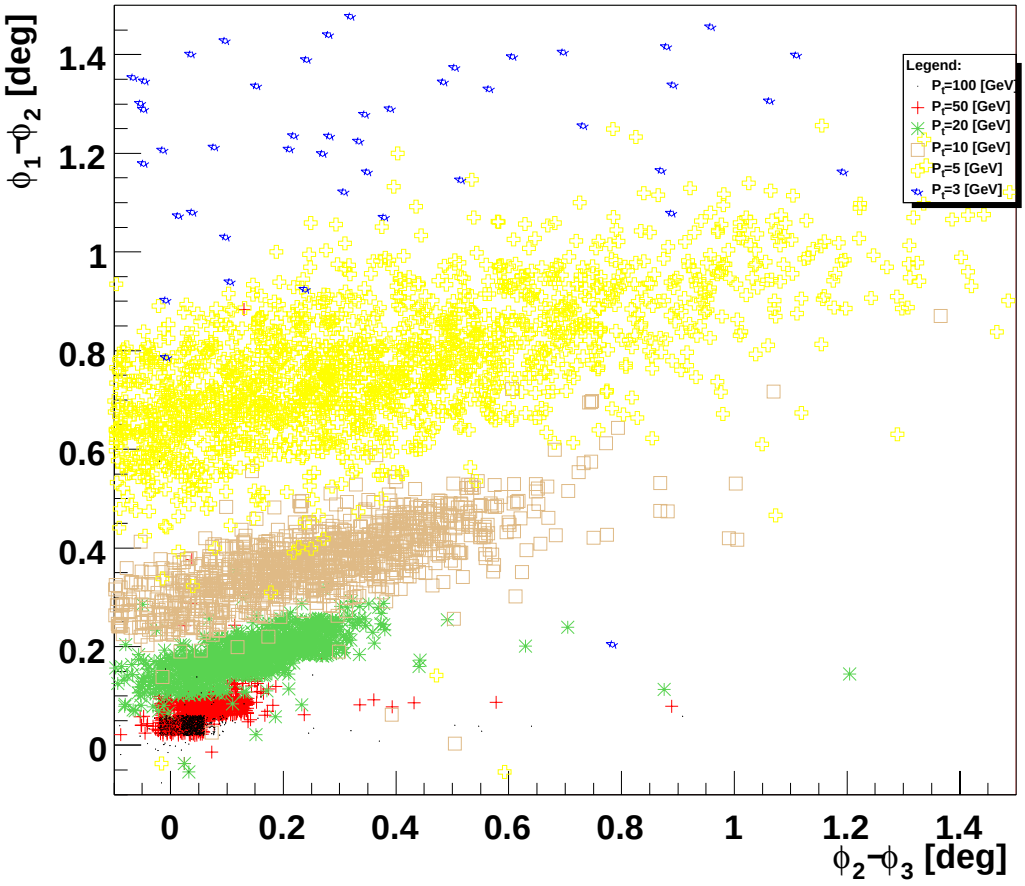


Figure 5.11: Track bending between ME1 and ME2 versus bending between ME2 and ME3 for muons of various $p_t$.

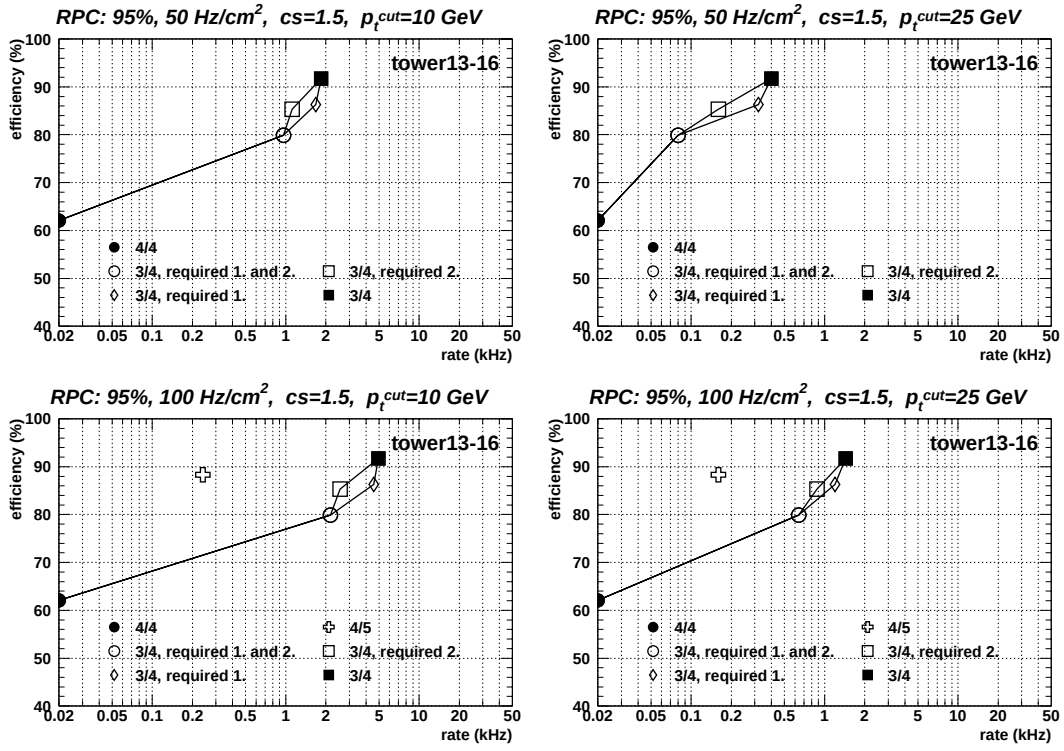


Figure 5.12: Trigger performance in tower 13-16 for various options.

$cm^{-2}$. As expected, the trigger rate depends very strongly on $noise_{RPC}$. A salient feature of Fig. 5.14 is the higher sensitivity to the RPC efficiency as the number of planes on which the algorithm is based increases.
The false trigger rate dependence on $noise_{RPC}$ is better shown in Fig. 5.15. The curves are calculated analytically whereas the points are the results of the detailed simulation described above. The hatched areas on the plot indicate safety margins which could be obtained by reducing the RPC noise or by adding a seventh plane. It is important to note that even from the rate point of view, the higher the number of planes the more sensitive the trigger is. This is evident if one compares the slopes of the curves corresponding to the 4/6 and 5/7 algorithms. It must be recalled that from the point of view of the hardware implementation a 4/6 full resolution algorithm has more chances to be feasible than a full resolution 5/7, which looks prohibitive due to the extremely high number of possible patterns to be stored in the processor memory. Moreover a full resolution 4/6 algorithm would further reduce the rate with respect to the values that have been reported above. Thus it would be envisageable to push toward a full resolution 4/6 algorithm rather than inserting an additional seventh plane in the barrel. On the other hand, as it has already been underlined, an additional plane in the endcap would be of great help.

## 5.4 Conclusions

The results presented in this chapter indicate that the RPC trigger performance can be largely improved. The extreme solution of oiling the chambers could be avoided if one succeeds in implementing a full resolution 4/6 algorithm in the barrel. In the endcap, where the false triggers are anyway less frequent, an additional detector layer would be extremely useful and could be enough to provide a robust system. Of course the final decision on the strategy to adopt can only be made when aging effects due to oil will be established. However it seems obvious that oiling the chambers is less dangerous in the barrel than it is in the endcap as a consequence of the much more severe radiation fluxes and detection rates expected in this latter region.

The GMT has been proved to represent an additional powerful shield against false triggers delivered by the RPC trigger. At the price of a negligible efficiency loss, the false trigger rate can be kept at acceptable levels even with the baseline system. However this must be considered the very last option as one does not want to make use of the redundancy of the muon system as a starting point.

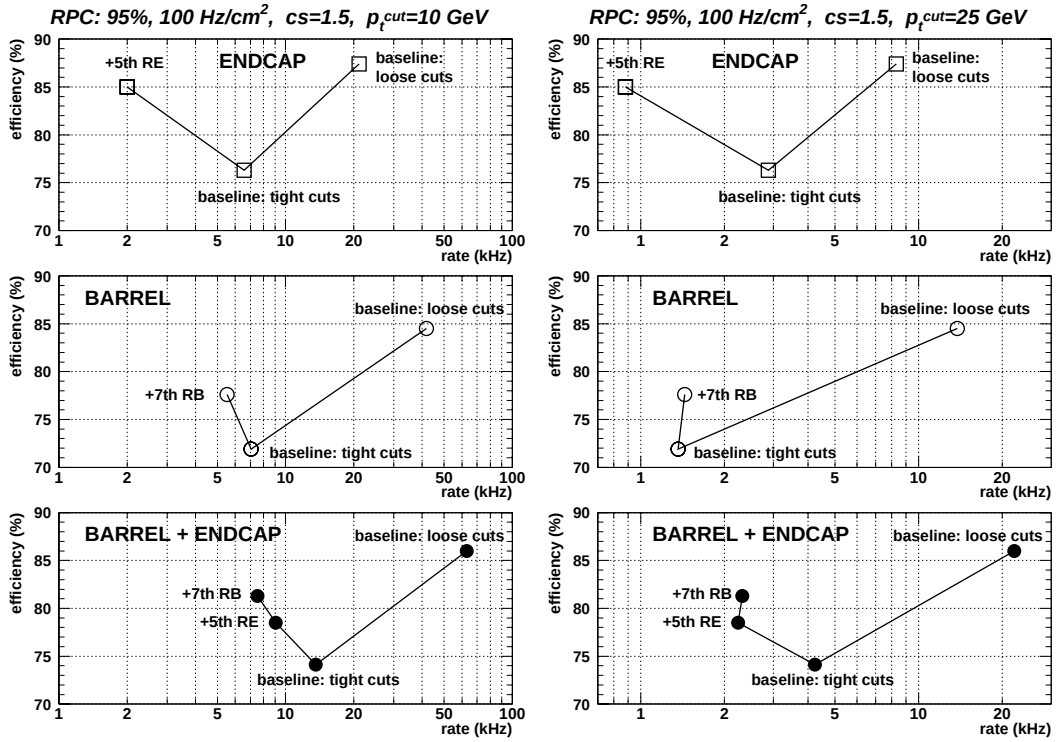


Figure 5.13: RPC trigger performance for selected options, as described in the text.

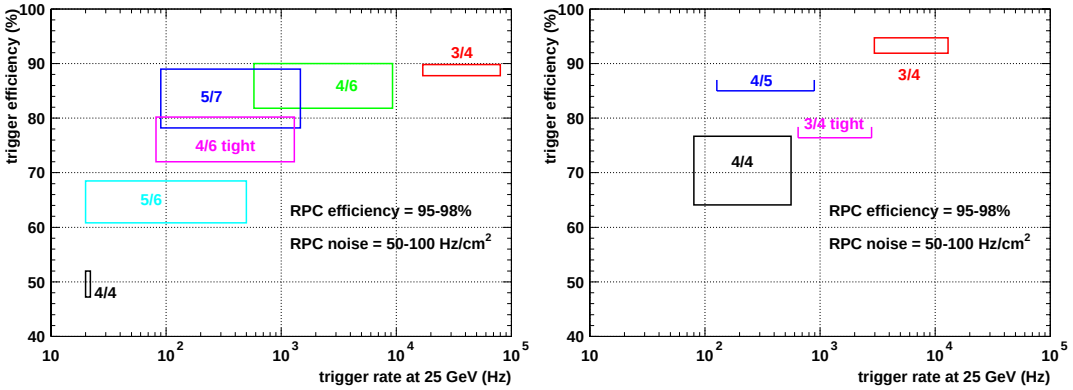


Figure 5.14: RPC trigger performance in the barrel towers 0-7 (left plot) and in the endcap towers 8-16 (right plot) for various options.

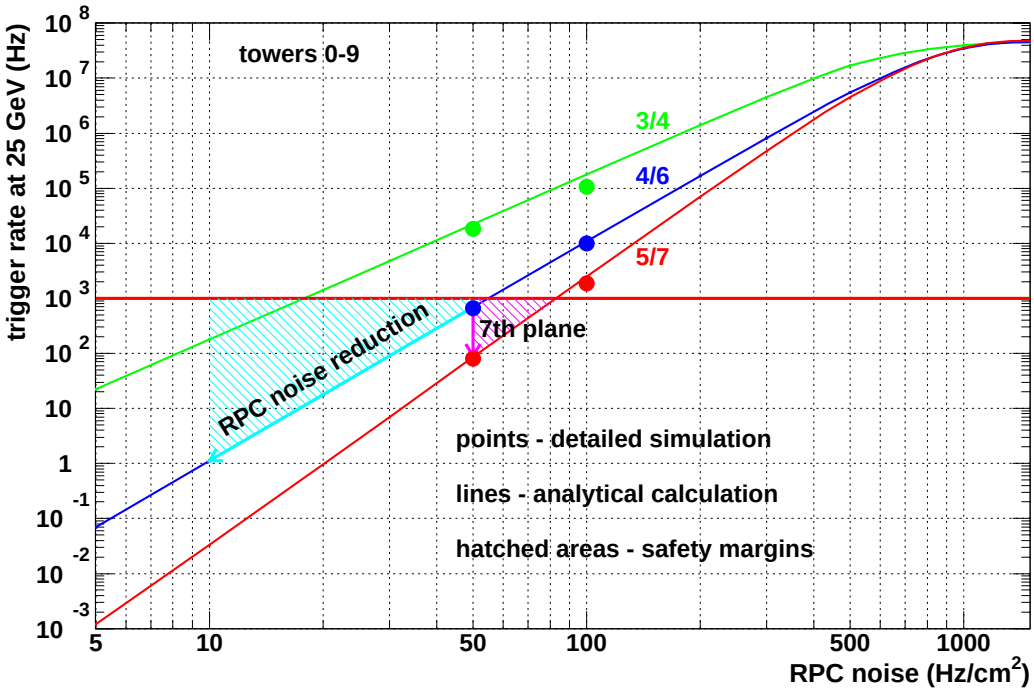


Figure 5.15: RPC false trigger rate as a function of the RPC noise.

# Chapter 6

# The High Level Trigger and the signal selection efficiency

## 6.1 Introduction

As it has been explained in chapter 2, the CMS High Level Trigger (HLT) works on the events selected by the L1 trigger and has to reduce the event rate from a maximum L1 output of 25 kHz to 100 Hz. The CMS HLT is entirely software implemented and therefore it is extremely flexible.
In this chapter, only the algorithms related to muon identification and reconstruction will be discussed.
Although the HLT can in fact consists of several filters, in what follows L2 will be called the first HLT trigger filter in which muon reconstruction is performed without the inner tracker information and L3 the following and final HLT filter accomplished by using the full detector data, which in the case of muon tracks consists of the muon system and inner tracker information.

The goal of the L2 trigger is to reduce by about an order of magnitude the L1 output rate on single objects by applying the same thresholds used at L1. This is expected to be possible due to the better momentum resolution that can be achieved at L2. Indeed, the $p_t$ distribution of the muons produced in the LHC collisions decreases exponentially (see Fig. 1.13) and for this reason the largest fraction of muons passing the L1 selection is represented by mismeasured low $p_t$ muons.
In chapter 2 it has been explained that at L1 it is not possible to exploit the full resolution of the muon detectors. The time resolution of the L1 DT trigger electronics is worse than the time resolution of the DAQ Time to Digital Converters whose information is used for

the HLT reconstruction. Also the method used in the CSC L1 local trigger is a simplified one. It allows to achieve only half a strip space resolution which is far from the $\sim 100$ $\mu$m that could be achieved by using the full charge information (see section 1.3.6). The latter is available and fully used at L2.
In addition to a non optimal local reconstruction, the L1 $p_t$ assignment is not the optimal one too. Indeed it is not obtained through a global fit to all measured points or segments but by matching the observed patterns with a set of predefined ones stored in look-up tables. Moreover the $p_t$ estimation is strongly biased due to the 90% threshold efficiency requirement.
Finally, at L3, use of the inner tracker data should allow to improve significantly the momentum resolution for muons with $p_t$ below 100 GeV/c.

In the following the algorithms for muon reconstruction adopted at L2 and L3 are described and their performance is presented. Then the selection efficiency for some representative signal samples is analysed in the last section.

## 6.2 Muon system stand-alone reconstruction

In general reconstruction is the data reduction process that produces the information relevant to the final physics analysis starting from what has been registered by the data acquisition system. Independently of the type of detector involved, it is possible to distinguish two different phases:

- **Local reconstruction**: this is accomplished at the level of single detector. It results in the production of what are called reconstructed hits (RHIT). The RHIT format depends on the type of detector under consideration. In the case of the muon chambers a RHIT can be a point or a segment in space with its errors.

- **Global reconstruction**: the objects produced in this phase are physics objects: tracks, vertexes, jets, etc. In general anything which is used for the physics analyses. Global reconstruction is not necessarily connected to only one type of detector.

### 6.2.1 Local reconstruction in the muon chambers

In both DT and CSC chambers the result of local reconstruction are track segments.
The drift velocity in the CMS DT is about 60 $\mu$m/ns. The distances from the wires in the various tubes are obtained starting from the times stored in Time to Digital Converters

(TDC)[1]. A straight line is fitted to the possible distances that depend on the unknown bunch crossing that generated the readout of the TDCs. Indeed signals related to at least 20 bunch crossings are stored at any time in the TDC). A successful fit returns both the bunch crossing and the actual drift times, i.e. distances. This is the principle of the meantimer technique [32] and is the same as that used at L1, with the difference that at L1 the signals are considered for possible alignment only every 12.5 ns, which therefore represents the time (space) resolution used at L1, and no parametrisation is used. The Drift Tube time resolution will not be worse than 4 ns and so is the TDC resolution. Every DT produces in each SL 2-dimensional segments characterised by a position along the direction orthogonal to the wires and an angle. The points used to make up the segments in the 2 $\varphi$-SL are then used to fit a longer lever arm segment. Finally segments in both views are matched to obtain a 3-dimensional segment characterised by two angles and two coordinates. If the matching is not successful only $\varphi$ segments are accepted for use in the global reconstruction. The CSC segments are always 3-dimensional since the crossing point is measured in both directions in each detector layer. The coordinate measured by the wires is rather imprecise because wires are read out in bunches of 5 to 16 of them. For what concerns the strips, first those strips with the largest charge are considered in each layer and then each of them with the corresponding four adjacent ones are used in the fit to the charge distribution that gives the position with high precision.
The average space resolutions on the measured points in the single layers are the following:

- Barrel
  - $\varphi$ view: 0.03 cm
  - $\theta$ view: 0.03 cm
- Endcap
  - strip coordinate: 0.0125 cm (ME1/1), 0.02 cm (ME1/2-3), 0.0234 cm (ME2-3-4/1), 0.0216 cm (ME2-3-4/2).
  - wire coordinate: 0.5-2.5 cm

[1] In the absence of magnetic field in the cells, the drift velocity is practically constant. Even small magnetic fields can result in a distortion of the electric drift field. Moreover the drift time depends significantly on the particle incident angle. Therefore at digitization level the distance from the wire is computed with a parametrisation that depends upon the radial and axial components of the magnetic field. This parametrisation has been obtained with a simulation based on the GARFIELD package [65]. However the present reconstruction code is higly simplified and assumes linear space-time relation with a constant value for the drift velocity

In the RPCs the result of local reconstruction are points in the plane of the detector. First a clustering procedure starting from all strips that carry signals is performed. The procedure consists of grouping all adjacent fired strips. Once all groups are formed, the reconstructed point is nothing but the "center of gravity" of the area covered by the cluster of strips. In the barrel, where strips are rectangular, it is simply the center of a rectangle. In the endcap, the computation is more complicated as the area covered by the clusters are trapezia of variable shape. The assumption here is that each group of strips is fired as a result of a single particle crossing and that this crossing can have taken place anywhere with flat probability over the area covered by the strips of the cluster. Errors are computed under the same assumption of flat probability. Therefore in the barrel they read simply $\sigma_i = L_i/\sqrt{(12)}$ $(i = 1, 2)$, where $L_i$ is the length of the $i^{th}$ side of the rectangle. In the endcap the expression is more complex.
It is necessary to comment on the assumption of flat probability. On one hand this assumption is too loose because, as it has been explained in section 4.3.2, there is a correlation between the central strip of a cluster and the actual crossing point of the particle that originates the cluster. On the other hand, muons can be accompanied by secondaries which can extend the cluster created by the muon hit in one or the other direction. Therefore the flat probability assumption is a sort of compromise which is of course subject to optimisation.

### 6.2.2 Global reconstruction in the muon chambers

The task of the muon global reconstruction is to identify muons, reconstruct their track and measure their momentum.
The reconstruction algorithm starts from a *seed*, which is the state vector (position and momentum) of a candidate muon at some point of the muon system. Then it tries to build up a trajectory collecting the RHITs that are compatible with the seed. The seed can be provided externally, using the L1 measurement, or internally if one builds it from the track segments of the wire chambers resulting from the local reconstruction. External seeding, being faster from a computational point of view, is particularly suitable for L2 purposes.
In more detail muon reconstruction consists of the following phases:

- *seeding:* for the purpose of L2, external seeding is used. Each muon found at L1 is used to produce a seed. The position of the muons at L1 are given at the second station, i.e. MB2 or ME2, however to start the reconstruction process the states are extrapolated before the first station. For this extrapolation and for all others described in the following, the GEANE package [34] is used to estimate the energy

loss in the material and the multiple scattering undergone by the muon. In this way the extrapolated position, direction and their errors are correctly computed.

- *pattern recognition:* RHITs are first collected proceeding outward. A RHIT is accepted on the basis of position (and eventually direction) compatibility between the state extrapolated on the surface of the detector where the RHIT is present and the RHIT itself. Every time a RHIT is accepted, it is combined with the previous ones using the Kalman filter [66] in order to update the state. To improve the direction measurement in the CSC, the single points that make up the segments are used in the fit. The improvement achievable with this procedure is expected to be less important in the DT where the magnetic field, which tends to make the particle trajectory deviate from a line, is much lower.

- *re-fit:* once a preliminary trajectory has been constructed exploring all the available chambers, the track is re-fitted starting from the outermost layer and going inward. This time the adopted $\chi^2$ cut is stricter. A minimum of two RHITs is required to make up a trajectory. No trajectory made out of just RPC RHITs is allowed. Regardless of the $\chi^2$ of the fit, priority is given to trajectories with two RHITs (segments) from wire chambers and then to those with only one wire chamber RHIT (segment).

- *vertex extrapolation:* the updated state in the innermost station is extrapolated to the point of minimum distance from the interaction vertex in order to have a measurement of the muon at its production.

- *vertex fit:* the nominal interaction point with its uncertainties is finally used in the fit. If the fit is successful, the state at the vertex is assumed to be the best estimate of the muon measurement.

- *trajectory filter:* a final filter on the found trajectories is applied in order to eliminate ghost trajectories.

All the results presented in this chapter have been obtained with the simulation tools described in section 4.3 except for the fact that digitization, simulation of the trigger algorithm and implementation of the reconstruction algorithms have been accomplished with the ORCA 5 program [35].

### 6.2.3 L2 muon trigger performance

In this section results on muon reconstruction performance using only the information of the muon detectors are presented.

Whenever RPCs are used it has been assumed for them efficiency of 95%, Gaussian time resolution of 2.7 ns and average cluster size of about 2 strips (corresponding to the parameter $cs = 1.5$, see sect. 3.2 in chapter 4) but neither intrinsic noise nor spurious hits due to the neutral particle background have been added. This choice has been dictated by the fact that these are the first results in which it has been made use of RPCs in the reconstruction. The aim of this study is to estimate the potential usefulness of RPCs even at the level of reconstruction. Once it is proved they can be of help, spurious hits will be included and their impact on the L2 performance will be studied. At that point the reconstruction algorithms will perhaps have to be refined in order to cope with intrinsic noise and neutral background hits.
The impact of spurious hits is however expected to be much less important at L2 than it is at L1. This point is discussed in more detail at the end of this section.

The L2 $p_t$ measurement, in case of successful fit, is defined in the following way:

1. $p_t$ of the fitted track at the interaction point with vertex constraint, or if it fails:
2. $p_t$ of the fitted track extrapolated at the point of minimum distance from the interaction vertex without vertex constraint, or if the extrapolation fails:
3. $p_t$ of the fitted track at the innermost muon station.

The L2 reconstruction efficiency has been studied using SAMPLE 0 (see section 2.3.1). The result is shown in Fig. 6.1 as a function of $\eta$. The L1 trigger efficiency is also shown and refers to the GMT as defined in chapter 2. Two cases are considered: the first (left plot) is reconstruction at L2 without RPC RHITs, the second (right plot) is reconstruction at L2 with RPC RHITs. It is evident the improvement achieved in the overlap region when information from all muon detectors is used. The dependence on $p_t$ of the reconstruction efficiency is shown in Fig. 6.2. Again in the left plot RPCs are not used at L2, while they are used in the result shown in the right plot.
The efficiency completion achieved by means of use of RPC information is not accompanied by a degradation of the $1/p_t$ resolution. This can be seen in Figs. 6.3 and 6.4 which show the $1/p_t$ resolution at L2 without RPCs and with RPCs respectively. The variable $(1/p_t^{rec} - 1/p_t^{gen})/1/p_t^{gen}$ is plotted separately for the barrel ($|\eta| < 0.8$, left plot), overlap ($0.8 < |\eta| < 1.2$, middle plot) and endcap ($1.2 < |\eta| < 2.4$, right plot). The corresponding values of the sigmas of the Gaussian fits are in both cases: 10.5%, 17.2% and 19.3%. In these plots, only the events for which the vertex constraint is successful are considered.
The $\varphi$ and $\theta$ resolutions are also not spoiled when RPCs are brought in. The $\varphi$ residual distribution ($\varphi^{rec} - \varphi^{gen}$) at L2 with (right) and without (left) RPCs are shown in Fig. 6.5.

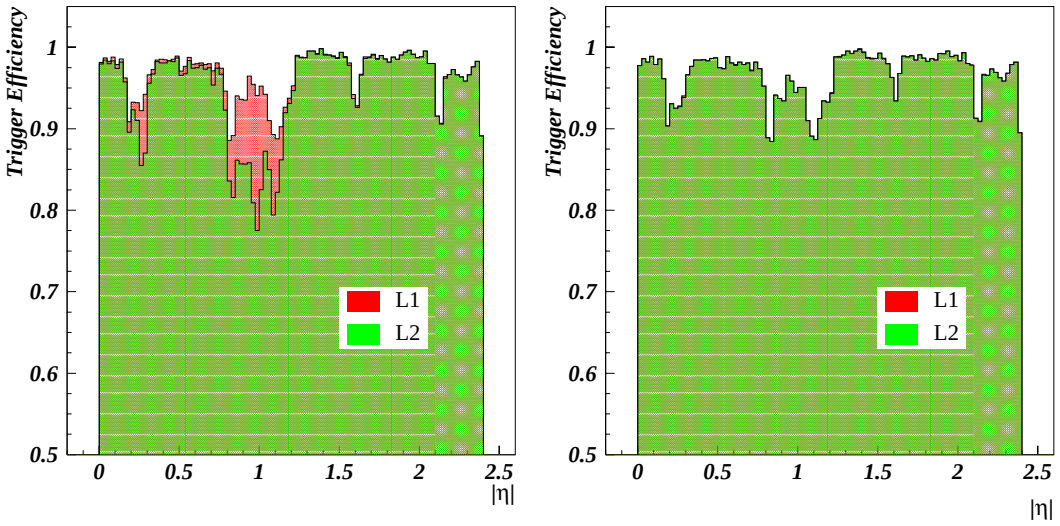


Figure 6.1: L1 and L2 muon reconstruction efficiency as a function of the $\eta$ of the muon at generation. In the left plot RPC information is not included at L2. In the right plot RPC information is included at L2.

The same distributions for $\theta$ are shown in Fig. 6.6.

The pull, defined as $(X^{rec} - X^{gen})/\sigma(X^{rec})$, distributions for the variables $1/p_t$, $\varphi$ and $\theta$ are shown in Fig. 6.7. They refer to the case in which RPC information is used. From the values of the sigmas of the Gaussian fits it turns out that errors are not well estimated in the muon detectors and need to be revisited. No difference is observed in the pull distributions obtained without RPC information.

The L2 (RPCs are used) single muon rate computed with SAMPLE 1 (see chapter 2) is shown in Fig. 6.8. The L1 trigger rate (GMT) and the rate at generation level are reported too. It is remarkable to note that the L2 is able to reduce the L1 output rate by almost one order of magnitude already at $p_t^{cut} = 10$ GeV/$c$. A comparison between the L2 trigger rate with and without RPCs is shown in Fig. 6.9. Only the muons generated up to $p_t = 10$ GeV/$c$ are considered in Fig. 6.9. The contribution of the rest of the spectrum is not expected to affect significantly this scenario. It is evident that the events recovered with the help of RPC information do not dramatically affect the output rate.

An important conclusion that can be drawn at this point is the potential usefulness of the RPC detectors also at the level of track reconstruction: their use at L2 allows to achieve full efficiency with respect to the L1 output. At the same time no relevant rate increase is

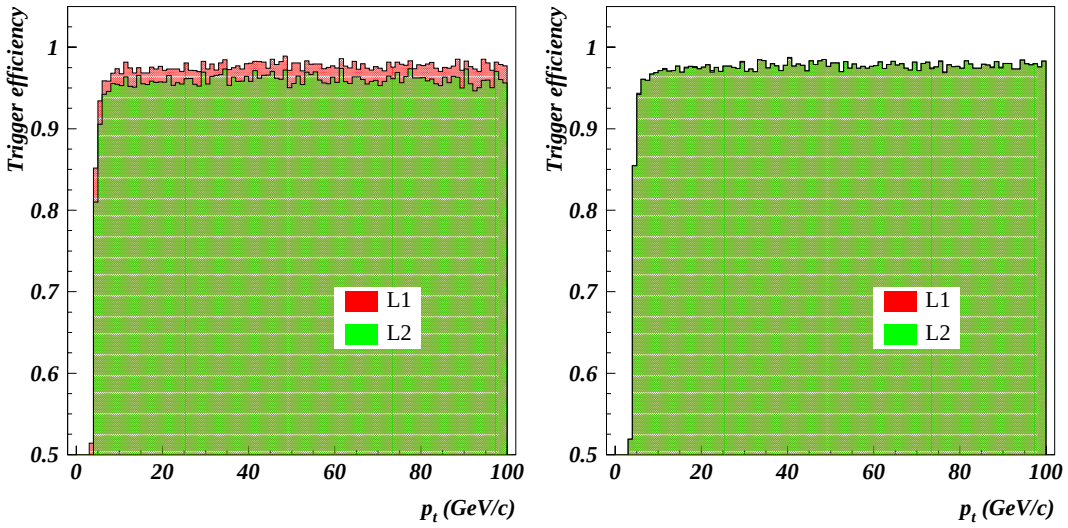


Figure 6.2: L1 and L2 reconstruction efficiency as a function of the muon $p_t$ at generation. In the left plot RPC information is not included at L2. In the right plot RPC information is included at L2.

observed.

It must be underlined that all the results involving use of RPCs that have been presented in this section are preliminary because neither intrinsic noise nor neutral background hits were included. These spurious hits may in fact disturb track reconstruction or even fake muon tracks exactly as they do at L1. Nevertheless several points in favour of L2 exist. First it must be noted that the L2 looks for muons only in the regions where the L1 trigger has found muons. Moreover one must not forget that the L2 operates just on the L1 output rate and its task is to reduce by only one order of magnitude the L1 output rate. On the other hand the L1 RPC trigger operates on the input rate of 40 MHz and has to reduce it by more than three order of magnitudes. In the L1 case it has been shown that even the small probability of $10^{-3}$ (see Fig. 4.11) of creating a false coincidence has dramatic effects on the performance of the system. On the contrary if the probability is proved to be of the same order at L2, it will be more than acceptable. In addition, at L2 one has the advantage of treating DT, CSC and RPC information at the same time.

For all these reasons it is reasonable to believe that the effect of spurious hits on the L2 performance should not be as dramatic as it is at L1. On the contrary one has to try to draw maximum benefit from use of RPCs in track reconstruction.

Once RPC noise and background hits are included, it is likely that the L2 reconstruction

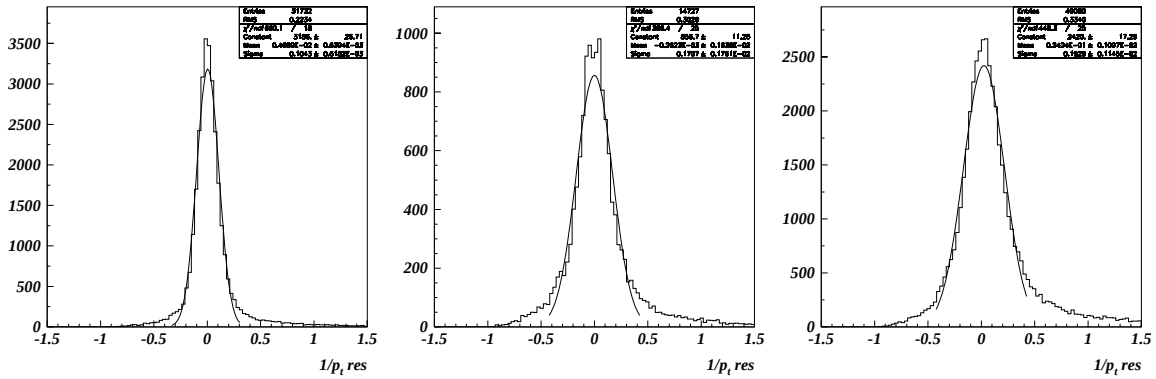


Figure 6.3: $1/p_t$ resolution at L2 without use of RPC information. The variable $(1/p_t^{rec} - 1/p_t^{gen})/1/p_t^{gen}$ is plotted separately in the barrel ($|\eta| < 0.8$, left), overlap($0.8 < |\eta| < 1.2$, middle) and endcap ($1.2 < |\eta| < 2.4$, right).

algorithm will have to be modified to preserve as much as possible the performance that has been presented in this section. It should also be noted that already in the algorithm adopted here no track was allowed to be reconstructed with just RPC RHITs.
In what follows the L2 muon trigger performance is assumed to be the one achievable with use of RPCs that has been presented in this section.

## 6.3 Muon system and inner tracker combined reconstruction

### 6.3.1 Muon reconstruction

After the L2 filter tracker information becomes available. The reconstruction algorithm that is described here does not pretend to be the optimal one and it must be underlined that large improvements are likely to be achieved.

At L3 a seed consists of a measurement in a tracker detector and a state vector on the plane of the detector that gives the measurement. The muon trajectories reconstructed at L2 are extrapolated to the outermost tracker layer where measurements are searched. A seed is created on the base of $\chi^2$ compatibility between the extrapolated point and the measured one. A multiplicative factor on the errors of the extrapolated state can be applied in order to augment the probability of finding the correct measurements. A factor 2 has been used. More layers can be used for this initial seed search. The higher the number, the higher the reconstruction efficiency but the higher the possibility of reconstructing a wrong

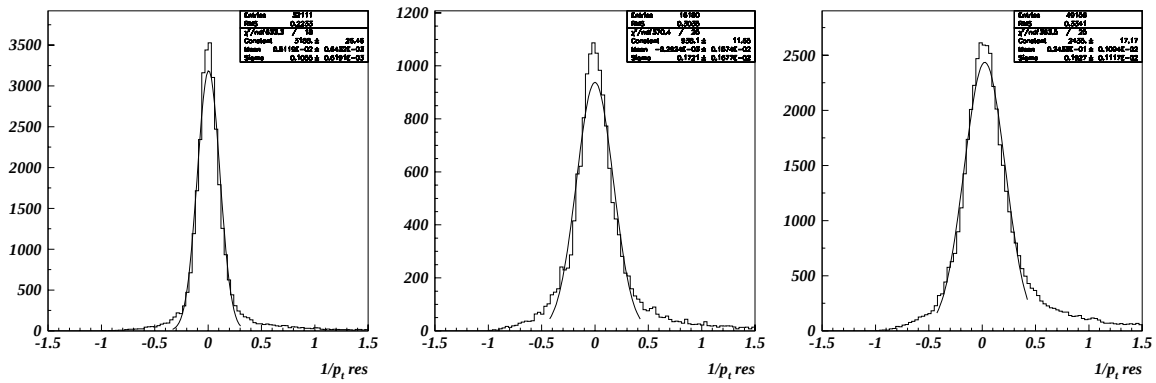


Figure 6.4: $1/p_t$ resolution at L2 with use of RPC information. The variable $(1/p_t^{rec} - 1/p_t^{gen})/1/p_t^{gen}$ is plotted separately in the barrel ($|\eta| < 0.8$, left), overlap($0.8 < |\eta| < 1.2$, middle) and endcap ($1.2 < |\eta| < 2.4$, right). The corresponding values of the sigmas ofthe Gaussian fits are: 10.5%, 17.2% and 19.3%

track. The three outermost tracker layers have been used.
For each seed the algorithm attempts to build a trajectory using the Kalman filter. Going to a new layer more than one compatible RHIT can be found. In this case the algorithm grows the possible trajectories in parallel. However, to avoid a combinatorial explosion, a maximum of 30 trajectories after each layer are allowed. The selection of the best trajectories is based on the best $\chi^2$.
The successfully built trajectories are then 'cleaned': for each pair of trajectories that share more than half of the RHITs owned by any of the two, the trajectory having less RHITs is rejected.
The final muon identification is performed by requiring that, at the interaction vertex, the direction of the L3 state is contained in the cone defined by the direction of the L2 state within its errors.

### 6.3.2 L3 muon trigger performance

The reconstruction efficiency at L3 as a function of $\eta$ and $p_t$ are shown in Fig. 6.10. The L1 and L2 efficiencies are also shown. The results have been obtained with SAMPLE 0 (see section 2.3.1). It is evident a degradation of the performance in the overlap region. The reasons for this are not yet fully understood, but could be due to an underestimation of the errors on the parameters of the L2 muon measurement which is used to create the seeds for the track finding algorithm in the inner tracker.

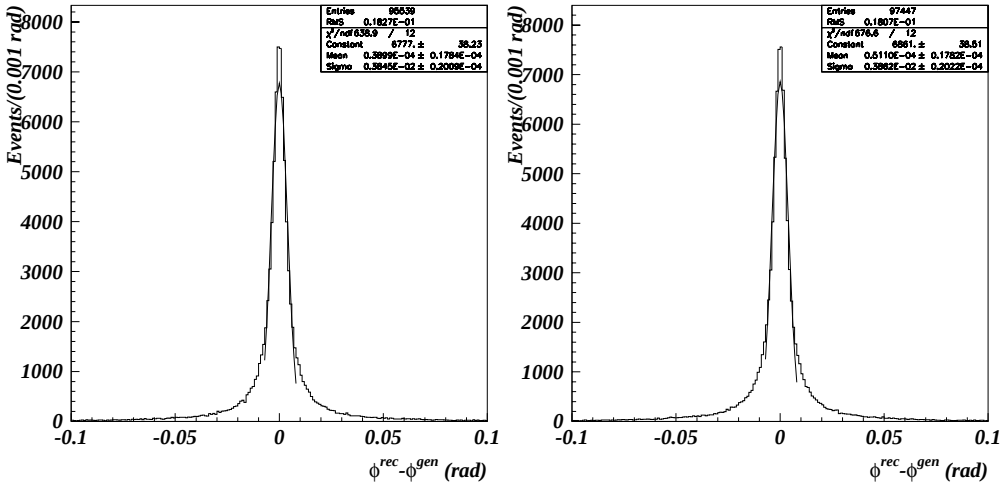


Figure 6.5: L2 $\varphi$ distribution of residuals with (right) and without (left) RPC information.

The L3 $1/p_t$ resolution is shown in Fig. 6.11. The variable $(1/p_t^{rec} - 1/p_t^{gen})/1/p_t^{gen}$ is plotted separately for the barrel ($|\eta| < 0.8$, left plot), overlap ($0.8 < |\eta| < 1.2$, middle plot) and endcap ($1.2 < |\eta| < 2.4$, right plot). The corresponding values of the sigmas of the Gaussian fits are: 1.3%, 1.9% and 2.1%. An improvement of almost one order of magnitude is obtained with respect to L2 in the considered $p_t$ range ($2.5 < p_t < 100$ GeV/c).

The L3 $\varphi$ and $\theta$ residual distribution are shown in Fig. 6.12.

Finally the pull distributions for the variables $1/p_t$, $\varphi$ and $\theta$ are shown in Fig. 6.13. In all cases the sigma of the Gaussian fit is very close to 1. This indicates that the estimation of the errors in the inner tracker detectors is correct.

## 6.4 Signal selection efficiency

In this section the selection efficiency for some representative signal samples will be presented. The following five signal samples have been considered:

1. $H(200\ \mathrm{GeV}/c^2) \longrightarrow Z^0Z^0 \longrightarrow \mu^+\mu^-\mu^+\mu^-$
2. $H(130\ \mathrm{GeV}/c^2) \longrightarrow Z^{0(*)}Z^{0(*)} \longrightarrow \mu^+\mu^-\mu^+\mu^-$
3. $H(160\ \mathrm{GeV}/c^2) \longrightarrow W^+W^- \longrightarrow \mu^+\mu^-\nu_\mu\bar{\nu_\mu}$
4. $B_s^0 \longrightarrow J/\psi\phi \longrightarrow \mu^+\mu^-K^+K^-$

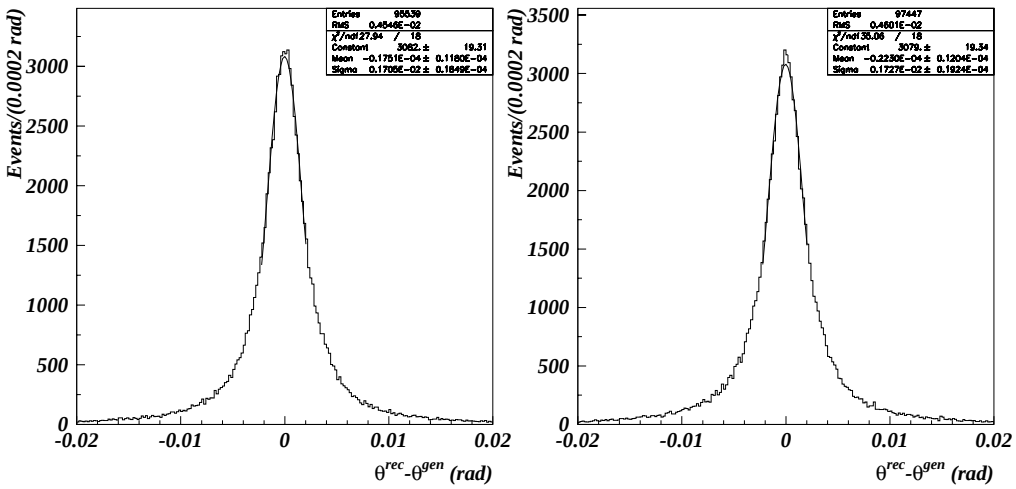


Figure 6.6: L2 $\theta$ distribution of residuals with (right) and without (left) RPC information.

5. $B_d^0 \longrightarrow \pi^+\pi^- + \mu_{tag}$

The channels corresponding to samples 1,2 and 3 have been extensively discussed in chapter 1. In particular the $H \longrightarrow ZZ \longrightarrow 4\mu$ mode is the most useful channel for an intermediate mass Higgs. It could also become an alternative discovery channel for a low mass Higgs, but in this case, compared to $H \longrightarrow \gamma\gamma$, it suffers from lower yield due to the lower total BR. Another difficulty comes from the fact that at least one $Z^0$ is virtual for a Higgs mass below 180 GeV/$c^2$, which prevents from adopting invariant mass constraints on the muon pairs. As already pointed out, the channel $H \longrightarrow WW \longrightarrow 2\mu 2\nu$ is particularly important for a Higgs having a mass around $2m_W$ ($\approx$ 160 GeV/$c^2$) because the BR($H \longrightarrow ZZ$) gets suppressed (see Fig. 1.7). It benefits from a relatively large yield, but much higher background and worse mass resolution are unavoidable due to the presence of the two neutrinos.

Channel 4 is a "gold-plated" mode for the LHC. In addition to the extraction of the $B_s^0 - \bar{B_s^0}$ mixing parameters $\Delta\Gamma_s$ and $\Delta M_s$, it may also allow to measure the Wolfenstein parameter $\eta$ [67]. A particularly interesting feature of $B_s^0 \longrightarrow J/\psi\phi$ decays is that they exhibit tiny CP-violating effects within the SM. Consequently they represent a sensitive probe for CP-violating contributions from physics beyond the SM [68]. Illustrations of the new physics effects in $B_s^0 \longrightarrow J/\psi\phi$ for specific scenarios of new physics can be found in [69]. This channel is of great relevance at the LHC as the $e^+e^-$ B factories operating at the $\Upsilon$(4S) resonance will not be in a position to explore the $B_s$ system. Event selection can be based

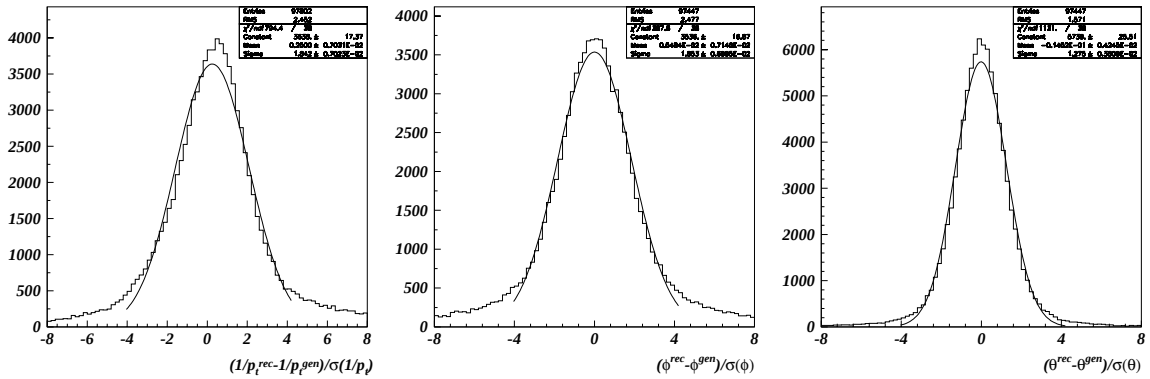


Figure 6.7: L2 pull distributions for the variables $1/p_t$ (left), $\varphi$ (middle) and $\theta$ (right).

on both single and di-muon trigger.
Channel 5 is a benchmark B decay to explore CP violation and to extract the angle $\alpha$ of the unitarity triangle [16, 70]. The observation of $B_d^0 \longrightarrow \pi^+\pi^-$ was announced by the CLEO collaboration in summer 1999 [71] with a branching ratio of $\approx 0.5 \times 10^{-5}$.
As anticipated in chapter 1, B channels are particularly critical from the event selection point of view as the muons involved have a rapidly decreasing $p_t$ spectrum (see e.g. Fig. 1.12).

All samples have been produced with PYTHIA version 6.152. At digitization level every signal event has been superimposed to a number of MB events without muons as expected at the luminosity of $2 \times 10^{33}$ cm$^{-2}$s$^{-1}$.
For what concerns samples 1,2 and 3 all possible Higgs production mechanisms have been switched on and the decay has been forced. All four muons (two in the case of sample 3) were required to satisfy the following kinematical cuts:

- $p_t > 3$ GeV/$c$
- $|\eta| < 2.4$

In the case of sample 4 and 5 particular care has been taken in order to generate the correct angular distribution affected by spin correlation effects (see e.g. [72]) which are not simulated in the standard PYTHIA program. It has been required that the signal muons (one in sample 5) satisfy:

- $|\eta| < 2.4$
- $p_t > 3$ GeV/$c$ in $|\eta| < 1.2$ or

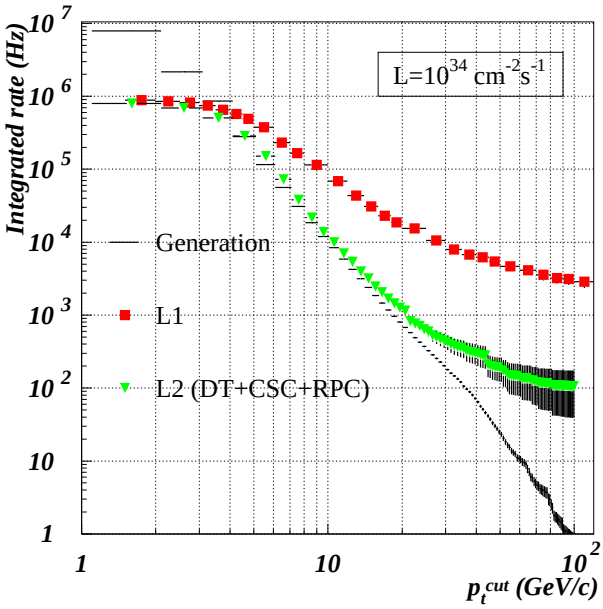


Figure 6.8: L2 (RPC in) single muon rate. The L1 trigger rate (GMT) and the rate at generation level are reported too.

- $p_t > 1.8$ GeV/$c$ in $1.2 < |\eta| < 1.7$ or
- $p > 4.5$ in $1.7 < |\eta| < 2.4$

In all cases the selection is based only on the single muon trigger and on the di-muon trigger although channel 3 can be accessible through an $E_t^{miss}$ single or combined trigger. In what follows the $p_t^{cut}$ adopted in the di-muon trigger will be the same for both muons. It has been proved (see Fig. 6.8) that the L2 is capable to reduce at the same $p_t^{cut}$ the L1 single muon rate by almost one order of magnitude over all the useful $p_t^{cut}$ range: $8 < p_t^{cut} < 100$ GeV/$c$. This may not be true for the di-muon trigger because of the much lower thresholds that have to be applied. Indeed the L2 rejection power decreases by lowering the $p_t^{cut}$. However in the di-muon trigger the L2 rejection power should be higher than that corresponding to the single muon trigger and above all the di-muon trigger rates are much lower than the single muon ones. For these reasons it is assumed that the same L1 thresholds can be adopted at L2 for both the single and the di-muon trigger. This is the choice that has been made to obtain the results that follow.
The selection efficiency in single and di-muon trigger as a function of $p_t^{cut}$ for the five considered samples are shown in Figs. 6.14, 6.15, 6.16, 6.17 and 6.18. In the case of sample

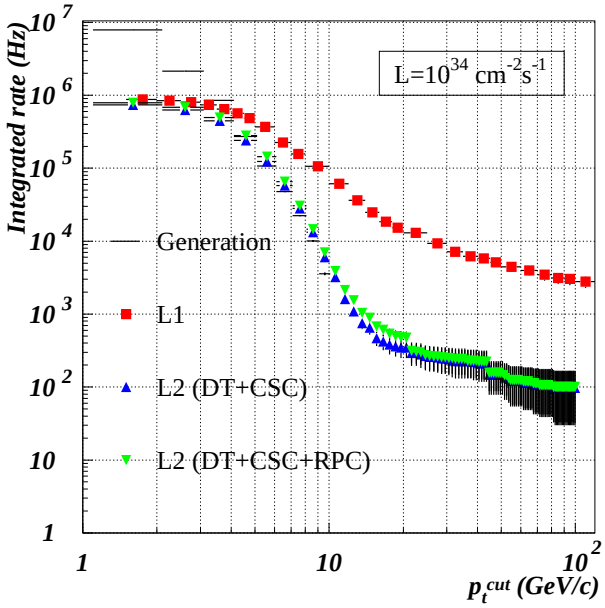


Figure 6.9: Comparison between the L2 single muon rates with and without RPC. The L1 trigger rate (GMT) and the rate at generation level are reported too.

5 only the single muon trigger is considered. In every plot it is shown the efficiency after L1 (dashed line) and after L2 (full histogram). Moreover the events passing L2 are divided according to the number of signal muons that are reconstructed at L3, i.e. are successfully matched with their track reconstructed in the inner tracker.

It can be seen that the Higgs decay mode into 4 muons is easily selected by means of both the single and di-muon trigger. However care must be taken in the matching between the muon system and the inner tracker. The efficiency of this algorithm is the crucial issue in this decay mode. Indeed only about 60% of the events have all four muons successfully reconstructed at L3.

The selection efficiency based on the di-muon trigger for the Higgs decay mode into a $W$ pair is not higher than 90% but it can be complemented with the single muon trigger, which however starts dropping at about 15 GeV/$c$. The combined efficiency will be discussed further on.

Having in mind typical $p_t^{cut}$ values, the channel $B_s^0 \longrightarrow J/\psi\phi$ looks most easily selectable by means of the di-muon trigger, especially if one looks at the fraction of events in which both muons are reconstructed at L3.

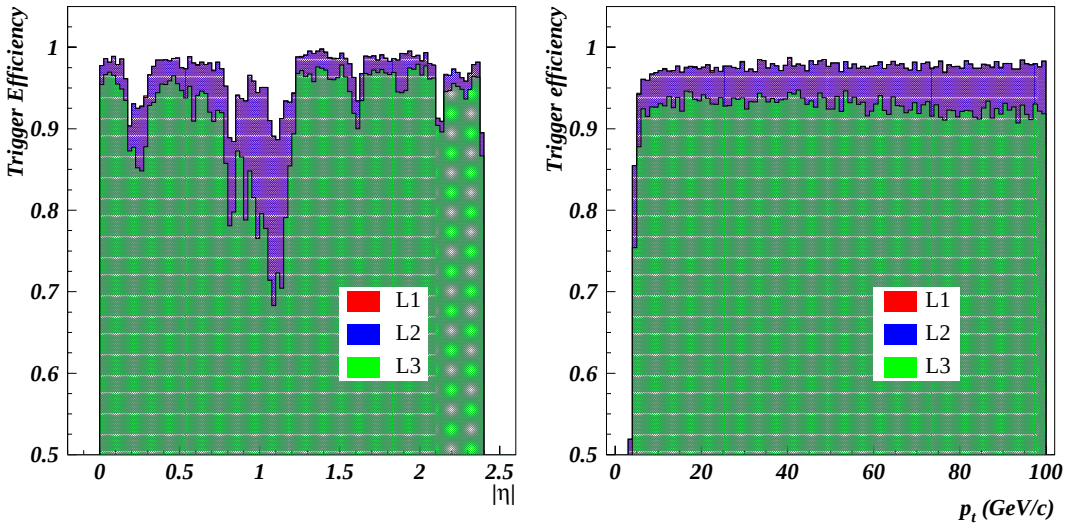


Figure 6.10: L3, L2 and L1 muon reconstruction efficiency as a function of the muon $\eta$ (left) and $p_t$ (right) at generation.

To have an idea of the actual total selection efficiency (obtained with the OR of the two triggers) and of the yield that can be accomplished on these five samples a set of cuts corresponding to three different scenarios from the point of view of the luminosity have been considered. The choice of the $p_t$ thresholds has been based on the requirement that the output rate at L1 of the single and di-muon trigger stays within 12.5 kHz (see Figs. 2.10 and 2.14) with some room left for the other combined triggers involving a muon. The same thresholds are used at L1 and L2. The three scenarios are the following:

1. **High luminosity ($10^{34}$ cm$^{-2}$s$^{-1}$ ):**
   - Single muon trigger: $p_t^{cut} = 35$ GeV/$c$
   - Di-muon trigger: $p_t^{cut} = 4$ GeV/$c$
2. **Medium luminosity ($2 \times 10^{33}$ cm$^{-2}$ s$^{-1}$):**
   - Single muon trigger: $p_t^{cut} = 12$ GeV/$c$
   - Di-muon trigger: $p_t^{cut} = 3$ GeV/$c$
3. **Low luminosity ($10^{33}$ cm$^{-2}$s$^{-1}$ ):**
   - Single muon trigger: $p_t^{cut} = 8$ GeV/$c$

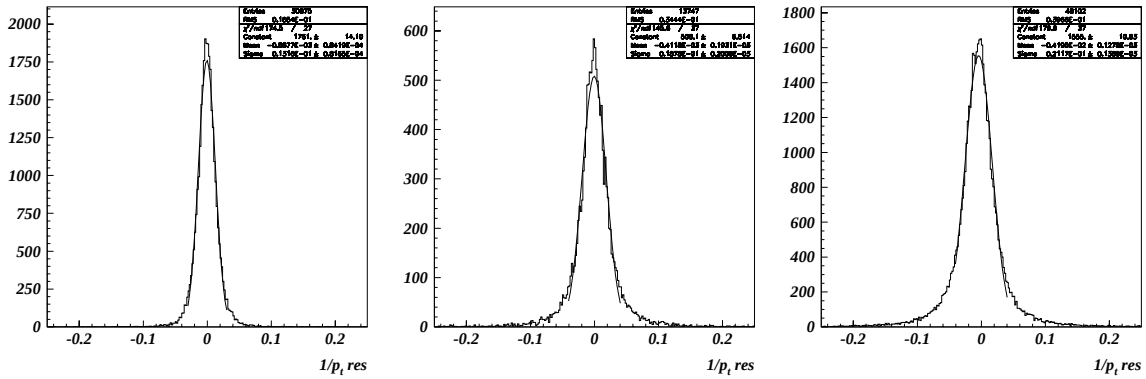


Figure 6.11: L3 $1/p_t$ resolution. The variable $(1/p_t^{rec} - 1/p_t^{gen})/1/p_t^{gen}$ is plotted separately for the barrel ($|\eta| < 0.8$, left), overlap ($0.8 < |\eta| < 1.2$, middle) and endcap ($1.2 < |\eta| < 2.4$, right). The corresponding values of the sigmas of the Gaussian fits are: 1.3%, 1.9% and 2.1%.

- Di-muon trigger: $p_t^{cut} = 2.5$ GeV/$c$

Some comment is necessary concerning the choice of the $p_t^{cut}$ for the di-muon trigger. The contribution marked in Fig. 2.14 as 2 muons from 2 events does not scale linearly with the luminosity, but it can be seen that is not the dominant one at $L = 2 \times 10^{33}$ cm$^{-2}$ s$^{-1}$. Although the L1 di-muon trigger rate is not reported in Fig. 2.14 for $p_t^{cut}$ values as low as 3 and 2.5 GeV/c it has been proved that the L1 rate stays within 1 kHz in both cases in the medium and low luminosity scenarios. In any case, from inspection of the figures showing the di-muon trigger efficiency for the various samples it turns out that the only channel that could be significantly affected by the lowering of the threshold is the $B_s^0 \longrightarrow J/\psi\phi$. In this case the total gain that one can achieve going from 4 to 2.5 GeV/$c$ is not more than a factor 2.

The results are resumed in Tables 6.1, 6.2 and 6.3 for the three considered scenarios. In the second column the cross section, as computed by PYTHIA, for the channel under consideration subject to the kinematical cuts described above is reported. In the third column it is reported the corresponding number of events expected in one year of LHC operation at the considered luminosity. It is assumed that one year of LHC running at low luminosity ($10^{33}$ cm$^{-2}$s$^{-1}$ ) corresponds to an integrated luminosity of 10 fb$^{-1}$ (about 2 full months of data taking). In the medium and high luminosity scenario one year of running corresponds to 20 and 100 fb$^{-1}$ of integrated luminosity respectively. Column 4 reports the selection efficiency at L1. For each channel column 5 contains in the first line the selection

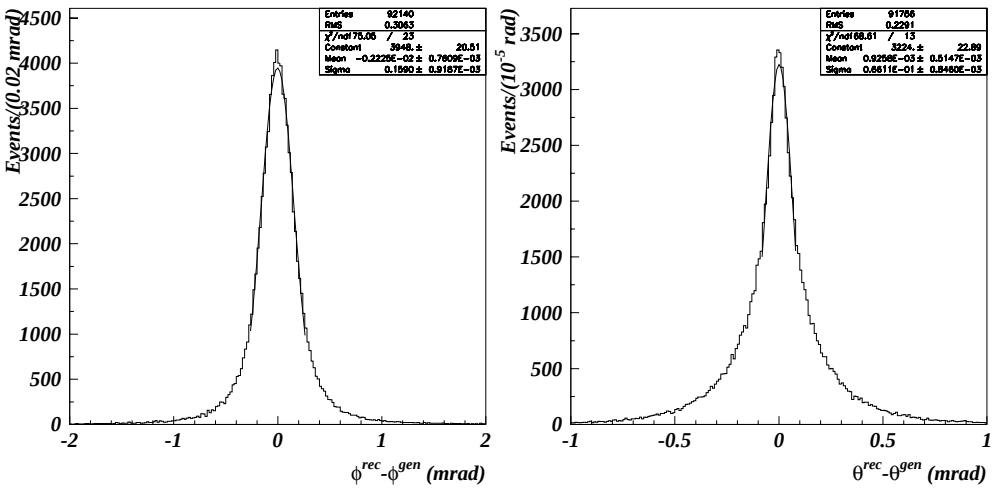


Figure 6.12: L3 $\varphi$ (left) and $\theta$ (right) residual distribution.

efficiency after L2 and in the lines below the fractions of events passing L2 and having a certain number (indicated in parenthesis) of signal muons successfully reconstructed at L3. Finally the number of events per year passing L2 and subdivided according to the number of successfully reconstructed signal muons at L3 is reported in column 6.

It can be seen that the Higgs into four muons is selected with full efficiency after L2 even with the severe cuts adopted in the high luminosity scenario. The yield, however, appears very low in the low and medium luminosity scenario due to the extremely low cross sections. The efficiency for selecting $H(160\ \mathrm{GeV}/c^2) \longrightarrow W^+W^- \longrightarrow 2\mu 2\nu$ after L2 is above 95% in all cases.

The absolute efficiency obtained on the B channels actually depends on the looseness of the adopted kinematical cuts and therefore it is not very significant. More meaningful is to look at the final yield. For what concerns the channel $B_s^0 \longrightarrow J/\psi\phi$ the period that looks most fruitful seems to be the high luminosity scenario, which despite the lower efficiency due to the more severe cuts benefits from the larger production rate. However the final reconstruction efficiency will be surely much lower due to the large number of pile-up events expected at high luminosity. At low luminosity the number of events per year with both muons reconstructed at L3 is about $10^6$, which is a quite remarkable result.

Finally the channel $B_d^0 \longrightarrow \pi^+\pi^-$, which can only rely on the single muon trigger, looks feasible only at low or medium luminosity. Its yield after L2 is maximum at low luminosity and is of about $3 \times 10^3$ events per year.

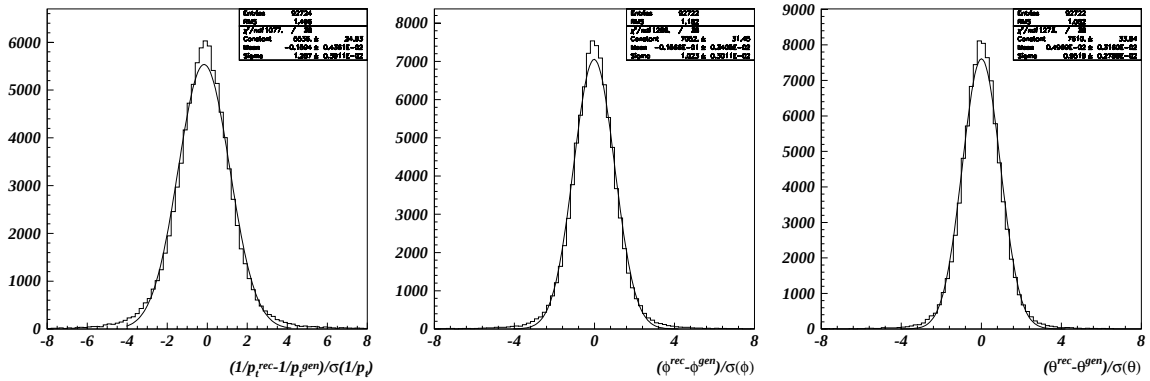


Figure 6.13: L3 pull distributions for the variables $1/p_t$ (left), $\varphi$ (middle) and $\theta$ (right).

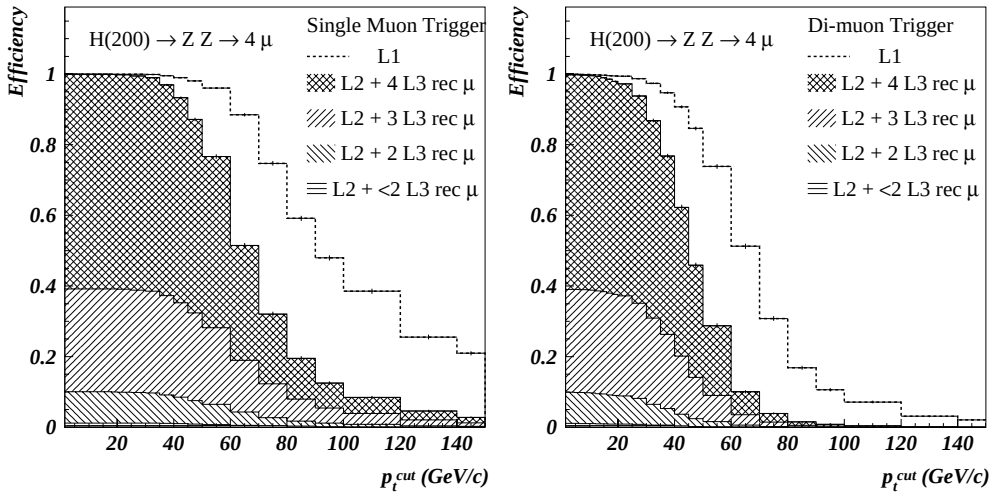


Figure 6.14: Single (left) and di-muon (right) trigger efficiency as a function of $p_t^{cut}$ for the channel $H(200\ \mathrm{GeV}/c^2) \longrightarrow Z^0Z^0 \longrightarrow \mu^+\mu^-\mu^+\mu^-$. The fraction of events passing L2 is further divided according to the number of signal muons that are successfully reconstructed at L3. The sample is subject to the kinematical cuts described in the text.

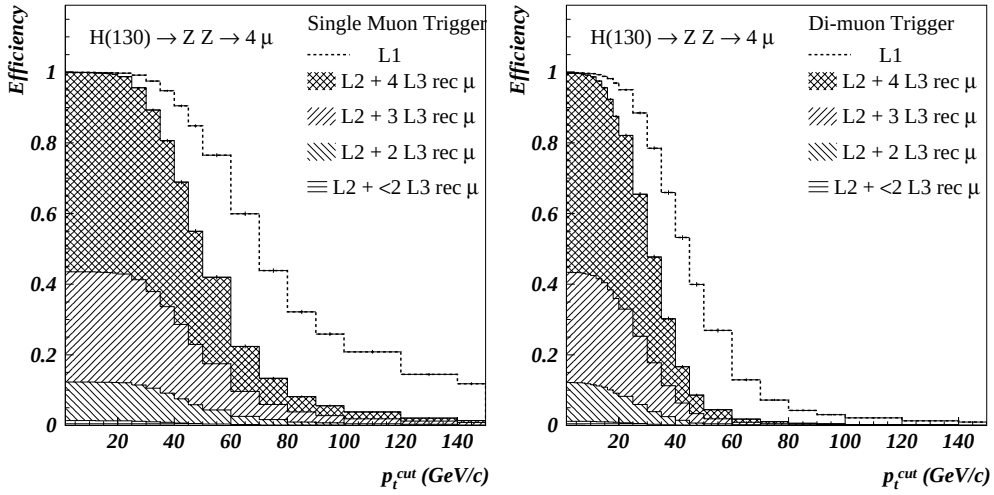


Figure 6.15: Single (left) and di-muon (right) trigger efficiency as a function of $p_t^{cut}$ for the channel $H(130\ \mathrm{GeV}/c^2) \longrightarrow Z^0Z^0 \longrightarrow \mu^+\mu^-\mu^+\mu^-$. The fraction of events passing L2 is further divided according to the number of signal muons that are successfully reconstructed at L3. The sample is subject to the kinematical cuts described in the text.

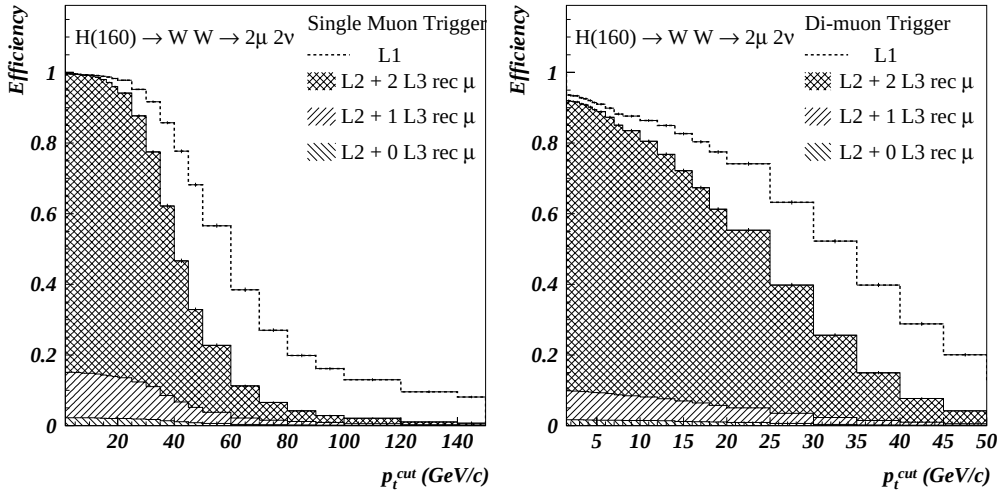


Figure 6.16: Single (left) and di-muon (right) trigger efficiency as a function of $p_t^{cut}$ for the channel $H(160\ \mathrm{GeV}/c^2) \longrightarrow W^+W^- \longrightarrow \mu^+\mu^-\nu_\mu\bar{\nu_\mu}$. The fraction of events passing L2 is further divided according to the number of signal muons that are successfully reconstructed at L3. The sample is subject to the kinematical cuts described in the text.

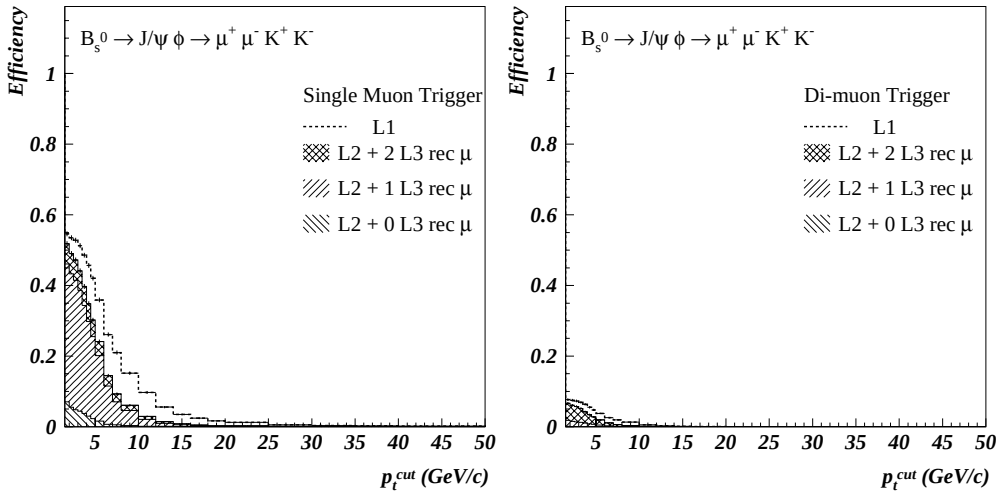


Figure 6.17: Single (left) and di-muon (right) trigger efficiency as a function of $p_t^{cut}$ for the channel $B_s^0 \longrightarrow J/\psi\phi \longrightarrow \mu^+\mu^-K^+K^-$. The fraction of events passing L2 is further divided according to the number of signal muons that are successfully reconstructed at L3. The sample is subject to the kinematical cuts described in the text.

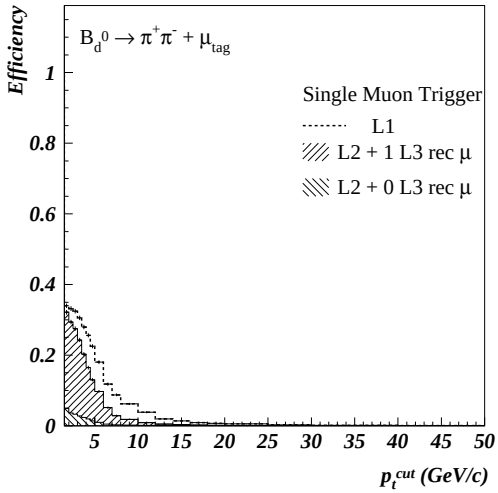


Figure 6.18: Single muon trigger efficiency as a function of $p_t^{cut}$ for the channel $B_d^0 \longrightarrow \pi^+\pi^- + \mu_{tag}$. The fraction of events passing L2 is further divided according to the number of signal muons that are successfully reconstructed at L3. The sample is subject to the kinematical cuts described in the text.

| $L = 10^{34}$ cm$^{-2}$s$^{-1}$ , $p_t^{cut}(single\ \mu) = 35$ GeV/$c$ , $p_t^{cut}(double\ \mu) = 4$ GeV/$c$ | | | | | |
|---|---|---|---|---|---|
| | $\sigma$(nb) | Events per year (100 fb$^{-1}$) | $\epsilon_{L1}$ | $\epsilon_{L2}$ | Events per year after L2 |
| $H(200)$ | $2.15 \times 10^{-6}$ | 215 | 100.0% | 100.0% | 215 |
| | | | | ——— | ——— |
| | | | | 60.8%(4) | 131 |
| | | | | 29.2%(3) | 63 |
| | | | | 8.9%(2) | 19 |
| | | | | 1.1%(1) | 2 |
| | | | | 0.0%(0) | 0 |
| $H(130)$ | $5.08 \times 10^{-7}$ | 51 | 99.9% | 99.8% | 51 |
| | | | | ——— | ——— |
| | | | | 56.5%(4) | 29 |
| | | | | 31.3%(3) | 16 |
| | | | | 11.0%(2) | 6 |
| | | | | 1.2%(1) | 1 |
| | | | | 0.0%(0) | 0 |
| $H(160)$ | $1.38 \times 10^{-4}$ | 13800 | 97.0% | 95.4% | 13159 |
| | | | | ——— | ——— |
| | | | | 87.1%(2) | 11460 |
| | | | | 10.8%(1) | 1427 |
| | | | | 2.1%(0) | 272 |
| $B_s$ | 1.96 | $1.96 \times 10^8$ | 5.7% | 3.4% | $6.7 \times 10^6$ |
| | | | | ——— | ——— |
| | | | | 76.3%(2) | $5.1 \times 10^6$ |
| | | | | 23.2%(1) | $1.6 \times 10^6$ |
| | | | | 0.5%(0) | $4. \times 10^4$ |
| $B_d$ | $1.54 \times 10^{-2}$ | $1.54 \times 10^6$ | 0.5% | 0.13% | $2.0 \times 10^3$ |
| | | | | ——— | ——— |
| | | | | 85%(1) | $1.7 \times 10^3$ |
| | | | | 15%(0) | $0.3 \times 10^3$ |

Table 6.1: Prospect of selection efficiency after L1 and L2 for some representative signal samples at $L = 10^{34}$ cm$^{-2}$s$^{-1}$. The adopted cuts are the same at L1 and L2 and are indicated at the top of the table. The $p_t^{cut}$ is common to both muons in the di-muon trigger. The cross section for each sample is the one computed by PYTHIA after the kinematical cuts described in the text. The events per year and the yield after L2 are computed assuming an integrated luminosity of 100 fb$^{-1}$. The efficiency and the yield after L2 are further subdivided according to the number of signal muons (indicated in parenthesis) that are successfully reconstructed at L3.

| $L = 2 \times 10^{33}$ cm$^{-2}$s$^{-1}$ , $p_t^{cut}(single\ \mu) = 12$ GeV/$c$ , $p_t^{cut}(double\ \mu) = 3$ GeV/$c$ | | | | | |
|---|---|---|---|---|---|
| | $\sigma$(nb) | Events per year (20 fb$^{-1}$) | $\epsilon_{L1}$ | $\epsilon_{L2}$ | Events per year after L2 |
| $H(200)$ | $2.15 \times 10^{-6}$ | 44 | 100.0% | 100.0% | 44 |
| | | | | —— | —— |
| | | | | 60.8%(4) | 26 |
| | | | | 29.2%(3) | 12 |
| | | | | 8.9%(2) | 4 |
| | | | | 1.1%(1) | 0 |
| | | | | 0.0%(0) | 0 |
| $H(130)$ | $5.08 \times 10^{-7}$ | 10 | 99.9% | 99.9% | 10 |
| | | | | —— | —— |
| | | | | 56.5%(4) | 6 |
| | | | | 31.3%(3) | 3 |
| | | | | 11.0%(2) | 1 |
| | | | | 1.2%(1) | 0 |
| | | | | 0.0%(0) | 0 |
| $H(160)$ | $1.38 \times 10^{-4}$ | 2760 | 99.3% | 99.1% | 2736 |
| | | | | —— | —— |
| | | | | 85.1%(2) | 2330 |
| | | | | 12.7%(1) | 346 |
| | | | | 2.2%(0) | 60 |
| $B_s$ | 1.96 | $3.92 \times 10^7$ | 10.4% | 6.1% | $2.4 \times 10^6$ |
| | | | | —— | —— |
| | | | | 66.5%(2) | $1.6 \times 10^6$ |
| | | | | 31.6%(1) | $0.8 \times 10^6$ |
| | | | | 1.9%(0) | $5 \times 10^4$ |
| $B_d$ | $1.54 \times 10^{-2}$ | $3.08 \times 10^5$ | 2.4% | 0.6% | $2.0 \times 10^3$ |
| | | | | —— | —— |
| | | | | 94%(1) | $1.9 \times 10^3$ |
| | | | | 6%(0) | $0.1 \times 10^3$ |

Table 6.2: Prospect of selection efficiency after L1 and L2 for some representative signal samples at $L = 2 \times 10^{33}$ cm$^{-2}$s$^{-1}$. The adopted cuts are the same at L1 and L2 and are indicated at the top of the table. The $p_t^{cut}$ is common to both muons in the di-muon trigger. The cross section for each sample is the one computed by PYTHIA after the kinematical cuts described in the text. The events per year and the yield after L2 are computed assuming an integrated luminosity of 20 fb$^{-1}$. The efficiency and the yield after L2 are further subdivided according to the number of signal muons (indicated in parenthesis) that are successfully reconstructed at L3.

| $L = 10^{33}$ cm$^{-2}$s$^{-1}$ , $p_t^{cut}(single\ \mu) = 8$ GeV/$c$ , $p_t^{cut}(double\ \mu) = 2.5$ GeV/$c$ | | | | | |
|---|---|---|---|---|---|
| | $\sigma$(nb) | Events per year (10 fb$^{-1}$) | $\epsilon_{L1}$ | $\epsilon_{L2}$ | Events per year after L2 |
| $H(200)$ | $2.15 \times 10^{-6}$ | 22 | 100.0% | 100.0% | 22 |
| | | | | —— | —— |
| | | | | 60.8%(4) | 13 |
| | | | | 29.2%(3) | 6 |
| | | | | 8.9%(2) | 2 |
| | | | | 1.1%(1) | 0 |
| | | | | 0.0%(0) | 0 |
| $H(130)$ | $5.08 \times 10^{-7}$ | 5 | 99.9% | 99.9% | 5 |
| | | | | —— | —— |
| | | | | 56.5%(4) | 3 |
| | | | | 31.3%(3) | 2 |
| | | | | 11.0%(2) | 0 |
| | | | | 1.2%(1) | 0 |
| | | | | 0.0%(0) | 0 |
| $H(160)$ | $1.38 \times 10^{-4}$ | 1380 | 99.4% | 99.3% | 1371 |
| | | | | —— | —— |
| | | | | 85.0%(2) | 1165 |
| | | | | 12.8%(1) | 176 |
| | | | | 2.2%(0) | 30 |
| $B_s$ | 1.96 | $1.96 \times 10^7$ | 18.4% | 10.3% | $2.00 \times 10^6$ |
| | | | | —— | —— |
| | | | | 45.2%(2) | $0.90 \times 10^6$ |
| | | | | 51.2%(1) | $1.00 \times 10^6$ |
| | | | | 3.6%(0) | $0.1 \times 10^6$ |
| $B_d$ | $1.54 \times 10^{-2}$ | $1.54 \times 10^5$ | 6.5% | 2.0% | $3.0 \times 10^3$ |
| | | | | —— | —— |
| | | | | 90%(1) | $2.7 \times 10^3$ |
| | | | | 10%(0) | $0.3 \times 10^3$ |

Table 6.3: Prospect of selection efficiency after L1 and L2 for some representative signal samples at $L = 10^{33}$ cm$^{-2}$s$^{-1}$. The adopted cuts are the same at L1 and L2 and are indicated at the top of the table. The $p_t^{cut}$ is common to both muons in the di-muon trigger. The cross section for each sample is the one computed by PYTHIA after the kinematical cuts described in the text. The events per year and the yield after L2 are computed assuming an integrated luminosity of 10 fb$^{-1}$. The efficiency and the yield after L2 are further subdivided according to the number of signal muons (indicated in parenthesis) that are successfully reconstructed at L3.

# Conclusions

The work presented in this thesis has concerned the muon system of the CMS experiment at the LHC. The CMS muon system comprises two subsystems of detectors: one of them is based on precise wire chambers, the other on fast planar detectors, the Resistive Plate Chambers (RPCs). The work has focused on the latter.

First it has been shown the performance of the First Level Muon Trigger of CMS. The combined use of both types of detectors results in a high performance trigger system which is capable to achieve high efficiency and low ghost occurrence with large control of the output rate. The results have been presented without inclusion of neither RPC noise nor spurious hits due to the neutral particle background.
At that point it was anticipated one of the main results obtained in this thesis: RPC noise (for values typical of non-oiled chambers, like the ones originally proposed for CMS) and neutral background hits drastically affect the performance of the RPC trigger that would then need important modifications.

Beam test experimental results on the performance of two RPC prototypes for CMS have been presented in chapter 3. The two detectors are equal in all respects but in the gap width (2 and 3 mm). Their efficiency and timing properties have been studied in great detail with emphasis on the possible spatial variations and disuniformities.
Disuniformities are particularly feared as they could spoil the global RPC timing performance and reduce the useful HV operating range. Previous studies had shown an important degradation of the global performance due to disuniformities, which were mainly localised around the gap spacers. In that case the spacers were staggered in the two gaps to avoid dead areas. To reduce disuniformities it was decided to adopt a more robust mechanical design with overlapped spacers. The chambers under test are the first built with this new design.
Both tested detectors have shown high global efficiency ($> 98\%$). Disuniformities have been observed on both detectors, but great improvements have been made with respect to detectors built with the old design. The impact of disuniformities on the RPC global

performance is less important in the 2 mm chamber. However the main advantage of the 2 mm gap RPC is its superior timing properties.

The detailed study of the performance of the baseline CMS RPC trigger system has been presented in chapter 4. Emphasis has been put on the impact of the detector parameters: efficiency, timing properties, strip multiplicity and intrinsic noise. Neutral particle background hits have been simulated too.
It has been demonstrated that the trigger system is particularly sensitive to drops in RPC efficiency. Particular care should then be taken in order to ensure that all chambers have an efficiency well above 90%. Time resolution appears not be an issue provided precise adjustment of the time gates is achieved. It has also been shown that the contribution to the total rate from decay muons is very similar to that from prompt muons. In both cases the increase of the trigger rate caused by "muon promotion" is not important. Strip multiplicity causes the rate to increase significantly (almost a factor 2 with respect to the ideal case).
However the main result is the contribution of false triggers to the total rate. It has been shown that the problem is particularly relevant if the noise rate is higher than 20 Hz $cm^{-2}$, which is definitely the case for non-oiled chambers. This result has raised the painful point of oiling or not the internal surface of the RPC electrodes. Aging effects are feared in case of use of oil, which on the other hand reduce the noise by more than one order of magnitude. Aging effects have not been treated in this thesis. Instead modifications of the RPC trigger system have been proposed in chapter 5. Full use of all RPC planes in the barrel and possible insertion of extra planes in both barrel and endcap have been examined. Use of information from the wire chambers in order to reject false triggers has been studied too. The results indicate that the RPC trigger performance can be largely improved. A full resolution 4 out of 6 coincidence algorithm could solve the problem in the barrel region. In the endcap, where the false triggers are anyway less frequent, an additional detector layer would be extremely useful and could be enough to provide a robust system.
Use of information from the wire chamber triggers has been proved to represent an additional powerful shield against the false triggers delivered by the RPC trigger.

The performance of the CMS High Level Trigger in muon track reconstruction has been presented in chapter 6. For the first time RPC information has been used in muon track reconstruction. Use of RPCs allows to recover the L2 trigger inefficiency (3-4%) with respect to the L1 trigger. At the same time the L2 trigger output rate is not significantly increased and meets the goal of reducing by one order of magnitude the L1 trigger rate.
Finally the selection efficiency of the First and High Level Trigger has been studied for some representative signal samples. It has been demonstrated that the Higgs decay modes

$H \longrightarrow Z^0 Z^0 \longrightarrow \mu^+\mu^-\mu^+\mu^-$ and $H \longrightarrow W^+W^- \longrightarrow \mu^+\mu^-\nu_\mu\bar{\nu_\mu}$ can be selected with full efficiency at any luminosity. However improvements are needed in the matching algorithm between the muon system and the inner tracker. The event yield for the B physics benchmark mode $B_s^0 \longrightarrow J/\psi\phi \longrightarrow \mu^+\mu^-K^+K^-$ looks promising. More critical is the channel $B_d^0 \longrightarrow \pi^+\pi^- + \mu_{tag}$ whose event yield strongly depends on the single muon trigger $p_t$ threshold. It seems hard to push this threshold below 8 GeV/$c$ even at low luminosity.

# Bibliography


[1] C. Quigg, *"Gauge Theories of the Strong, Weak and Electromagnetic Interactions"*, Benjamin-Cummings, Reading (1983).

[2] S.L. Glashow, Nucl. Phys. 22 (1961) 579;
S. Weinberg, phys. Rev. Lett. 19 (1967) 1264;
A. Salam, Proc. 8th Nobel Symposium , Stockholm 1968, ed. N. Svartholm (Almqvist and Wiksells, Stockholm 1968), p. 367.

[3] Results presented at the XXXth International Conference on High Energy Physics, Osaka (2000).

[4] A. Linde, JETP Lett. 12 (1976) 64; Phys. Lett. B62 (1976) 435;
S. Weinberg, Phys. Rev. Lett. 36 (1976) 294;
S. Coleman and E. Weinberg, Phys. Rev. D7 (1973) 188.

[5] S. Dawson, *"The Standard Model intermediate mass Higgs boson"*, in the Perspectives on Higgs Physics II, ed. Gordon L. Kane, World Scientific (1997).

[6] G. Altarelli and G. Isidori, Phys. Lett. B337(1994).

[7] C. Tully, *"Status of LEP-wide Higgs searches"*, talk presented at LEPC Seminar, CERN, Geneva, September 5, 2000.

[8] L. Susskind, Phys. Rev. D20 (1979) 2619;
G. 't Hooft *"Recent Developments in Gauge Theories"*, ed. G. 't Hooft et al. (Plenum Press, 1980).

[9] P. Ramond, Phys. Rev. D3 (1971) 2415.
A. Neveu and J.H. Schwarz, Phys. Rev. D4 (1971) 1109.

[10] D.V. Volkov and V.P. Akulov, Phys. Lett. 46B (1973) 109.

[11] J. Wess and B. Zumino, Nucl. Phys. B70 (1974) 39.

[12] J. Iliopoulos and B. Zumino, Nucl. Phys. B76 (1974) 310.
S. Ferrara, J. Iliopoulos and B. Zumino, Nucl. Phys. 77 (1974) 413.

[13] D.Z. Freedman, P. van Nieuwenhuizen and S. Ferrara, Phys. Rev. D13 (1976) 3214.

[14] S. Deser and B. Zumino, Phys. Lett. 62B (1976) 335.

[15] D. Bailin and A. Love *"Supersymmetric Gauge Field Theory and String Theory"*, published by Institute Of Physics Publishing, London, 1996.

[16] C. Jarlsmog *"Phenomenology of CP violation"*, eds. J. Bernabeu, A. Ferrer, J. Velasco, World Scientific.

[17] J. H. Christenson et al., Phys. Rev. Lett. 13 (1964) 138.

[18] D. Denegri, *"Standard Model physics at the LHC"*, in Proceedings of the Large Hadron Collider Workshop vol. I (1990) 55, CERN, Geneva, October 1990.

[19] M. Spira, *"QCD Effects in Higgs Physics"*, hep-ph/9705337.

[20] R. N. Cahn, Rep. Prog. Phys. 52 (1989) 389.

[21] B. W. Lee, C. Quigg and H. B. Thacker, Phys. Rev. D16 (1977) 1519.

[22] T. G. Rizzo, Phys. Rev. D22 (1980) 389;
W. Y. Keung and W. J. Marciano, Phys. Rev. D30 (1984) 248.

[23] P. Fayet e S. Ferrara, Physics Reports 32C (1977) 249.

[24] T. Sjostrand, *"PYTHIA 5.7 and JETSET 7.4 Physics and Manual"*, CERN-TH 7112/93.

[25] B. Muller, *"The physics of the Quark Gluon Plasma"*, Lecture Notes in Physics (1985) 255.

[26] H. Satz, Proceedings of Hot Hadronic Matter: theory and experiment, ed. by Letessier et al., Plenum Press, New York (1995).

[27] RD5 Collaboration (C. Albajar et al.), CERN-PPE-95-061, May 1995. Published in Z.Phys.C69:415-426,1996.

[28] A. Beretvas et al., *"Dijet Mass Resolution at High Luminosity in the CMS Calorimeter"*, CMS TN/94-326 (1994).
W. Wu et al., Proceedings of MC93 (International Conference on Monte Carlo Simulation in High Energy and Nuclear Physics), Tallahassee, 1993, World Scientific (1993).

[29] R. S. Gilmore, *"Single particle Detection and Measurement"*, Taylor and francis (1992).

[30] E. Conti et al., *"Experimental Test of the Q2 Drift Tubes prototype Chamber for the CMS Muon Barrel"*, CMS Note/97-019.

[31] G. Charpak et al., Nucl. Instr. and Meth. 167 (1979) 455.

[32] F. Gasparini et al., Nucl. Instr. and Meth. A 336 (1993) 91.

[33] CMS detector simulation software group, *"CMS Simulation Package CMSIM - Users' Guide and Reference Manual"*,
http://cmsdoc.cern.ch/cmsim/manual/cms121/manual.html.

[34] *"GEANT – Detector Description and Simulation Tool"*, CERN Program Library Long Writeup W5013.

[35] *"ORCA 5.3.1- User Guide"*,
http://cmsdoc.cern.ch/orca/Manuals/UserGuide_ORCA_5_3_1/html/UserGuide.html

[36] N. Neumeister et al., *"Monte Carlo simulation for High Level Trigger studies in single and di-muon topologies"*, CMS IN 2000/053.

[37] A. Fengler et al., *"Ghosts Buster for the RPC Based Muon Trigger"*, CMS NOTE-1998/012.

[38] G. Bressi et al., *"An apparatus to search for free neutron-antineutron oscillations"*, Nucl. Instr. and Meth. A261 (1987) 449-461;
A. Antonelli at al., *"The FENICE detector at the e+e- collider ADONE"*, Nucl. Instr. and Meth. A337 (1993) 34-43;
E. Gorini, *"The Resistive Plate Counter muon system of E771"*, Nucl. Instr. and Meth. B (Proc. Suppl.) 23A (1991) 249-253;
C. Bacci et al., *"A hodoscope made of Resistive Plate Chambers to identify muons in a fixed target beauty hadroproduction experiment"*, Nucl. Instr. and Meth. A324 (1993) 83-92; P. D. Sheldon, *"The FOCUS experiment RPC Muon identification array"*, Proc. of the III Int. Workshop on Resistive Plate Chambers and Related Detectors, 11-12 Oct.

1995, Pavia, Italy, Scientifica Acta (Ed. S.P.Ratti, M. Merlo) XI (1996) 437-444;
M. Abbrescia et al., *"A horizontal muon telescope implemented with Resistive Plate Chambers"*, Nucl. Instr. and Meth. A336 (1993) 322-329.

[39] A. Aloisio et al., *"The L3 forward-backward muon RPC trigger system"*, Nucl. Instr. and Meth. A360 (1995) 340.

[40] The BABAR Collaboration, Technical Design Report (march 1995).

[41] The ATLAS Collaboration, Technical Design Report, CERN/LHCC/97-22.

[42] E.D. Lozanskii, *"Development of electron avalanches and streamer"*, Usp.Fiz.Nauk 117 (1978) 493.

[43] J.W. Keuffel, Phys. Rev. 73 (1948) 531; Rev. Sci. Instr. 20 (1949) 202.

[44] Y.N. Pestov e G.V. Fedotovich, Preprint IYAF 77-78, SLAC Translation 184 (1978);
Y.N. Pestov, Nucl. Instr. and Meth. 196 (1982) 45.

[45] R. Santonico e R. Cardarelli, Nucl. Instr. and Meth. 187 (1981) 377.

[46] M. Abbrescia et al., *"Effect of the linseed oil surface treatment on the performance of Resistive Plate Chambers"*, Nucl. Instr. and Meth. A394 (1997) 13.

[47] R. Cardarelli et al., Nucl. Instr. and Meth. A263 (1988) 20.

[48] M.Bertino et al., Nucl. Instr. and Meth. A283 (1989) 654;
A. Bohrer et al., CERN/DRDC/91-53 (1992).

[49] M. Abbrescia et al., *"The simulation of resistive plate chambers in avalanche mode: charge spectra and efficiency"*, Nucl. Instr. and Meth. A431 (1999), 413.

[50] H. Fishle et al., *"Experimental determination of ionization cluster size distributions"*, Nucl. Instr. and Meth. 301 (1991) 202.

[51] F. Lapique et al., *"Simulation of the measurement by primary cluster counting of the energy lost by a relativistic ionising particle in argon"*, Nucl. Instr. and Meth. 175 (1980) 297.

[52] H. Genz et al., *"Single electron detection in proportional gas counter"*, Nucl. Instr. and Meth. 112 (1973) 83.

[53] M. Abbrescia et al., *"Resistive Plate Chambers in avalanche mode: a comparison between model predictions and experimental results"*, Nucl. Instr. and Meth. 409 (1998) 1.

[54] P. Camarri et al., *"Streamer suppression with SF-6 in RPCs operated in avalanche mode"*, Nucl. Instr. and Meth. A414 (1998) 317.

[55] General Tecnica, Private Communication.

[56] A. Manarin et G. Vismara, *"The delay wire chamber description"*, LEP/BI-TA/Note 85-3.

[57] M. Abbrescia at al., *"Beam test results on double-gap Resistive Plate Chambers proposed for the CMS experiment"*, CMS Note 1997-062, Nucl. Instr. and Meth. A414 (1998) 135.

[58] G. Bruno et al., *"RPC System Geometry Simulated in CMSIM 118-120 and ORCA 4.2"*, CMS IN-2000/054.

[59] M. Gorski et al., *"High Speed Data Transmission and Compression for the CMS RPC Muon Trigger"*, Proceedings of the 3rd Workshop on LHC Electronics, London 1998.

[60] M. Konecki et al., *"Simulation study of the single muon RPC based trigger for CMS"*, CMS TN/92-039.

[61] M. Cwiok and G. Wrochna, *"Muon rates in UA1, D0, CDF and CMS predicted by PYTHIA 5.7"*, CMS TN-1995/150.

[62] G. Bruno et al., *"RPC Pattern Comparator Trigger Simulation in CMSIM 121 and ORCA 4.4"*, CMS Internal Note in preparation.

[63] C. Zeinitz, T.A. Gabriel, *"The GEANT-CALOR interface and benchmark calculations of ZEUS test calorimeters"*, Nucl. Instr. and Meth. A(1994)106-111.

[64] M. Abbrescia et al., CMS NOTE in preparation.

[65] R. Veenhof, *"Garfield, a Drift-Chamber Simulation Program user's guide"*, CERN Program Library W5050, 1994.

[66] R. E. Kalman, *"A New Approach to Linear Filtering and prediction problems"*, transaction of the ASME-Journal of Basic Engineering, pp. 35-45 (March 1960).

[67] R. Fleischer and I. Dunietz, Phys. Rew. D55 (1997) 259.
A.S. Dighe, I. Dunietz and R. Fleischer, Eur. Phys. J. C6 (1999) 647.

[68] Y. Nir and D. Silverman, Nucl. Phys. B345 (1990) 301.

[69] D. Silverman, Phys. Rew. D58 (1998) 095006.
P. Ball and R. Fleischer, Phys. Lett. B475 (2000) 111.

[70] M. Gronau and D. london, Phys. Rew. Lett. 65 (1990) 3381.
H. Lipkin et al., Phys. Rew. D44 (1991) 1454.

[71] D. E. Jaffe (CLEO Coll.), hep-ex/9910055.

[72] A.S. Dighe, I. Dunietz and R. Fleischer, hep-ph/9804253.

# List of Figures

# List of Tables

# *Acknowledgements*

*I wish to spend a few words on the human side behind this thesis. I am grateful to my tutor, Prof. Sergio P. Ratti for having supported me in these three years of doctorate, interrupted by a break of 14 months in which I have served my country. I wish to thank Dr. Daniel Denegri for having read carefully my thesis and for the advice he has given me. I am also grateful to several people that have helped me in different ways during all this time: Giuseppe Iaselli, Grzegorz Wrochna, Hannes Sakulin, Marcello Maggi, Marcin Konecki, Nicola Amapane, Norbert Neumeister, Paolo Vitulo, Stefano Lacaprara and Yves Lemoigne. This is a good place to thank a long series of people for their closeness: my family and all my friends.*